



Coupled Thermo-Hydro-Mechanical- Chemical Behaviour Of MX80 Bentonite In Geotechnical Applications

RAMAKRISHNA BAG

Geoenvironmental Research Centre
Cardiff School of Engineering
Cardiff University

Thesis submitted in candidature for the degree of Doctor of Philosophy at
Cardiff University
November 2011

DECLARATION

This work has not previously been accepted in substance for any degree and is not concurrently submitted in candidature for any degree.

Signed (Ramakrishna Bag)

Date30/11/2011.....

STATEMENT 1

This thesis is being submitted in partial fulfilment of the requirements for the degree of Doctor of Philosophy (PhD).

Signed (Ramakrishna Bag)

Date30/11/2011.....

STATEMENT 2

This thesis is the result of my own independent work/investigation, except where otherwise stated. Other sources are acknowledged by explicit references.

Signed (Ramakrishna Bag)

Date30/11/2011.....

STATEMENT 3

I hereby give consent for my thesis, if accepted, to be available for photocopying and for inter-library loan, and for the title and summary to be made available to outside organisations.

Signed (Ramakrishna Bag)

Date30/11/2011.....

Acknowledgements

I would like to sincerely thank my supervisors Dr. Snehasis Tripathy and Professor Hywel Rhys Thomas for their continuous support, motivation and invaluable academic guidance throughout this research, without their support this thesis would not become a reality.

I would like to express my gratitude to Dr. Philip Vardon for his help during my computational work.

The invaluable financial support for this research through PhD fellowships from the Cardiff School of Engineering and the Geoenvironmental Research Centre is gratefully acknowledged. The travel grant provided by ARC for conducting experimental work in Germany is deeply acknowledged.

The ENGIN technical support staffs deserve a very special thanks especially: Len, Harry, Brian, Paul, Ravi, Jeff, Martin and Des for their enormous support during my laboratory work.

I am thankful to Professor Tom Schanz for allowing me to use the chilled-mirror hygrometer during my visit to Ruhr University.

I also owe gratitude to all my friends and colleagues at GRC: Yuhyi, Majid, Hesham, Claire, Shakil, Rao, Anil, Suresh, Khalid, Alex, Pauline (Townsend), Pauline (Welsh), Rob, Mojgan, Lee, Dan, Jamie, Matt and Manju.

I would like to express my greatest gratitude to my parents, Mr. Sudhir Chandra Bag and Mrs. Kajal Rani Bag for their love, support and guidance throughout my research. I am also thankful to my siblings Padma, Pratima and Bibek for their invaluable love, guidance and sacrifice.

A special thanks to my friends specifically: Mahdi, Nishant, Sasthi, Subho, Manjunath and Rufus for their continuous encouragement and making my stay at Cardiff, a memorable one.

Finally, a great thank you to everyone who has contributed directly or indirectly for completing my thesis.

Abstract

Due to their high swelling ability, high water retention capacity and low permeability, compacted bentonites have been considered as a key component of cover lining systems for storage of low and medium level toxic wastes and as barrier and backfilling materials for long-term safe storage of high level toxic waste in many countries. This thesis presents an experimental, theoretical and numerical study of thermo-hydro-mechanical-chemical behaviour of MX80 bentonite in geotechnical applications.

The determination of swelling pressures of compacted bentonites is an important aspect of most bentonite-based barrier systems. Swelling pressures of bentonites are usually determined in the laboratory under constant volume conditions using oedometers. Powdered bentonites are usually compacted in stainless steel cylindrical specimen rings and tested immediately after the compaction process is completed. The swelling pressures thus measured are influenced by some post compaction residual stresses. However, bentonites in the form of pellets and bricks are prepared and used in repository conditions that, in turn, are free from any post compaction residual stresses. The influence of post compaction residual stress on swelling pressures of compacted bentonites for a range of dry density that are of interest has not been explored in the past. Such studies are of potential interest for the safe and efficient designs of toxic waste disposal repositories. Many of the waste repositories are commissioned in locations where the ground water either contains significant amount of salts or the repositories are anticipated to receive saline water from sea. Additionally, in some cases, the wastes that are disposed emit very high temperatures (e.g. spent fuel). Under these repository conditions, compacted bentonite barriers are subjected to both thermal and hydraulic loadings at opposite boundaries. A detailed study devoted to appreciate the combined influence of an elevated temperature, bulk fluid type and solute transport due to both hydraulic and thermal gradients are necessary to better the understanding of the mechanical behaviour of compacted bentonites in many practical engineering problems.

Constant volume swelling pressure tests were carried out on compacted MX80 bentonite specimens in order to study the influence of post compaction residual stress, electrolyte concentration and temperature (for isothermal conditions) on the swelling pressure. The dry density of the bentonite was varied between 1.1 to 1.9 Mg/m³ to cover a wide range of compaction conditions. Theoretical assessments of swelling pressures were made using the Gouy-Chapman diffuse double layer theory and the Stern theory, as applicable to interacting clay platelet systems. Further, the experimental and the theoretical swelling pressures were compared in order to bring out the applicability of the electrical theories in assessing swelling pressures of bentonites for both compacted saturated and initially saturated slurried conditions. A series of thermal and thermo-hydraulic tests were carried out on bentonite specimens under laboratory scale settings. During the thermal tests, temperatures of 85 and 25 °C were applied at the bottom and top ends of the specimens, respectively. During the thermo-hydraulic tests, in addition to unequal temperature at opposite ends, distilled water was supplied from the top end of the specimens. The temperature and the relative humidity were monitored along predetermined depths of the specimens during both types of testing methods. The swelling pressure variations were monitored at the opposite end of the heat source. Changes in water content, dry density and concentrations of cations and anions along predetermined depths of the specimens were measured after termination of each of the tests. A thermo-hydro-mechanical finite element simulation was undertaken specifically for swelling pressures using the numerical code COMPASS (COde for Modelling PArtially Saturated Soils). Further, the experimental and the simulated results were compared both for thermal and thermo-hydraulic boundary conditions.

Compacted bentonite specimens with post compaction residual stresses exhibited lesser swelling pressures as compared to their stress released counterparts. Agreements between the calculated swelling pressures from the Stern theory and the experimental swelling pressure results were found to be reasonable for compaction dry densities of less than 1.45 Mg/m³, whereas at higher dry densities, agreements between the measured swelling pressures and those calculated from the electrical theories were found to be poor. Conversely, compressibility behaviour of initially saturated slurried bentonites was found to be captured well by the electrical theories. On account of vapour flow under thermal gradients, compacted bentonite specimens exhibited swelling pressures at the opposite end of the heat source. The measured swelling pressure for the thermal gradient adopted varied between 0.5 to 1.2 MPa, whereas greater swelling pressures were noted due to an applied thermo-hydraulic gradient. Evaporation, condensation, diffusion and advection processes influenced the distribution of ions in compacted bentonite when subjected to both thermal and thermo-hydraulic gradients. The finite element code, COMPASS, enabled assessing changes in suction and swelling pressure of compacted bentonite satisfactorily under both thermal and thermo-hydraulic hydraulic gradients.

Table of Contents

Contents	Page no
Chapter 1 Introduction	
1.1 Introduction	1
1.2 Scope and objectives of the research	6
1.3 Thesis outline	8
Chapter 2 Literature Review	
2.1 Introduction	13
2.2 Structure of montmorillonite	16
2.3 Structure of compacted bentonite	18
2.4 Suction of unsaturated soils	20
2.4.1 Suction versus water content relationship	23
2.4.2 Effect of dry density and temperature on suction-water content relationship	24
2.5 Mechanisms governing swelling of expansive clays	25
2.5.1 Swelling pressure	26
2.5.2 Determination of swelling pressure of compacted bentonites	27
2.5.3 Swelling pressure measurement devices	28
2.5.4 Effect of post compaction residual stress release on swelling pressure	30
2.5.5 Effect of temperature on swelling pressure	30
2.5.6 Effect of electrolyte concentration on swelling pressure	31
2.5.7 Physical state of water in compacted bentonite	32
2.6 Compressibility behaviour of bentonite	34
2.7 Theoretical assessment of swelling pressure	35
2.8 Effect of Stern layer on swelling pressure and compressibility of bentonite	36
2.9 Thermo-hydro-mechanical-chemical tests on compacted bentonite	39
2.9.1 Thermo-hydro-mechanical-chemical test conditions	40
2.9.2 Thermo-hydraulic testing devices	43
2.10 Mechanisms governing heat, water and solute transfer in soil	44
2.10.1 Variation of cations and anions concentrations	48

2.11 Numerical models for coupled thermo-hydro-mechanical-chemical simulations	49
2.12 Summary	52

Chapter 3 Material and Methods

3.1 Introduction	54
3.2 Properties of bentonite studied	55
3.3 Suction versus water content relationship	58
3.3.1 Suction versus water content relationship from chilled-mirror hygrometer	62
3.4 Experimental program	66
3.4.1 Swelling pressure tests	67
3.4.1.1 Specimen preparation method	67
3.4.1.2 Constant volume swelling pressure measuring device	69
3.4.1.3 Calibration of oedometer cells against deformation	72
3.4.1.4 Calibration of oedometer cells against temperature	73
3.4.1.5 Constant volume swelling pressure tests	75
3.4.2 Consolidation test	76
3.4.3 Thermal and thermo-hydraulic tests	78
3.4.3.1 Specimen preparation method	78
3.4.3.2 Description of the testing device	80
3.4.3.3 Calibration of temperature and relative humidity measuring probes	83
3.4.3.4 Thermal and thermo-hydraulic tests	85
3.4.3.5 Extrusion of specimen after thermal and thermo-hydraulic tests	87
3.4.3.6 Chemical analysis	89
3.5 Summary	92

Chapter 4 Effect of post compaction residual stress on swelling pressure of compacted bentonite

4.1 Introduction	94
4.2 Experimental program	95

4.3 Extrusion and re-insertion of compacted bentonite specimens	98
4.4 Applied compaction load and dry density of specimens prior to testing	100
4.5 Deformation history of the compacted specimens prior to testing	101
4.6 Swollen dry density	103
4.7 Results and discussion	105
4.7.1 Time-swelling pressure plot at ambient temperature	106
4.7.2 Swelling pressure test results at ambient temperature	108
4.7.3 Influence of post-compaction residual stresses on swelling pressure	111
4.7.4 Influence of electrolyte concentration on swelling pressure	115
4.7.5 Saturated water content after swelling pressure tests at ambient temperature	117
4.7.6 Influence of temperature on swelling pressure	119
4.7.6.1 Time-swelling pressure plot at elevated temperature of 70 °C	120
4.7.6.2 Swelling pressure test results at elevated temperature of 70 °C	121
4.7.6.3 Saturated water content after swelling pressure tests at elevated temperature	125
4.8 Concluding remarks	126

Chapter 5 Swelling pressure of compacted bentonite from physico-chemical considerations

5.1 Introduction	128
5.2 Stern theory for interacting clay platelet system	130
5.2.1 Charge and potential distribution	130
5.2.2 Relationships of ψ_δ , ψ_d , σ , σ_1 and σ_2 with d	132
5.2.3 Dry density-swelling pressure and vertical pressure-void ratio Relationships	133
5.3 Gouy-Chapman diffuse double layer theory (constant surface potential case)	134
5.4 Choice of parameters for theoretical calculations	135

5.4.1 Surface potential (ψ_0)	135
5.4.2 Stern layer thickness (δ)	136
5.4.3 Dielectric constant of fluid within Stern layer (ϵ')	137
5.4.4 Other parameters (v , n_0 , and ϵ_0)	137
5.5 Results and discussion	139
5.5.1 Charge and potential distribution	144
5.5.2 Parametric study	147
5.5.2.1 Effect of valence	148
5.5.2.2 Effect of electrolyte concentration	150
5.5.2.3 Effect of dielectric constant of pore fluid in Stern layer	151
5.5.2.4 Effect of specific adsorption potential	153
5.5.2.5 Effect of surface potential	154
5.5.3 Comparison between experimental and theoretical swelling pressure results	156
5.5.3.1 Tests conducted at a temperature of 25 °C using distilled water	157
5.5.3.2 Tests conducted at a temperature of 70 °C using distilled water	159
5.5.3.3 Tests conducted at temperatures of 25 °C and 70 °C using 0.1 M NaCl	160
5.5.3.4 Tests conducted at temperatures of 25 °C and 70 °C using 1.0 M NaCl	162
5.6 Concluding remarks	163

Chapter 6 Effect of Stern-layer on compressibility behaviour of bentonites

6.1 Introduction	165
6.2 Consolidation test	166
6.2.1 Properties of the bentonites studied	166
6.2.2 Experimental Methods	168
6.3 Comparison between experimental and theoretical results	168
6.4 Concluding remarks	172

Chapter 7 Effect of temperature and hydraulic gradients on thermo-hydro-mechanical behaviour of compacted bentonite

7.1 Introduction	173
7.2 Experimental program	174
7.3 Results and discussion	180
7.3.1 Transient temperature variation	181
7.3.2 Transient relative humidity variation	183
7.3.3 Transient suction variation	185
7.3.4 Swelling pressure due to thermal loading	187
7.3.5 Swelling pressure due to thermal and hydraulic loadings	192
7.3.6 Water content variation	194
7.3.6.1 Effect of thermal gradient	194
7.3.6.2 Effect of thermal and hydraulic gradients	195
7.3.7 Comparison of swelling pressures with oedometer test results	197
7.3.8 Dry density and degree of saturation variation	198
7.3.8.1 Effect of thermal gradient	198
7.3.8.2 Effect of thermal and hydraulic gradients	200
7.4 Concluding remarks	201

Chapter 8 Effects of temperature and hydraulic gradients on solute transport in compacted bentonite

8.1 Introduction	203
8.2 Experimental procedure	205
8.3 Results and discussion	208
8.3.1 Chloride (Cl^-) distribution	209
8.3.2 Sulphate (SO_4^{2-}) distribution	210
8.3.3 Nitrate (NO_3^-) distribution	212
8.3.4 Sodium (Na^+) distribution	213
8.3.5 Calcium (Ca^{2+}) distribution	215
8.3.6 Magnesium (Mg^{2+}) distribution	216
8.3.7 Potassium (K^+) distribution	217

8.4 Concluding remarks	218
------------------------	-----

Chapter 9 Simulation of thermo-hydro-mechanical tests

9.1 Introduction	220
9.2 Theoretical formulation	222
9.2.1 Heat flow	223
9.2.2 Water flow	224
9.2.2.1 Mechanism of liquid water flow	226
9.2.2.2 Mechanisms of water vapour flow	227
9.2.3 Governing equations for water flow	229
9.2.4 Deformation behaviour	233
9.2.4.1 Elasto plastic constitutive relationships	235
9.2.4.2 Material behaviour under elastic condition	235
9.2.4.3 Yield function	236
9.2.4.4 Flow rule	236
9.2.4.5 Hardening laws	237
9.3 Numerical simulation	238
9.3.1 Geometry and discretisation	239
9.3.2 Initial conditions	240
9.3.3 Boundary conditions	241
9.3.4 Material parameters	241
9.3.4.1 Thermal parameters	242
9.3.4.2 Hydraulic parameters	243
9.3.4.2.1 Suction versus degree of saturation relationship	244
9.3.4.3 Mechanical parameters	247
9.4 Results and discussion	249
9.4.1 Influence of thermal and hydraulic gradient on temperature profile	249
9.4.2 Effect of thermal and hydraulic gradients on suction profiles	251
9.4.3 Development of swelling pressure due to thermal and hydraulic gradients	254
9.5 Concluding remarks	256

Chapter 10 Conclusions	257
References	262

List of Tables

Table 2.1 Summary of reported reported suction measurement methods	22
Table 2.2 Summary of reported thermal and thermo-hydraulic tests	42
Table 2.3 Different processes considered in numerical codes	52
Table 3.1 Properties of MX80 bentonite	56
Table 3.2 Chilled-mirror hygrometer test results	65
Table 4.1 Detailed experimental program of swelling pressure tests	96
Table 4.2 Applied compaction load and dry density of the specimens prior to testing	100
Table 4.3 Summary of the swelling pressure results for series I and II tests	109
Table 4.4 Summary of swelling pressure results for series III and IV tests	110
Table 4.5 Summary of swelling pressure results for series V, VI and VII tests	121
Table 5.1 Parameters used to establish relationships between electrical charge and electrical potential with $2d$	140
Table 5.2 Determination of charges, potentials, swelling pressures, and void ratios from Stern theory for interacting clay platelets ($\psi_0 = 300$ mV)	142
Table 5.3 Determination of charge, potential, swelling pressures, and void ratios from Gouy-Chapman diffuse double layer theory ($\psi_0 = 300$ mV)	143
Table 6.1 Properties of the bentonites studied	167
Table 7.1 Experimental program of thermal and thermo-hydraulic tests	176
Table 7.2 Additional tests	180
Table 8.1 Solubilised minerals of MX80 bentonite determined from aqueous extraction method	207
Table 8.2 Experimental program for chemical analysis	207
Table 9.1 Material parameters used for simulations	242
Table 9.2 Thermal parameters used for the numerical simulations	243
Table 9.3 Hydraulic conductivity relationships used for the numerical simulations	244
Table 9.4 Hydraulic parameters used for the numerical simulations	246
Table 9.5 Mechanical parameters used for the numerical simulations	249

List of Figures

Figure 2.1. Schematic representation of toxic waste disposal concept in the UK (modified after NDA report)	14
Figure 2.2. Design of final repository for Low and Intermediate level nuclear waste (Roffey, 1990)	14
Figure 2.3. Schematic diagram of the montmorillonite mineral (Mitchell and Soga, 2005)	17
Figure 2.4. Representation of micro structure of expansive clays (modified from Nagaraj and Murthy, 1985)	19
Figure 2.5. Typical SWCCs for different types of soil	24
Figure 2.6. Swelling pressure measured using different methods (Modified after Sridharan et al., 1986).	27
Figure 2.7. Setup for measuring the swelling pressure (Madsen and Müller-vonmoos, 1985)	29
Figure 2.8. Schematic diagram of devices used for measuring the swelling pressure by constant volume method developed by Romero (1999)	29
Figure 2.9. Schematic diagram of Stern and Gouy layer and charge distribution in clay-water electrolyte system	37
Figure 2.10. Experimental setup for the infiltration test (Villar et al., 1996, 2007; Fernandez and Villar, 2010; Gomez-Espina and Villar, 2009)	44
Figure 2.11. Schematic presentation of some physical processes occurring in an unsaturated porous medium in response to heating (after Bear and Gilman, 1995; Pusch and Yong, 2006)	45
Figure 3.1. Grain size distribution of MX80 bentonite	55
Figure 3.2. X-ray diffractometer used in the study	57
Figure 3.3. X-ray diffraction chart for MX80 bentonite	58
Figure 3.4. Pressure plate apparatus	60
Figure 3.5. Pressure plate apparatus with initially slurried bentonite specimens	60
Figure 3.6. Slurried bentonite specimens inside the desiccators (Vapour Equilibrium test)	61
Figure 3.7. Shrinkage test (with molten wax) setup	62
Figure 3.8. Photograph of chilled-mirror hygrometer	63

Figure 3.9. Suction-water content relationship of MX80 bentonite established from desiccators and chilled mirror hygrometer tests	65
Figure 3.10. Various components of the compaction mould	68
Figure 3.11. Compaction mould with compacted specimen inside	68
Figure 3.12. Schematic diagram of constant volume swelling pressure measurement device	70
Figure 3.13. Components of the modified oedometer	70
Figure 3.14. Experimental setup of constant volume swelling pressure test	71
Figure 3.15. Applied pressure versus deformation relationships of the modified oedometer cells used in the investigation	73
Figure 3.16. Experimental setup of temperature calibrations in the specimen chamber	74
Figure 3.17. Equilibration temperatures at inner and outer housing unit of the cell	75
Figure 3.18. One dimensional consolidation test apparatus	77
Figure 3.19. Components of the compaction mould	79
Figure 3.20. High stress compaction device	79
Figure 3.21. Schematic diagram of the cell used to carry out the thermal and thermo-hydraulic tests	80
Figure 3.22. Components of the thermal and thermo-hydraulic test setup	81
Figure 3.23. Thermal and thermo-hydraulic test setup	82
Figure 3.24. Relative humidity calibration of the probes	84
Figure 3.25. Relative humidity equilibration of the probes under calibration	84
Figure 3.26. Change in suction or error in suction measurement due to change in temperature (Agus, 2005)	85
Figure 3.27. Components of the specimen extruder	88
Figure 3.28. Extraction of a bentonite specimen after testing	88
Figure 3.29. Photograph of the reciprocal shaker and the bentonite-water mixture	90
Figure 3.30. Sigma GK-15 centrifuge	91
Figure 3.31. Filtration process by applying vacuum through Buchner funnel	91
Figure 3.32. Ion Chromatography (DIONEX ICS-2000)	92
Figure 3.33. Perkin Elmer Optima 2100 DV Inductively Coupled Plasma Optical Emission Spectroscopy (ICP-OES)	92

Figure 4.1. Compaction condition of the specimens and experimental program	93
Figure 4.2. Specimen extrusion and re-insertion process prior to swelling pressure tests; (a) after removal of static load, (b) and (c) after extrusion, (d) after dimension manipulation, (e) after re-insertion	95
Figure 4.3. Stress history of compacted specimens prior to swelling pressure tests	98
Figure 4.4. Physical appearance of a specimen after terminating the test	102
Figure 4.5. Time-swelling pressure plots for Series I, II, III and IV tests	103
Figure 4.6. Influence of post compaction residual lateral stresses on swelling pressure	107
Figure 4.7. Effect of density of water on dry density-swelling pressure relationship	109
Figure 4.8. Influence of bulk solution type on swelling pressure	110
Figure 4.9. Swollen dry density versus water content of the specimens for series I, II, III and IV tests	112
Figure 4.10. Time swelling pressure plots for series V, VI and VII tests	115
Figure 4.11. Comparison of swelling pressures measured at ambient and elevated temperature using distilled water as bulk fluid	117
Figure 4.12. Comparison of swelling pressures measured at ambient and elevated temperature using 0.1 M NaCl solution as bulk fluid	117
Figure 4.13. Comparison of swelling pressures measured at ambient and elevated temperature using 1.0 M NaCl solution as bulk fluid	118
Figure 4.14. Swollen dry density versus saturated water contents for series V, VI and VII tests	119
Figure 5.1. Change of charges with $2d$ from Stern theory and Gouy-Chapman diffuse double layer theory ($\psi_0 = 300$ mV)	138
Figure 5.2. Change of electrical potentials with $2d$ from the Stern theory and the Gouy-Chapman diffuse double layer theory ($\psi_0 = 300$ mV)	139
Figure 5.3. Influence of hydrated ionic radii and valence on (a) e -log p and (b) dry density-swelling pressure relationships	143
Figure 5.4. Influence of bulk fluid concentration on (a) e -log p and (b) dry density-swelling pressure relationships	144
Figure 5.5. Influence of dielectric constant of pore fluid in Stern layer on (a) e -log p and (b) dry density-swelling pressure relationships	146

Figure 5.6. Influence of specific adsorption potential on (a) $e\text{-log } p$ and (b) dry density-swelling pressure relationship	148
Figure 5.7. Influence of surface potential (ψ_0) on (a) $e\text{-log } p$ and (b) dry density-swelling pressure relationship	149
Figure 5.8. Experimental and theoretical dry density-swelling pressures for the specimens tested at 25 °C using distilled water as bulk fluid	152
Figure 5.9. Experimental and theoretical dry density-swelling pressures for the specimens tested at 70 °C using distilled water as bulk fluid	153
Figure 5.10. Experimental and theoretical dry density-swelling pressures for the specimens tested at temperatures of 25 and 70 °C using 0.1 M NaCl as bulk fluid	155
Figure 5.11. Experimental and theoretical dry density-swelling pressures for the specimens tested at 25 °C and 70 °C using 1.0 M NaCl as bulk fluid	156
Figure 6.1. Theoretical and experimental $e\text{-log } p$ relationships for MX80 bentonite (in this study)	163
Figure 6.2. Theoretical and experimental $e\text{-log } p$ relationships for Na-Ca MX80 bentonite	164
Figure 6.3. Theoretical and experimental $e\text{-log } p$ relationships for Calcigel bentonite	164
Figure 7.1. Schematic representation of temperature, relative humidity and swelling pressures measured in compacted bentonite specimens during thermal tests	171
Figure 7.2. Schematic representation of temperature, relative humidity and swelling pressures measured in compacted bentonite specimens during thermo-hydraulic tests	173
Figure 7.3. Transient temperature variations at specified depths of the specimens due to thermal, thermal and hydraulic loading (test no. 5)	176
Figure 7.4. Transient relative humidity variations at specified depths of the specimens during thermal, and thermal and hydraulic loading (test no. 5)	178
Figure 7.5. Transient suction variations at specified depths of the specimen (test no. 5)	180
Figure 7.6. Time versus swelling pressure plots in (a) semi-logarithmic scale and (b) arithmetic scale during thermal tests on compacted bentonite specimens	182
Figure 7.7. Time versus axial pressure plots during thermal tests on dummy PTFE specimen and compacted Speswhite kaolin	183

Figure 7.8. Time-swelling pressure plots in (a) semi-logarithmic scale and (b) arithmetic scale during thermo-hydraulic tests on compacted bentonite specimen	186
Figure 7.9. Distribution of water contents in bentonite specimens after thermal tests	188
Figure 7.10. Physical appearances of the bentonite specimen at three sensors level after thermo-hydraulic test no. 4 (Photographs were taken while dismantling)	189
Figure 7.11. Physical appearances of the bentonite specimen after dismantling thermo-hydraulic test no. 5	189
Figure 7.12. Distribution of water contents in bentonite specimens after thermo-hydraulic tests	190
Figure 7.13. Dry density and degree of saturation variation along the depth of the specimen after thermal test of 67 days (test no. 3)	193
Figure 7.14. Dry density and degree of saturation variation along the depth of the specimen after thermo-hydraulic test of 182days (test no. 5)	194
Figure 8.1. Influence of thermal and thermo-hydraulic gradients on chloride transport in compacted bentonite specimen	203
Figure 8.2. Influence of thermal and thermo-hydraulic gradients on sulphate transport in compacted bentonite specimen	205
Figure 8.3. Influence of thermal and thermo-hydraulic gradients on nitrate transport in compacted bentonite specimen	206
Figure 8.4. Influence of thermal and thermo-hydraulic gradients on sodium transport in compacted bentonite specimen	208
Figure 8.5. Influence of thermal and thermo-hydraulic gradients on calcium transport in compacted bentonite specimen	209
Figure 8.6. Influence of thermal and thermo-hydraulic gradients on magnesium transport in compacted bentonite specimen	210
Figure 8.7. Influence of thermal and thermo-hydraulic gradients on potassium transport in compacted bentonite specimen	212
Figure 9.1. A general two dimensional stress system	228
Figure 9.2. Geometry of the model and initial and boundary conditions for first phase (phase I) simulation	233
Figure 9.3. Geometry of the model and initial and boundary conditions for second phase (phase II) simulation	234

Figure 9.4. Suction versus degree of saturation relationships	241
Figure 9.5. Suction and vertical pressure versus void ratio of MX80 bentonite	242
Figure 9.6. Transient temperature changes along the depth of the specimen during thermal loading	244
Figure 9.7. Transient temperature changes along the depth of the specimen during thermal and thermo-hydraulic loading	245
Figure 9.8. Transient suction changes along the depth of the specimens during thermal and thermo-hydraulic tests	246
Figure 9.9. Swelling pressure development at the cold end of the specimen due to thermal and thermo-hydraulic loading	249

Nomenclature

a_w	Water activity
\mathbf{b}	Vector of body forces
C_{la}	Defined in eq. (9.29)
C_{ll}	Defined in eq. (9.27)
C_{lT}	Defined in eq. (9.28)
C_{lu}	Defined in eq. (9.30)
C_{pda}	Specific heat capacity of dry air
C_{pl}	Specific heat capacity of liquid
C_{pv}	Specific heat capacity of vapour
C_{ua}	Defined in eq. (9.51)
C_{ul}	Defined in eq. (9.49)
C_{uT}	Defined in eq. (9.50)
C_{uu}	Defined in eq. (9.52)
D	Permittivity of vacuum
D_{atms}	Molecular diffusivity of vapour through air
Dep	Elasto-plastic stress-strain matrix
E_{ss}	Sink/source term representing vaporisation and condensation
e	Void ratio
e'	Electronic charge
f	Flow area factor
G_s	Specific gravity of soil
H_c	Heat capacity of unsaturated soil
h	suction head
J_l	Defined in eq. (9.34)

k	Boltzmann's constant
k_l	Unsaturated hydraulic conductivity
K_l	Effective permeability
K_{la}	Defined in eq. (9.33)
K_{ll}	Defined in eq. (9.31)
K_{IT}	Defined in eq. (9.32)
L	Latent heat of vapourisation
LC	Loading-collapse
M	Molarity of electrolytes
M	Molecular wt of solvent
m	Differential operator
N_1	No of adsorption spots on 1m^2 area of surface
N_A	Avogadro number
n	Porosity
n_0	Concentration of bulk fluid
P	Strain matrix
p	Swelling pressure
Q	Total heat flow
Q_1	Plastic potential for LC yield surface
Q_2	Plastic potential for SI yield surface
R	Universal gas constant
RH	Relative humidity
S	Specific surface area of soil
S_a	Degree of saturation of pore air
SI	Suction increase
s	Suction head

S_l	Degree of saturation of pore water
S_r	Degree of saturation
T	Temperature
T_r	Reference temperature
u_d	The non dimensional potential function at Gouy layer
u_a	Pore air pressure
u_l	Pore water pressure
\mathbf{u}	Displacement
ν	Valence of cations and anions
ν_a	Velocity of air
ν_l	Velocity of liquid
ν_v	Velocity of vapour
w	Water content
z	elevation
z_δ	The non dimensional potential function at Stern layer
δ	Thickness of Stern layer
κ	Thickness of Gouy layer
ε_0	Dielectric constant of pore fluid at outer surface
ε'	Dielectric constant of pore fluid at Stern layer
Φ	Specific adsorption potential
ψ_0	The charge potential at the surface
ψ_δ	The charge potential at Stern layer
ψ_d	The charge potential at Gouy layer
ρ_d	Dry density
ρ_{da}	Density of dry air
ρ_l	Density of liquid

ρ_s	Density of soil solids
ρ_v	Density of vapour
ρ_w	Density of water
σ	The total surface charge
σ_1	Charge at Stern layer
σ_2	Charge at Stern Gouy layer
ξ	Zeta potential
∇	Gradient operator
∂V	Incremental volume
Ω	Heat content of a partially saturated soil per unit volume
λ_T	Thermal conductivity
θ	Volumetric water content
θ_l	Volumetric liquid content
θ_v	Volumetric vapour content
θ_a	Volumetric air content
μ_l	Absolute viscosity of pore liquid
γ_l	Unit weight of liquid
τ_v	Tortuosity factor
η_1, η_2	Vapour flow factors
ε_v	Volumetric strain
σ''	Net mean stress
σ	Total stress
dv	Change in specific volume
dp	Change in mean stress
κ	Elastic stiffness parameter for change in net mean stress

dv_s	Change in specific volume due to swelling (wetting path)
κ_s	Elastic stiffness parameters for changes in suction
p_0	Preconsolidation stress
p_0^*	Preconsolidation stress for saturated conditions
p^c	Reference stress
Θ	Normalized water content
ψ_r	Residual suction
ψ	Suction

Chapter 1

Introduction

1.1 Introduction

The sustainability of the geoenvironment is highly affected by the continued depletion of natural resources and imposing physical, chemical and biological impacts to the geoenvironment from the various human activities, indicating an increasing threat to the environment (Yong et al., 2006). Developments within the fields of civil and environmental engineering focused on the sustainable development, remediation of contaminant land and management of municipal and radioactive waste (Thomas et al., 1998). Therefore, it is necessary to develop a better appreciation of the physical and chemical processes occurring in geoenvironment and to improve the knowledge and technology for appropriate management of geoenvironmental resources (Yong et al., 2006).

The safe disposal of radioactive waste is an important aspect in geoenvironmental engineering (Thomas et al., 1998). Similarly, proper disposal and management of low and intermediate level nuclear waste (Roffey, 1990) and municipal solid waste (Rowe et al., 1995; Sharma and Reddy, 2004; Benson, 2005; Cruz-Guzman et al., 2006) are necessary to minimise the migration of contaminants of chemical species into the ground water and environment. One of the possible solutions for the safe disposal of high level radioactive waste is the deep geological disposal. In the deep geological disposal concept, the spent fuel canisters are planned to be stored at a minimum depth of 500 m below the ground surface (Pusch, 1982). The waste canisters are placed in a regular fashion in tunnels which are bored inside the host rock. Host rock of waste disposal repositories are different types such as crystalline, sedimentary, claystone, volcanic and salt rock depending on retrievability requirement (IAEA, 2009). In case of crystalline rock the retrievability is feasible than salt rock. However, salt rocks will creep and will close the mined gaps, thereby creating better water tightness and generate pressure on the repository. Salt rock formation exists in low seismic areas as well as thermal properties of salt rock are better than any other type of rock.

Several types of soil such as Opalinus clay (Gens et al., 2007, 2009), Boom clay (Vaunat and Gens, 2007; Alonso et al., 2010), Avolena clay (Yong et al., 1997), Foca and Serata Clays (Vaunat and Gens, 2007) and compacted bentonites (Pusch, 1982, Pusch and Yong, 2006) are used as possible barrier and backfilling in waste disposal repositories. Compacted bentonites in the form of rings are planned to be placed in the gap between the canister and the host rock (Pusch and Yong, 2006; Delage et al., 2006). Compacted bentonites are preferred to be used as barrier and backfilling material in the high level radioactive waste disposal repositories in order to (i) structurally hold the radioactive

waste canisters in place and prevent collapse of the excavation and (ii) create a very high level of water tightness to limit the access of water into the geosphere, and, simultaneously should transfer the heat generated in the waste to the host rock (Tripathy et al., 2004).

During the operational period of radioactive waste disposal repositories, compacted bentonite systems are subjected to thermal and hydraulic loading at opposite ends of the barrier. The section of bentonite, that is in contact with waste canisters is subjected to elevated temperature upon receiving heat from the radioactive waste, whereas the other section of the compacted bentonite in contact with saturated host rock receive ground water from the saturated host rock. In case of direct disposal of radioactive wastes, the bentonite buffer will be subjected to a temperature between 110 and 150 °C. At temperatures higher than 100 °C, the smectite mineral may transform to illite (Pusch et al., 2010). Therefore, understanding the behaviour of compacted bentonites under thermal, hydraulic and mechanical loading is necessary for long term safety assessment of the waste disposal repositories.

During the hydration process and under restrained boundary conditions, compacted bentonite is expected to exhibit swelling pressures on the canisters. The swelling pressures exerted by compacted bentonites may damage the fuel canister and cause rock failure in the waste repository (Pusch and Yong, 2006). In the past, swelling pressure measurements were carried out on compacted bentonite specimens in controlled laboratory environment by several researchers (Müller-Vonmoos and Kahr, 1982; Pusch, 1982; Dixon and Gray, 1985; Swedish Nuclear Fuel and Waste Management Company, 1983; Komine and Ogata, 1994; Empresa Nacional de Residuos Radiactivos SA, 200;

Villar and Lloret, 2004, 2008; Karnland et al., 2007; Komine et al., 2009; Schanz and Trpathy, 2009). For the laboratory tests, compacted bentonite specimens were hydrated immediately after completion of the compaction process.

For actual use in repositories, compacted bentonites are usually planned to be prepared by compacting the bentonite powder. After completion of the compaction process, compacted bentonites are usually removed from the compaction mould and hence the post compaction residual stresses are released. The release of post compaction residual stresses may cause significant lateral expansion of the compacted bentonites. The influence of release of post compaction residual stresses on the swelling pressures of compacted bentonites has not been studied.

In the waste disposal repositories, the compacted bentonites may receive ground water from saturated host rock. The migrated ground water from the saturated host rock may contain different electrolytes. Additionally, concentration of NaCl solution in ground water may vary. The swelling pressure of compacted bentonites is known to be affected by the presence of NaCl solution in bulk fluid (Pusch, 1982, 1985; ENRESA, 2004; Karnland et al., 2007; Herbert et al., 2008; Komine et al., 2009). Similarly, the effect of temperature on swelling pressure has been reported by a number of researchers (Pusch, 1980; Romero et al., 2003, 2005; Villar and Lloret, 2004; Pusch and Yong, 2006). However, the effect of temperature and electrolytes on the swelling pressure of bentonites after releasing the post compaction residual stresses has not been studied yet.

Assessments of swelling pressure and compressibility of bentonites are usually carried out using Gouy-Chapman diffuse double layer theory for interacting clay platelet

systems (Bolt, 1956; Sridharan and Jayadeva, 1982; Komine and Ogata, 1996; Tripathy et al., 2004; Tripathy and Schanz, 2007; Schanz and Tripathy, 2009). The Stern theory (Stern, 1924) proposed the closest approach of a counter-ion to the charged clay surface. Application of the Stern theory for interacting clay platelet systems to determine the swelling pressure of compacted bentonites and to assess the compressibility behaviour of saturated bentonite have not been explored in the past.

In the high level radioactive waste disposal repositories, compacted bentonites are subjected to elevated temperature close to the waste canisters. Additionally, compacted bentonites in contact with saturated host rock may imbibe ground water. Due to thermal and hydraulic loading applied at opposite ends, compacted bentonites may undergo local swelling and shrinkage processes. The temperature, the relative humidity, suction, water content and concentrations of cations and anions in compacted bentonites are known to be changed with elapsed time. For understanding the long term performance of compacted bentonites under the conditions of high level radioactive waste disposal repositories, it is necessary to study the variation of temperature, suction, water content and cations and anions concentrations in compacted bentonites with elapsed time due to applied thermal and hydraulic gradients. In the past, several studies have been carried out to study the behaviour of bentonite under thermal and hydraulic gradients (Ewen and Thomas, 1987, 1989; Villar et al., 1996; Yong et al., 1997; Martín et al., 2000; Börgesson et al., 2001; Folly, 2001; Collin et al., 2002; Cuevas et al., 2002; Cuisinier and Masrouri, 2005; Romero et al., 2005; Hoffmann et al., 2007; Singh, 2007; Castellanos et al., 2008; Samper et al., 2008; Villar et al., 2007, 2008; Åkesson et al., 2009; Fernández and Villar, 2010; Gómez-Espina and Villar, 2010). The studies concerning only the thermal loading and its

influence on the development of swelling pressure away from the hot end of the bentonite specimen is scarce in the literature (Singh, 2007; Åkesson et al., 2009).

In the past, thermo-hydraulic tests were conducted by subjecting the bentonite specimens to thermal and hydraulic loading simultaneously; anticipating simultaneous application thermal and hydraulic loadings from radioactive and the host rock, respectively, in repository conditions. However, studies concerning only thermal loading on compacted bentonites, simulating the early stage loading conditions of the repository is very limited. During the operational period of waste disposal repositories, compacted bentonites will be subjected to both thermal and hydraulic loading. The behaviour of compacted bentonites under thermal loading followed by thermal and hydraulic loading has not been explored in detail.

In order to study the solute transport phenomenon in compacted bentonites, the change in concentrations of cations and anions have been measured after termination of thermo-hydraulic tests (Fernández et al., 2001; Martín et al., 2000; Cuevas et al., 2002; Samper et al., 2008; Fernández and Villar, 2010; Gómez-Espina and Villar, 2010). The change in concentrations of cations and anions in compacted bentonites due to thermal loading is scarce in the literature (Singh, 2007).

1.2 Scope and objectives of the research

Concerning the use of compacted bentonites as barrier and backfilling materials in high radioactive waste disposal repositories, the main objectives of this research was to study the following aspects:

- (1) To establish the effect on swelling pressure when post compaction residual stresses were released
- (2) To determine the effects of electrolyte concentration and temperature on swelling pressure.
- (3) To assess the swelling pressure and compressibility of bentonite using electrical theories (the Stern theory and the diffuse double layer theory) based on interacting clay platelet systems.
- (4) To investigate the influence of thermal and thermo-hydraulic gradients on the development of swelling pressure of compacted bentonite, particularly at opposite end of the heat source
- (5) To investigate the influence of thermal and thermo-hydraulic gradients on concentration changes in of cations and anions, across the length of compacted bentonite.
- (6) To implement the numerical code COMPASS (Thomas et al., 1998) to assess the thermo-hydro-mechanical behaviour of compacted bentonites both for applied thermal and hydraulic loading conditions.

Experimental studies concerning the swelling potential, the hydraulic conductivity, the compressibility behaviour of compacted saturated bentonites, and the use of numerical code to assess the changes in concentration of cations and anions along the depth of compacted bentonite specimens due to both thermal and hydraulic loading conditions are beyond the scope of this study.

1.3 Thesis outline

This thesis is divided into ten consecutive chapters.

Chapter 1 presents the background of the research, the main objectives of this research and outline of the thesis.

Chapter 2 presents a review of literature pertaining to this study. A brief review of the structure of montmorillonite and compacted bentonite is detailed, along with the concept of suction in unsaturated soils, methods of measuring and controlling suction that have been reported, as well as the effects of dry density and temperature on suction in unsaturated soils are presented. The mechanisms of swelling of expansive clays and the swelling pressure of expansive clays are discussed. The methods of determining swelling pressure of compacted bentonites, the devices used are presented. The influence of post compaction residual stress release, electrolyte concentration and temperature effects on the swelling pressure of compacted bentonites are also discussed.

Assessments of swelling pressures of compacted bentonites using electrical theories are briefly reviewed. Effects of the Stern-layer on the swelling pressure and compressibility of bentonites is presented.

The initial and testing conditions of thermal and thermo-hydraulic tests reported in the literature are reviewed. The testing devices and the experimental setup used for carrying out thermal and thermo-hydraulic tests are briefly reviewed. The mechanisms of coupled heat, water and solute transport in unsaturated soils are presented. The numerical

models, known as codes, used to study coupled thermo-hydro-mechanical behaviour of unsaturated soils are reviewed.

Compacted MX80 bentonite has been considered as a reference barrier and backfilling material in the high level toxic waste disposal repositories in many countries (Pusch and Yong, 2006). The properties of MX80 bentonite used for this research and the experimental methods adopted are described in **Chapter 3**. The physical and chemical properties of the bentonite studied are presented. The suction-water content relationships for the bentonite established from desiccator tests and from chilled-mirror dew-point technique are presented. Chapter 3 also describes the modified oedometers used for measuring swelling pressures of compacted bentonite specimens by constant volume method and the cylindrical cell used to carry out the thermal and thermo-hydraulic tests. Calibration of the modified oedometers for deformation and temperature are presented. Calibration of the relative humidity sensors used to measure temperature and relative humidity during thermal and thermo-hydraulic test are presented.

The method used for preparing compacted specimens adopted for swelling pressure tests, thermal and thermo-hydraulic tests are described in detail. Test procedures adopted for constant volume swelling pressure test, one-dimensional consolidation test and thermal and thermo-hydraulic test methods are described. Dismantling procedure of thermal and thermo-hydraulic test setup and chemical analysis of bentonite specimens after the thermal and thermo-hydraulic tests is described.

Chapter 4 presents the swelling pressure of the MX80 bentonite as affected by: (i) compaction load, (ii) release of post compaction residual stresses, (iii) electrolyte

concentration and (iv) temperature. Once the compaction process was over, the compacted bentonite specimens were extruded and re-inserted back to the ring before testing. The process of extrusion and re-insertion of compacted bentonite specimens is described. The effect of electrolyte concentration on swelling pressure of compacted bentonite is studied by saturating the bentonite specimens with distilled water, 0.1 M NaCl and 1.0 M NaCl solutions. To evaluate the effect of temperature on the swelling pressure of compacted bentonite, swelling pressure tests are conducted at ambient (25 °C) and elevated (70 °C) temperatures.

Chapter 5 presents the theoretical assessment of swelling pressures of compacted MX80 bentonite using the Stern theory and the Gouy-Chapman diffuse double layer theory. The Stern theory equations for interacting clay platelet systems are presented following Verwey and Overbreek (1948)'s approach. The distribution of electrical potential and electronic charge with distance between clay platelets is presented. The effects of various parameters, such as electrolyte concentration, the weighted average valence of exchangeable cations, the dielectric constant of pore fluid in the Stern layer, the specific adsorption potential and the surface potential on the pressure – void ratio and the dry density-swelling pressure relationships of compacted bentonite are brought out. Comparisons between experimental and theoretical dry density-swelling pressure relationships are shown.

Chapter 6 presents the influence of the Stern-layer on the compressibility behaviour of initially saturated slurried bentonite (initial water content > liquid limit). Compressibility tests are carried out on initially saturated slurried MX80 bentonite specimen. The pressure-void ratio relationships reported in the literature for a Na-Ca

bentonite and a Ca-bentonite are also considered for comparing with the theoretical results. Comparisons between experimental and theoretical pressure versus void ratio relationships calculated based on the Stern theory and diffuse double layer theory for three bentonites are presented.

Chapter 7 presents the thermal and thermo-hydraulic test results. During the thermal tests, compacted cylindrical bentonite specimens were subjected to temperatures of 85 °C and 25 °C at the bottom and at top ends of the specimens, respectively. Variations of the temperature and the relative humidity with elapsed time at predetermined heights of the bentonite specimens are presented. The variation of suction was calculated from the measured temperature and relative humidity. The elapsed time versus swelling pressure at the opposite end of the heat source of the compacted bentonite specimens during the thermal and the thermo-hydraulic tests are presented. The water content, the dry density and the degree of saturation variations along the depth of the compacted bentonite specimens were computed after completion of thermal and thermo-hydraulic tests.

Chapter 8 presents the change in concentrations of cations and anions along the depth of the compacted bentonite specimens after completion of thermal and thermo-hydraulic tests. The concentrations of anions and cations were measured using Ion Chromatography (IC) and Inductively Coupled Plasma Optical Emission Spectroscopy (ICP-OES), respectively. The change in concentrations of Na^+ , K^+ , Ca^{2+} , Mg^{2+} , Cl^- , NO_3^- and SO_4^{2-} ions with distance from the heater are presented. The effect of thermal and thermal and hydraulic gradients on solute transport in compacted bentonite is brought out in detail.

Chapter 9 presents the results of thermo-hydro-mechanical numerical simulation of two dimensional axi-symmetric model using a finite element based code COMPASS (COde for Modelling PArtially Saturated Soils) (Thomas and He, 1994; Thomas et al., 1998, 2003). The theoretical formulations considered heat flow, water flow, water vapour flow and the deformation of unsaturated soils. The heat flow in unsaturated soil was studied considering Ewen and Thomas (1989)'s approach. The liquid water and water vapour flow were formulated using Darcy's law (1856) and equations suggested by Philip and de Vries (1957), respectively. The deformation behaviour was formulated using Barcelona Basic Model (BBM) proposed by Alonso et al. (1990). The initial and boundary conditions of the simulation are presented. The material parameters were obtained from experimental results. Some parameters were also chosen from results reported in the literature. The transient temperature and suction variations at predetermined depths of the model were calculated. The swelling pressure variations at the opposite end of the heat source were calculated. Comparisons between experimental and simulated results for temperature, suction and swelling pressure with elapsed time are presented.

The main conclusions drawn based on the findings of this research are presented in **Chapter 10**.

Chapter 2

Literature Review

2.1 Introduction

One of the important applications of bentonite is its use as barrier and backfilling material in waste disposal repositories (Thomas et al., 1998; Cleall et al., 2011). Radioactive and toxic wastes are planned to be stored underground at a depth of about 500 to 1000 m surrounded by compacted bentonites. The toxic waste canisters are planned to be stored in deposition holes excavated in crystalline rock. A schematic diagram of deep geological disposal concept is shown in Fig. 2.1. Compacted bentonites are planned to be placed immediate vicinity to the waste canisters are known as bentonite buffer. The excavated tunnels and access galleries are proposed to be sealed after storing the waste canisters using backfilling materials. In engineered barrier systems, compacted

bentonites around the waste canisters will be subjected to elevated temperature and hydraulic pressure. Similarly, bentonites are used as barrier material in low and intermediate level nuclear waste disposal repositories (Fig. 2.2).

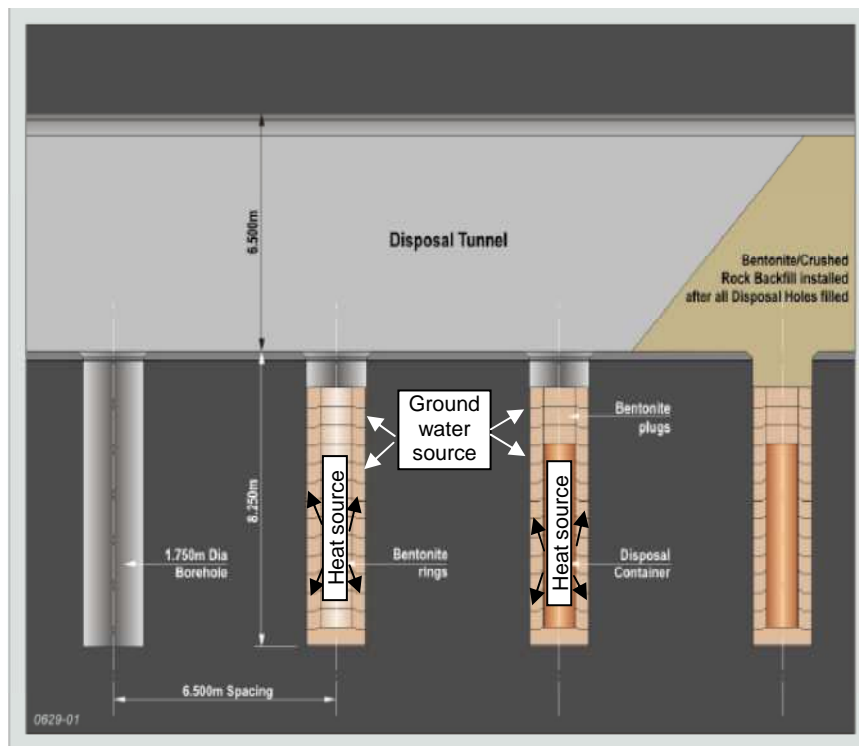


Figure 2.1. Schematic representation of toxic waste disposal concept in the UK (modified after NDA report, 2009).

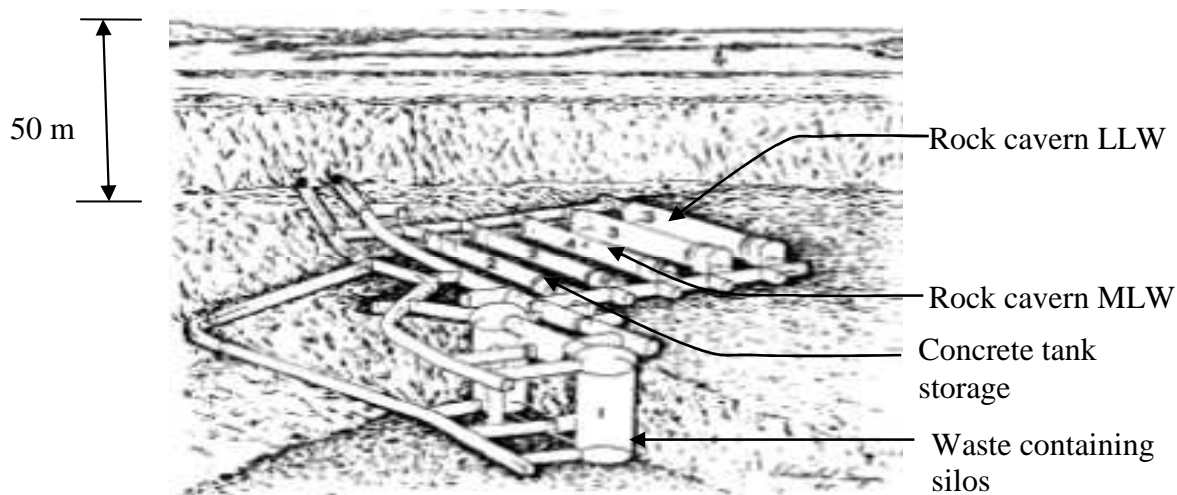


Figure 2.2. Design of final repository for Low and Intermediate level nuclear waste (Roffey, 1990).

Several physical and physico-chemical processes are anticipated in the compacted bentonites during the operational period of waste disposal repositories. This chapter presents a detailed literature review on the physico-chemical aspects and the physical processes that may occur in the compacted bentonites in order to understand the long term behaviour of compacted bentonites in the waste disposal repositories. The structure of montmorillonite and the micro-structure of compacted bentonites are presented in sections 2.2 and 2.3, respectively. Section 2.4 presents the suction of unsaturated soils, methods available for measuring and controlling suction in unsaturated soils. The influence of dry density and temperature on the suction of unsaturated soil is presented. Section 2.5 presents the mechanisms governing swelling of expansive clays. The swelling pressure of expansive soil is defined. Methods adopted for measuring the swelling pressure of compacted bentonites are briefly reviewed. Devices used to carry out swelling pressure tests in the past are reviewed. The effect of post compaction residual stress, temperature and electrolyte concentration on the swelling pressure of compacted bentonites is discussed. The physical state of water molecules in compacted bentonites is presented.

Section 2.6 presents the determination of swelling pressure of compacted bentonites using Gouy-Chapman diffuse double layer theory (Gouy, 1910; Chapman, 1913) and the Stern theory (Stern, 1924). The effect of Stern-layer on swelling pressure and compressibility behaviour of bentonites is brought out in section 2.7.

Section 2.8 presents brief review of laboratory scale thermal and thermo-hydraulic test conditions. Various devices used to carry out thermal and thermo-hydraulic tests are reviewed. Section 2.9 presents the mechanisms governing heat, water and solute transfer

in soils. Variation of cations and anions concentrations along the depth of the compacted bentonites due to thermal gradient and thermal and hydraulic gradients are presented. Section 2.10 presents a brief review on the efficiency of theoretical models used to assess the long term behaviour of compacted bentonites under simulated conditions of the waste disposal repositories. A summary of the chapter is presented in section 2.11.

2.2 Structure of montmorillonite

Bentonite, a smectite group of clay contains large quantity of montmorillonite mineral. Montmorillonite in contact with water either in liquid form or in vapour form expands in volume. The expansion or swelling of clays is due to the mineralogical composition of the elementary layer or structural unit. According to Mitchell and Soga (2005), the structure of montmorillonite is a unit made of an alumina octahedral sheet sandwiched between two silica tetrahedral sheets (Fig. 2.3). The alumina octahedral sheet is composed of an aluminium atom at the centre and six hydroxyls at each corner of an octahedral, whereas the silica tetrahedral is composed of a silicon atom at the centre and four oxygen atoms at each corner of a tetrahedron.

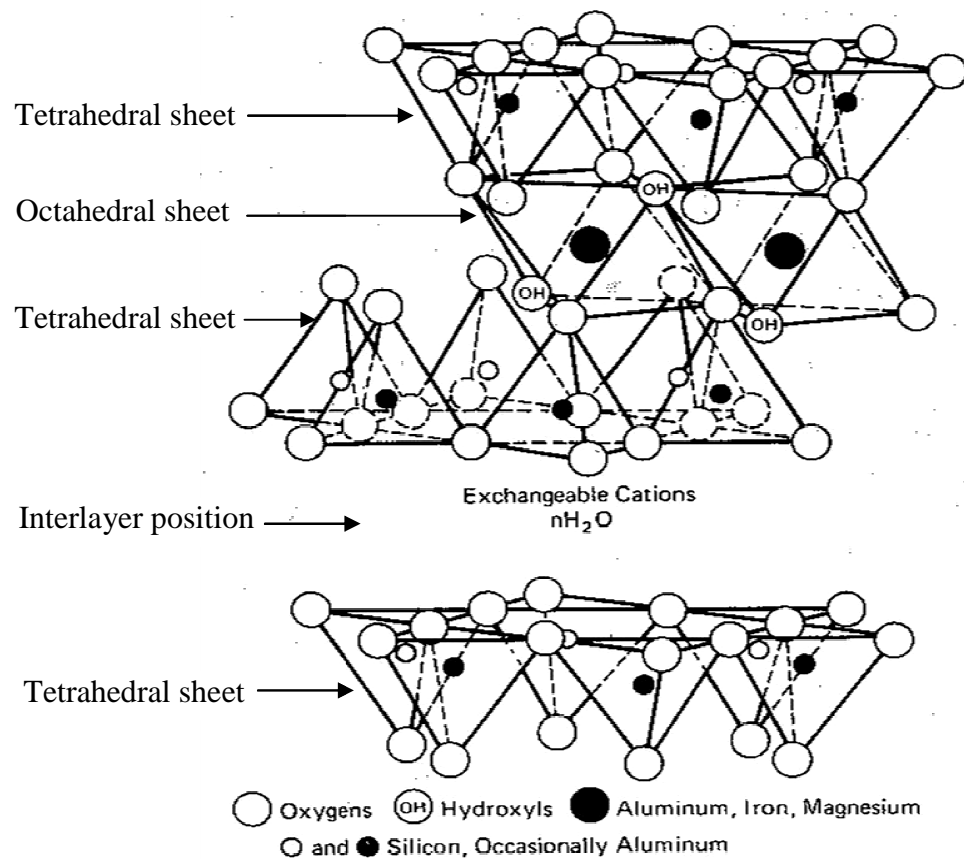


Figure 2.3. Schematic diagram of montmorillonite mineral (Mitchell and Soga, 2005).

An aggregate is made of several stacks of elementary clay minerals (Mitchell and Soga, 2005). Clay particles carry net negative charges on their surfaces due to isomorphous substitution in their crystal lattice (Mitchell and Soga, 2005). Exchangeable cations present in the clay media are attracted to these negative charges. The negatively charged surfaces of the clay platelets, the water and the ions in the clay media, form an electrical double layer around the clay platelets. The physico-chemical interaction between montmorillonite mineral and water molecules is considered as the basis for analysis of the behaviour of bentonites in contact with water or electrolytes (Mitchell and Soga, 2005).

2.3 Structure of compacted bentonite

Depending on the water content and the exchangeable cations present in montmorillonite, particles of bentonites are made of several elementary layers (Pusch et al., 1990; Mitchell, 1993; Pusch, 2001; Saiyouri et al., 2004; Schanz and Tripathy, 2009). Compacted bentonites consists of aggregates of closely spaced mineral particles (Dixon et al., 1999; Delage et al., 2006). Dixon et al. (1999) stated that the spaces between aggregates depend on the energy used during the compaction process.

The presence of structural units, particles and aggregates form different types of pores in bentonites. In general, compacted bentonites possesses two types of pores, namely micro-pores and macro-pores (Pusch, 1982; Gens and Alonso, 1992; Yong, 1999; Pusch and Moreno, 2001; Delage et al., 2006). The micro-pores are the pores within the aggregates (i.e., pores between the elementary layers and between the particles) or called as the intra-aggregate pores (Delage et al., 2006). The macro-pores are the pores between the aggregates or called as the interaggregate pores. The pores between the particles are sometimes called as the interparticle pores or mesopores (Delage et al., 2006).

The number of elementary layers that constitute bentonite particles may vary due to change in the water content (Delage et al., 2006). Therefore, the microstructure of compacted bentonite changes with a change in the water content (Lloret et al., 2003). The behaviour of compacted bentonites is quite complex as a result of interactions between the aggregates and particles and rearrangement of the macrostructure formed by aggregates (Pusch, 2001; Lloret et al., 2003). Delage et al. (2006) noted the time-dependent change in microstructure of compacted MX80 bentonites is due to the

redistribution of the pore water. Based on Mercury Intrusion Porosimetry (MIP) results on compacted bentonites, several researchers have reported bimodal pore size distribution (i.e., inter-aggregate and intra-aggregate porosity) (Dixon et al., 1999; Lloret et al., 2003; Delage et al., 2006).

A schematic representation of the microstructure of montmorillonite showing different pore spaces and presence of water molecule is presented in Fig. 2.4 (Nagaraj and Murthy, 1985). Water molecules, referred to as ‘adsorbed water’, are present between the elementary layers, in pore spaces known as micropores. A number of elementary layers are arranged in stacks to form particles. The formation of clay clusters is due to the arrangement of several aggregates. In the cases of particles and clusters, void spaces between these are known as macropores, with any fluid contained within these voids referred to as bulk fluid.

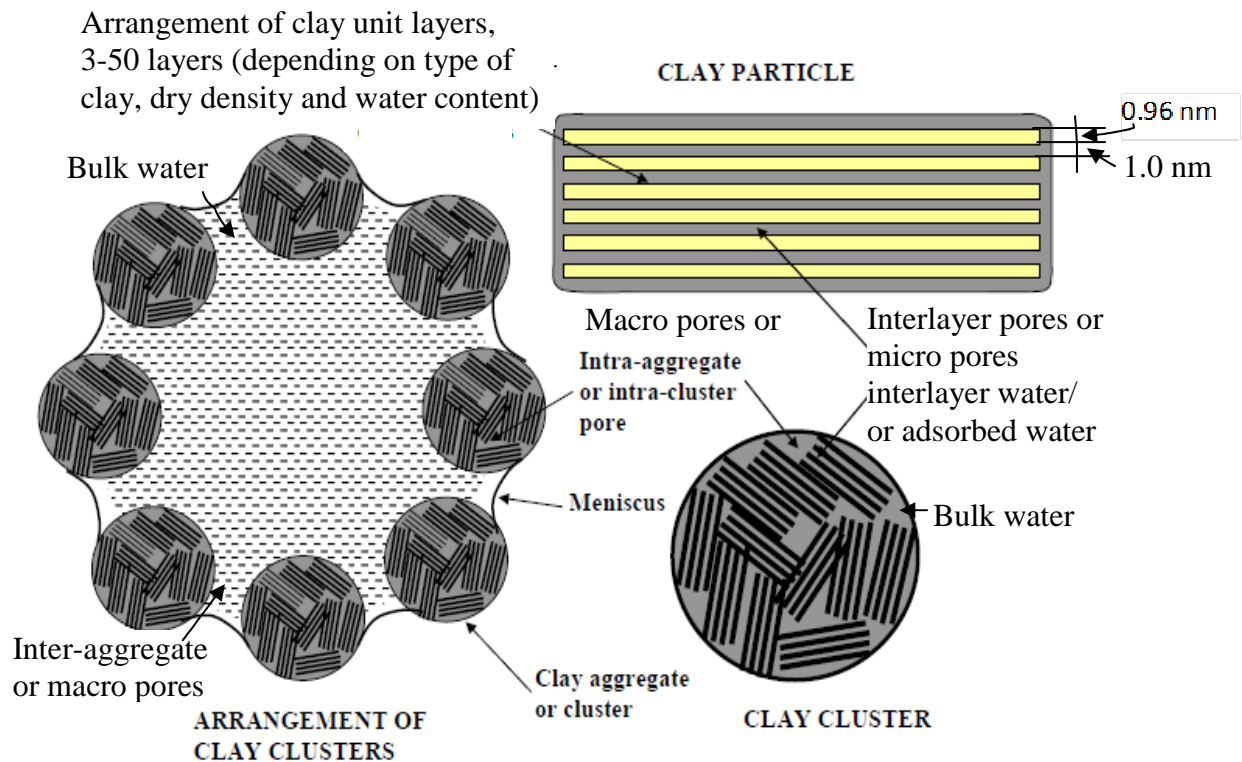


Figure 2.4. Representation of micro structure of expansive clays (modified from Nagaraj and Murthy, 1985).

The change in microstructure of compacted bentonites is responsible for change in hydraulic conductivity, swelling pressure and cation/anion diffusion capacities (Pusch, 2001). Pusch et al. (1990) and Pusch (2001) stated that gel-filled channels are present in compacted saturated bentonites. During the hydration process of bentonites under constant volume condition, the tortuous channels are formed by interconnected voids. Komine and Ogata (2003) and Komine (2004) have considered parallel platelets of montmorillonite to assess the swelling pressure and hydraulic conductivity of compacted bentonites. Thomas et al. (2003) stated that the hydraulic conductivity of compacted bentonites decreases as the water content of bentonite increases. Increase in the water content results in an expansion of the microstructure thereby the void spaces in the macrostructure reduces (Thomas et al., 2003).

The interparticle pores in compacted bentonites are known as free porosity (Pusch et al., 1990; Bourg et al., 2003, 2006; Kozaki et al., 2001; Muurinen, 2009; Muurinen et al., 2004; Suzuki et al., 2004). The anion diffusion in compacted bentonites depend on the amount of available free porosity in bentonites.

2.4 Suction of unsaturated soils

The soil suction is referred to as the free energy state of soil water (Edlefsen and Anderson, 1943). The total soil suction can be measured in terms of relative humidity in the soil-water system (Fredlund and Rahardjo, 1993). The total suction has two components, namely matric and osmotic suctions. Matric suction is the component of the suction arising from the combined effects of capillary and short-range adsorption forces

(due to surface charge, van der Waals attraction and exchangeable cation hydration) in soils (Lu and Likos, 2004). Osmotic suction is commonly associated with the chemical concentration of the pore fluid in soils (Fredlund and Rahardjo, 1993).

Several methods can be employed for applying, controlling and for measuring suction in unsaturated soils. Table 3.1 presents the methods adopted for measuring and controlling suction by several researchers in the past.

Table 2.1 Summary of reported suction measurement methods

Suction measurement method	References
Pressure plate apparatus	Richards, 1941; Croney et al., 1952; Croney and Coleman, 1961; Klute, 1986; Vanapalli et al., 1999; Leong et al., 2004; Oliveria and Fernando, 2006; Péron et al., 2007; Cresswell et al., 2008
Osmotic technique	Zur, 1966; Kassif and Ben Shalom, 1971; Delage et al., 1987; Cui and Delage, 1996; Delage et al., 1998; Fleureau et al., 2002; Blatz et al., 2008, Delage et al., 2008; Tarantino et al., 2011
Vapour equilibrium technique	Delage et al., 1998; Blatz et al., 2008; Delage et al., 2008
Null type axis translation technique	Fredlund and Rahardjo, 1993; Delage et al., 2008; Tarantino et al., 2011
Relative humidity probes	Agus and Schanz, 2005; Fredlund, 2006
Tensiometers	Fleureau et al., 2002; Tarantino et al., 2011
Chilled-mirror hygrometer technique	Leong et al., 2003; Agus and Schanz, 2005
Thermal conductivity sensors	Shaw and Baver, 1939; Fredlund and Wong, 1989; Fredlund et al., 2000; Shuai et al., 2003; Feng and Fredlund, 2003; Feng et al., 2002; Nichol et al., 2003; Rahardjo and Leong, 2006; Leong et al., 2011
Psychrometers	Richards, 1965; Krahn and Fredlund, 1972; Ridley and Wray, 1996; Harrison and Blight, 2000; Tang et al., 2002; Pan et al., 2010
Filter paper method	Gardner, 1937; Fredlund and Rahardjo, 1993; Houston et al., 1994; Bulut et al., 2000, 2001; Likos and Lu, 2002; Leong et al., 2003; Marinho and Oliviera, 2006; Bulut and Leong, 2008; ASTM D 5298-94, 2010

Saiyouri et al. (1998, 2000) showed that hydration of compacted bentonite proceeds by the combined action of the progressive adsorption of water layers along the clay layers inside the particles and the simultaneous division of the particles. At fully hydrated state, the elementary layers dissociate to about 10 layers from the initial 350 layers. The dissociation of elementary layers creates interparticle porosity inside the saturated aggregates as a function of density and water content. During the hydration process, the inter-aggregate porosity decreases and inter-layer porosity increases in relation to the development of interparticle pores inside the aggregates (Delage et al., 2006). The suction in compacted unsaturated bentonite progressively reduces due to progressive insertion of successive layers of water molecules in the interlayer spaces inside the particles (Delage et al., 2006).

2.4.1 Suction versus water content relationship

The relationship between suction versus degree of saturation or water content is commonly known as the soil water characteristics curve (SWCC), when the specimens have been subjected to continuous drying or continuous wetting. Typical SWCCs of sandy and clayey soils are presented in Fig. 2.5. The SWCC normally exhibits a sigmoidal function. The suction corresponding to the oven-dried conditions is 1000 MPa (Croney and Coleman, 1961). During drying and wetting, the void ratio of clayey soils changes. The amount of water drained out of the specimen during drying from saturated conditions is accompanied by a reduction in the void ratio of the soil. Therefore, although a significant reduction in the amount of water in the specimen takes place, the clayey soil remains saturated up to relatively high suction value. This is due to dominant physico-chemical effects of the clay-water system at the microscopic level. The SWCC can be

divided into three regimes: (i) a saturation regime where soil remains saturated under negative pore water pressure characterised by negative pore water pressure, often referred to as the capillary fringe; (ii) a desaturation regime characterised by a continuous water phase, and (iii) a residual regime characterised by a discontinuous water phase (Lu and Likos, 2004).

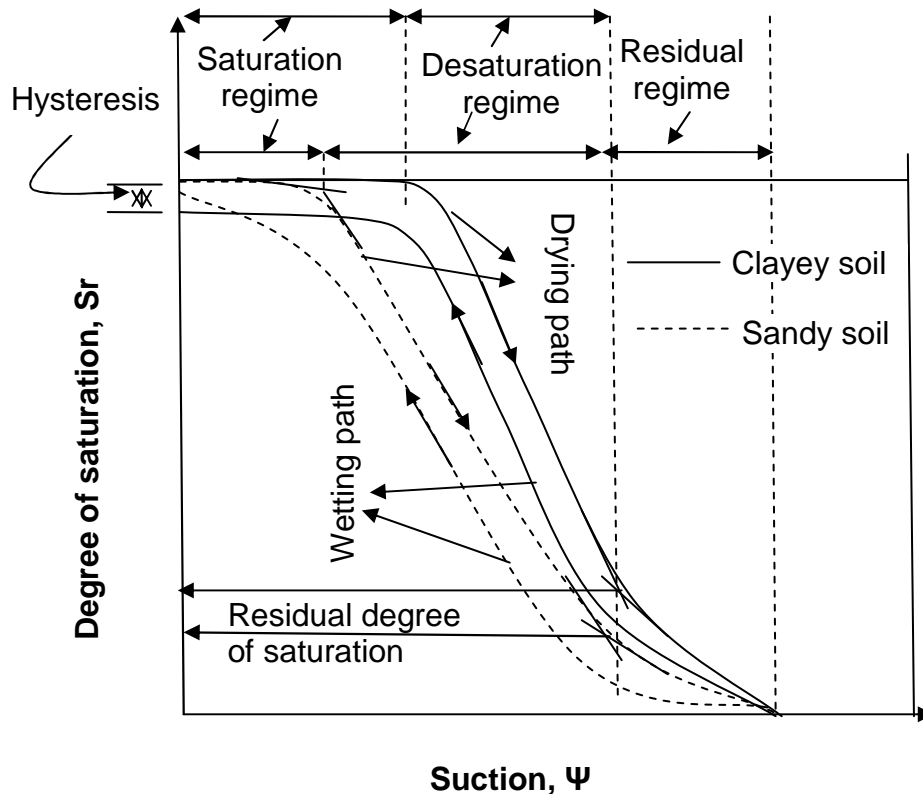


Figure 2.5. Typical SWCCs for different types of soil.

2.4.2 Effect of dry density and temperature on suction-water content relationship

The behaviour of unsaturated soil is greatly influenced by suction-water content relationship of the soil. At higher temperatures fabric of the soil changes and surface tension of water decreases (Klute, 1986). The water retention capacity of unsaturated soil at elevated temperature reduces due to change in the soil fabric and the surface tension of water (Romero et al., 2000; Villar and Lloret, 2004; Tang and Cui, 2005). Klute (1986)

stated that the effect of temperature on the adsorptive forces are obscure; however, increase in temperature leads to reduction in water content of the soil at a given matric suction. The effect of temperature on suction-water content relationship is not very large (Klute, 1986).

Suction measurement at elevated temperatures are usually conducted in an autoclave during water equilibration process (Villar and Lloret, 2004; Jacinto et al., 2009). Jacinto et al. (2009) noted that the effect of temperature on suction-water content relationship is limited only at low suction levels. Beyond the suction of 30 MPa, the dry densities of compacted bentonites have insignificant influence on the suction-water content relationship (Jacinto et al., 2009). Similar effect of the dry density on the suction-water content relationship of compacted bentonites were noted in other studies (ENRESA, 2004; Delage et al., 2006; Tang and Cui, 2010).

The previous studies showed that at higher suctions both an increase in the dry density and the temperature have insignificant influence on suction-water content relationships of compacted bentonites.

2.5 Mechanisms governing swelling of expansive clays

Swelling of expansive clays exposed to water or electrolytes is primarily due to two mechanisms: (i) the crystalline swelling and (ii) the diffuse double-layer swelling (van Olphen, 1977). The crystalline swelling occurs because of the hydration of ions and surfaces of the clay platelets (van Olphen, 1977, Madsen and Müller-vonmoos, 1995). During the crystalline swelling, 0 to 4 discrete layers of water molecules are intercalated

between elementary layers within a smectite particle (van Olphen, 1977). The crystalline swelling is controlled by the layer charge, interlayer cations, properties of adsorbed liquid, particle size and temperature (Yong, 1999). Considering the presence of various potential energies in between the elementary layers, the crystalline swelling is balanced by the Columbic and van der Waals attraction and Born repulsion (Laird, 2006).

In heavily compacted unsaturated bentonites, the crystalline swelling is of major importance pertaining to its use as a containment barrier for the nuclear waste repository (Bucher and Müller-Vonmoos, 1989). Beyond the crystalline swelling, the double layer swelling is significant (van Olphen, 1977). The double-layer swelling occurs due to overlapping diffuse double layer in between the particles (Pusch et al., 1990; Bradbury and Baeyens, 2003; Laird, 2006) and also in between elementary layers (Mitchell, 1993; Delage et al., 2006). Diffuse double layer swelling depends on the specific surface area, electrolyte concentration of the bulk fluid, dielectric constant, valence of the cations and the distance between the elementary layers (Sridharan and Jayadeva, 1982). An increase in temperature increases the thickness of diffuse double layer and decreases the surface potential of soil. However, an increase in temperature decreases dielectric constant of pore fluid. Therefore, the change in temperature has lesser influence in double layer swelling of expansive clays (Mitchell, 1993).

2.5.1 Swelling pressure

The volume of unsaturated bentonite increases when exposed to water or electrolytes. Under restrained conditions, compacted bentonites exhibit swelling pressure during the hydration process. Swelling pressure is defined as the pressure required to

maintain a constant void ratio of the specimens during the hydration process of unsaturated expansive soils (Sridharan et al., 1986). The quantification of swelling pressure during hydration of compacted specimens is an important aspect in order to provide safe design of toxic waste disposal barriers. Determination of the swelling pressure of compacted bentonites is discussed in detail in the following section.

2.5.2 Determination of swelling pressure of compacted bentonites

The swelling pressures of expansive soils can be measured by three different methods, namely swell load test, swell under load test and constant volume test (Sridharan et al., 1986). The swell load test has been reported to give the highest value of swelling pressure, swell-load test to give the least value and constant volume test to give intermediate value (Sridharan et al., 1986). Different methods of swelling pressure measurement are illustrated in Fig 2.6.

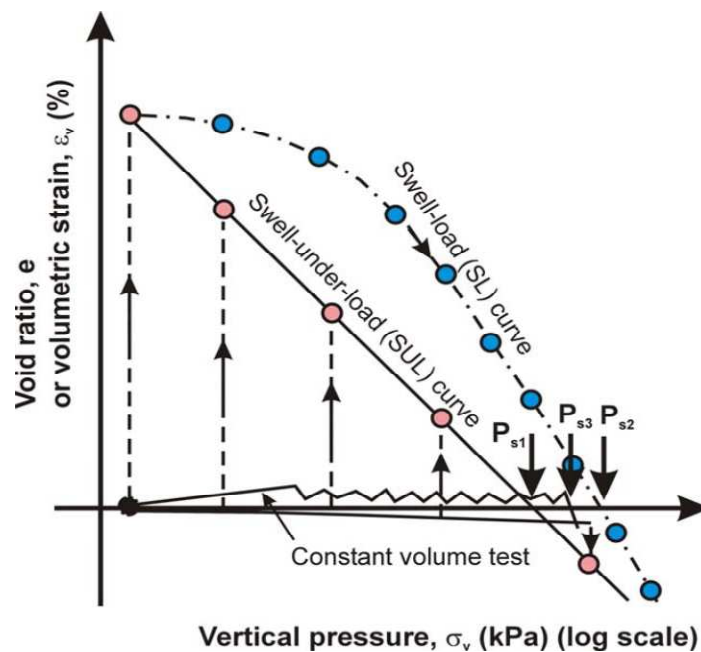


Figure 2.6. Swelling pressure measured using different methods (Modified after Sridharan et al., 1986).

Several experimental studies have been reported on the swelling pressure of compacted bentonites (Müller-Vonmoos and Kahr, 1982; Pusch, 1982; Dixon and Gray, 1985; Swedish Nuclear Fuel and Waste Management Company, 1983; Komine and Ogata, 1994; Empresa Nacional de Residuos Radiactivos SA, 2000; Villar and Lloret, 2004; Karnland et al., 2007; Villar and Lloret, 2008; Komine et al., 2009; Schanz and Tripathy, 2009). The swelling pressure of expansive soils is measured by the constant volume method in laboratory considering placement conditions of compacted bentonites in the repository where the volume change is restricted (Madsen and Müller-vonmoos, 1985; Madsen, 1989; Madsen and Müller-vonmoos, 1989).

2.5.3 Swelling pressure measurement devices

The swelling pressure tests are usually carried out in oedometers. Madsen and Müller-vonmoos (1985) used a modified oedometer to measure the swelling pressure of compacted bentonites (Fig. 2.7). Madsen and Müller-vonmoos (1985) monitored the deflection of the specimen using two dial gauges. The swelling pressure was measured by accommodating a pressure cell in between a loading plunger and a restrained bar. Romero (1999) developed a device known as Barcelona cell for measuring swelling pressures of compacted bentonites by constant volume method (Fig. 2.8). The device was facilitated with a load cell for measuring the swelling pressure. Clay specimens were hydrated by circulating fluid from both the top and the bottom of the clay specimens. Several researchers have used the modified oedometer (Romero, 1999) for measuring the swelling pressure of compacted bentonites under constant volume condition (Hoffman et al., 2007; Castellanos et al., 2008; Schanz and Tripathy, 2009).

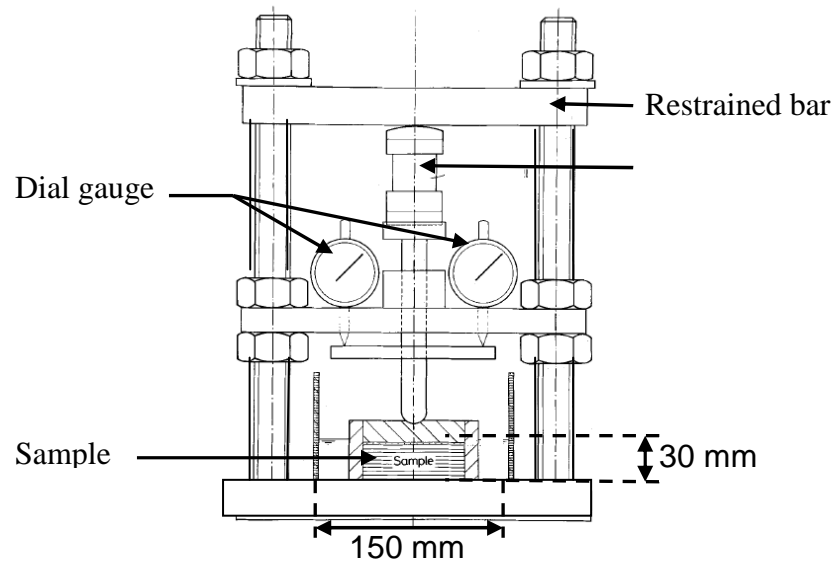


Figure 2.7. Setup for measuring the swelling pressure (Madsen and Müller-vonmoos, 1985).

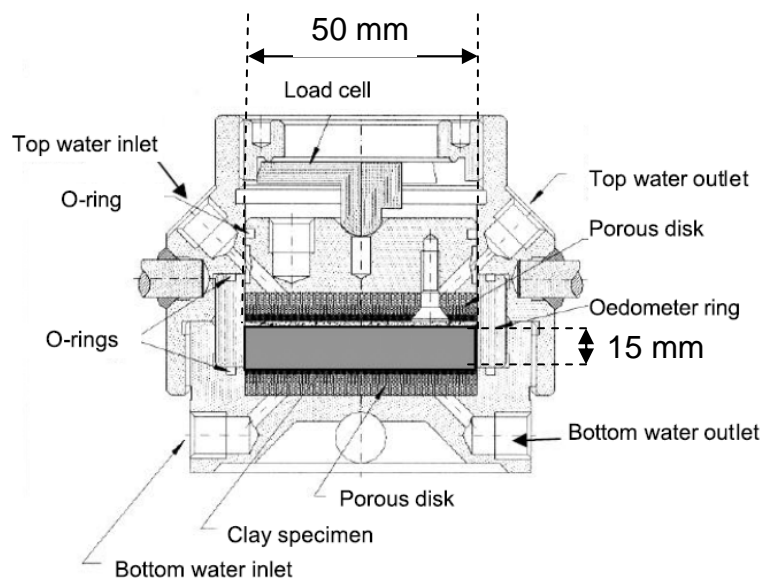


Figure 2.8. Schematic diagram of devices used for measuring the swelling pressure by constant volume method developed by Romero (1999).

A limited number of devices are available to measure the swelling pressures at elevated temperatures (Agus, 2005; Arifin, 2007). In order to conduct the swelling

pressure tests at elevated temperature, a special arrangement and modification of the existing devices are required.

2.5.4 Effect of post compaction residual stress release on swelling pressure

In practice, compacted bentonites are prepared by compacting bentonite powder by applying a static compaction load. After completion of the compaction process, the compacted bentonites are removed from the compaction mould. Upon removing from the compaction mould, the post compaction residual stresses on compacted bentonites are eliminated. Release of the post compaction residual stresses of compacted bentonites may cause lateral expansion. Therefore, the swelling behaviour of compacted bentonites may be affected due to the release of post compaction residual stresses. A review of literature suggests that most of the swelling pressure tests reported so far were carried out in laboratory condition by hydrating specimens immediately after the compaction process was completed. The effect of post compaction residual stress release on swelling pressure of compacted bentonites has not been explored so far.

2.5.5 Effect of temperature on swelling pressure

Pusch (1980) measured the swelling pressures of compacted MX80 bentonite at temperatures of 20 °C and 90 °C by hydrating the specimens with distilled water and different electrolytes. Pusch (1980) reported significantly lower swelling pressure for the specimens tested at 90 °C temperature than the specimens tested at 20 °C. Pusch (1980) stated that the reduction of swelling pressure was due to the presence of less stable interlayer and interparticle water at higher temperature. Pusch et al. (1990) noted that an

increase in the temperature resulted in a decrease of swelling pressure of Ca-bentonite. Similar results were reported by Villar and Lloret (2004) for FEBEX bentonite (i.e., Ca-Mg bentonite). Romero et al. (2003) reported the temperature effects on controlled-suction swelling pressure test or multi-step swelling pressure test for compacted Boom clay. It was noted that the swelling pressure values at each equilibrium suction (i.e. suctions of 4500, 2000, 600 kPa and saturated condition) at 22 °C were higher than those at 80 °C.

In general, an increase in the temperature results in decreasing the swelling pressures of compacted bentonites. Further investigation is required to evaluate the effect of temperature on swelling pressure of bentonite specimens devoid of post compaction residual stresses.

2.5.6 Effect of electrolyte concentration on swelling pressure

In several geotechnical engineering applications, bentonites are used as barrier and backfilling material in waste disposal repositories. The bentonites used may be subjected to groundwater or electrolytes migrated from the subsurface. The swelling pressure of compacted bentonites is known to be affected due to the pressure of electrolytes in bulk fluids. Pusch (1980) measured the swelling pressures of MX80 bentonites using 0.6 M NaCl and 0.3 M CaCl₂ solutions. It was noted that the swelling pressure of compacted bentonites reduced for the bulk densities of compacted bentonites lower than 2.05 Mg/m³. Pusch (1980) concluded that the pore water salinity was not a determinant of the swelling pressure above the bulk density of 2.05 Mg/m³. Karnland et al. (2007) studied the effect of electrolyte concentration on the swelling pressure of

compacted MX80 bentonite. The specimens in their case were hydrated with 0.1 M, 0.3 M and 1.0 M NaOH solutions. Significant reduction in the swelling pressure was noted for the specimens that were tested with 0.3 and 1.0 M NaOH solutions. Karnland et al. (2007) stated that the reduction in swelling pressure was due to an instant osmotic effect and a continuous dissolution of silica minerals leading to a mass loss and consequently to a decrease of the bentonite density.

Castellanos et al. (2008) noted lesser swelling pressures at lower dry densities by saturating compacted FEBEX bentonite specimens using saline solutions. At dry densities above 1.60 Mg/m^3 , the reduction in swelling capacity was reported to be smaller. Similar observations were reported by Komine et al. (2009) for Na^+ and Ca^{2+} type bentonites.

The swelling pressure test results reported by earlier researchers were conducted immediately after completion of the compaction process without extrusion of specimens from the compaction ring. Further investigation is required to study the effect of electrolyte solutions on swelling pressures of compacted bentonite specimens devoid of post compaction residual lateral stresses.

2.5.7 Physical state of water in compacted bentonite

The surfaces of montmorillonite form electrical bonding with water molecules. The possible mechanisms for clay-water interaction are hydrogen bonding, hydration of exchangeable cations, attraction by osmosis, charged surface-dipole attraction, and attraction by London dispersion forces (Mitchell, 1993). The properties of sorbed water in montmorillonite surfaces differ than that of bulk water. The adsorbed water is denser and

viscous than that of the bulk water (Langmuir, 1917; Terzaghi, 1928; Winterkorn, 1943; Baver and Winterkorn, 1936). Grim and Culbert (1945) and Sposito and Prost (1982) have shown that the difference between adsorbed water molecules and those in the bulk liquid is due to the exchangeable cations presents in clay. The type of adsorbed ions (valence, size and geometry) and the nature of packing greatly influence the properties of the adsorbed water in clays (Grim, 1967). Low (1979) concluded that the hydrogen-bonded structure of water adsorbed by Na-montmorillonite is more extensible and compressible but also less easily fractured than the structure of the bulk liquid water. Low (1976, 1979) and Bourg (1999) shown that the viscosity of the adsorbed water is higher than that of bulk water and increases exponentially with deceasing water content.

Martin (1962) stated that the density of water sorbed in Na-montmorillonite varies with water content of clays. Tscapcek (1934) reported the density of adsorbed water in montmorillonite as 1.70 Mg/m^3 . Anderson and Low (1957) noted the density of water in Na-montmorillonite as 0.97 Mg/m^3 . Skipper et al. (1995) shown that the density of water in Na-montmorillonite as 1.14 Mg/m^3 . Karnland et al. (2006) shown that the adsorbed water density in compacted MX80 bentonite specimens varies between 1.03 to 1.3 Mg/m^3 for the dry densities of compacted bentonite specimens between 1.0 to 2.3 Mg/m^3 . Villar and Lloret (2008) showed that the calculated pore fluid density for compacted FEBEX bentonite hydrated with distilled water increased from 1.04 to 1.22 Mg/m^3 for an increase in the dry density of compacted specimens from about 1.25 to 1.85 Mg/m^3 .

The presence of inorganic compounds such as NaCl, CaCl_2 in bentonite is attributed to higher adsorbed water density (Karnland et al., 2006). Karnland et al. (2006)

shown that the density of water increases with increasing concentration of NaCl and CaCl₂ in the pore water of montmorillonite.

From the above literature review, it is evident that the density of pore water in montmorillonite varies due to electrical bonding. A review of the literature suggested that the density of water in Na-montmorillonite may vary between 0.97 Mg/m³ and 1.14 Mg/m³. Consideration of change in the density of water during the hydration of compacted bentonites is an important aspect in order to analyse the behaviour of compacted bentonites at saturated condition.

2.6 Compressibility behaviour of bentonite

In geological waste disposal repositories, compacted bentonites exhibit swelling pressures upon imbibing fluid from the saturated host rock. Schanz and Tripathy (2005) stated that in this condition, the stress convergence of the host rock becomes an important issue and hence so is the pressure – void ratio relationship of the compacted saturated bentonites. A number of studies have been carried out on the compressibility behaviour of expansive clays covering a wide range of void ratios owing to large pressure changes (Bolt, 1956; Mesri and Olson, 1971; Low, 1980; Sridharan et al., 1986; Al-Mukhtar et al., 1999; Fleureau et al., 2002; Marcial et al., 2002). The basis of analysing compressibility behaviour of bentonites was based on initially saturated clays with water content greater than the liquid limit. The saturated condition of clays is considered as reference condition to study behaviour of clays. Tripathy and Schanz (2007) showed that the pressure-void ratio relationship of bentonites at large pressures can be obtained based on the void ratios at smaller pressure and using Gouy-Chapman diffuse double layer theory. Baille et al.

(2010) studied the compressibility behaviour of compacted saturated bentonites at large pressures.

2.7 Theoretical assessment of swelling pressure

In the past, electrical theories were considered for determining the swelling pressures of bentonites. The Derjaguin–Landau–Verwey–Overbeek (DLVO) theory (Verwey and Overbeek, 1948) considered the repulsive electrostatic double layer forces and the attractive van der Waals forces in a clay–electrolyte system. An empirical relationship between dry density and swelling pressure for Na-montmorillonite clays was suggested by Low and Margheim (1979) and Low (1980). The anisotropic hypernetted chain (HNC) theory (Kjellander and Mačelja, 1985) took into account the effect of bivalent cations (e.g., Ca-clay) in the swelling of clays. Sridharan and Choudhury (2002) proposed a semi-empirical method for determining the swelling pressure of Na-montmorillonite.

Several researchers have used the Gouy-Chapman diffuse double layer theory to assess the swelling pressure and the compressibility behaviour of bentonites (Bolt, 1956; van Olphen, 1977; Mitchell, 1993; Tripathy et al., 2004; Schanz and Tripathy, 2009). The diffuse double theory assumes that ions in the diffuse double layers are regarded as point charges and the ion distribution is assumed to follow the Boltzmann distribution equation. The clay platelets are assumed to be parallel to each other. The electrical potential is assumed to be determined by the Poisson equation in a similar form to that used in the electromagnetism theory. No interactions between ions in the diffuse double layers and parallel clay platelet arrangements. Because diffuse double layer theory assumes the ions in

solution have point charges and hence any specific effect related to ion size is neglected (Verwey and Overbeek, 1948). Such assumptions have been shown to yield high values of ion concentration near the surfaces of the clay platelets (Verwey and Overbeek, 1948; van Olphen, 1954; Hunter, 1981; Mitchell, 1993).

A review of literature suggested that consideration of the Stern-layer (i.e., a compact ion-layer proximity to clay platelet surfaces) is a more realistic representation of clay-water electrolyte systems (Stern, 1924; Verwey and Overbeek, 1948; van Olphen, 1977; Pashley, 1981; Israelachvili and Wennerström, 1996; Marčelja, 1997). The Stern theory proposed by Stern (1924) has been applied to determine the electrical potential distribution in single clay platelet systems (Shang et al., 1994; Sridharan and Satyamurty, 1996), to reproduce electrochemical and electrokinetic properties for colloidal suspensions (Leroy and Revil, 2004) and to determine the swelling pressure of Na-montmorillonite (Gonçalvès et al., 2007). Applications of the Stern theory to study the swelling and the compressibility behaviour of bentonites from interacting electrical diffuse double layers consideration are scarce in the literature.

2.8 Effect of Stern layer on swelling pressure and compressibility of bentonite

Stern (1924) proposed that the finite size of the ions (either hydrated or not), limits the closest approach of a counter-ion to the charged clay surfaces. Therefore, the concentration of ions near the clay surface is appreciably lesser as compared to that calculated by treating the ions as point charges. This may have some influence on charge distribution of the clay-water system that in turn, may influence the swelling pressure of bentonites.

Figure 2.7 shows the salient features of the interacting double layers with an inclusion of the Stern layer on the clay platelets. In the 2:1 (silica tetrahedral-aluminium octahedral silica tetrahedral) clay mineral montmorillonite, the outer sheet of the mineral carries the siloxane surface sites (Si-O-Si). The total charge, σ (C/m²), at the surface is primarily due to the isomorphous substitutions in the octahedral sheets (Al-O-Al). According to Stern (1924), due to the adsorption of cations on the surfaces of clay platelets, the total charge, σ (C/m²), in the clay-water system can be divided into two parts (Fig. 2.9). The Stern-layer charge, σ_1 (C/m²), is considered to be concentrated in a plane at a distance δ from the surfaces of clay plates.

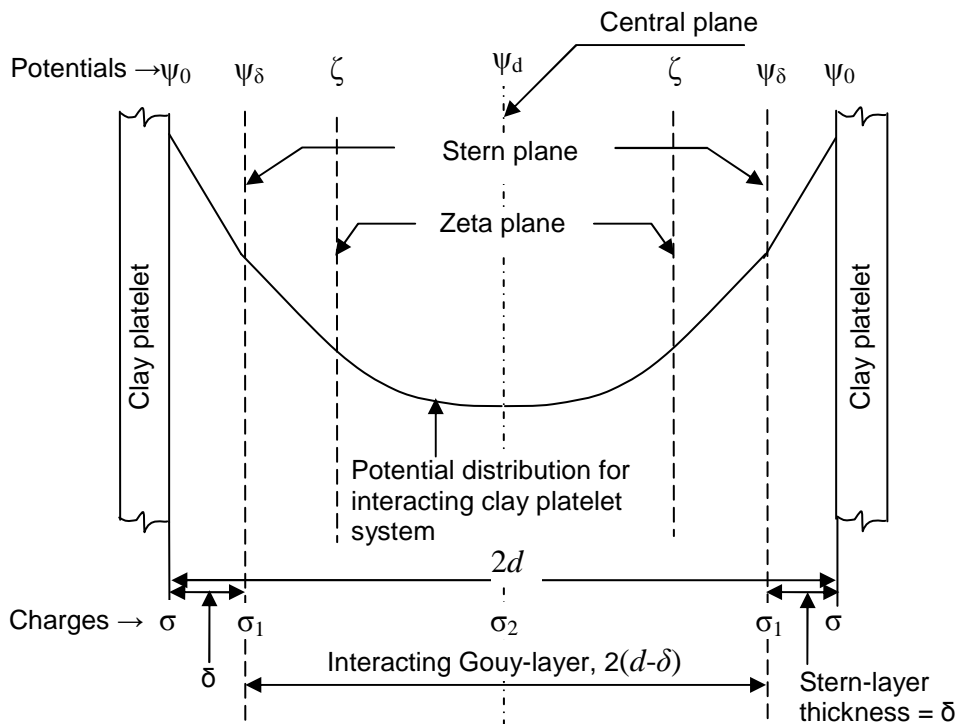


Figure 2.9. An appreciation of Stern and Gouy layer and charge distribution in clay-water electrolyte system.

The charge is null within the Stern layer that acts as a molecular condenser. The Gouy-layer charge, σ_2 (C/m²), extends from the Stern-plane in accordance with the

Poisson-Boltzmann's distribution. The electrical potential decreases linearly from a value ψ_0 (V) at the surfaces of the clay platelets to a value ψ_δ (V) at the Stern-plane. The zeta plane (or the shear plane) is usually further away from the Stern plane (Hunter 1981) and has a potential of ζ (V). The distribution of the electrical potential in the Gouy-layer and its value at the central plane between clay platelets, ψ_d (V), depend upon ψ_δ and the charge available in the Gouy-layer (σ_2).

The Stern theory can be used to determine electrokinetic and electro-chemical properties, potential energy and swelling pressure of clay-water electrolyte systems by considering either a constant charge or a constant electrical potential at the surfaces of the clay platelets (Verwey and Overbeek, 1948; van Olphen, 1977). Traditionally, because of isomorphous substitution, clay minerals such as montmorillonite and illite have been regarded as constant charge (variable potential) surfaces (Horikawa et al., 1988). Electrical theory based on the surfaces of constant charge, such as the Gouy-Chapman diffuse double layer theory (without Stern-layer) has been extensively used in the geotechnical engineering literature to establish the swelling pressure-void ratio relationships and hydraulic conductivity of clays (Tripathy et al., 2004). On the other hand, Verwey and Overbeek (1948), Chan et al. (1984) and McCormack et al. (1995) stated that the clay surfaces appear to behave more like constant-potential than constant-charge surfaces.

van Olphen (1977) presented the theoretical procedure for determining distribution of the electrical potential for single clay platelet systems and the procedure for determining the swelling pressure for the case of interacting diffuse double layers as applicable to large clay platelet distances using the Stern theory. Both the procedures are

based on the constant charge at the surfaces of the clay platelets. For strong interactions, the constant surface charge method needs further modification (van Olphen, 1977). Verwey and Overbeek (1948) presented the Stern theory to establish distributions of the charge and the electrical potential at the Stern-plane and in the Gouy-layer for both single and interacting clay platelet systems. Although the Stern theory dealt with by Verwey and Overbeek (1948) has been extensively used in various fields of engineering and science, studies concerning the influence of Stern-layer on the dry density-swelling pressure and pressure-void ratio relationships of bentonites are scarce.

2.9 Thermo-hydro-mechanical-chemical tests on compacted bentonite

In several geotechnical engineering applications, bentonites are subjected to elevated temperature and hydraulic gradient. Several physical processes are expected to occur due to the thermal and the hydraulic loading conditions (Pusch and Yong, 2006). For example, to assess the behaviour of compacted bentonites in waste disposal repositories, understanding the heat and water flow processes in compacted bentonites are of great importance. Compacted bentonites are usually subjected to elevated temperature and the hydraulic gradients in such a situation. Due to the elevated temperature and the hydraulic gradient, several processes are expected to occur, such as: (i) swelling and shrinkage of the compacted bentonites, (ii) the suction, the water content, the dry density and the degree of saturation along the compacted bentonite barriers may get altered and (iii) the concentrations of cations and anions along the compacted bentonite barriers may change due to diffusion and advection processes.

Due to migration of ground water from the subsurface, the water content of bentonites is likely to increase resulting in a variation of dry density (Pusch and Yong, 2006; Villar et al., 2008). Pusch and Yong (2006) stated that swelling of the constrained bentonite in presence of water will produce resultant swelling pressures and local compression of the material. Gens et al. (2007) stated that the pore water pressure generation in unsaturated compacted bentonites during thermal loading is controlled primarily by an increase in temperature.

2.9.1 Thermo-hydro-mechanical-chemical test conditions

In the past, several experimental investigation and numerical modelling works were undertaken to understand the physico-chemical processes occurring in engineered barrier systems. The effects of physico-chemical processes occurring in engineered barrier systems on the thermo-hydro-mechanical behaviour of compacted bentonites were evaluated. Table 2.1 presents the initial and testing conditions of laboratory scale and in-situ thermo-hydraulic tests carried out using several bentonites. The maximum applied temperature on the compacted specimens was varied between 70 and 140 °C. During the hydration process, hydrating fluid was injected with a maximum applied pressure of 1.2 MPa. The tests were conducted for a range of dry density of compacted bentonites between 1.50 and 1.72 Mg/m³. The tests were carried out for different duration of time varying from 1 day to 8 years.

Most of the previous studies were conducted by subjecting compacted bentonites to elevated temperature and hydraulic pressure simultaneously at opposite ends. Studies concerning the behaviour of compacted bentonites subjected to only thermal gradient

require further investigation. Similarly, the variation of swelling pressure under temperature gradient across compacted bentonites has not been explored in detail. During the operational period of toxic waste disposal repositories, compacted bentonites may undergo thermal loading at the early stage. In the later stage, the bentonites will be subjected to both thermal and hydraulic gradients. Therefore, it is necessary to study the behaviour of compacted bentonites under thermal gradient followed by thermal and hydraulic gradients.

Table 2.2 Summary of reported thermal and thermo-hydraulic tests

Type of test	Material used (bentonite)	Specimen Size		Initial compaction condition		Temperature (°C)	Fluid injection pressure	Reference
		Ht. (mm)	Dia. (mm)	ρ_d (Mg/m ³)	w (%)			
T	Buffer	600	262	1.66	17.5	100, 80	--	Selvadurai (1996)
TH	Avonlea	110	75	1.67	17.7	100, 80, 60	--	Yong et al. (1997)
TH	FEBEX	146	150	1.65	11.23	100	1 MPa	Samper et al. (2001)
TH	Bentonite OT-9607	100	50	1.65	16	70, 25	--	Börgesson et al. (2001)
TH	FEBEX	76	38	1.63	15.33	80, 30	--	Pintado et al. (2002)
TH	FEBEX	25	50	1.65	14.1	100, 60, 35	1 MPa	Martín et al. (2000); Cuevas et al. (2002)
TH	FEBEX	7040	2280	1.7	14.4	100, 30	--	Villar et al. (1996); Samper et al. (2008); Gens et al. (2007)
TH	Kyugnju	7830	2250	1.5	13	90, 25	--	Lee et al. (2008)
TH	Calcigel	300	100	1.65	13.5	80	--	Mishra et al. (2008)
TH	FEBEX	200	-	1.7	13.3	120, 84	--	Åkesson et al. (2009)
TH	MX80	--	--	1.65	17.7	130, 90	1.5 MPa	Pusch et al. (2009)
TH	FEBEX	600	70	1.65	13.6	100	1.2 MPa	Villar et al. (2008); Fernández and Villar (2010)
TH	MX80	200	70	1.72	16	140, 30	10 kPa	Gómez-Espina and Villar (2010)
T	Opalinus clay	14000	300	2.22	4.2-8.0	100	--	Gens et al. (2009)

T-Thermal, TH-Thermo-hydraulic

2.9.2 Thermo-hydro-mechanical-chemical testing devices

In the past, several researchers have carried out thermo-hydraulic tests on compacted bentonites using custom made devices. Yong and Mohamed (1992) conducted infiltration experiments on unsaturated expansive soils using a cylindrical cell. The device was facilitated with a metal heater at the top of the compacted specimen. Kanno et al. (1996) designed an experimental device so that the coupled heat and water flow had a one-dimensional vertical movement. Koniger et al. (2008) studied the moisture spreading in a multi-layer hydraulic sealing system in isothermal condition through a column test. Börgesson et al. (2001) conducted thermal gradient tests in a twin apparatus called KIDBEN. Pintado et al. (2002) performed laboratory scale thermo-hydraulic tests in the specially designed experimental apparatus. Cuevas et al. (2002) conducted a thermo-hydraulic test on compacted bentonites using a hermetic cell made up of Teflon. Gatabin and Billaud (2005) conducted thermal gradient and thermo-hydraulic gradient test on MX80 bentonite. The cell used was capable of measuring transient pore water pressure, swelling pressure, temperature and relative humidity. Cleall et al. (2011) used a custom made device in order to carry out thermal and thermo-hydraulic tests.

Figure 2.10 presents the thermo-hydraulic test setup used by Villar et al. (1996). A series of experimental investigations were carried out using the test setup in several studies (Villar et al., 2007; Fernandez and Villar, 2010; Gomez-Espina and Villar, 2010). A metal heater was accommodated at the bottom end of the cylindrical specimens to apply desired temperature on the specimens. In order to apply hydraulic loading, fluid was supplied from the top end of bentonite specimens. The fluid supply chamber was facilitated with volume change and data acquisition systems.

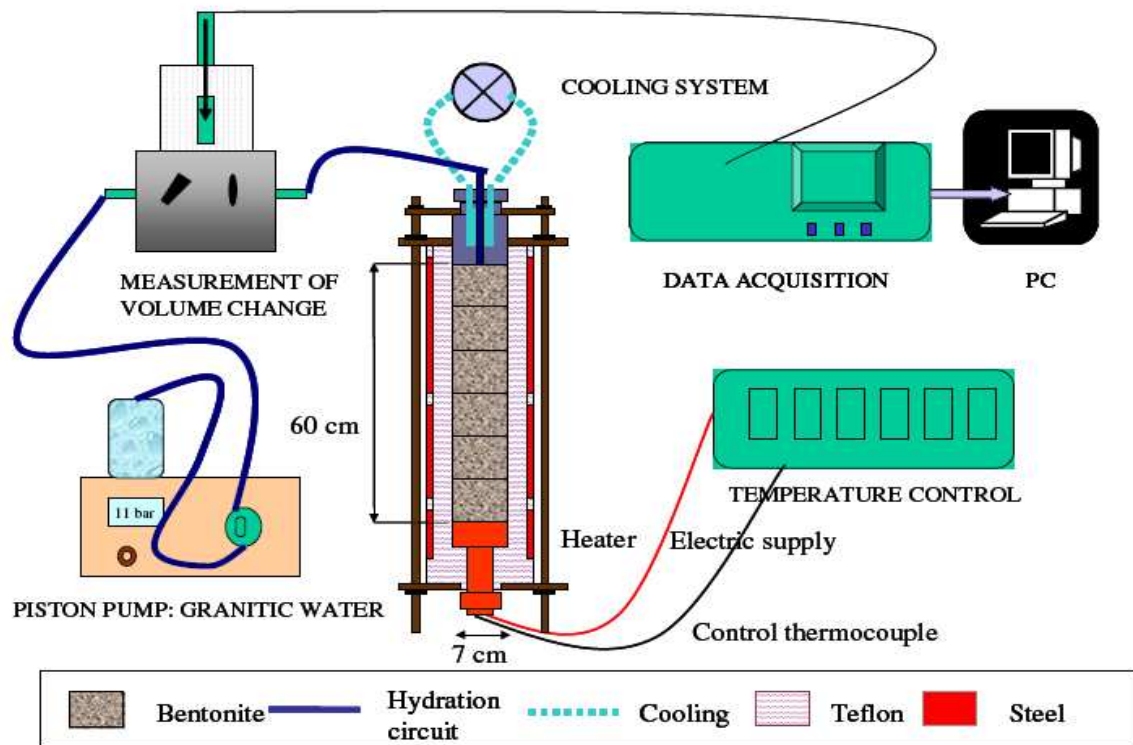


Figure 2.10. Experimental setup for the infiltration test (Villar et al., 1996, 2007; Fernandez and Villar, 2010; Gomez-Espina and Villar, 2009).

Most of the devices used by previous researchers to conduct the thermal and thermo-hydraulic tests did not have the facilities for measuring the swelling pressure of the specimen at the opposite end of the heat source. In order to study the variation of swelling pressure of compacted bentonites due to the thermal gradient and the thermal and hydraulic gradients, the testing device needs to be designed and fabricated specially.

2.10 Mechanisms governing heat, water and solute transfer in soil

In geotechnical engineering applications, bentonites may be subjected to elevated temperature and hydraulic loading at opposite ends. For example, in toxic waste disposal repositories, compacted bentonites are subjected to heating in vicinity to the waste

canisters and hydration close to the saturated host rock. Under these conditions, several physical processes are expected to occur in the bentonite. Bear and Gilman (1995) and Pusch and Yong (2006) have described the various physical processes occurring in compacted bentonites in response to heating and hydration at opposite ends, as shown in Fig. 2.11.

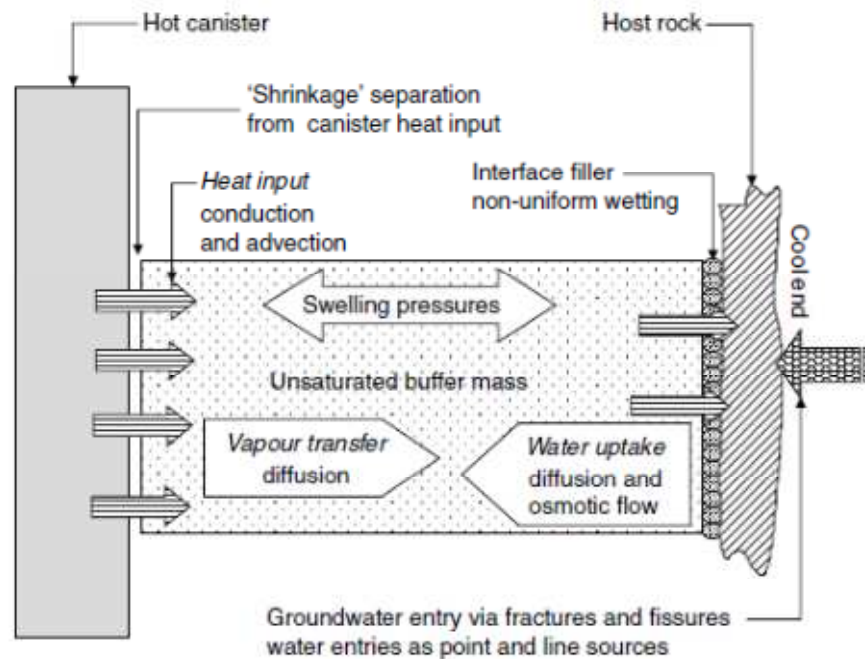


Figure 2.11. Schematic presentation of several processes occurring in an unsaturated porous medium in response to heating (Bear and Gilman, 1995; Pusch and Yong, 2006).

Heat is transferred from the waste canister towards the host rock by heat conduction (Mitchell, 1993; Ewen and Thomas, 1987, 1989; Gens et al., 2007). Water vapour transferred from the hotter region towards the cooler region of compacted bentonites due to an applied thermal gradient. Compacted bentonites receive groundwater from the saturated host rock which is transferred towards the canister. Due to an increase in the water content, compacted bentonites may exhibit swelling pressure on the engineered barrier system (Fig. 2.11).

The anticipated heat can be transported with the moving vapour in the form of latent heat (Ewen and Thomas, 1987, 1989). During thermal and thermo-hydraulic tests, the transient temperature distribution in compacted bentonites depends on power of the and geometry of the heater and relatively independent of the water content of the specimen (Villar et al., 1996).

Bear and Gilman (1995) stated that because of higher vapour pressure near the heat source, diffusive vapour flux directed away from the heater. The overall pressure in the gas phase increases, resulting in a certain advective flux of vapour away from the heat source. Water movement in the buffer material occurs as a result of the thermal gradient generated by the two different temperatures at the opposing ends of the bentonite (Pusch and Yong, 2006). Since vapour formation occurs, total transfer of water will include both liquid water and vapour when a thermal gradient is applied to compacted bentonites. The surface tension of water and capillary pressure decreases with the rise in temperature (Bear and Gilman, 1995). Thus, the pressure in the liquid phase tends to increase near the heat source, resulting in a water flux away from the heat source. This water flux tends to make the distribution of capillary pressure uniform.

Due to applied temperature and hydraulic gradients, water movement occurs in compacted bentonites. Liquid water carries dissolve salts with it by advection from the hydration zone of compacted bentonites (Bear and Gilman, 1995). In the zone of evaporation, the concentration of salts increases, producing a diffusive flux of dissolved salts away from the heat source (Gurr et al., 1952; Nassar and Horton, 1989; Bear and Gilman, 1995; Villar et al., 2008; Cleall et al., 2011). Advective and diffusive fluxes of solute transport may or may not be equal to each other, following a certain increase in

concentration (Bear and Gilman, 1995; Cleall et al., 2007; Gómez–Espina and Villar, 2010; Buil et al., 2010; Cleall et al., 2011). If the advective and diffusive fluxes are not equal to each other the salt concentration near the heat source will increase until it reaches the solubility threshold and salt will begin to precipitate (Bear and Gilman, 1995; Villar et al., 2008; Gómez–Espina and Villar, 2010).

The solute transport phenomenon in bentonites is affected by chemical and mineralogical interaction in the bentonite, dissolution and precipitation of minerals, ion-exchange reactions and transformation (Murrinen and Lehtikoinen, 1998; Fernández et al., 2001, 2004; Cleall et al., 2007; Samper et al., 2008; Fernández and Villar, 2010; Steefel et al., 2010). The transport rate of ion species in clays depends on their diffusivity and their concentration gradients (Pusch and Yong, 2006). The temperature is the variable that mostly influences the process of transport (Martín et al., 2000). In highly compacted bentonites the main mechanism of solute transport is diffusion in consequences of low hydraulic conductivity and smaller hydraulic gradients (Mitchell, 1993; Martín et al., 2000). Kozaki et al. (2001) stated that the surface diffusion of ions increases with an increase in the dry density. A better connectivity of montmorillonite particles attained at higher dry densities. Pusch and Yong (2006) stated that diffusive anion transport capacity is proportional to the ratio of the pore space of the voids between the stacks of smectite lamellae. With increasing density the available pore space for anions migration reduces, therefore, diffusion coefficient of anions decreases with increasing density. Diffusion of anions is affected by the pore water and also by water in the region adjacent to the montmorillonite surfaces (Kozaki et al., 2001).

Buil et al. (2010) stated that the sealing and thermo-hydro-mechanical properties of the engineered barriers may not be affected due to solute diffusion process. During the solute transport processes the chemical dissolution/ precipitation and exchange reaction occurs causing further change in solute concentrations (Fernández et al., 2001, 2004, 2008; Villar et al., 2008; Gómez-Espina and Villar, 2010). It is necessary to carry out detailed investigation on the processes of heat, water and solute transfer in compacted bentonites subjected to thermal and hydraulic gradients in order to improve the understanding.

2.10.1 Variation of cation and anion concentrations

The change in concentrations of cations and anions in compacted bentonite is affected by interaction between soil and the chemical species. However, the conservative species such as chloride do not interact with soil (Fernández et al., 2001, 2004, 2008; Bradbury and Baeyens, 2003; Samper et al., 2008; Cleall et al., 2011). Fernández et al. (2001, 2004, 2008) and Samper et al. (2008) stated that that the measured ion concentrations of soil depend on the solid: liquid ratio of the system.

In the past, several studies were conducted to determine the change in cations and anions concentrations along the depth of compacted bentonites after completion of the thermo-hydraulic tests (Fernández et al., 2001, 2004, 2008; Cuevas et al., 2002; Martín et al., 2002; Villar et al., 2007, 2008; Samper et al., 2008; Gómez-Espina and Villar, 2010; Fernández and Villar, 2010; Cleall et al., 2011). The effect of thermal gradient followed by the thermal and the hydraulic gradients on the variations of cations and anions concentrations has not been studied in detail. Further investigation is necessary to

determine the change in concentrations of cations and anions along the depth of compacted bentonites subjected to the thermal gradient followed by the thermal and hydraulic gradients for better appreciation of the solute transport processes in bentonite.

2.11 Numerical models for coupled thermo-hydro-mechanical-chemical simulations

The general nature of the processes is expected to occur due to thermal and hydraulic loading condition in bentonite is presented in Section 2.10. This section presents the numerical models, the termed codes that have been used for coupled thermo-hydro-mechanical and chemical behaviour of unsaturated soils. The codes were used to study the behaviour of the buffer and backfilling materials in relation to the temperature, the water migration, the deformation behaviour and the solute transport. Some of the popular codes, such as CODE-BRIGHT (COupled DEformation of BRine Gas and Heat Transport), THAMES (Thermal, Hydraulic And MEchanical System analysis) and COMPASS (COde for Modelling PARTially Saturated Soils) are presented in the following sections.

The CODE-BRIGHT (Olivella et al., 1994, 1996; Gens et al., 1995, 1998, 2006, 2007; Vaunat and Gens, 2003; Ledesma and Chen, 2003; Gens and Olivella, 2003) is a finite element code for the analysis of thermo-hydro-mechanical (THM) problems in geological media was developed by UPC-CIMNE, Barcelona, Spain. The basic approach considered a porous medium composed of solid grains, water and gas. The problem was formulated in a multiphase and multispecies approach taken into account of thermal, hydraulic and mechanical aspects. The formulations were based on the principal of the following: (i) balance of momentum for the medium as a whole was reduced to the

equation of stress equilibrium together with a mechanical constitutive model to relate stresses with strains, (ii) small strains and small strain rates are assumed for solid deformation, (iii) balance of momentum for dissolved species and for fluid phases are formulated using Fick's law and Darcy's law and (iv) Physical parameters in constitutive laws are function of pressure and temperature. The governing equations that can be solved using CODE-BRIGHT are, (i) mass balance of solid, (ii) mass balance of water, (iii) mass balance of air, (iv) momentum balance for the medium and (v) internal energy balance for the medium.

The finite element code THAMES (Chijimatsu and Sugita, 2001; Millard et al., 2004; Rutqvist et al., 2004) developed in Japan can be used for analysis of coupled thermal, hydraulic and mechanical processes in a saturated–unsaturated porous medium. The unknown variables considered were: (a) total pressure, (b) displacement vector and (c) temperature. The governing equations were derived with fully coupled thermal, hydraulic and mechanical processes. The following assumptions were made to derived the governing equations: (i) the medium is poro-elastic, (ii) Darcy's law is valid for the flow of water through a saturated–unsaturated medium, (iii) heat flow occurs only in solid and liquid phases, (iv) heat transfer among three phases (solid, liquid and gas) were disregarded, (v) Fourier's law holds for heat flux and (vi) water density varies depending upon temperature and the pressure of water.

COMPASS (Ewen and Thomas, 1987, 1989; Thomas and King, 1991; Thomas and He, 1995; Thomas and Lee, 1995; Seetharam, 2003; Cleall et al., 2007; Vardon, 2009) is based on a mechanistic theoretical formulation developed at Geoenvironmental Research Centre, Cardiff University. The formulation includes heat transfer, moisture

migration, solute transport and air transfer in unsaturated soil, coupled with stress/strain behaviour. Partly saturated soil was considered as a three-phase porous medium consisting of solid, liquid and gas. The liquid phase was considered as pore water containing multiple chemicals and the gas phase as pore air. A set of coupled governing differential equations were developed to describe the flow and deformation behaviour of the soil.

The main features of the theoretical formulation governing heat, water and solute transport in unsaturated soils were: (i) moisture flow included both liquid and vapour flow, (ii) heat transfer included conduction, convection and latent heat of vaporization, (iii) flow of dry air arising from an air pressure gradient and dissolved air in the liquid phase was considered and (iv) deformation effects were included via either a non-linear elastic, state surface approach or an elasto-plastic formulation. Liquid flow was assumed to be described by a generalized Darcy's Law, whereas vapour transfer was represented by a modified Philip de Vries's approach. The bulk flow of air was represented by the use of a generalized Darcy's Law. Henry's Law was employed to calculate the quantity of dissolved air and its flow was coupled to the flow of the pore liquid. Deformation was considered to be dependent on suction, stress and temperature changes. Table 2.3 presents different processes considered in three numerical codes described above.

Table 2.3 Different processes considered in numerical codes

Different processes	THAMES	Code bright	COMPASS
Thermal	√	√	√
Hydraulic	√	√	√
Mechanical	√	√	√
Chemical	--	--	√

The numerical code COMPASS has been used in several studies to further understand coupled thermo-hydro-mechanical-chemical behaviour of unsaturated soil (Thomas and He, 1994; Thomas et al., 1998, 2003). In the current study, COMPASS was used to study thermo-hydro-mechanical behavior of compacted bentonite. Details of the constitutive equations, numerical simulation and the comparison between experimental and the simulated results are presented in chapter 9.

2.12 Summary

A detailed literature review on the behaviour of compacted bentonites pertaining to its use as liner material in engineered barrier system is presented in this chapter. The structure of montmorillonite and the microstructure of compacted bentonites are presented. The various parameters affecting the suction and the swelling pressure of compacted unsaturated bentonite are reviewed. Theoretical assessment of the swelling pressure and the compressibility of bentonites based on physico-chemical considerations are presented. A brief review of mechanisms governing coupled mass, heat and solute transport in compacted bentonites are presented. The theoretical models used to assess the

coupled thermo-hydro-mechanical-chemical behaviour of unsaturated soil are briefly reviewed.

A review of the literature pertaining to the behaviour of compacted bentonites suggested that some of the aspects concerning the use of bentonites as barrier materials in engineered barrier systems require further investigations. These aspects include: (i) the influence of the post compaction residual lateral stress on the swelling pressure, (ii) application of the diffuse double layer theory and the Stern theory in assessing the swelling pressure and the compressibility of bentonites, (iii) the influence of thermal and thermo-hydraulic gradients on the swelling pressure variation at the cooler region of compacted bentonites, (iv) the influences of thermal and thermo-hydraulic gradients on chemical transport in compacted bentonite and (v) efficiency of the numerical code, COMPASS, in assessing the mechanical behaviour of compacted bentonite due to both applied thermal and thermo-hydraulic gradients.

Chapter 3

Material and Methods

3.1 Introduction

This chapter presents the properties of MX80 bentonite used in this investigation. The details of the apparatus used and the test methods adopted are described. In section 3.2, the physical and chemical properties of the bentonite are presented. The suction-water content relationship of the bentonite is presented in section 3.3. The test methods adopted are described in Section 3.4. The modified oedometers used for measuring the swelling pressures and the cell used to carry out the thermal and thermo-hydraulic tests are presented. The test procedure includes: calibration of the modified oedometers against deformation and temperature, specimen preparation, swelling pressure tests, consolidation test, calibration of the relative humidity and temperature measurement probes, thermal

and thermo-hydraulic tests, removal of specimens after thermal and thermo-hydraulic tests and chemical analysis. A summary of the chapter is presented in section 3.5.

3.2 Properties of bentonite studied

Commercially available MX80 bentonite was used in this study. The grain size distribution was found out by hydrometer analysis following British standard (BS 1377-2-1990). Figure 3.1 presents the grain size distribution of the bentonite. From the hydrometer test results it was noted that the bentonite consists of about 84% of clay fraction. The grain size distribution of MX80 bentonite reported by Singh (2007) is presented in Fig. 3.1 for comparison. The fractions of clay size in both bentonites were similar. The finer percentage of the clay particles can be determined using Laser Particle Sizing (LPS) method (Agus, 2005).

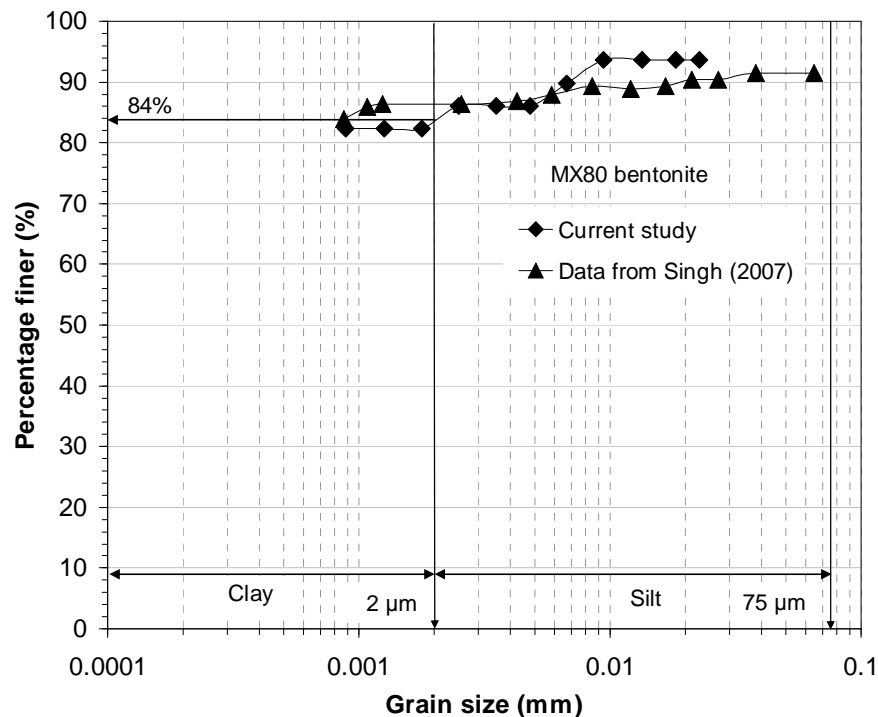


Figure 3.1. Grain size distribution of MX80 bentonite.

The liquid limit, the plastic limit, and the specific gravity of the bentonite were determined following the procedures laid out in British standards (BS 1377-2-1990, BS 1377-3-1990). The properties of the bentonite are presented in Table 3.1. The specific gravity of soil solids was determined using kerosene as the dispersing fluid. The density correction for kerosene was applied for calculating the specific gravity of soil solids. The specific gravity of the soil solids was found to be 2.76.

Table 3.1 Properties of MX80 bentonite

Properties of Material	Value
Liquid limit (%)	385
Plastic limit (%)	43
Shrinkage limit (%)	15.8
Specific gravity, G	2.76
Specific surface area, S (m^2/g)	640
Cation exchange capacity, B (meq/100 g)	
Na ⁺	45.7
Ca ²⁺	31.9
Mg ²⁺	9.31
K ⁺	1.55
Total Cation Exchange Capacity	88.44
Weighted average valence of cations*	1.47

* ratio of sum of the product of individual cation exchange capacity and valence of exchangeable cations to the total cation exchange capacity.

The specific surface area of the bentonite was determined using Ethylene glycol mono ethyl ether (EGME) method (Heilman et al., 1965) and was found to be 640 m^2/g . The external and the total specific surface areas of clays are measured using Brunauer-Emmette-Teller adsorption (BET) method and Ethylene glycol mono ethyl ether (EGME) method, respectively. In the current study, EGME method was adopted because the total specific surface area was of interest.

The total and the fractional cation exchange capacity (CEC) were determined by ammonium acetate method at pH 7 (Grim, 1968; Thomas, 1982). The fractions of exchangeable Na^+ , K^+ , Ca^{2+} and Mg^{2+} were found to be 45.7, 1.55, 31.9 and 9.13 meq/100 g, respectively. The weighted average valence (Tripathy et al., 2004) of exchangeable cations was found to be 1.47.

The mineralogical composition of the bentonite was investigated by X-ray diffraction analysis (Mitchell and Soga, 2005). According to Bragg's law, the XRD determines the minerals based on the relationship between the intercept angle and the c -axis spacing. A Philips automated powder diffractometer PW 1710, was used for XRD analysis. The diffractometer consists of a Goniometer (specimen holder), a copper X-ray generator and a controller (Fig. 3.2).



Figure 3.2. X-ray diffractometer used in the study.

The procedure adopted for X-ray diffraction analysis was as follows. Two grams of MX80 bentonite at hygroscopic water content was treated with Ethylene Glycol prior to testing. The X-ray diffraction analysis of the bentonite is shown in Fig. 3.3. A semi-

quantitative analysis was carried out to determine the percentage of various minerals presents in the bentonite. The X-ray diffraction analysis indicated that the bentonite contains 76% montmorillonite, 14% cristobalite and 10% quartz. Similar percentage of montmorillonite was found in MX80 bentonite reported by Gómez-Espina and Villar (2010). The results indicated that majority of constitutive mineral of the bentonite was montmorillonite.

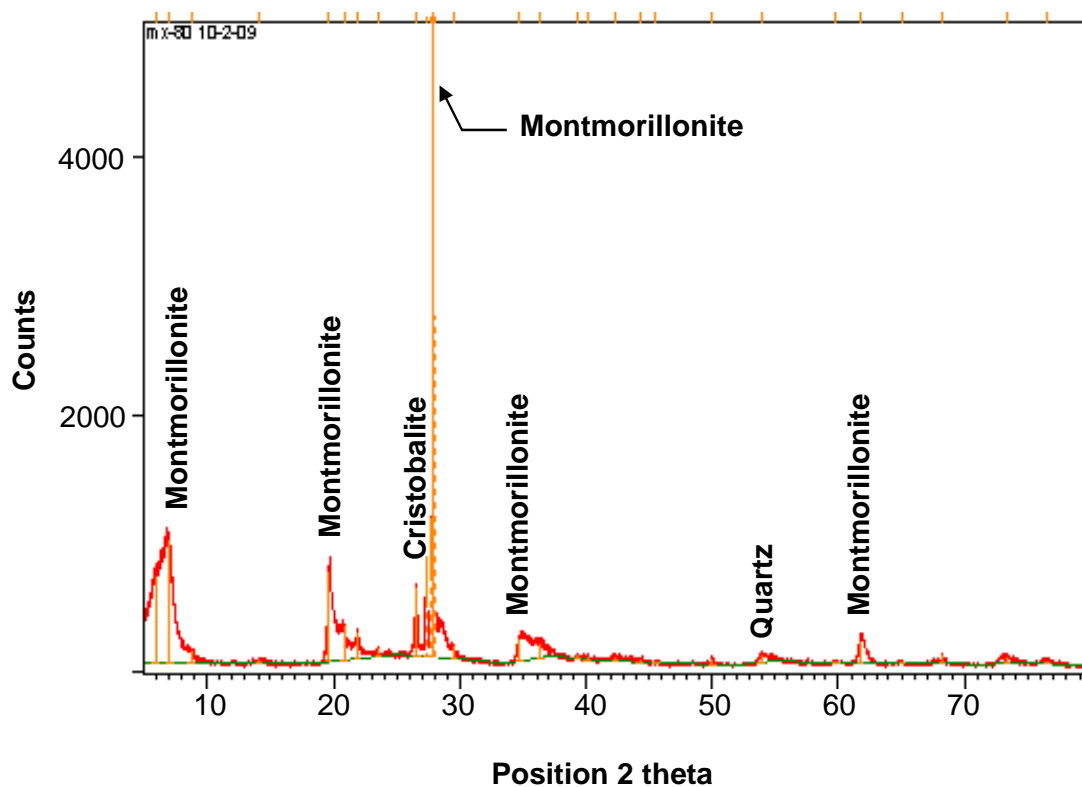


Figure 3.3. X-ray diffraction chart for MX80 bentonite.

3.3 Suction versus water content relationship

The relationship between the water content and the suction of a soil is commonly referred to as the soil-water characteristic curve (Fredlund and Rahardjo, 1993). The soil-water characteristic curve (SWCC) of the bentonite was established by employing pressure plate tests and the salt solution technique. Clay-water mixture was prepared by

thoroughly mixing the bentonite powder with distilled de-aired water. The targeted initial water content of clay-water mixture was equal to 1.15 times the liquid limit of the bentonite. The clay-water mixture was stored in plastic bag and kept in air-tight container in a temperature controlled room and allowed for water equilibration to take place for 7 days. During this period, the clay-water mixture was mixed intermittently.

Cylindrical stainless-steel specimen rings were used to prepare the test specimens. The inner surfaces of the specimen rings were lubricated with silicon grease. The specimen ring was made to rest on a wet filter paper kept over a flat surface. The filter paper used had a greater diameter than that of the specimen ring. Bentonite-water mixture was carefully worked into the ring, a part at a time, using a spoon and a spatula. Light tapping helped to eliminate air bubbles from the bentonite specimen. The excess bentonite was trimmed off using a spatula. The mass of the bentonite specimen along with the filter paper and the lubricated specimen ring was measured.

In pressure plate tests, the applied air pressure equals the matric suction of the soil specimen at equilibrium (Fredlund and Rahardjo, 1993; Leong et al., 2004). The pressure plate tests were carried out by applying air pressures of 50, 100 and 400 kPa on the saturated bentonite specimens using a 5 bar pressure plate extractor. At each suction, at least three specimens were tested. Care was exercised while preparing the duplicate bentonite specimens. It is important that during the pressure plate tests, the ceramic disks remain saturated to avoid air-entrapment and delay in the expulsion of water from the soil specimens (Leong et al., 2004).

Figures 3.4 and 3.5 show the pressure plate apparatus with the bentonite specimens on ceramic disc. The mass change of the bentonite specimens was monitored

periodically to infer the suction equilibration. The bentonite specimens were equilibrated within about 15 days in pressure plate tests at each suction level. The void ratios of the bentonite specimens in the pressure plate tests were calculated based on the volume-mass relationships and the equilibrium values of the following at each applied suction: (i) the total volume of the specimen measured by wax method (ASTM D 4943-08-2008), (ii) the total mass of the specimen and (iii) the water content. Knowledge of the density of the molten wax at specified test temperature is crucial for precise determination of the volumes of soil specimens. The density of the molten wax used was measured to be 0.745 Mg/m^3 in this study.

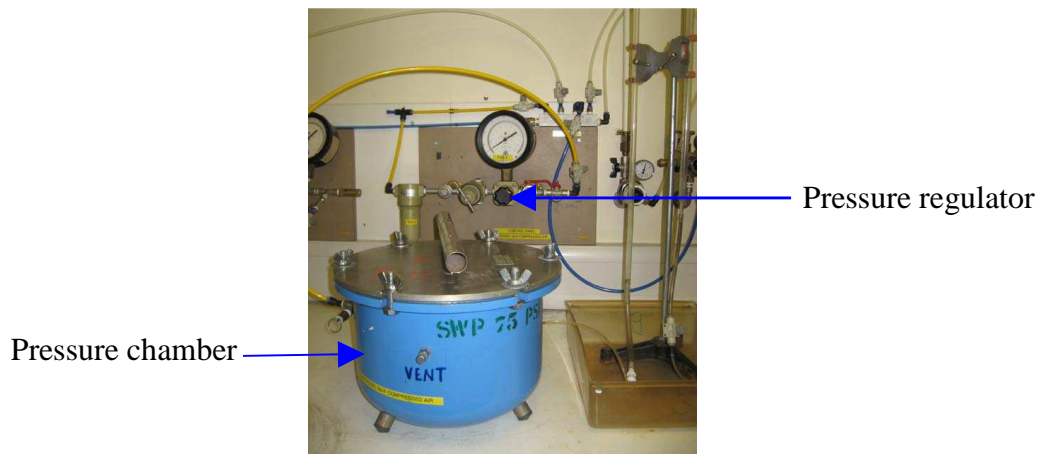


Figure 3.4. Pressure plate apparatus.

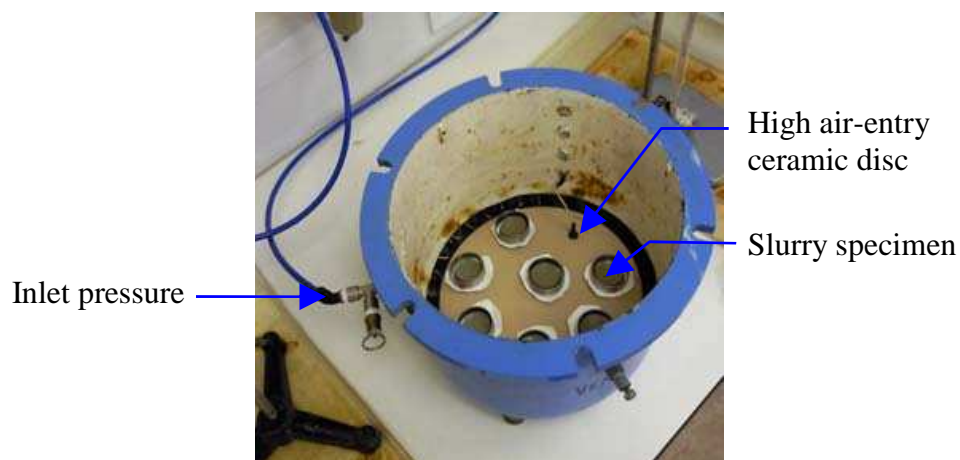


Figure 3.5. Pressure plate apparatus with initially slurried bentonite specimens.

The salt solution tests, also known as the vapour equilibrium technique (Delage et al., 1998; Blatz et al., 2008), were carried out in closed-lid desiccators for inducing higher suctions of 21.8, 38, 82.3, 113.3 and 294.8 MPa using saturated salt solutions of KCl, NaCl, $\text{Mg}(\text{NO}_3)_2$, K_2CO_3 and LiCl, respectively (ASTM E 104-85 1998). The bentonite specimens tested in the desiccators were first subjected to a suction of 400 kPa in pressure plates before being transferred to the test desiccators containing various saturated salt solutions. The procedure adopted saved significant testing time.

Figure 3.6 shows the bentonite specimens kept for water content equilibration inside the desiccators. The relative humidity within the closed-lid desiccators was periodically measured using a commercial relative humidity probe manufactured by Rotronic limited. The accuracy of the probes was $\pm 1.0\%$ for the range of relative humidity between 0 and 100%. The accuracy of the probes for temperature measurement was $\pm 1^\circ\text{C}$ for the range of temperature between -40 and 100°C . The desiccator tests were conducted at a temperature of 25°C .

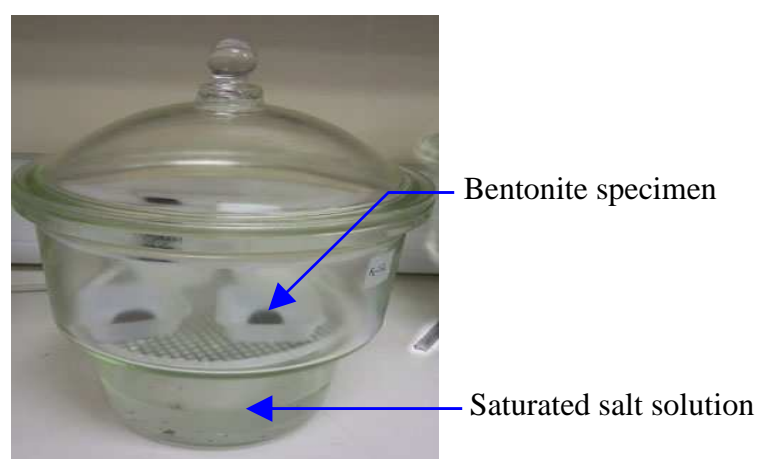


Figure 3.6. Slurried bentonite specimens inside the desiccators (Vapour Equilibrium test).

The relative humidity of saturated salt solutions is related to the total suction of soil (Fredlund and Rahardjo, 1993; ASTM E 104-85 1998). After the equilibrium, at each suction level the water contents of the specimens were determined. The volumes of the specimens were measured using the molten wax (ASTM D 4943-08-2008). Figure 3.7 shows the tested bentonite specimen tested in desiccators kept for air-drying after coated with molten wax. The equilibration time for salt solution tests took about 15 days to several months depending on the suction level. In general, a greater equilibration time was required at smaller suctions.

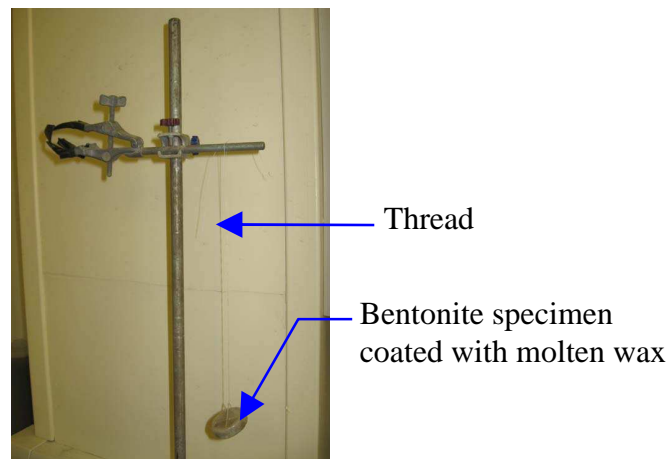


Figure 3.7. Shrinkage test (with molten wax) setup.

3.3.1 Suction versus water content relationship from chilled-mirror hygrometer

Soil-water characteristic curves at higher suctions can be established using a chilled-mirror hygrometer (ASTM D 6836-02). A chilled-mirror hygrometer yields soil-water characteristic curves in terms of total suction of soil. Different models of chilled mirror hygrometers are available. Some models measure the water activity (a_w) of soil specimens which is the ratio of the vapour pressure of a liquid to the vapour pressure of water at the same temperature. In the current investigation, the water activity and

temperature of bentonite-water mixtures were measured. From the measured water activity and temperature data, the total suctions of bentonite-water mixtures were calculated. The bentonite-water mixtures were prepared and tested following the procedure laid out in ASTM D 6836-02. A photograph of the chilled-mirror hygrometer is shown in Fig. 3.8.

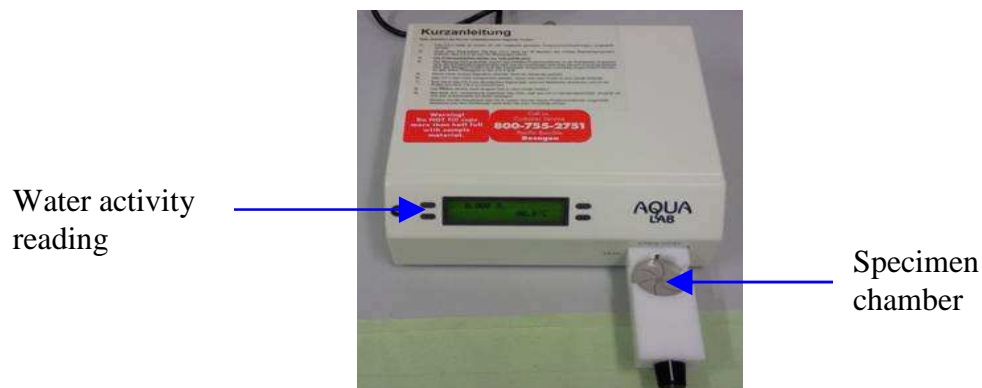


Figure 3.8. Photograph of chilled-mirror hygrometer.

A set of nine bentonite-water mixtures were prepared. The bentonite-water mixtures were prepared by adding water to bentonite starting from the hygroscopic water content of 11% in an increment of 3%. The bentonite-water mixtures were stored in air-tight containers in a temperature controlled room and allowed for water equilibration to take place for 7 days prior to testing them in the hygrometer.

The chilled-mirror hygrometer was calibrated using saturated salt solutions of known water activity. The bentonite-water mixtures were transferred to the specimen chamber inside a retaining dish. The water activity and temperature were noted for each bentonite-water mixture. The measurements were repeated thrice for each bentonite-water mixture. The water content of each bentonite-water mixture were measured after the tests.

The total suctions of bentonite-water mixture were calculated from the measured water activity and temperature using the Kelvin's equation expressed as:

$$\text{Total suction, } \psi = \frac{RT}{M} \ln(a_w) \quad (3.1)$$

where R is the universal gas constant ($\text{Jmol}^{-1}\text{K}^{-1}$), T is the laboratory temperature ($^{\circ}\text{K}$), a_w is the water activity and M is the molecular mass of water. The water content, temperature, water activity and suction results are presented in Table 3.2.

The suction versus water content test results from the desiccator tests and from the chilled-mirror hygrometer tests are shown in Fig. 3.9. Although, the conditions of the samples tested were different for the desiccator and the chilled mirror hygrometer tests, a good agreement was noted for water contents in the overlapping suction ranges. Filter paper method can be used to establish the suction versus water content of soil. Agus and Schanz (2005) reported that filter paper method determines larger suctions than that of the chilled mirror hygrometer, for specimens having the same water content and dry density. Agus and Schanz (2005) also stated that the difference in suction measurement was attributed to the differences in time required to reach an equilibrium suction for both techniques.

Table 3.2 Chilled-mirror hygrometer test results

Final Water content (%)	Temperature ($^{\circ}\text{C}$)	Water activity	Suction (MPa)
(1)	(2)	(3)	(4)
11.0	20.8	0.783	98.83
12.8	20.8	0.557	79.23
15.5	20.8	0.650	58.32
17.4	20.8	0.723	43.91
20.0	20.7	0.826	25.87
22.6	20.7	0.891	15.62
25.3	20.8	0.927	10.26
28.1	20.7	0.944	7.80
32.8	20.8	0.967	4.54

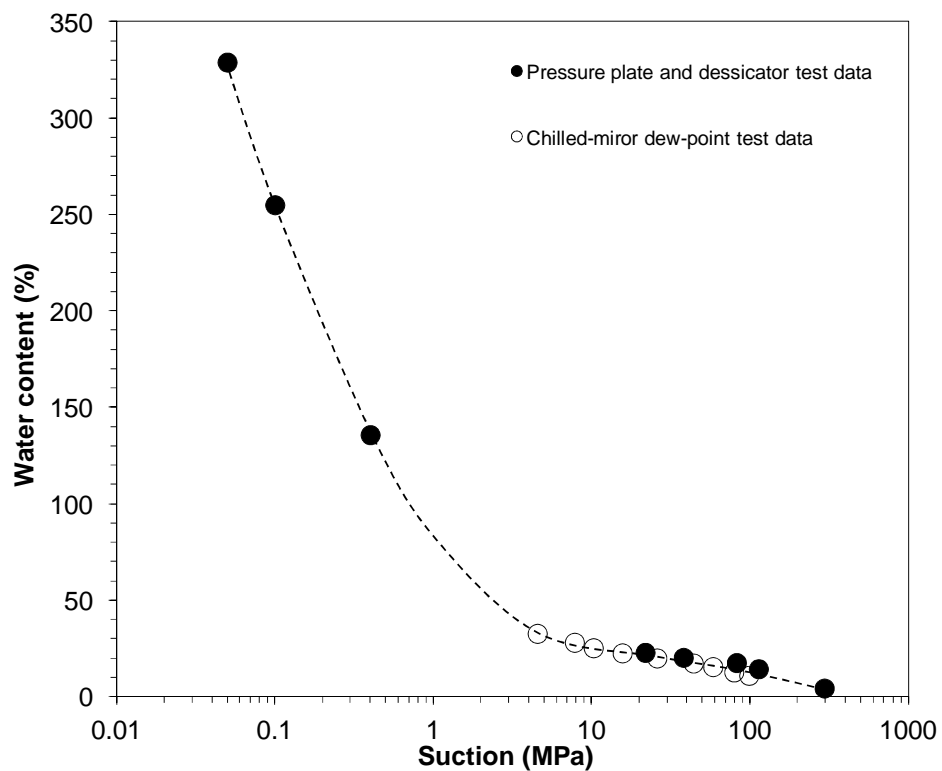


Figure 3.9. Suction versus water content test results for MX80 bentonite from pressure plate and dessicator and chilled mirror hygrometer tests.

Delage et al. (2006) reported the suction-water content relationship of MX80 powder and compacted specimens of dry density 1.7 Mg/m^3 . The suction-water content relationships were established by desiccators tests. For compacted specimens, the swelling of the specimens were prevented by placing the specimens inside a rigid cell. Delage et al. (2006) showed a good agreement between suction-water content relationship for MX80 powder and compacted specimens at higher suction levels between 10 and 100 MPa. Delage et al. (2006) concluded that the suction values (between 10 and 100 MPa) primarily depend on the water content of the soil specimen. Tang and Cui (2010) conducted tests on MX80 bentonite by vapour equilibrium technique for the range of dry density between 1.4 and 1.8 Mg/m^3 . Tang and Cui (2010) showed nearly identical suction-water content relationship for compacted and powder MX80 bentonite specimens. From the above studies it was noted the dry density have insignificant influence on suction versus water content relationship of bentonites at suction levels beyond 10 MPa.

3.4 Experimental program

The experimental program consists of three types of tests (i) swelling pressure tests, (ii) consolidation test and (iii) thermal and thermo-hydraulic tests. Modified oedometers were used to carry out the swelling pressure tests on compacted bentonites by constant volume method. The swelling pressure tests were carried out at elevated (temperature = 70°C) and ambient temperatures and with distilled water, 0.1 M NaCl and 1.0 M NaCl solutions as bulk fluids. A consolidation test was carried out on saturated MX80 bentonite specimen using a conventional oedometer. Laboratory scale thermal and thermo-hydraulic tests were carried out on cylindrical compacted bentonite specimens.

The following sections describe the testing devices used, the test setups, calibration of the devices and the detailed procedures adopted to carry out the laboratory tests.

3.4.1 Swelling pressure tests

The swelling pressure of initially unsaturated expansive soils can be measured by three methods (Sridharan et al., 1986), namely swell load test, swell under load and constant volume test. The difference between the three methods is discussed in chapter 2 (section 2.5.2). Delage et al. (2006) stated that constant volume condition may be closer to the in-situ conditions of engineered barrier systems. Therefore, the swelling pressures of compacted bentonite specimens in this investigation were measured under constant volume condition.

Several series of constant volume swelling pressure tests were carried out. The effects of post compaction residual stress, electrolyte concentration and temperature on swelling pressures of compacted bentonite specimens were studied. The following sections describe the constant volume swelling pressure measurement device, calibration of the devices against deformation and temperature and the experimental procedure adopted to measure swelling pressure of compacted bentonites.

3.4.1.1 Specimen preparation method

Compacted bentonite specimens were statically compacting bentonite powder to predetermined dry densities using a specimen ring and a newly designed compaction mould. The components of the compaction mould used are shown in Fig. 3.10. The

compaction mould has four main parts; (i) a base, (ii) a collar, (iii) a spacer and (iv) connecting ring. The specimen ring was rested on the base of the compaction mould. The collar and the connecting ring were attached and tightened with bolts. Figure 3.11 shows a photograph of an assembled compaction mould.

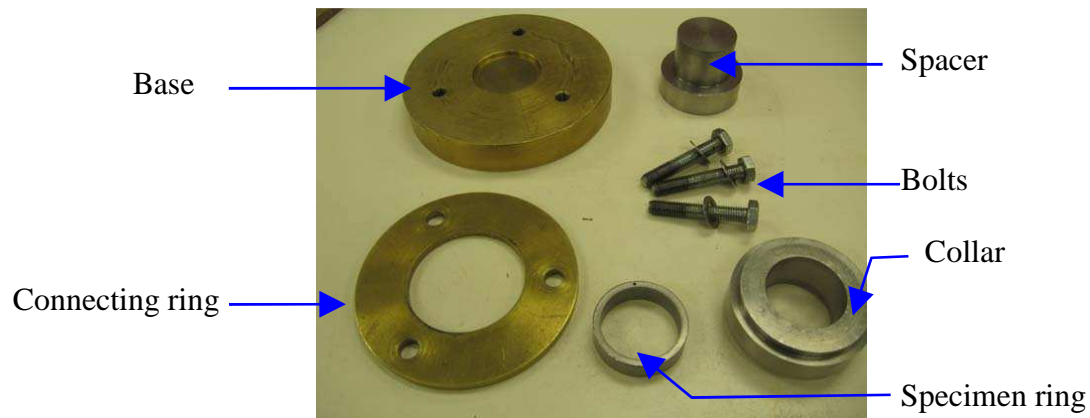


Figure 3.10. Various components of the compaction mould.

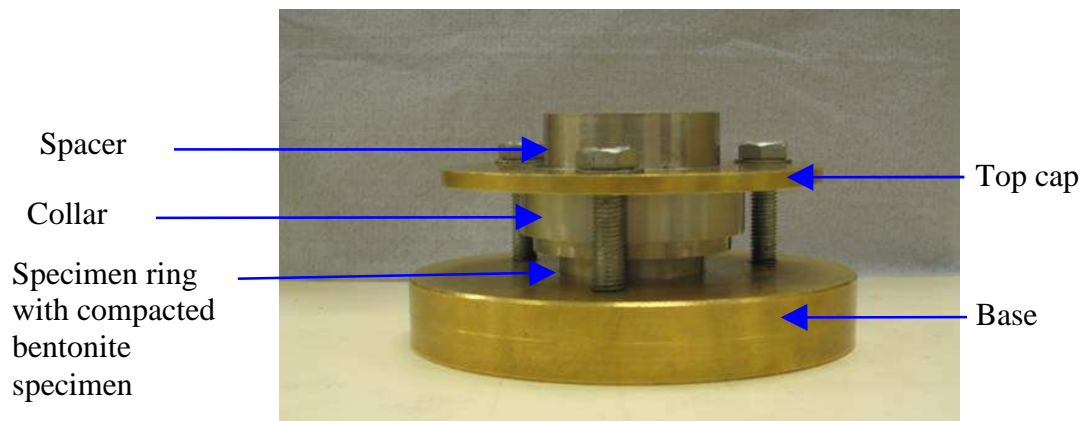


Figure 3.11. Compaction mould with compacted specimen inside.

The inner surfaces of the specimen ring and the spacer were lubricated with silicon grease to minimise the friction. The amount of bentonite required to prepare the specimen of a predetermined dry density was determined. Bentonite powder was transferred into the ring gently with a spoon. The top surface of the bentonite was

smoothened with a spoon and a spatula. The spacer was placed on top of the bentonite surface.

The compaction mould with bentonite inside the specimen ring was transferred to a high capacity static compaction machine and required load was applied. After the compaction process was over, the actual dry densities of the specimens were calculated from the measured height and the diameter of the specimens. The specified diameter and height of specimens were 42 and 10 mm, respectively.

To study the effect of release of post-compaction residual stresses on the swelling pressures of compacted bentonite, compacted bentonite specimens were extruded from the specimen ring and were re-inserted back prior to testing for swelling pressure. The extrusion and re-insertion processes of test specimens are described in chapter 4.

3.4.1.2 Constant volume swelling pressure measuring device

Modified oedometers with abilities to measure swelling pressures both at ambient and at elevated temperatures were used. The devices were used as suction controlled oedometers (Folly, 2001). The oedometers were modified to accommodate a load cell that facilitated measuring swelling pressures of compacted bentonite specimens under constant volume condition. A schematic diagram of the modified oedometer is shown in Fig. 3.12. The external diameter and height of the oedometer are 184 and 151 mm, respectively (Fig. 3.12). The cell body of the oedometers are made of grade 304 austenitic stainless steel (Folly, 2001). The components of the suction controlled

oedometer used are shown in Fig. 3.13. Figure 3.14 presents the experimental setup for constant volume swelling pressure tests.

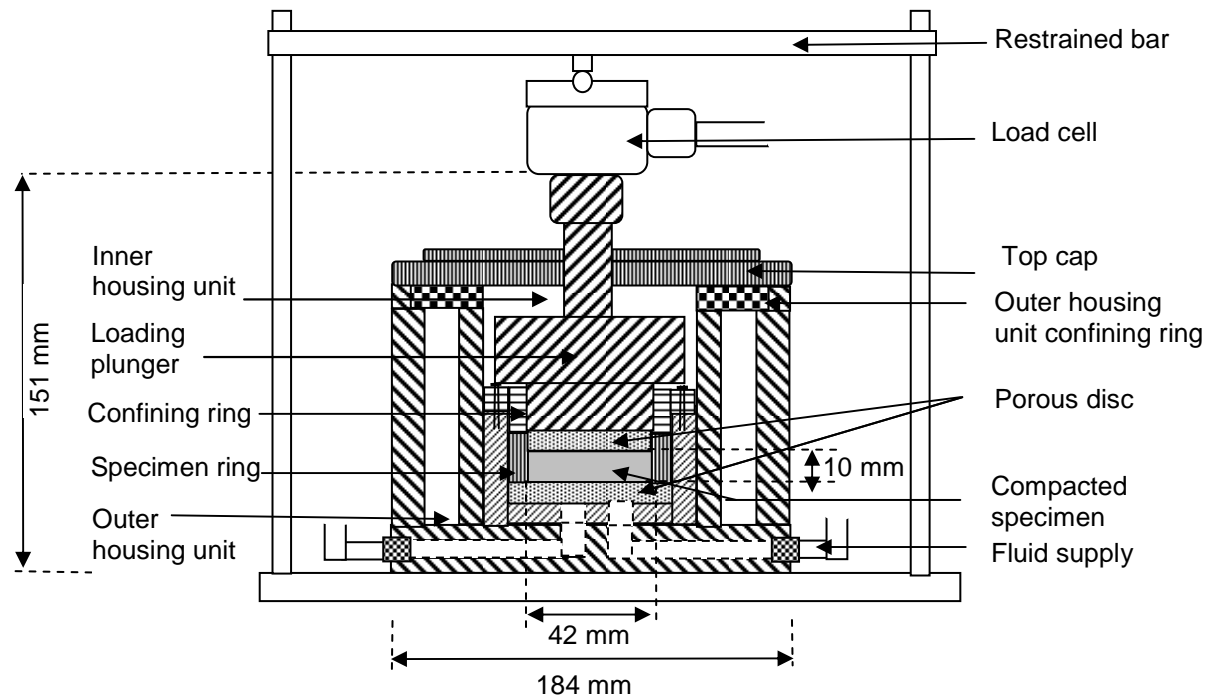


Figure 3.12. Schematic diagram of constant volume swelling pressure measurement device.

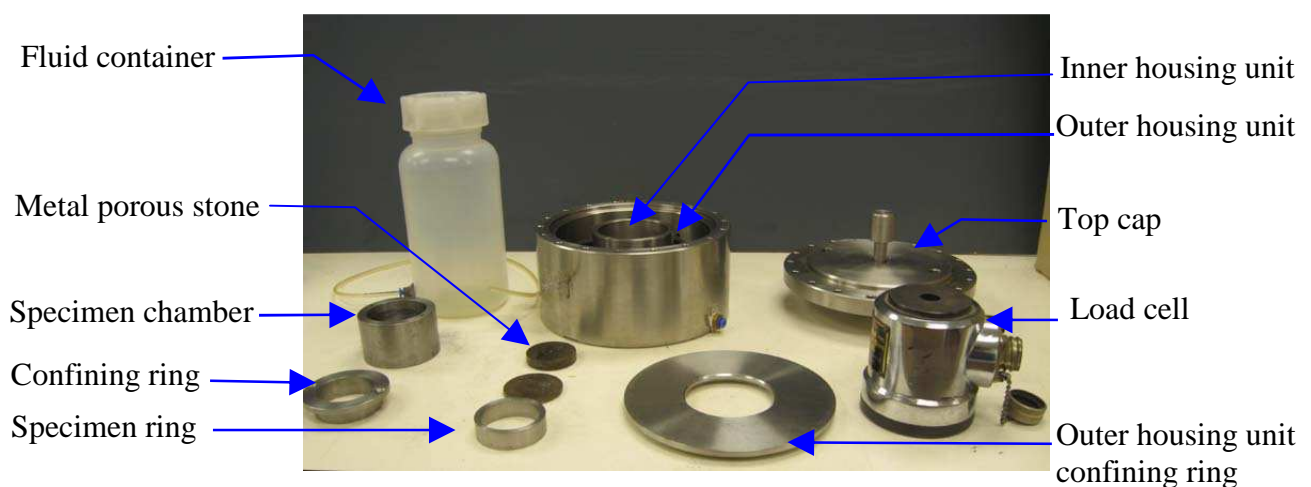


Figure 3.13. Components of the modified oedometer.

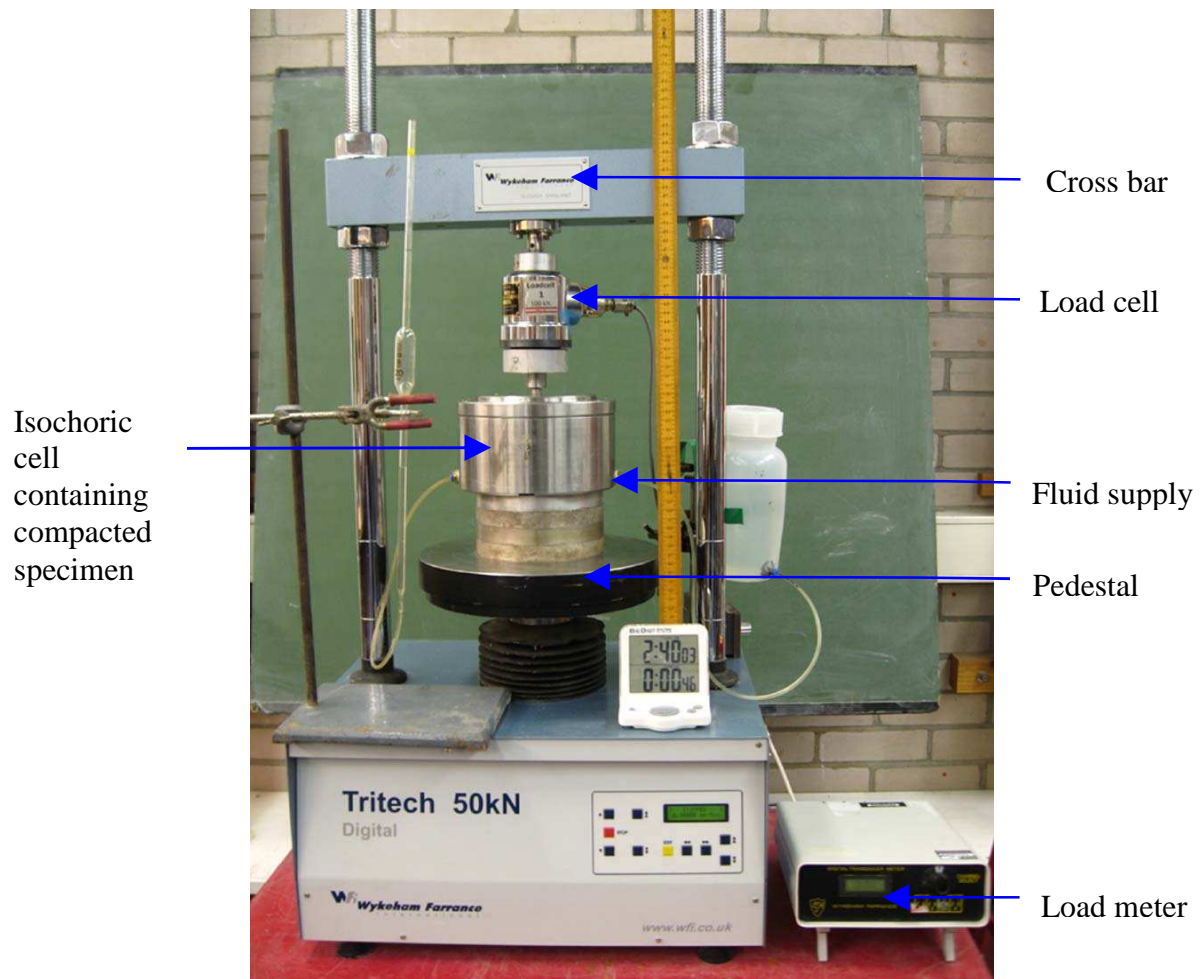


Figure 3.14. Experimental setup for constant volume swelling pressure tests.

The modified oedometers used have two compartments; (i) the inner housing unit or the specimen chamber accommodating the specimens to be tested and (ii) the outer housing unit or oil chamber accommodating the heater element in order to apply desired temperature on the test specimens. Stainless steel rings were used to prepare the compacted bentonite specimens. The inner diameter and the height of the specimen ring were 42 and 14 mm, respectively. The height of the compacted specimens was about 10 mm. Two openings at the base of the cell allowed circulating fluid in order to hydrate the specimens. A load cell was accommodated between the top of a loading plunger and a restrained bar of loading frame (Figs. 3.12 and 3.14). The load cell was connected to a load meter and the load increment during the hydration process was monitored. The

swelling pressure was calculated from the measured load and the cross-sectional area of the specimens.

The oedometer cells were calibrated against deflection due to applied pressure prior to the swelling pressure tests. One of the two oedometers available was used to carry out constant swelling pressure tests at elevated temperature. Therefore, the latter was calibrated against temperature and the maximum temperature in the specimen chamber was determined.

3.4.1.3 Calibration of oedometer cells against deformation

During the swelling pressure measurements, expansion of the specimen ring was anticipated. Therefore, the modified oedometers were calibrated against deformation due to applied vertical pressures. External loads were applied on a dummy stainless steel specimen (diameter = 42 mm, height = 10 mm) and the corresponding deformations were recorded from the displacement transducer. The pressure versus deformation relationships are shown in Fig. 3.15. For each oedometer cell the deformations against applied pressures was checked twice. The average deformations from two sets of data were considered. The deformation correction of the cells was applied to calculate the swollen dry densities of the bentonite specimens for each measured swelling pressure. The deformations corresponding to measured swelling pressures in each test were determined using the equations shown in Fig 3.15. The height and diameter of the specimens were corrected for the calculated deformation. Using the corrected diameter and height of the specimens, the volumes of the specimens were calculated and hence the swollen dry densities of the specimens.

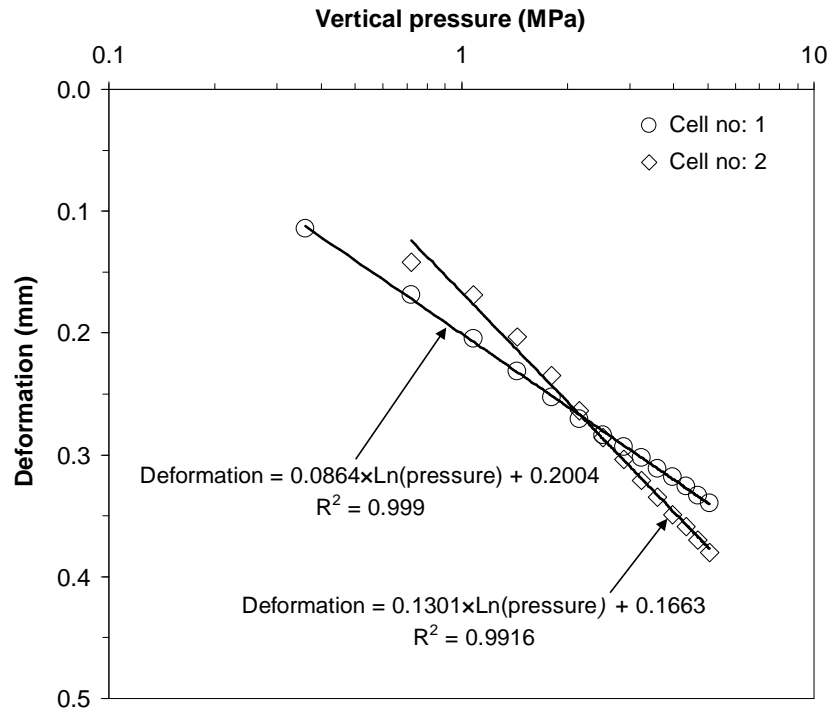


Figure 3.15. Applied pressure versus deformation relationships of the modified oedometers used in this investigation.

3.4.1.4 Calibration of oedometer cell against temperature

For swelling pressure tests at elevated temperature, the oedometer used was calibrated against temperature. The specimen chamber of the swelling pressure device is surrounded by a heating coil (Fig. 3.16). The oil chamber was filled with commercially available industrial graded oil. The thermocouple mounted in the outer chamber of the cell was connected to a heater controller (Fig. 3.16). The heater controller maintains the temperature of the heater element. The cell was originally designed to sustain a maximum temperature of 90 °C (Folly, 2001).

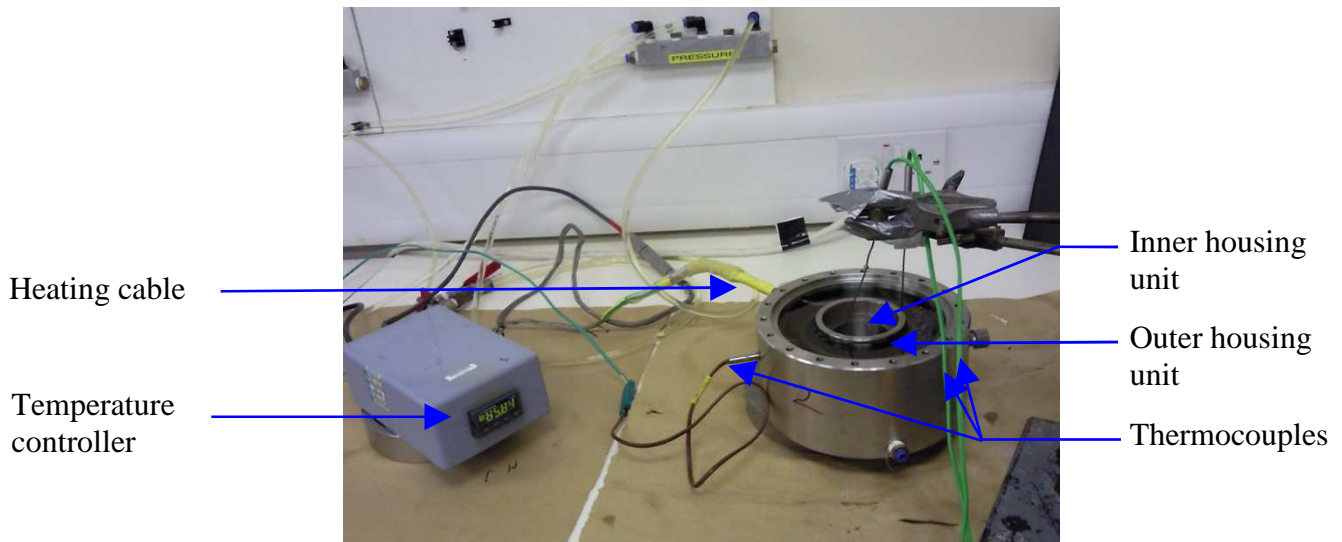


Figure 3.16. Experimental setup of temperature calibrations in the specimen chamber.

Figure 3.17 presents the equilibrium temperatures at inner and outer housing unit of the cell. The maximum temperature of the heater was set at 90°C . The maximum temperature at equilibrium in the specimen chamber was found to be 70.8°C . The calibration was checked up to 150 minutes duration until the measured temperatures were equilibrated. The temperature in the specimen chamber (inner housing unit) and in the oil chamber (outer housing unit) was measured without the specimen. However, during swelling pressure tests the temperature measurement in the specimen chamber was not possible. Therefore, the test results were analysed by considering a temperature of 70°C in the specimens.

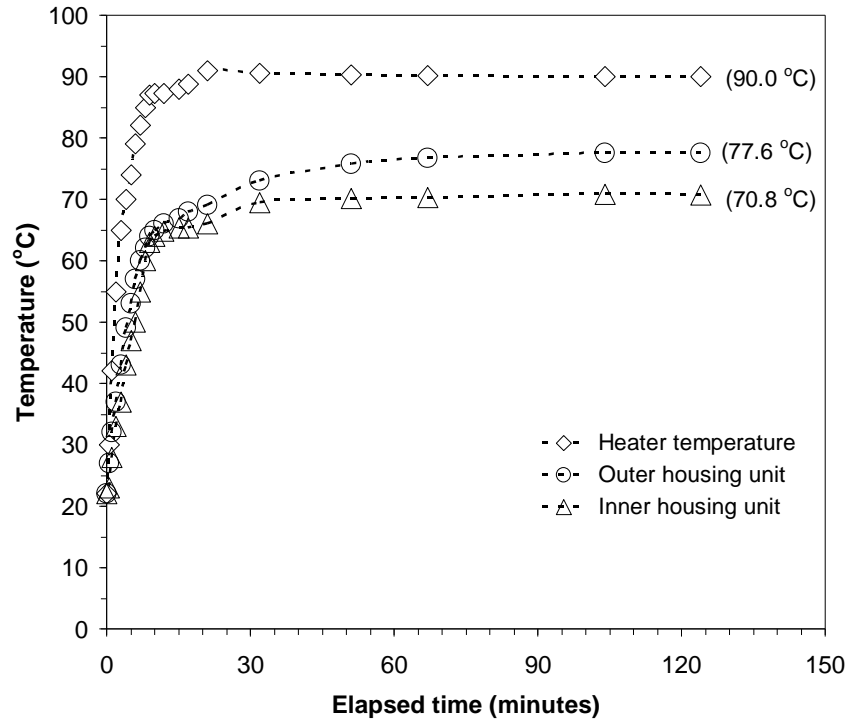


Figure 3.17. Equilibration temperatures at inner and outer housing unit of the cell.

3.4.1.5 Constant volume swelling pressure tests

The swelling pressure tests were carried out for the range of targeted dry densities between 1.1 and 1.9 Mg/m³. The compacted bentonite specimens were placed inside the specimen chamber (Fig. 3.13). Two filter papers were placed at the top and at the bottom of the specimens. The specimens were confined between two porous stones, one at the top and the other at the bottom of the specimen (Fig. 3.12). The loading plunger and the top cap of the cell were attached. The oedometer cell along with the compacted bentonite specimen was transferred to a 50 kN capacity load frame (Fig. 3.14). The load cell was attached in between the top of the loading plunger and the restrained bar of the load frame. The load cell was connected to a load meter (see Fig. 3.14). The load meter was calibrated prior to the tests. Fluid inlet and outlet tubes at the base of the cell were connected to the fluid chambers (Fig. 3.14). Once the fluid was supplied through the fluid

inlets of the oedometers, the swelling pressure started to develop. The swelling pressures exerted by the bentonite specimens were monitored with elapsed time. The tests were terminated once the swelling pressures exerted by the bentonite specimens were equilibrated. In general, 7 to 10 days were required for swelling pressure equilibration.

After dismantling the test setup, bentonite specimens were sliced into two pieces along the height using a spatula and the water contents of both slices were measured. The variation of water content between top and bottom slices was within about 1% for all the tests. The average water contents of each slice were used to calculate the degree of saturation of the specimens. The swollen dry densities of the specimens were calculated considering the deformation correction for each test.

3.4.2 Consolidation test

In deep geological waste disposal repositories, compacted bentonites may undergo very high overburden pressures and hence studies concerning compressibility behaviour of bentonites at large pressures are necessary (Schanz and Tripathy, 2007). In the past, the compressibility behaviour of bentonites for different range of pressures have been reported (Bolt, 1956; Mesri and Olson, 1971; Low, 1980; Sridharan et al., 1986; Al-Mukhtar et al., 1999; Marcial et al., 2002; Fleureau et al., 2002; Tripathy and Scanz, 2007; Baille et al., 2010). Bolt (1956) studied the compressibility behaviour Wyoming bentonite up to maximum applied pressure of 1700 kPa. Olson and Mesri (1971) conducted consolidation tests on sodium and calcium montmorillonites applying maximum pressure of 4000 kPa. Sridharan et al. (1986) studied the consolidation characteristics of homoionized bentonites for the range of pressures between 6.25 and 300

kPa. Marcial et al. (2002) studied the compressibility behaviour of three bentonites at high pressure of 30 MPa. Baille et al. (2010) studied the large stress compressibility behaviour of compacted bentonites for the maximum applied pressure of 25 MPa.

In the current study, a compressibility test was carried out on MX80 bentonite for the range of applied pressures between 6.25 kPa and 3200 kPa. The test was carried out on initially saturated bentonite specimen following BS 1377:5 (1990) using a conventional oedometer. The consolidation test apparatus is shown in Fig. 3.18. The lever arm factor of the consolidation apparatus used for the current investigation was 1:10. The diameter and height of the specimen ring used were 38 and 10 mm, respectively. Three nos. of saturated slurry bentonite specimens were tested applying predetermine load in the hanger bar. Detailed description of specimen preparation, test methods and consolidation test results are presented in chapter 6.



Figure 3.18. One dimensional consolidation test apparatus.

3.4.3 Thermal and thermo-hydraulic tests

A series of thermal and thermo-hydraulic tests were carried out on compacted bentonite specimens. The thermal test referred to as the tests carried out with thermal loading only, whereas thermo-hydraulic tests referred to as the tests carried out by subjecting the specimens to both thermal and hydraulic loadings. During the thermal tests, temperatures of 85 and 25 °C were applied at the bottom and at the top of the cylindrical bentonite specimens. During the thermo-hydraulic tests, in addition to the temperatures applied during the thermal tests, distilled water was supplied from the top of the specimens. The following sections describe the specimen preparation method, the testing device, the experimental setup, the calibration of relative humidity and temperature measurement sensors, the detailed test methods adopted and the chemical tests carried out to determine the change in cation and anion concentrations at predetermined heights of the bentonite specimens.

3.4.3.1 Specimen preparation method

Cylindrical specimens were prepared by statically compacting bentonite powder (water content = 11%) to a targeted dry density of 1.60 Mg/m³ in four layers, each 20 mm thick. The height and diameter of the specimens were 80 and 100 mm, respectively. Compaction was carried out inside the central section of the cell using the compaction mould shown in Fig. 3.19. An aluminium disc was placed at the bottom of the central section of the cylindrical cell during the compaction process. The inner surfaces of the central part of the cell were lubricated with silicon grease. The required amount of bentonite was filled inside the central section of the cell and the bentonite surface was

smoothened. The spacer was placed on top the bentonite surface. Static load was applied in order to compact the specimens to a targeted dry density using a high capacity compaction device (Fig. 3.20). Removal of the applied compaction stress caused an axial expansion of the bentonite specimens. The actual dry densities of the compacted specimens were calculated based on the mass of compacted specimens and dimensions (height and diameter) measurements.



Figure 3.19. Components of the compaction mould.

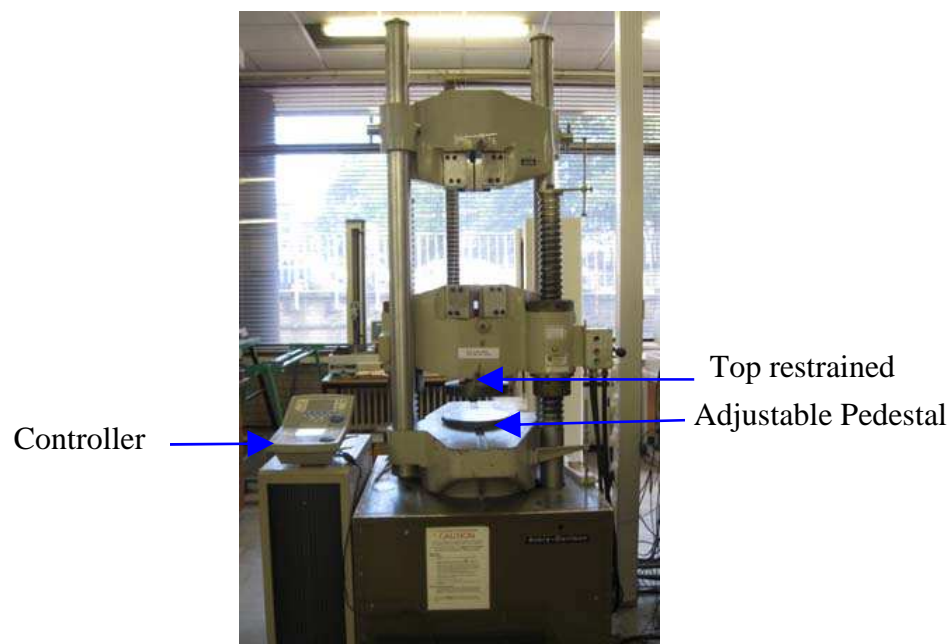


Figure 3.20. High stress compaction device.

3.4.3.2 Description of the testing device

Thermal and thermo-hydraulic tests were carried out on compacted bentonite specimens using a cylindrical stainless steel cell with a PTFE (Polytetrafluoroethylene) liner inside. The inner diameter and height of cylindrical cell was 100 and 80 mm, respectively. The device was developed by Singh (2007). The device available was modified to measure swelling pressures exhibited by compacted bentonite specimens during the thermal and the thermo-hydraulic tests. A schematic diagram of the modified cell is shown in Fig. 3.21. The cell wall was made of a hollow stainless steel pipe. The main components of the cell consist of a base, a central section, an interconnecting ring, and a top part.

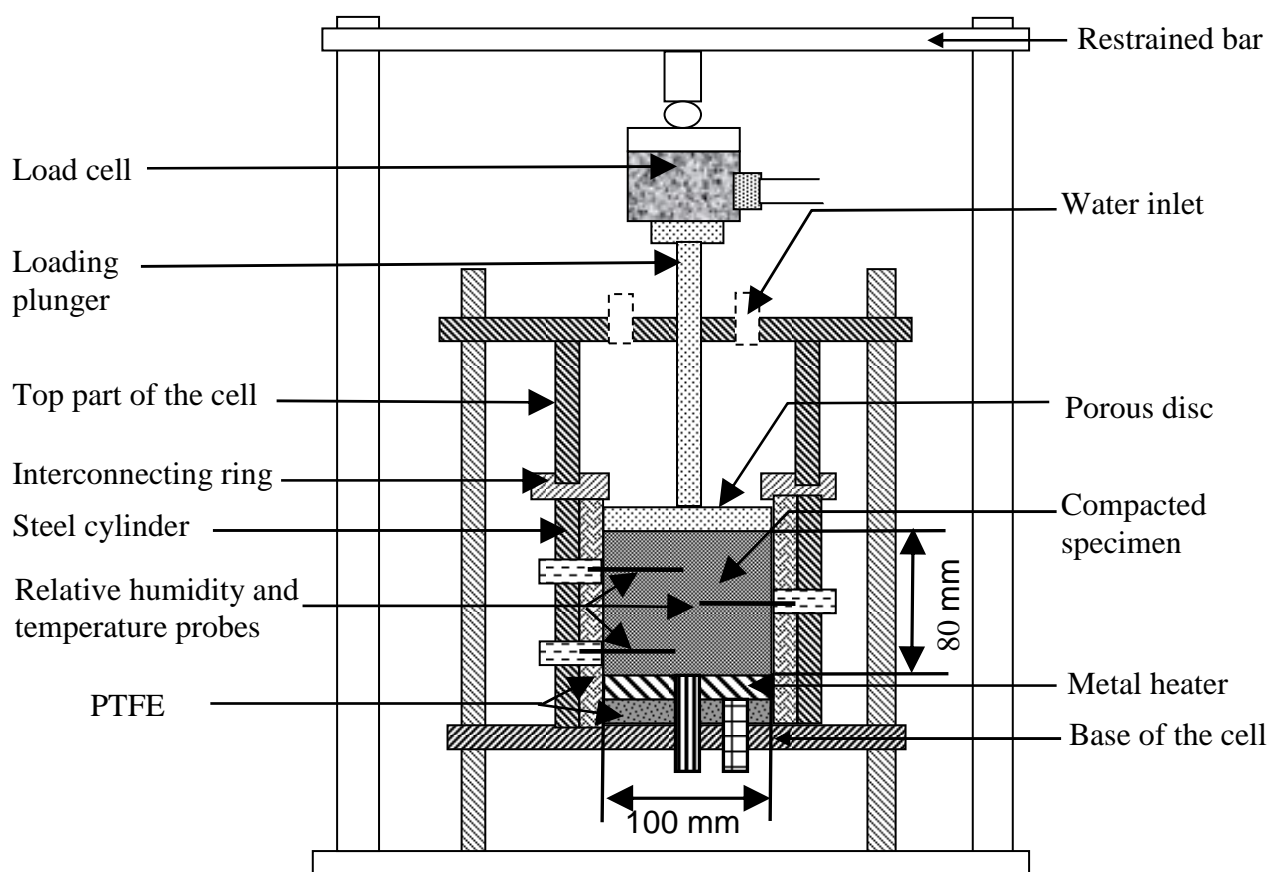


Figure 3.21. Schematic diagram of the cell used to carry out the thermal and thermo-hydraulic tests.

Figure 3.22 presents the components of the thermo-hydraulic test setup. Figure 3.23 presents the experimental setup used to carry out the thermal and the thermo-hydraulic tests.

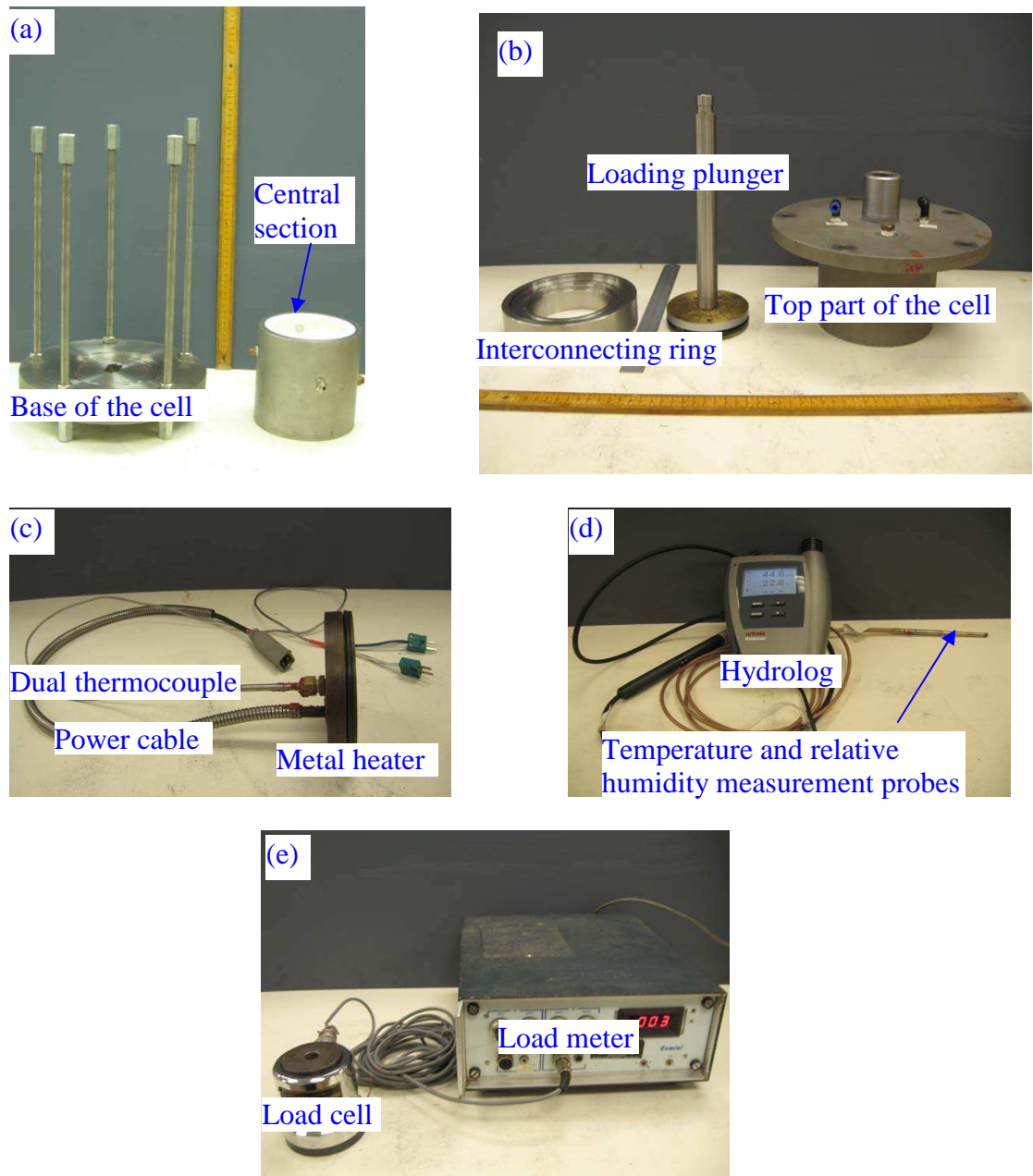


Figure 3.22. Components of thermal and thermo-hydraulic test setup: (a) base of the cell and central section, (b) loading plunger, top part of the cell and interconnecting ring, (c) metal heater, (d) hydrolog and temperature and relative humidity measurement probes and (e) load cell and load meter.

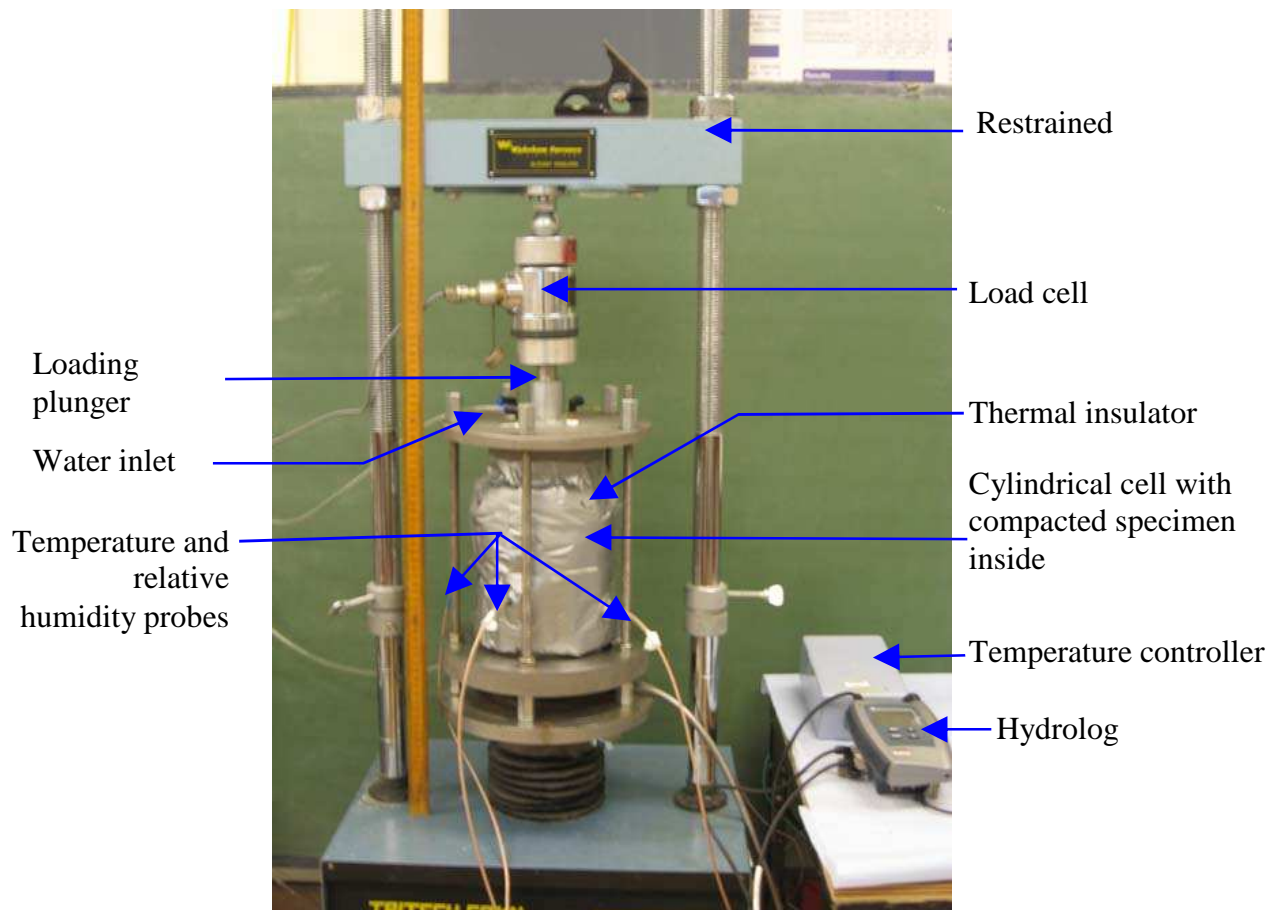


Figure 3.23. Thermal and thermo-hydraulic test setup.

A hollow PTFE liner of 20 mm thick was used inside the central section of the cell to reduce the heat loss through the outer wall of the cell during the thermal and the thermo-hydraulic tests (Fig. 3.22). As described earlier (section 3.4.3.1), the central section was used to prepare the specimens. A metal heater (Figs. 3.21 and 3.22) was used to apply thermal loading at the bottom end of the specimens. A dual thermocouple was attached at the centre of the heater. One of the thermocouple was connected to the heater controller and other one was connected to a data logger. The thermocouple connected to the heater controller maintained the temperature of the metal heater. The other thermocouple measured the actual temperature on the surface of the heater. A loading plunger (Figs. 3.22 and 3.23) with a metal porous disc was rested on top of the specimens

and measured swelling pressures exerted by compacted bentonite specimens during the thermal and the thermo-hydraulic tests.

The cell contained 3 holes in the central section at every 20 mm distance along the depth. Similarly, three nos. of holes were drilled on the specimens for accommodating the relative humidity and temperature measurement probes. The relative humidity and temperature measuring probes were manufactured by Rotronic Instruments Ltd. The accuracy of the probes used was $\pm 1.0\%$ for the range of relative humidity between 0 to 100% and $\pm 1^\circ\text{C}$ for the range of temperature measurement between - 40 to 100°C . The probes were calibrated using saturated NaCl solution at 25°C (one-point calibration) (section 3.4.3.3). For accurate measurement of relative humidity when the probes are buried inside the specimens are necessary. During the thermo-hydraulic tests, distilled water was supplied from the top of the specimens through the openings at the top of the cell.

3.4.3.3 Calibration of temperature and relative humidity probes

The relative humidity and temperature measuring probes were calibrated prior to testing using saturated sodium chloride solutions. The saturated sodium chloride (NaCl) solutions were prepared in 1000 ml glass flasks. Figure 3.24 shows the relative humidity and temperature measurement probes inside a flask during the calibration tests. The necks of the flasks were sealed air-tight during the calibration tests. The relative humidity inside the glass flask corresponding to saturated NaCl solutions would be 75.5% at a temperature of 25°C (ASTM E 104-85 1998). The temperature and relative humidity readings were monitored with elapsed time.

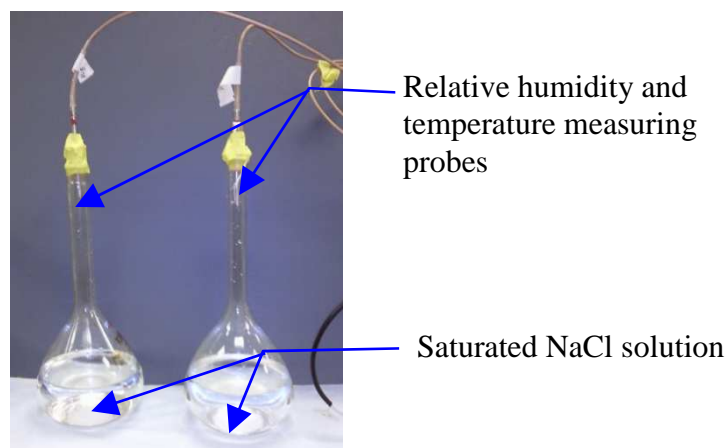


Figure 3.24. Relative humidity calibration of the probes.

The measured relative humidity with elapsed time is shown in Fig. 3.25. The standard relative humidity corresponding to the saturation NaCl solution is shown in Fig. 3.25. For clarity, the equilibration of relative humidity with time for three sensors used are shown in the inset of Fig. 3.25. The equilibrium relative humidity of the three probes was within the range of $\pm 1\%$ of the standard relative humidity for saturated NaCl solution.

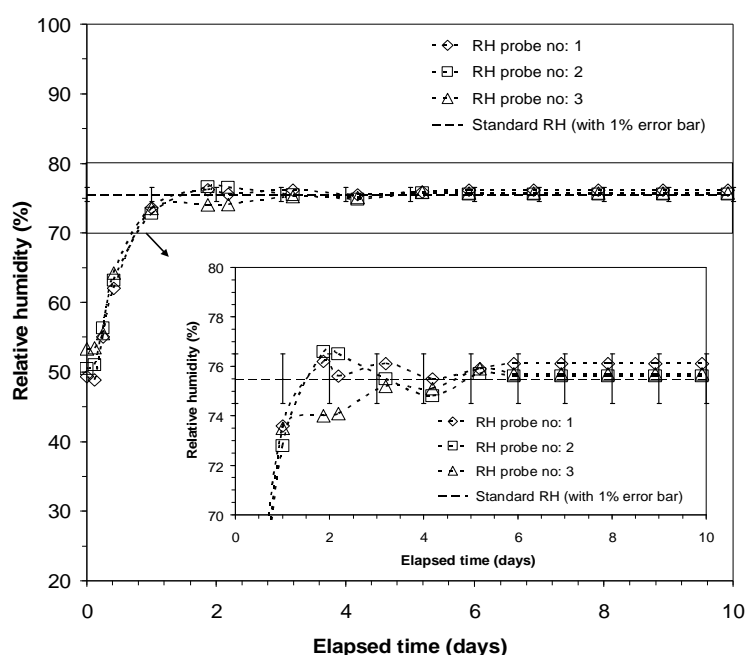


Figure 3.25. Relative humidity equilibration of the probes under calibration.

Agus (2005) reported that the measured suction in the laboratory environment could be affected due to change in relative humidity. The degree of error measured would be dependent on the range of suction considered. Figure 3.26 presents the error in suction measurement due to change in suction or relative humidity (Agus, 2005). In the current study the effect was not considered.

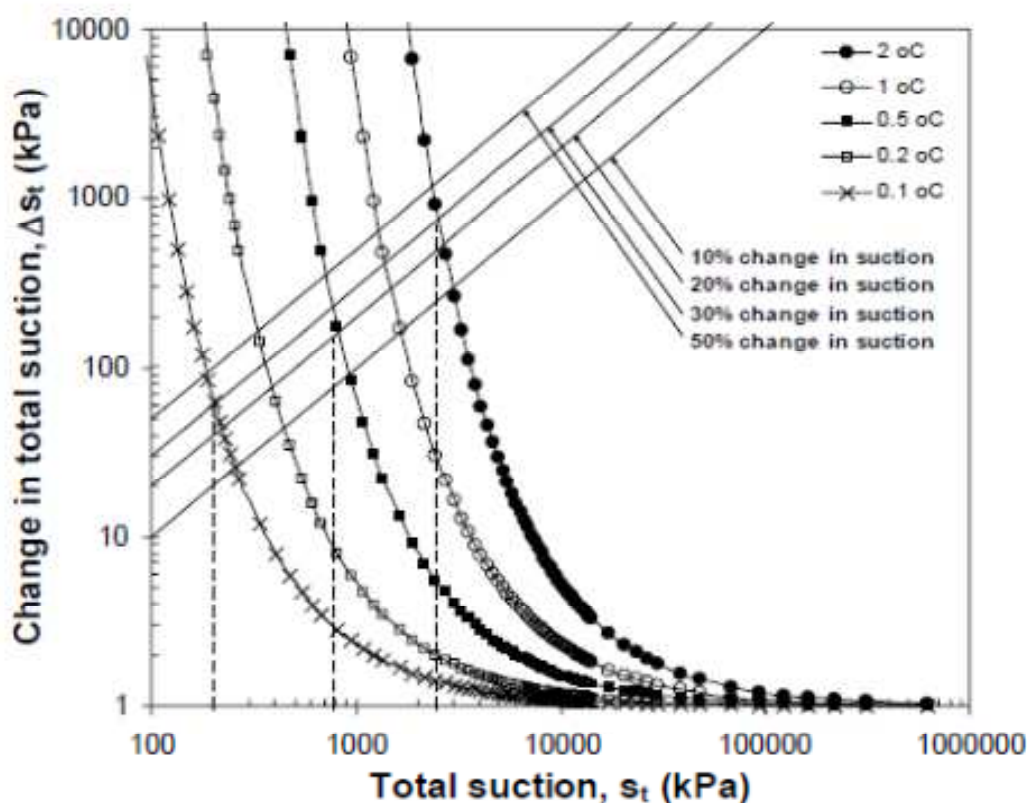


Figure 3.26. Change in suction or error in suction measurement due to change in temperature (Agus, 2005).

3.4.3.4 Thermal and thermo-hydraulic tests

The experimental setup used for the thermal and the thermo-hydraulic tests is shown in Fig. 3.23. Compacted bentonite specimens were prepared at a targeted dry density of 1.60 Mg/m^3 (section 3.4.3.1). The electric heater was attached at the bottom

end of the compacted bentonite specimen inside the central section of the cylindrical cell (Figs. 3.21 and 3.22). A PTFE disc was placed in between the metal heater and the base of the cell (Fig. 3.21). The top surface of the specimen was covered with a filter paper. The loading plunger with the metal porous disc was rested on the top end the specimens (Figs. 3.21 and 3.22). The interconnecting ring and the top part of the cell were connected (Figs. 3.21 and 3.22). Three holes were drilled in the specimens at the specified depths of the specimen using an electric driller. The entire cell was transferred to a 50 kN capacity load frame. The relative humidity and temperature measurement probes were inserted through the predrilled holes (Fig. 3.23). High temperature grease was applied at the junctions between different sections of the cell to prevent the vapour leakage. The entire cell was covered with thermal insulator (Fig. 3.23). The load cell was placed on top of the plunger and restrained against any movement (Fig. 3.23).

During the thermal tests, the compacted bentonite specimens were heated to a temperature of 85°C at the bottom end. The temperature at the top end of the specimens was maintained at 25°C by circulating water from a constant temperature water bath. The water was circulated inside a metal coil mounted inside the top part of the cell that will prevent hydration of the specimens. The transient temperature, relative humidity and swelling pressures were monitored during all tests. During the thermo-hydraulic tests, in addition to the temperatures applied during the thermal tests, distilled water was supplied from the top of the specimens. The empty space on top the loading plunger was filled with distilled water and the specimens were allowed to hydrate. Similar to the thermal tests the temperature, the relative humidity and the swelling pressures were monitored during the thermo-hydraulic tests.

The modified oedometers and the thermo-hydraulic cell were not facilitated with volume change measurement devices. Therefore, the volume of water at inlet and outlet of the devices during swelling pressure tests and thermo-hydraulic tests were not measured. The water uptake capacity of unsaturated bentonite specimens can be found out from the measurement of water volume at the inlet and outlet of the devices.

3.4.3.5 Extrusion of specimens after thermal and thermo-hydraulic tests

After completion of any thermal and thermo-hydraulic tests, the electric heater was switched off. The relative humidity and temperature measuring probes were removed from the specimens and were retrieved. During the thermo-hydraulic tests, it was very difficult to retrieve the relative humidity and temperature measurement probes which were placed closer to the hydration end of the specimens. The load cell was removed from the top of the plunger and disconnected from the load meter. The top part of the cell and the interconnecting ring were removed. The central section of the cell along with the heater and the PTFE disc were mounted on top of a hydraulic extruder that enabled extrusion of the tested bentonite specimens.

Figure 3.27 shows the components of the specimen extruder. The extruder consists of a metal frame, a hydraulic jack, a reaction frame and a handle. The specimen inside the central section of the cell along with the heater and the bottom porous disc were made to rest above the top plate of the extruder. The reaction frame was attached and tightened. The top plate of the extruder was gradually pushed up and the specimen was extruded from the cell as shown in Fig. 3.28.

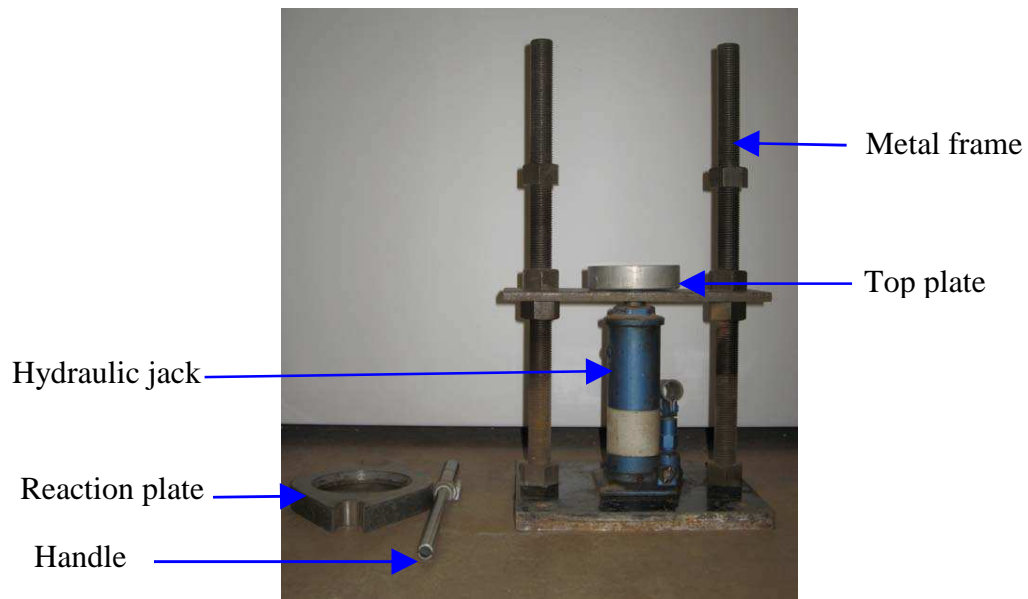


Figure 3.27. Components of the specimen extruder.

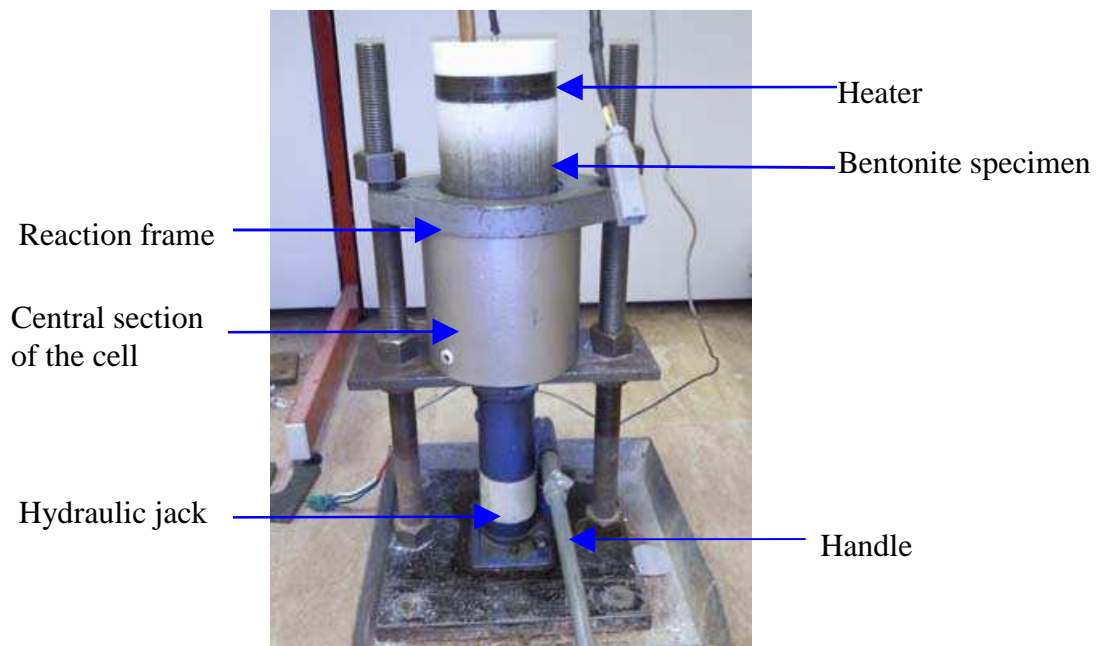


Figure 3.28. Extrusion of a bentonite specimen after testing.

After the extrusion process, the bentonite specimens were sliced into 8 pieces of each 10 mm thick. The water contents of each slice of the specimens were measured. For

each slice, the average water content of two measurements were considered. Parts of the specimen were stored for chemical analysis.

The concentrations of soluble cations and anions of each slice were determined by aqueous extraction technique (section 3.4.3.6). The chemical analysis was repeated twice for each slice. The volume of each slice of the tested bentonite specimens were measured using molten wax. The final dry density and the degree of saturation of each slice were calculated using volume-mass relationships from the measured water contents and volumes of each slice.

3.4.3.6 Chemical analysis

During the thermal and thermo-hydraulic tests, ion exchange, dissolution and precipitation of minerals occur in compacted bentonites (Fernández et al., 2001, 2004, 2008; Cuevas et al., 2002; Villar et al., 2008; Samper et al., 2008; Gómez–Espina and Villar, 2010; Fernández and Villar, 2010). The concentrations of cations and anions along the depth of the bentonite specimens are expected to alter due to several physical and chemical processes occurring in the bentonite specimens in response to the thermal and the hydraulic gradients. Several studies have been carried out to determine the changes in concentrations of cations and anions due to the thermal and the hydraulic gradients (Fernández et al., 2001, 2004, 2008; Cuevas et al., 2002; Singh, 2007; Villar et al., 2008; Samper et al., 2008; Gómez–Espina and Villar, 2010; Fernández and Villar, 2010). In the current investigation, the change in concentration of cations and anions were measured by aqueous extraction technique.

The bentonite specimens of each slice were oven dried and grounded to powder. One gram of bentonite powder from each slices were mixed with 10 ml of distilled water. The sample mixtures were shaken in a reciprocating horizontal mechanical shaker (Fig. 3.29) for 24 hours. After the shaking process, the sample mixtures were transferred into 50 ml centrifuge tube and were centrifuged (Fig. 3.30). After centrifugation the supernatant solutions were collected. A one litre vacuum extraction flask was connected to a Buchner funnel fitted with a Whatman no. 42 filter paper. The supernatant solutions after centrifugation were transferred into the Buchner funnel shown in Fig. 3.31. The Buchner funnel was connected with vacuum supply. The sample mixtures were filtered. The filtered solutions at the bottom of the flask were collected for further chemical analysis.

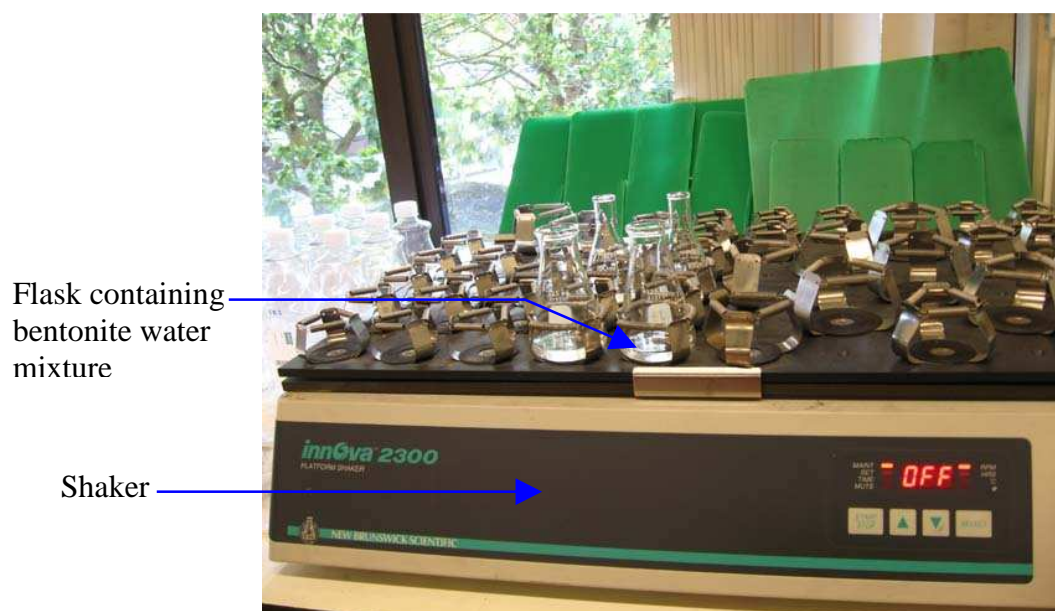


Figure 3.29. Photograph of the reciprocal shaker and the bentonite-water mixture.



Figure 3.30. Sigma GK-15 centrifuge.

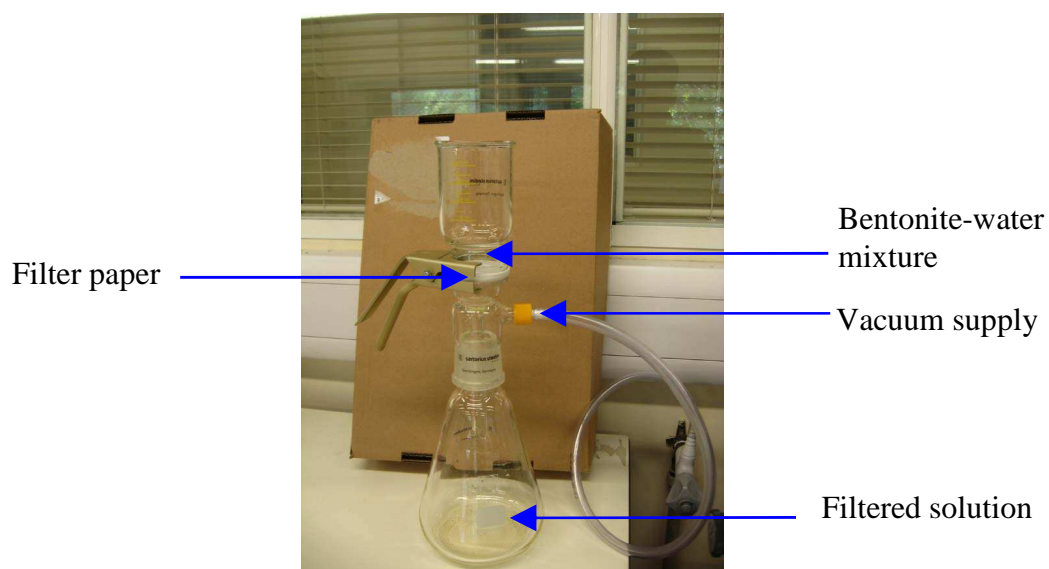


Figure 3.31. Filtration process by applying vacuum through Buchner funnel.

The filtered solutions collected at the bottom of the Buchner Funnels were tested. The concentrations of Cl^- , SO_4^{2-} and NO_3^- were determined using Ion Chromatography (IC; Fig. 3.32) and the concentration of Na^+ , Ca^{2+} , Mg^{2+} and K^+ were determined using Inductively Coupled Plasma Optical Emission Spectroscopy (ICP-OES; Fig. 3.33).



Figure 3.32. Ion Chromatography (DIONEX ICS-2000).

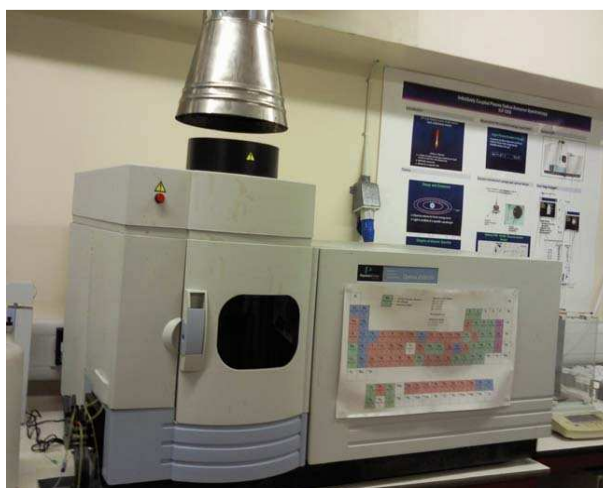


Figure 3.33. Perkin Elmer Optima-2100 DV Inductively Coupled Plasma Optical Emission Spectroscopy (ICP-OES).

3.5 Summary

The properties of MX80 bentonite used for the investigation are presented in this chapter. The physical and chemical properties of the bentonite, such as the liquid limit, the plastic limit, the shrinkage limit, the specific gravity, the specific surface area, the

cation exchange capacity and the weighted average valence of exchangeable cations are presented. The suction versus water content relationship of the bentonite established from dessicator tests and from the chilled-mirror hygrometer tests are presented. The results indicated that at higher suction levels (> 10 MPa) the dry density have insignificant influence on the suction versus water content relationship of the bentonite. At higher suction levels, the suction of bentonite specimens was found to depend on the water content of the bentonite.

Modified oedometers used for measuring swelling pressure of compacted bentonite and the cell used to carry out the thermal and thermo-hydraulic tests has been presented. Procedures adopted for specimen preparation, calibration of the devices, constant volume swelling pressure tests, consolidation test, thermal and thermo-hydraulic tests, removal of specimens after thermal and thermo-hydraulic tests and chemical analysis have been presented.

Chapter 4

Effect of post compaction residual stress on swelling pressure of compacted bentonite

4.1 Introduction

Compacted bentonites used in nuclear waste repositories are usually prepared either in the form of bricks or pellets. Bricks and pellets of bentonites are prepared by statically compacting bentonite powder in metal moulds. Following the compaction process the bricks or pellets are extruded from the moulds prior to using them in repository conditions. Removal of applied compaction stresses causes vertical expansion of compacted bentonites, whereas their extrusion from moulds causes total release of post compaction stresses. In the past, studies concerning swelling pressures of compacted bentonites were primarily on specimens with post compaction residual stresses (Müller-

Vonmoos and Kahr, 1982; Pusch, 1982; Dixon and Gray, 1985; Komine and Ogata, 1996; Villar, 2000; Karnland et al., 2007; Herbert et al., 2008; Villar and Lloret, 2008; Komine et al., 2009; Schanz and Tripathy, 2009). The influence of post compaction residual stresses on swelling pressure of compacted bentonite has not been explored yet.

The main objective of this chapter is to show the effect of post compaction residual lateral stresses release, electrolyte concentrations of bulk fluid and temperature, on the swelling pressure of compacted MX80 bentonite. Section 4.3 presents the extrusion and re-insertion process of compacted bentonite specimens. The compaction loads applied and the dry densities of compacted bentonite specimens prior to the swelling pressure tests are presented in section 4.4. Section 4.5 presents the stress history of the compacted bentonite specimens. Section 4.6 presents determination of the swollen dry densities of the specimens. Section 4.7 presents the swelling pressure as influenced by post compaction residual lateral stresses, electrolyte concentration and temperature. Variation of saturated water content with swollen dry density of compacted specimens are presented. Concluding remarks from this chapter are presented in section 4.7.

4.2 Experimental program

The swelling pressures of MX80 bentonite specimens were measured using modified oedometers shown in Fig. 3.12. The constant volume swelling pressure test setup is presented in Fig. 3.14. The calibration of the device against deformation and temperature are shown in Figs. 3.15 and 3.17, respectively.

In total 54 swelling pressure tests were carried out in seven series of tests described as series I, II, III, IV,V, VI and VII. The detailed experimental program is illustrated in Table 4.1 and Fig. 4.1. Series I (11 tests), II (12 tests), III (9 tests) and IV (8 tests) tests were conducted at ambient temperature (25 °C) and series V (5 tests), VI (4 tests), and VII (5 tests) tests were conducted at an elevated temperature of 70 °C (Table 4.1 and Fig. 4.1). Series I tests were conducted immediately after the compaction process was completed. For all other series of tests (test series II, III, IV, V, VI and VII), the specimens were extruded from compaction rings and were re-inserted back prior to testing them. This process was adopted in an attempt to release the post compaction residual lateral stresses (Fig. 4.1).

Table 4.1 Detailed experimental program of swelling pressure tests

Test series	Specimen condition	No. of tests	Bulk fluid used	Testing temperature
(1)	(2)	(3)	(4)	(5)
I	Compacted and tested	11	Distilled water	Ambient temperature (25 °C)
II	Compacted, extruded, re-	12	Distilled water	Ambient temperature
III	inserted	9	0.1 M NaCl	(25 °C)
IV	and tested	8	1.0 M NaCl	
V	Compacted, extruded, re-	5	Distilled water	Elevated temperature
VI	inserted	4	0.1 M NaCl	(70 °C)
VII	and tested	5	1.0 M NaCl	

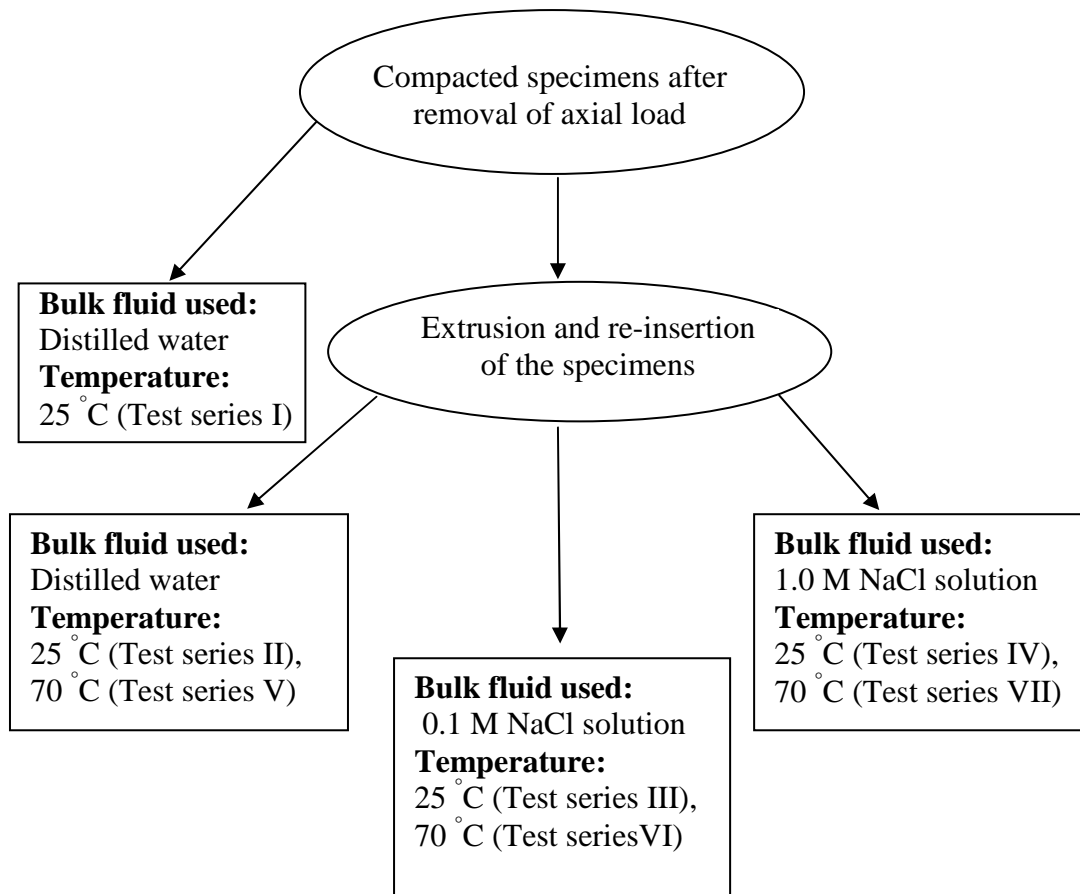


Figure 4.1. Compaction condition of the specimens and experimental program.

The effect of release of post compaction stress was studied by comparing the swelling pressure results of series I and II tests. However, the effects of temperature and electrolyte concentrations were not studied independently for the specimens with and without post compaction stresses. Effects of electrolyte concentration and temperature were studied using specimens without post compaction stresses.

Sodium chloride is the primary salt present in sea water amongst other salts. The NaCl concentration in sea water is about 0.6 M. In this study, distilled water approximately equivalent to 0.0001 M NaCl, 0.1 M NaCl and 1.0 M NaCl solutions were used as bulk fluids to study the effect of weak and strong electrolytes on the swelling pressure of MX80 bentonite. For the test series I, II and V, the bentonite specimens were

hydrated using distilled water (Table 4.1 and Fig. 4.1). Test series III and VI were conducted by saturating the specimens using 0.1 M NaCl solution (Table 4.1 and Fig. 4.1). Series V and VII tests were carried out by saturating the specimens using 1.0 M NaCl solution (Table 4.1 and Fig. 4.1). Test series V, VI and VII were carried out at a temperature of 70 °C.

4.3 Extrusion and re-insertion of test specimens

Once the compaction process was completed, the specimens were extruded from the specimen ring using an extruder. Upon extrusion, the lateral dimension of the specimens increased. The specimens were then held between two reference stainless steel plates of diameter slightly less than that of the specimen rings. The excess materials were removed by carefully scrubbing the circumference of the specimens with the help of a smooth metal file. Based on the new dimensions of the specimens, the mass of the specimens, and for known water content (= 11%), the modified dry densities of the specimens were calculated. The specimens were then carefully inserted back into the specimen rings for the swelling pressure tests.

The extrusion and re-insertion processes of the specimens are shown in Fig. 4.2. Figure 4.2 (a) shows a compacted specimen within an oedometer ring after removal of an applied static load. The specimen after extrusion from the oedometer ring is shown in Figs. 4.2 (b) and (c). The specimen after dimension manipulation and reinserted into the oedometer ring is shown in Figs. 4.2 (d) and (e), respectively. Figure 4.2 (e) indicates that a small gap existed between the inner surfaces of the oedometer ring and the specimen after the re-insertion process. During the hydration process, the gap between the

ring and the inner surfaces of the oedometer ring was replenished due to expansion of the specimen. This was accomplished by testing trial specimens.

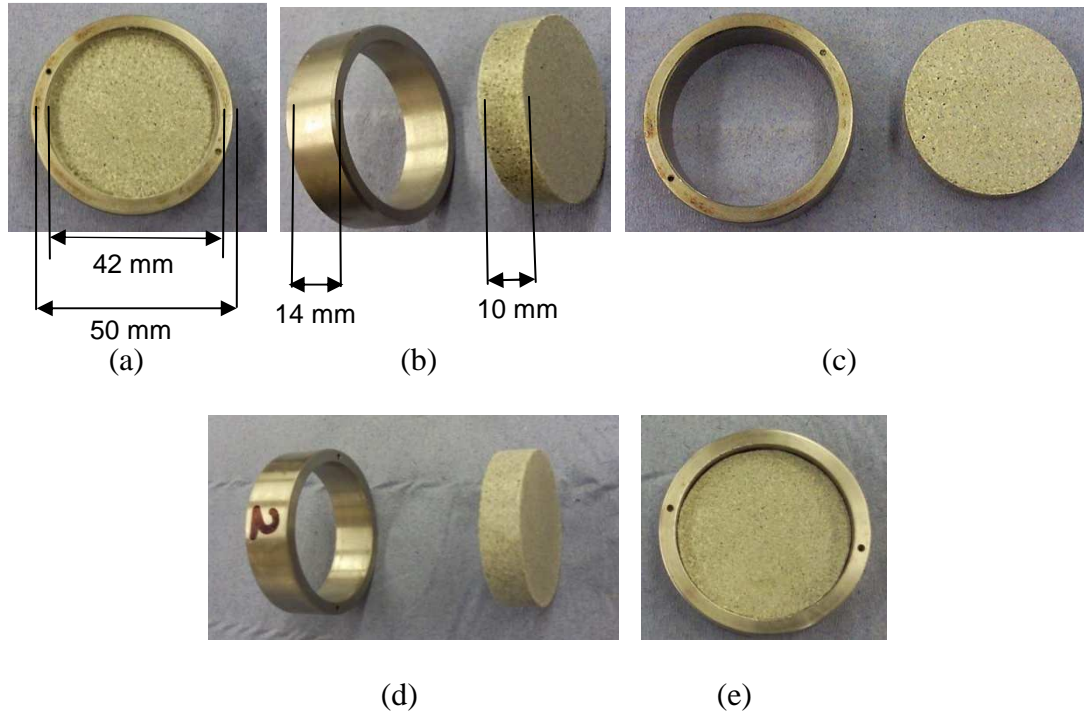


Figure 4.2. Specimen extrusion and re-insertion processes prior to swelling pressure tests; (a) after removal of static load, (b) and (c) after extrusion, (d) after dimension manipulation, (e) after re-insertion.

The swelling pressure tests were carried out for the range of targeted dry densities of the bentonite specimens between 1.1 and 1.9 Mg/m³. At higher dry densities, the extrusion and re-insertion of the specimens did not cause any significant disturbance of the specimens. However, at dry densities lower than 1.30 Mg/m³, the specimens were fractured while extruding from the rings. Therefore, the post compaction residual lateral stress release effect was studied for the specimens with dry densities greater than 1.30 Mg/m³.

4.4 Applied compaction load and dry density of specimens prior to testing

Prior to preparation of the specimens, the oedometer rings were lubricated with technical grade silicon grease to minimise the side friction. A high capacity compression testing device was used for compacting the specimens. The maximum static load applied to prepare the specimens and the dry densities of the compacted specimens before testing are presented in Table 4.2.

Table 4.2 Applied compaction load and dry density of the specimens prior to testing

Test series I		Test series II		
Load applied (kN)	Dry density after release of axial load	Load applied (kN)	Dry density after removal of axial load	Dry density after extrusion and re-insertion
--	1.10	10	1.43	1.37
--	1.33	12	1.52	1.40
--	1.43	16	1.55	1.45
11	1.48	29	1.61	1.57
12	1.52	34	1.64	1.61
25	1.58	48	1.72	1.64
38	1.67	65	1.78	1.72
60	1.76	70	1.80	1.75
76	1.81	78	1.83	1.77
82	1.85	98	1.92	1.81
112	1.95	92	1.88	1.82
		105	1.94	1.86

Specimen preparation method for the test series II, III, IV, V, VI and VII, the bentonite specimens were similar. Therefore, in order to avoid the repetition of information, the applied compaction loads and the dry densities of the specimens prior to

testing of specimens in test series I and II are presented in Table 4.2. The maximum applied load at the highest dry density was 112 kN (applied pressure ≈ 72 MPa), whereas the applied loads were less at lesser dry densities (Tables 4.2). Comparing the dry density of the specimens for test series T and II (Table 4.2), it is evident that to achieve same dry density of the specimen a lesser static load was required for test series I than that for test series II. Similarly, for the test series III, IV, V, VI and VII, a higher load was required to achieve any dry density than that required for test series I.

4.5 Deformation history of the compacted specimens prior to testing

The height of the compacted specimens was found to increase after releasing the axial compaction load. Therefore, the dry densities of the compacted bentonite specimens were lesser than the targeted dry densities. Further, the extrusion of the specimens from the specimen rings caused lateral expansion of the specimens and hence the dimensions were adjusted to re-insert back into the ring. Therefore, the dry density of the specimens was further reduced due to extrusion and re-insertion processes.

The dry densities of the specimens prior to the swelling pressure tests are plotted against the corresponding applied static loads for all series of tests in Fig. 4.3. Apart from some scatter in the data due to the workmanship and errors in dimensions measurements, the dry densities were found to fall on two distinct curves shown as MN and MP. Curve MN represents the dry densities of the specimens after removal of axial loads. Curve MP represents the dry densities of the specimens after the extrusion and re-insertion processes. The minimum and maximum dry densities of the specimens achieved after the compaction process was at M and at N, respectively. It was noted that upon extrusion and

re-insertion processes, there was not any significant decrease in the dry density at M. However, at higher dry densities the extrusion and re-insertion process caused significant decrease in the dry densities.

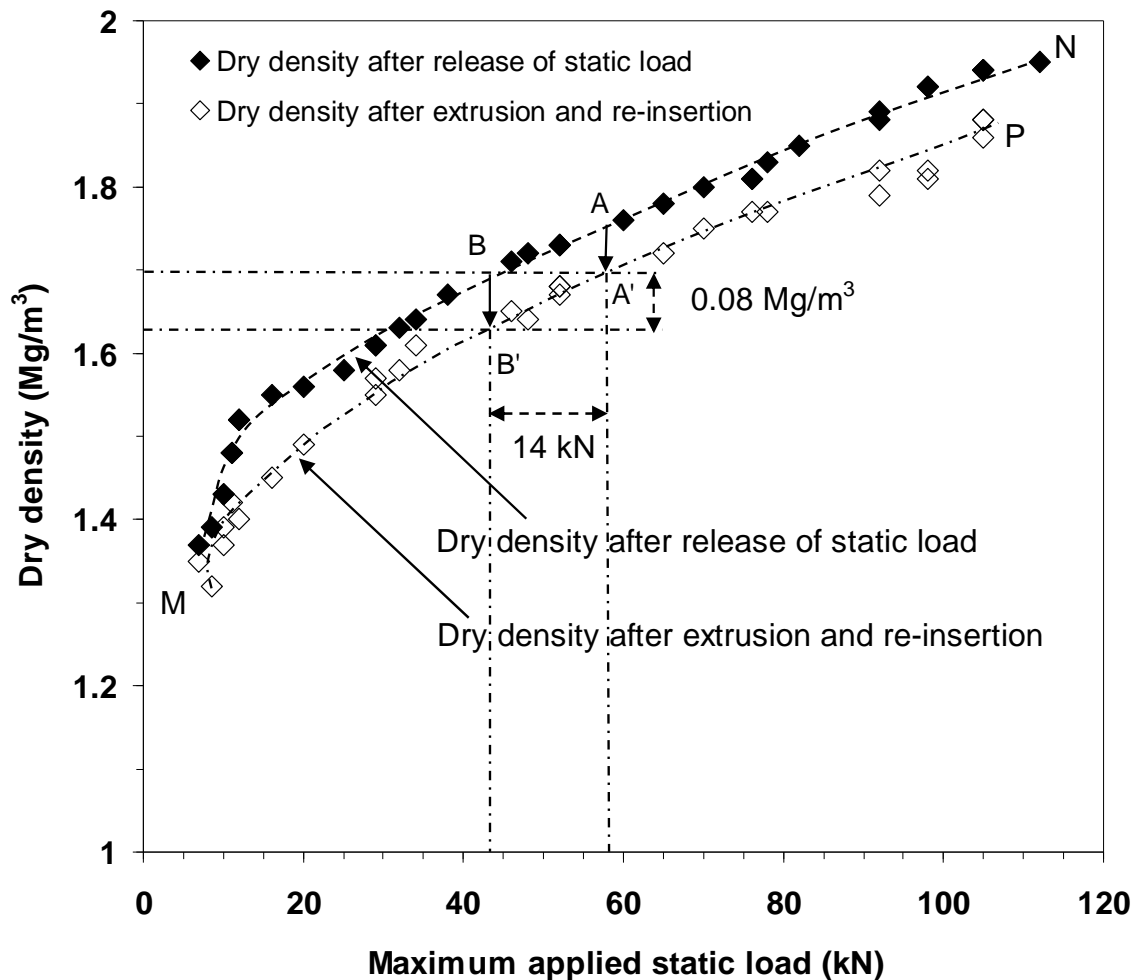


Figure 4.3. Deformation history of compacted specimens prior to swelling pressure tests.

The slopes of the curves MN and MP were found to be dissimilar at lesser applied loads, whereas the slopes were found to be similar at dry densities greater than about 1.50 Mg/m³ (about 14 kN of applied axial load required for an increase in the dry density of 0.08 Mg/m³). This indicates that the ratios between the changes in the dry densities due to

an axial stress release and that due to both axial and the lateral expansion and further dimension manipulations were similar.

To explain the compaction condition of the specimens in test series I and others, the dry densities of specimens at points A, B, A' and B' are shown on the curves MN and MP. For example, In Fig 4.3, points A and B on curve MN represent the dry densities of specimens for test series I prior to testing. The compaction load required to achieve the dry density of the specimens at points A and B were 58 and 43 kN, respectively. After the extrusion and re-insertion processes, the dry densities of the specimens at points A and B on the curve MN shifted to the points at A' and B' on curve MP. The dry densities of specimens at points A' and B are similar. Therefore, it is evident that a lesser load was required to achieve the same dry densities for the specimens tested in series I tests as compared to series II, III, IV, V, VI and VII tests.

The dry densities of the specimens after completion of swelling pressure tests were calculated considering expansion of the device. Therefore, the swollen dry densities of the specimens were lesser than that shown on the curve MP in Fig. 4.3.

4.6 Swollen dry density

The swollen dry densities of the specimens in swelling pressure tests were calculated based on the measured water contents and the volume of the specimens. For each test, expansion of the specimen ring was determined using the pressure versus deformation relationship (section 3.4.1.2). The expansion of the ring was added to the diameter and the height of the specimens for calculating the dimensions after the swelling

pressure tests. The mass and water contents of the specimens were measured after the swelling pressure tests. For known mass, water content and volume of the specimens, the dry density and void ratio of the specimens were calculated. Knowing the void ratio, the degree of saturation of the specimens were calculated.

It was noted that the degree of saturation of the specimens after the swelling pressure tests varied between 102 and 148%. Several researchers have reported that the degree of saturation of bentonite specimens may exceed 100% (Martin, 1962; Komine and Ogata, 1994; Villar, 2000; Villar and Lloret, 2008; Marcial, 2010). It was hypothesized that the structure of water molecules changes while in contact with montmorillonite surfaces and the density of water varies in bentonite-water systems (Pusch and Carlsson, 1985; Sposito and Prost, 1982; Karnland et al., 2006; Villar and Lloret, 2008). A review of literature suggested that the density of water in compacted Na-bentonite may vary between 0.97 (Anderson and Low, 1957) and 1.14 Mg/m³ (Skipper et al., 1991).

The degree of saturation is the ratio of volume of water in voids to the total volume of voids. Therefore, the degree of saturation of the specimens may not exceed 100%. Restricting the degree of saturation to 100% and considering the density of water as 0.97, 1.0 and 1.14 Mg/m³, the swollen dry densities of the specimens were recalculated using following equations.

$$\begin{aligned}
 S_r e &= w G_s \\
 &= w \frac{\rho_s}{\rho_w}
 \end{aligned}
 \tag{4.1}$$

$$\begin{aligned}
\rho_d &= \frac{G_s \rho_w}{1 + e} \\
&= \frac{\left(\frac{\rho_s}{\rho_w} \right)}{1 + e} \times \rho_w \\
&= \frac{\rho_s}{1 + e}
\end{aligned} \tag{4.2}$$

where S_r is the degree of saturation, e is the void ratio, w is the water content (%), G_s is the specific gravity of the bentonite = 2.76, ρ_s is the density of soil solids, ρ_w is the density of water and ρ_d is the dry density. Considering the degree of saturation = 100% and for known water content, the density of soil solids and the density of water, the corresponding void ratio was calculated using eq. (4.1). Knowing the void ratio, the swollen dry density was calculated using eq. (4.2). The calculated swollen dry densities of the specimens were used for analysis of test results in the following sections.

4.7 Results and discussion

Figure 4.4 shows the physical appearance of a bentonite specimen after terminating a swelling pressure test. The uniform texture at both sides of the ring indicates that the specimen was uniformly saturated. The gap between the specimen and the inner surface of the specimen ring prior to testing was filled by the saturated specimen as evident from Fig. 4.4.



Figure 4.4. Physical appearance of a specimen after swelling pressure test.

4.7.1 Time-swelling pressure plot at ambient temperature

The time versus swelling pressure plots for the series I, II, III and IV tests are presented in Fig. 4.5. All these tests were conducted at ambient temperature (Table 4.1 and Fig. 4.1). In series I tests, compacted bentonite specimens were tested immediately after completion of the compaction process and further hydrating the specimens using distilled water (Table 4.1 and Fig. 4.1). For series II, III and IV tests, the compacted bentonite specimens were extruded from the specimen ring and re-inserted back prior to testing (Table 4.1 and Fig. 4.1). Distilled water, 0.1 M NaCl solution and 1.0 M NaCl solution were used for hydrating the specimen in tests series II, III and IV, respectively.

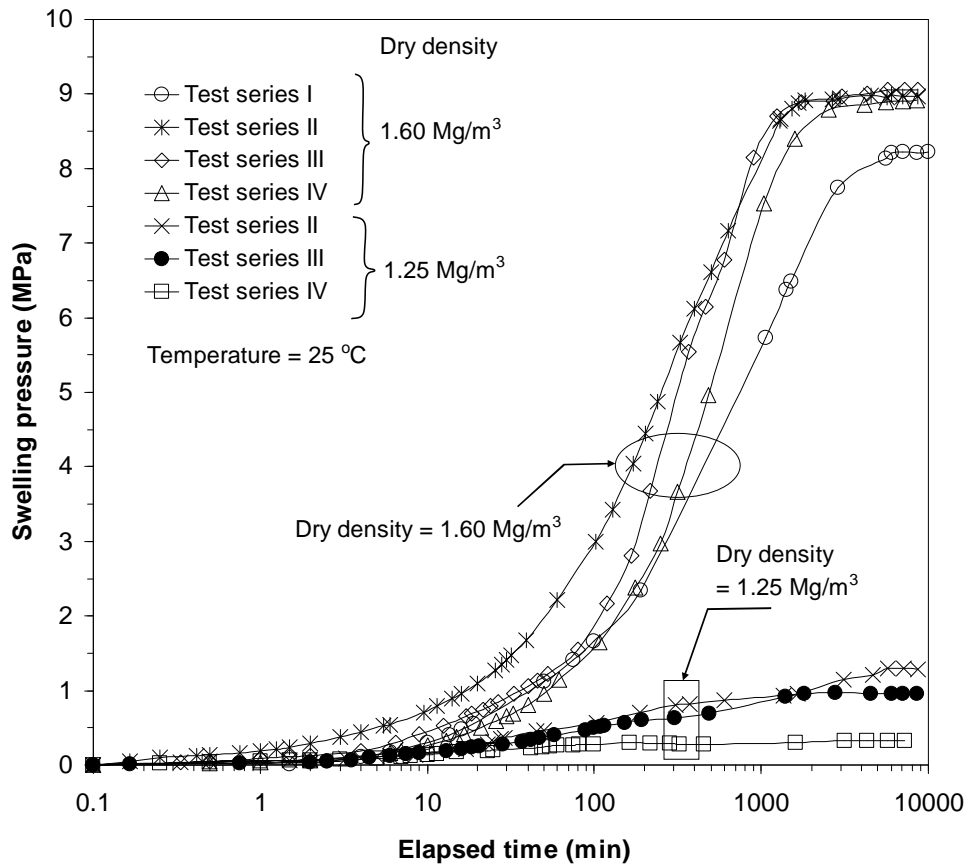


Figure 4.5. Time-swelling pressure plots for Series I, II, III and IV tests.

Typical time versus swelling pressure results for specimens at swollen dry densities of 1.60 Mg/m^3 and 1.25 Mg/m^3 are shown in Fig. 4.5. The swelling pressures were found to be equilibrated within about 7 days for all cases irrespective of the dry density of the specimens and the bulk fluid type used. Referring to the test results presented in Fig. 4.5, at a dry density of 1.60 Mg/m^3 , the swelling pressures were very nearly similar and independent of the bulk fluid type for the specimens tested under series II, III, and IV tests, whereas the swelling pressure was found to be significantly less for the specimen that was tested immediately after the compaction process (i.e., test series I). At a dry density of 1.25 Mg/m^3 , the effect of electrolyte concentration in bulk solution was distinct in that with an increase in NaCl concentration in the bulk fluid, the swelling pressure was found to decrease.

For initially unsaturated compacted bentonite specimens, the time required to reach equilibrium swelling pressure is dependent on the dry density and thickness of the specimens. Several researchers (Pusch, 1980, 1982, Madsen and Muller-Vonmoos, 1989; Villar and Lloret, 2008) have reported that the time required to reach maximum swelling pressure is about 7-10 days; the current study agrees with this. However, the phenomenon of the double maxima in the swelling pressure development, which has been reported by Pusch (1982) and Schanz and Tripathy (2009) has not been observed during the testing procedure.

4.7.2 Swelling pressure test results at ambient temperature

The swelling pressures of the specimens tested at a temperature of 25 °C are shown in Tables 4.3 and 4.4. Table 4.3 presents the test results for series I and II tests, whereas Table 4.4 presents the test results for series III and IV. The bulk fluids used to hydrate the specimens, specimen preparation history, the dry densities of the specimens after release of static load, the dry densities of the specimens after extrusion and re-insertion processes, the swollen dry densities, the swelling pressures and the measured water contents at the end of the swelling pressure tests are presented in Tables 4.3 and 4.4.

The swelling pressures of compacted bentonite specimens were found to increase with an increase in the dry densities for all the tests carried out in this study concurrent with earlier findings reported in the literature (Pusch, 1982; Bucher and Müller-Vonmoos, 1989, Komine and Ogata, 1994; Villar and Lloret, 2004, 2008; Schanz and Tripathy, 2009).

Table 4.3 Summary of the swelling pressure results for series I and II tests

Test series (Bulk fluid used)	Specimen preparation history	Dry density after release of static load (Mg/m ³)	Dry density after extrusion and re-insertion (Mg/m ³)	Swollen dry density (Mg/m ³)	Swelling pressure (MPa)	Water content at the end of swelling pressure test (%)
(1)	(2)	(3)	(4)	(5)	(6)	(7)
I (Distilled water)	Static load	1.10		1.09	0.22	55.1
	released	1.33		1.24	0.85	44.6
		1.43		1.29	1.20	41.3
		1.48		1.35	1.91	37.7
		1.52		1.37	2.11	36.8
		1.58	--	1.42	2.86	34.1
		1.67		1.46	3.70	32.2
		1.76		1.49	4.52	31.0
		1.81		1.53	5.85	29.0
		1.85		1.56	6.04	28.0
		1.95		1.60	8.22	26.1
II (Distilled water)	Static load	1.43	1.37	1.26	0.99	43.4
	released,	1.52	1.40	1.28	1.30	41.9
	specimen	1.55	1.45	1.40	2.70	35.2
	extruded and	1.61	1.57	1.39	2.81	35.8
	re-inserted	1.64	1.61	1.42	3.26	34.4
	back to the	1.72	1.64	1.43	4.06	33.7
	specimen ring	1.78	1.72	1.49	5.20	31
		1.80	1.75	1.52	5.90	29.7
		1.83	1.77	1.52	6.57	29.5
		1.92	1.81	1.55	7.06	28.1
		1.88	1.82	1.53	7.33	29.1
		1.94	1.86	1.60	9.00	26.3

Table 4.4 Summary of swelling pressure results for series III and IV tests

Test series (Bulk fluid used)	Specimen preparation history	Dry density after release of static load (Mg/m ³)	Dry density after extrusion and re-insertion (Mg/m ³)	Swollen dry density (Mg/m ³)	Swelling pressure (MPa)	Water content at the end of swelling pressure test (%)
(1)	(2)	(3)	(4)	(5)	(6)	(7)
III (0.1 M NaCl)	Static load released	1.13	--	1.08	0.22	56.2
	Static load released,	1.37	1.35	1.24	0.55	44.4
	specimen	1.43	1.39	1.24	0.77	44.1
	extruded and	1.48	1.42	1.29	0.95	41.4
	re-inserted	1.61	1.55	1.40	2.14	35.0
	back to the	1.63	1.58	1.43	2.83	34.8
	specimen ring	1.71	1.65	1.49	4.08	30.9
		1.81	1.77	1.56	6.35	31.4
		1.94	1.88	1.59	9.05	26.5
IV (1.0 M NaCl)	Static load released	1.13	--	1.08	0.04	55.6
	Static load released,	1.39	1.32	1.27	0.33	42.7
	specimen	1.56	1.49	1.37	1.08	36.7
	extruded and	1.73	1.67	1.49	2.67	31.1
	re-inserted	1.73	1.68	1.50	2.82	30.5
	back to the	1.73	1.68	1.51	2.94	29.8
	oedometer ring	1.89	1.79	1.55	4.70	28.3
		1.92	1.82	1.56	5.55	27.4
		1.94	1.88	1.59	8.92	26.6

The minimum and maximum measured swelling pressures for the bentonite were 40 kPa (test series IV) and 9.05 MPa (test series III). The swelling pressures of MX80 bentonites reported by other researchers (Pusch, 1982; Bucher and Müller-Vonmoos, 1989; Börgesson et al., 1995; Karnland et al., 2007) were found to be similar to the measured swelling pressure values obtained in test series I.

4.7.3 Influence of post-compaction residual stresses on swelling pressure

Figure 4.6 shows the swelling pressure test results for series I and II tests that were carried out with distilled water as the bulk fluid. The results are plotted based on the swollen dry densities of the specimens. Determination of swollen dry densities of the specimens is explained in section 4.5. The swollen dry densities of the specimens after the swelling pressure tests were calculated considering the density of water as 1.0 Mg/m^3 .

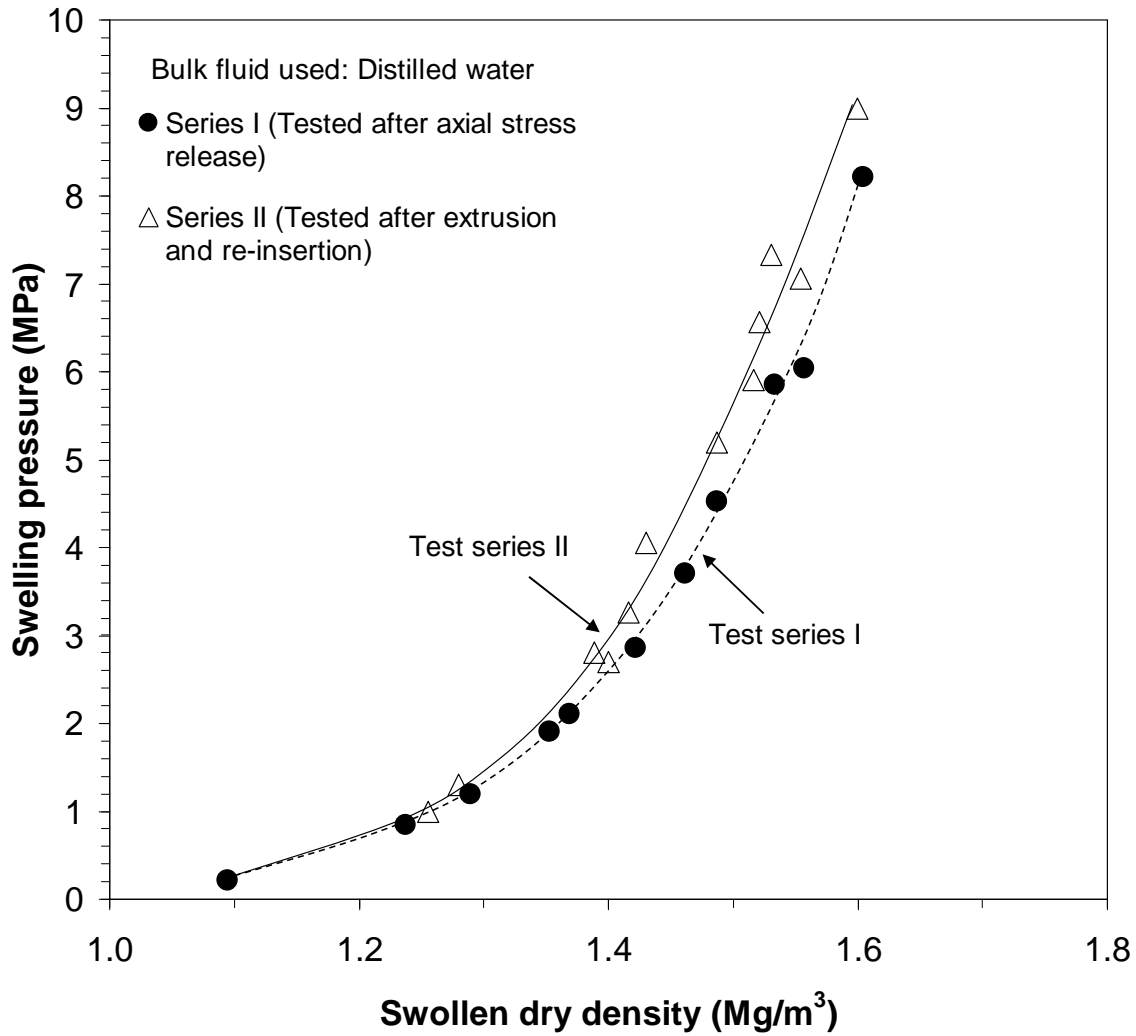


Figure 4.6. Influence of post compaction residual stresses on swelling pressure.

The swelling pressures for series II specimens were invariably found to be greater than that for specimens tested in series I at all dry densities considered in this study. Stress relaxation upon extrusion of the specimens from the specimen rings affected the dry densities of the specimens. On the other hand, as shown in Fig. 4.3, at any given dry density a greater load was applied for preparing series II specimens than that for series I specimens. An increase in the swelling pressure for the specimens in test series II was between 8 to 25% as compared to the swelling pressures of specimens in tests series I.

Considering that an increase in the dry density at constant water content causes a decrease in the interaggregate pores in compacted clays (Sridharan et al., 1971; Delage et al., 2006) and further considering the stress paths followed by the compacted specimens following the axial and the lateral stress release in this study (Fig. 4.3), the following conclusions are made. At any given dry density, the increased swelling pressures for the specimens tested in series II are on account of higher compressive load applied during specimen preparation causing reduction in interaggregate pores. Additionally, the release of the post compaction residual stresses upon extrusion of the specimens from specimen rings caused further changes in the pore size distribution and particle reorientation within the specimens (Delage et al., 2006). Note that devoid of the latter, the dry density-swelling pressure relationship for the bentonite may be expected to be unique.

Figure 4.7 shows the comparison between the maximum swelling pressures obtained from series I and series II tests conducted in this study, with those results reported in the literature. While there is good agreement with those results reported by Karnland et al. (2007), the results presented by Bucher and Müller-Vonmoos (1989) are lower for dry densities greater than 1.50 Mg/m^3 .

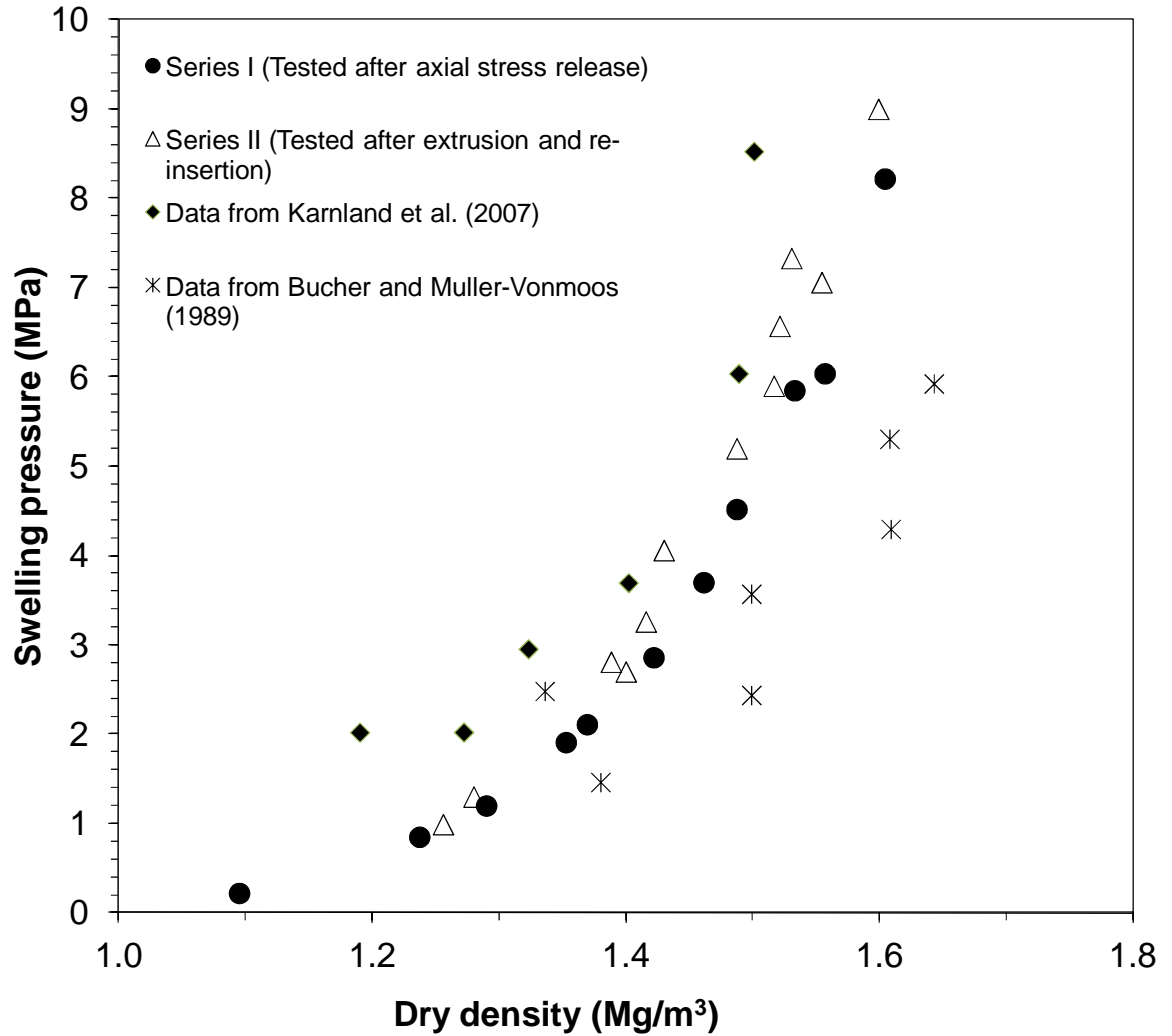


Figure 4.7. Comparison between maximum swelling pressures obtained with reported results.

Figure 4.8 shows the swelling pressure test results for series I and II tests. The swollen dry densities of the specimens in this case were calculated considering the density of water as 0.97 and 1.14 Mg/m³. For comparison test results with $\rho_w = 1.0 \text{ Mg/m}^3$ are shown in Fig. 4.7. It was noted that the swollen dry densities of the specimens increased as the density of water was increased. Irrespective of the density of water, the swelling pressures measured in series II tests were found to be significantly higher than that of series I tests. Henceforth, the density of water (ρ_w) considered as 1.0 Mg/m³. Further analysis of swelling pressure test results in this chapter are based on $\rho_w = 1.0 \text{ Mg/m}^3$.

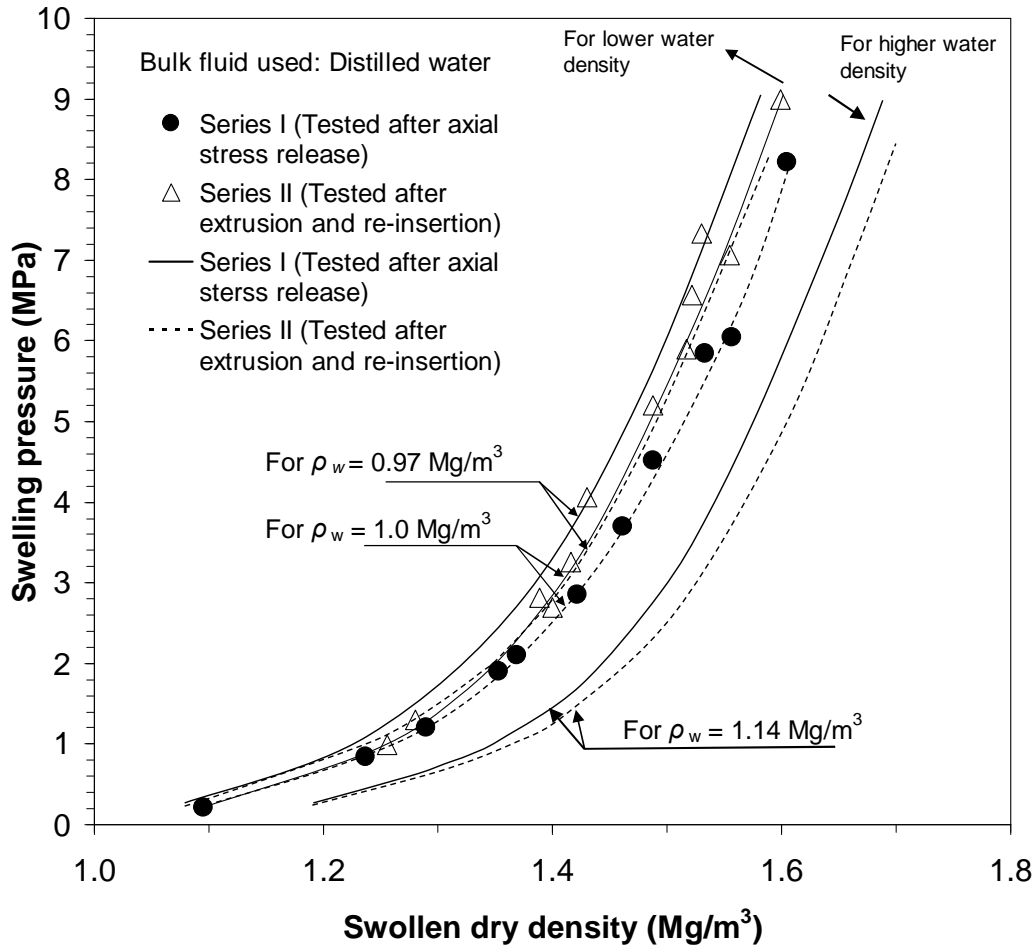


Figure 4.8. Effect of density of water on dry density-swelling pressure relationship.

4.7.4 Influence of electrolyte concentration on swelling pressure

Figure 4.9 shows the swelling pressures of the specimens in test series III and IV that were hydrated with 0.1 M and 1.0 M NaCl. The swelling pressures test results for test series II are also shown in Fig. 4.9 for comparison. The specimens tested in series II, III and IV had similar stress history and hence the test results are comparable. An increase in electrolyte concentration of bulk fluid clearly affected the swelling pressures of the specimens at swollen dry densities less than 1.60 Mg/m^3 . The test results are concurrent with the results reported by several researchers in the past (Pusch, 1982; Karnland et al., 2006, 2007; Komine et al., 2009).

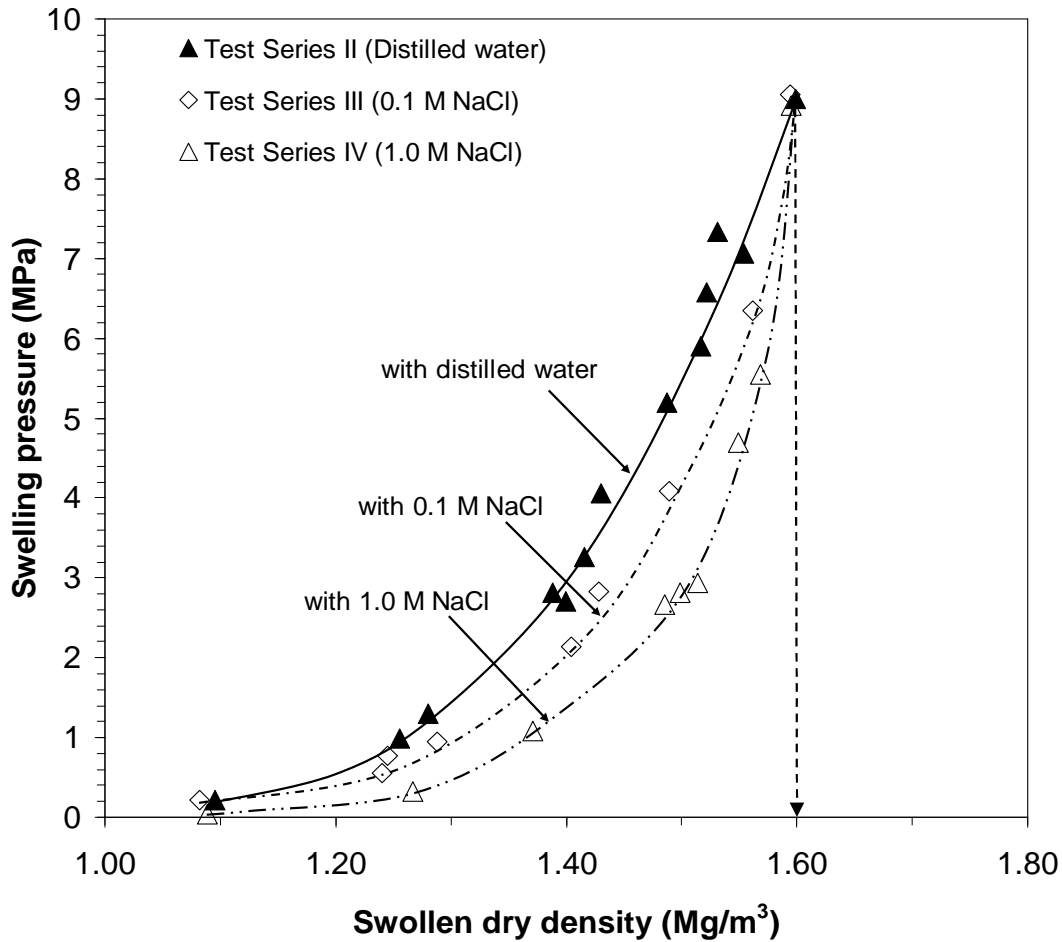


Figure 4.9. Influence of bulk solution type on swelling pressure.

Comparing the swelling pressures exhibited by the specimens with distilled water, reductions in the swelling pressure were found to be about 33% for 0.1 M NaCl and 66% for 1.0 M at a dry density of about 1.25 Mg/m^3 . Similarly, a reduction in the swelling pressure was about 21.5% for 0.1 M and 48% for 1.0 M NaCl at a dry density of about 1.50 Mg/m^3 as compared to the swelling pressure of the bentonite with distilled water. Figure 4.9 shows that at a dry density of 1.60 Mg/m^3 , all the specimens tested exhibited very nearly similar swelling pressures (shown as the dotted line). The swelling pressures exhibited by the specimens hydrated with different bulk fluids were similar at lower (1.10 Mg/m^3) and higher (1.60 Mg/m^3) dry densities.

The reduction in swelling pressure may be attributed to suppression of diffusion double layer (Verwey and Overbreek, 1948; van Olphen, 1977; Pusch, 1982; Mitchell, 1993) due to an increase in electrolyte concentration of the bulk fluid. At higher dry densities, the swelling mechanism is governed by hydration of cations and the diffuse double layer swelling is not very significant (Verwey and Overbreek, 1948; van Olphen, 1977). Therefore, at dry density of 1.60 Mg/m^3 all the specimens exerted similar swelling pressure.

4.7.5 Saturated water content after swelling pressure tests at ambient temperature

The water contents at the end of swelling pressure tests for series I, II, III, and IV (Columns (5) and (7) of Tables 4.3 and 4.4) are plotted against the corresponding swollen dry densities in Fig. 4.10. The water contents of the specimens against dry densities were calculated based on the density of water as 1.0 Mg/m^3 . For any dry density the corresponding void ratio was calculated knowing the density of water and the density of soil solids using eq. (4.3). Knowing the void ratio and the density of soil solids, the saturated water content was calculated using eq. (4.1). The water contents of the specimens after swelling pressure tests was found to decrease with an increase in the swollen dry density for all the tests.

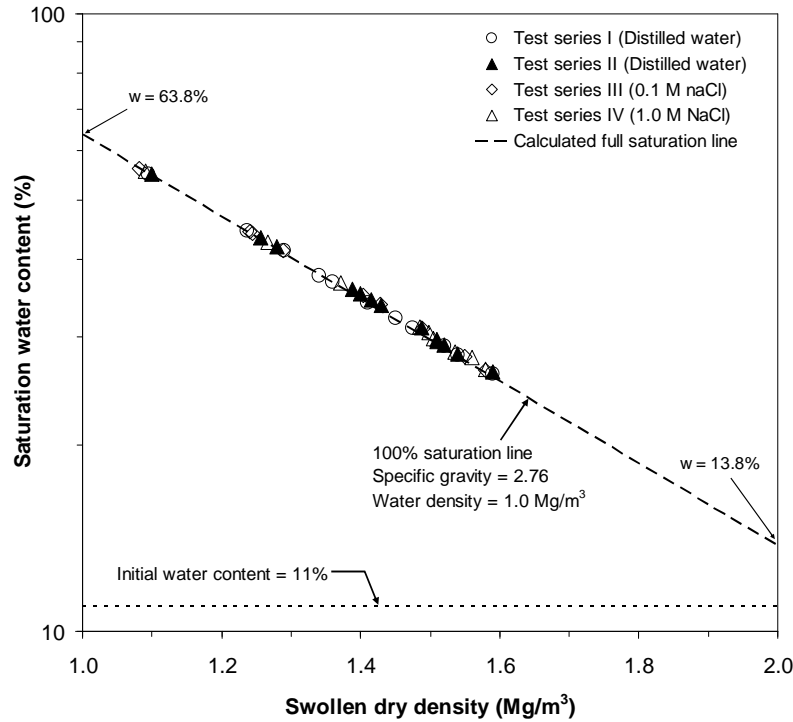


Figure 4.10. Swollen dry density versus water content of the specimens for series I, II, III, and IV tests.

The saturated water contents of the specimens varied between 26 and 56% for a range of dry density considered in this study. Considering the density of water as 0.97 Mg/m^3 , the calculated saturation water contents varied between 13.4% and 61.9% for a range of dry density between 1.0 and 2.0 Mg/m^3 , whereas the saturation water contents varied between 15.7% and 72.7% for the same dry densities when the density of water considered was 1.14 Mg/m^3 .

The swollen water contents of the specimens in series I were about 2.5 – 3.0% greater than that for test series II at dry densities greater than about 1.25 Mg/m^3 . Higher water contents and lesser swelling pressures for series I specimens indicated that at any dry density, the volumes of the interaggregate pores were more (Sridharan et al., 1971; Delage et al.,

2006) as compared to that of the specimens tested in series II, comparison being made at similar dry densities.

The saturated water contents for the specimens exposed to 1.0 M NaCl were found to be lesser than that for specimens in series II and III tests. The results clearly suggested that for compacted bentonites exposed to various concentration of NaCl solutions, at any dry density the variation in the water content is within about 0 to 3.5% for the range of swollen dry densities between 1.10 to 1.60 Mg/m³.

The swelling pressures and water content results indicated that suppression of the electrical double layer (Verwey and Overbeek, 1948; van Olphen, 1977; Pusch, 1982; Mitchell, 1993) occurs due to an increase in the ionic concentration of the bulk fluid at low dry densities that was manifested on the reduction in the swelling pressures of the specimens. However, it is hypothesized that its influence is only restricted on the boundary of aggregate pores that expanded due to the collapse of the interlayer pores accommodating an equivalent increased amount of the fluid within the interaggregate pores. At very high dry densities (= 1.60 Mg/m³) the effect was different since the swelling mechanism followed is only due to the hydration of cations and overlapping of the Stern layers (Verwey and Overbeek, 1948; van Olphen, 1977). Therefore, all the specimens tested absorbed nearly similar water contents.

4.7.6 Influence of temperature on swelling pressure

In order to study the effect of temperature on swelling pressure of compacted bentonites, several swelling pressures tests were conducted at an elevated temperature of 70

°C. The specimen condition and the experimental program are presented in Table 4.1. Three series of tests were conducted at an elevated temperature of 70 °C described as series V (5 tests), series VI (4 tests) and series VII (5 tests) tests. The swelling pressure tests were carried out after extrusion and re-insertion of compacted bentonite specimens. In series V tests, the bentonite specimens were hydrated using distilled water. Test series VI and VII were conducted by saturating the specimens using 0.1 M and 1.0 M NaCl solutions.

After specimen preparation was over, the bentonite specimens were placed in specimen chamber of the modified oedometer (Fig. 3.12). The entire device was transferred to a 50 kN capacity load frame. The load cell was attached on top of the loading plunger and the heater was connected to electric power. The electric heater was switched on for conducting the tests at an elevated temperature of 70 °C. Once the temperature of the heater reached the equilibrated (within about 20 minutes), fluid was supplied to hydrate the bentonite specimens. The swelling pressures were then monitored with elapsed time.

4.7.6.1 Time-swelling pressure plot at elevated temperature of 70 °C

The time versus swelling pressure plots for series V, VI and VII tests at swollen dry density of 1.43 Mg/m³ are shown in Fig. 4.11. The time required to attain the equilibrium swelling pressure for the tests conducted with distilled water and 0.1 M NaCl solutions were about 7-10 days. Note that the swelling pressures at ambient temperature also equilibrate in about 7-10 days. It was noted that the specimens tested at a temperature of 70 °C and saturated with 1.0 M NaCl solution attained equilibrium swelling pressures at significantly lesser elapsed time.

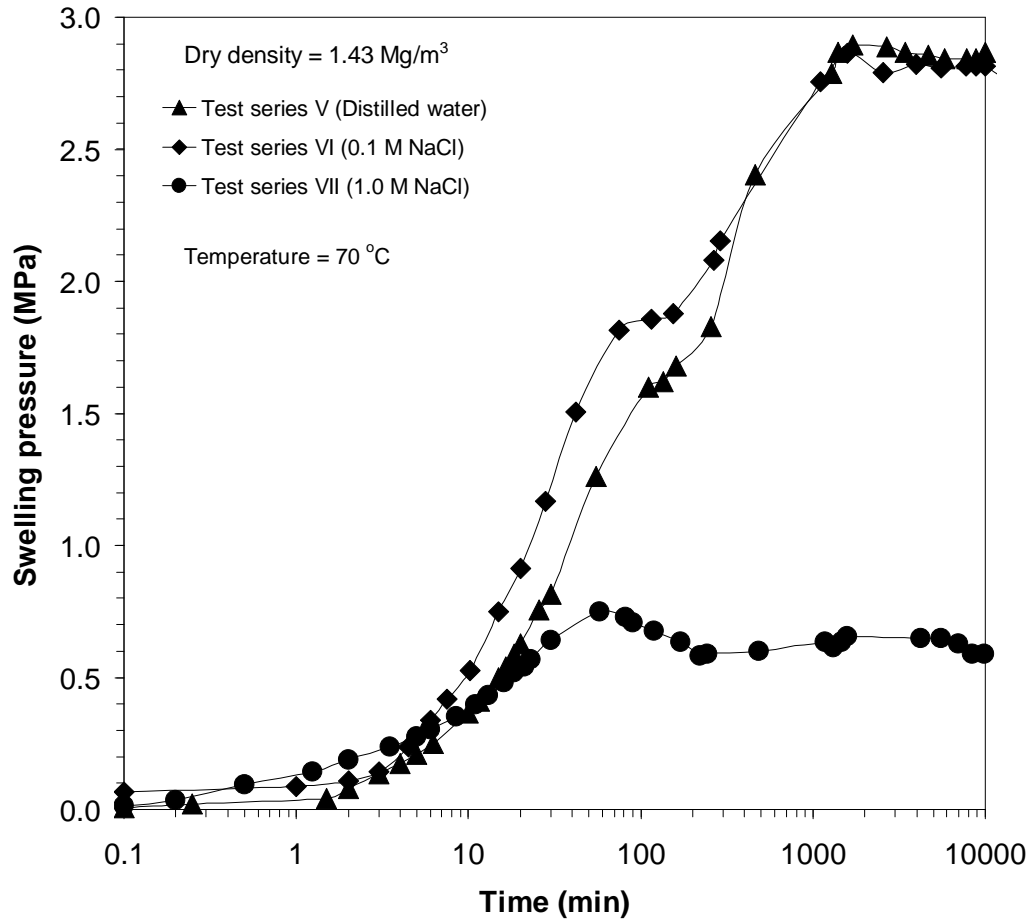


Figure 4.11. Time swelling pressure plots for series V, VI and VII tests.

4.7.6.2 Swelling pressure test results at elevated temperature of 70 °C

A summary of swelling pressure results for series V (distilled water, 70 °C), VI (0.1 M NaCl, 70 °C) and VII (1.0 M NaCl, 70 °C) are presented in Table 4.5. The specimen preparation history, the dry densities of the specimens after release of static load, the dry densities of the specimens after extrusion and re-insertion processes, the swollen dry densities, the measured swelling pressures and the water contents at the end of swelling pressure tests are presented in Table 4.5. The maximum and minimum obtained in series III tests swelling pressures were 9.14 MPa and 0.73 MPa.

Table 4.5 Summary of swelling pressure test results for series V, VI and VII tests

Test series (Bulk fluid used)	Specimen preparation history	Dry density after release of static load (Mg/m ³)	Dry density after extrusion and re-insertion (Mg/m ³)	Swollen dry density (Mg/m ³)	Swelling pressure (MPa)	Water content at the end of swelling pressure test (%)
(1)	(2)	(3)	(4)	(5)	(6)	(7)
V (distilled water)	Static load released, specimen extruded and re-inserted into the oedometer ring	1.56	1.49	1.39	2.15	35.8
		1.65	1.61	1.42	2.77	34.1
		1.62	1.58	1.43	2.90	33.7
		1.74	1.70	1.51	5.11	30.0
		1.86	1.83	1.58	7.36	27.0
VI (0.1 M NaCl)	Static load released, specimen extruded and re-inserted into the oedometer ring	1.53	1.50	1.38	1.40	36.4
		1.62	1.58	1.44	2.86	33.0
		1.76	1.70	1.52	4.19	29.7
		1.87	1.79	1.59	7.20	26.7
VII (1.0 M NaCl)	Static load released, specimen extruded and re-inserted into the oedometer ring	1.55	1.50	1.44	0.74	33.4
		1.61	1.59	1.54	1.88	28.9
		1.66	1.61	1.52	1.92	29.7
		1.78	1.72	1.59	4.35	26.7
		1.88	1.85	1.66	9.13	24.0

Comparison between the swelling pressures measured at ambient and elevated temperatures using distilled water, 0.1 M NaCl and 1.0 M NaCl solutions as bulk fluids are shown in Figs. 4.12, 4.13 and 4.14. Note that the final dry densities of the specimens calculated considering the density of water as 1.0 Mg/m³.

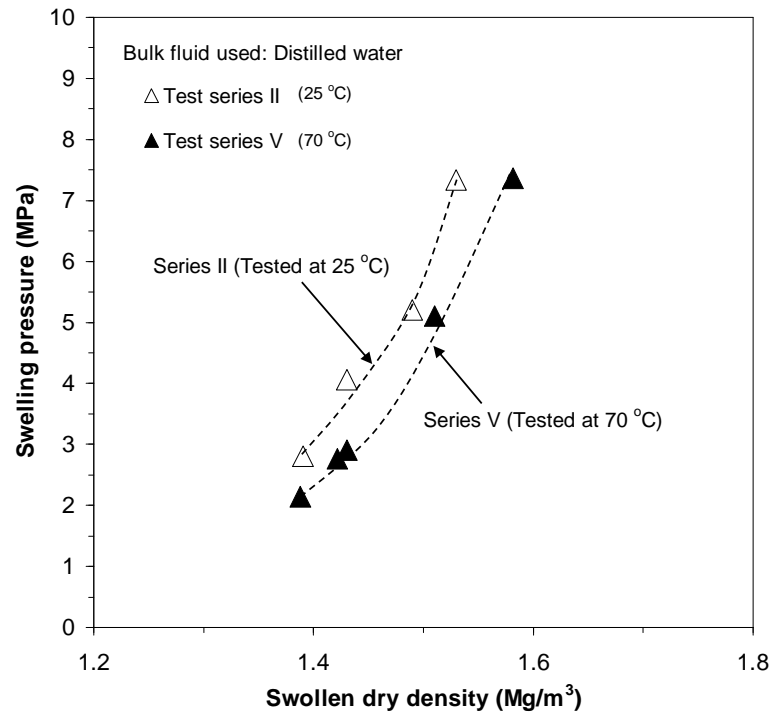


Figure 4.12. Comparison of swelling pressures measured at ambient and elevated temperatures using distilled water as bulk fluid.

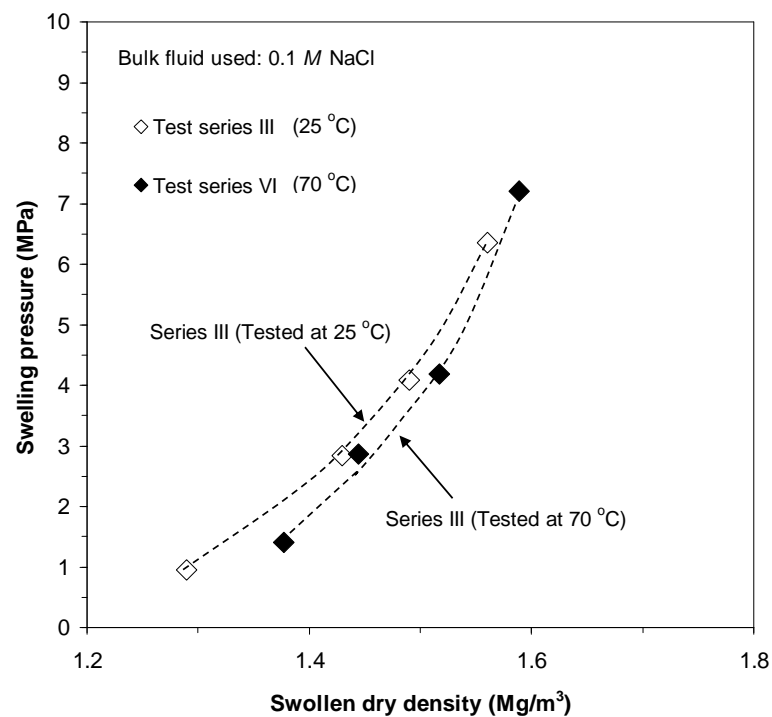


Figure 4.13. Comparison of swelling pressures measured at ambient and elevated temperatures using 0.1 M NaCl solution as bulk fluid.

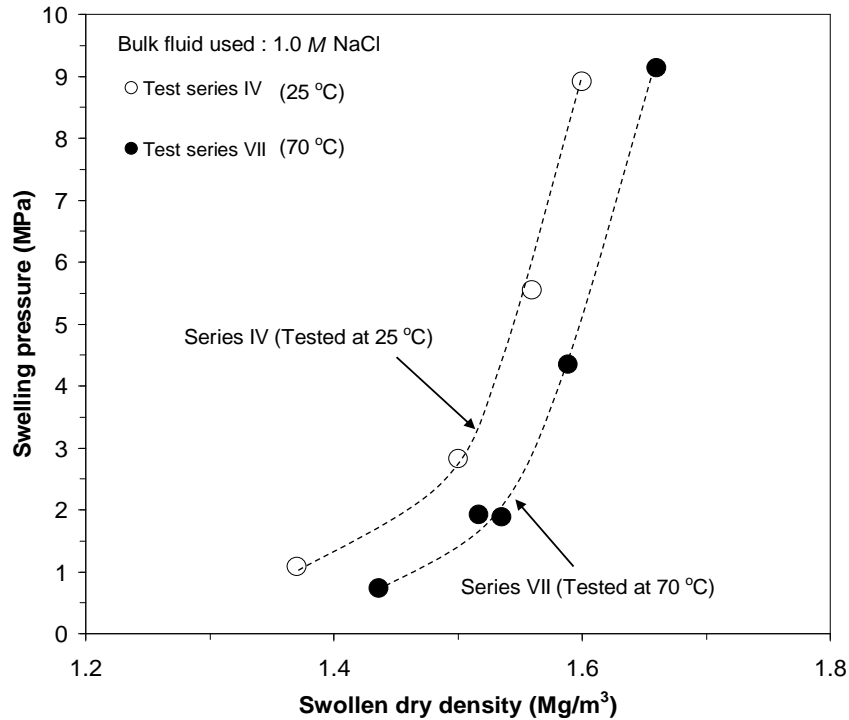


Figure 4.14. Comparison of swelling pressures measured at ambient and elevated temperatures using 1.0 M NaCl solution as bulk fluid.

The swelling pressures measured at an elevated temperature of 70 °C were lesser than the swelling pressures measured at ambient temperature (25 °C) at equal swollen dry densities of the specimens. The effect of temperature was significant for series VII tests. Similar results were reported by several researchers in the past (Pusch, 1980; Villar and Lloret, 2004; Romero et al., 2005).

Mitchell (1993) stated that an increase in the temperature increases the diffuse double layer thickness between clay platelets, decreases the surface potential and the dielectric constant of pore fluid. The combined effect of an increase in the diffuse double layer thickness and decrease in surface potential and dielectric constant resulted in development of lesser swelling pressure of MX80 bentonite at an elevated temperature of 70 °C.

4.7.6.3 Saturated water content after swelling pressure tests at elevated temperature

The measured water contents against the swollen dry densities of the specimens for series V, VI and VII tests are plotted in Fig. 4.15. The measured water contents of the specimens after swelling pressure tests are plotted against the calculated dry densities considering the density of water as 1.0 Mg/m^3 .

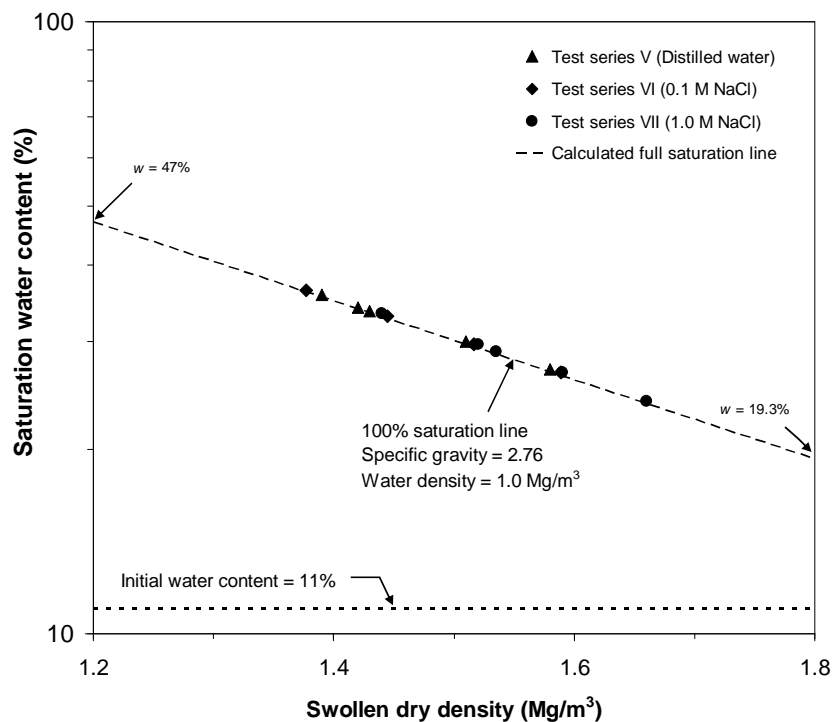


Figure 4.15. Swollen dry density versus saturated water contents for series V, VI and VII tests.

The water contents measured after dismantling the swelling pressure tests conducted at a temperature of 70°C were found to be lesser than the water contents measured after swelling pressure tests conducted at a temperature of 25°C . The least water content for the specimens tested at room temperature was found to be 26.1% (Series IV), whereas the least water content for the specimens tested at a temperature of 70°C was 24% (series VII). Bayer

and Winterkorn (1936) stated that an increase in the temperature increases the kinetic energy of the water molecules and reduces the hydration of the particles.

4.8 Concluding remarks

The effects of post compaction residual stress, electrolyte concentration and temperature on swelling pressure of compacted MX80 bentonite is brought out in this chapter. The extrusion and re-insertion processes of the compacted bentonite specimens, stress history of the compacted bentonite specimens prior to testing, calculation of swollen dry density of the specimens are presented. The results of swelling pressures tests conducted at ambient and elevated temperature using distilled water, 0.1 M NaCl and 1.0 M NaCl as bulk fluids are presented. The measured water contents of specimens after swelling pressure tests are shown. The following concluding remarks can be made from the study.

Compacted bentonite specimens with post compaction residual stress exhibited about 8 to 25% less swelling pressures as compared to their stress released counterparts for the range of swollen dry density between 1.25 and 1.60 Mg/m³. The difference in the swelling pressures of specimens with and without post compaction residual stresses can be attributed to differences in structure and fabric owing to applied compaction loads during preparation of the specimens. The test results showed that in repository conditions compacted bentonite bricks or pellets may exhibit greater swelling pressures than that have been reported by several researchers.

The influence of higher NaCl concentration in the bulk fluid was found to reduce the swelling pressures of compacted bentonite specimens with dry densities between 1.20 to 1.55 Mg/m³. The reduction in swelling pressure is attributed to suppression of electrical double

layer at lower dry densities. At higher dry densities, the swelling mechanism is only due to the hydration of cations and overlapping of the Stern layers (van Olphen, 1977). Therefore, the effect of electrolyte concentrations on the swelling pressures of compacted bentonites at higher dry densities was negligible.

An increase in the temperature reduced the swelling pressure of compacted specimens on account of reduction in dielectric constant of pore fluid and surface potential of bentonites (Mitchell, 1993). The swelling pressure measured at elevated temperature had significantly decreased when the specimens were saturated with 1.0 M NaCl solution. These test results are for specimens devoid of post compaction residual lateral stresses. The trend is similar to what has been reported in the literature for the specimens tested with post compaction lateral stresses.

Chapter 5

Swelling pressure of compacted bentonite from physico-chemical considerations

5.1 Introduction

The experimental swelling pressure results obtained from constant volume swelling pressure tests are presented in chapter 4. In this chapter, the dry density-swelling pressure relationship of compacted MX80 bentonite was established from physico-chemical considerations. The main objective of the study was to compare the experimental and theoretical dry density-swelling pressure relationships and bring out the applicability of the diffuse double layer and the Stern theory in assessing swelling pressures of compacted bentonites.

In this chapter, the equations used to determine the electrical charge and potential distribution and the procedure used to establish the dry density-swelling pressure and vertical pressure-void ratio relationships in clay-water-electrolyte systems for interacting clay platelet systems are presented. The equations are presented following the Stern theory and the diffuse double layer theory as given by Verwey and Overbreek (1948). The experimental swelling pressure results presented in chapter 4 are compared with the theoretical results obtained from the diffuse double layer and the Stern theory. The analysis was carried out considering the constant surface potential method (Verwey and Overbreek, 1948). The influence of various parameters on the dry density-swelling pressure and the vertical pressure-void ratio relationships were also studied.

In section 5.2, the Stern theory for interacting clay platelet system is presented. The procedure used to establish the pressure-void ratio and the dry density-swelling pressure relationship is described. The Gouy-Chapman diffuse double layer theory for constant surface potential case is presented in section 5.3. The parameters chosen for analysis are presented in section 5.4. An example calculation to establish the dry density-swelling pressure relationship from the Stern theory is presented. Section 5.5 presents the effect of various parameters on the vertical pressure-void ratio and the dry density-swelling pressure relationships and comparisons between the experimental and the theoretical dry density-swelling pressure relationships for compacted MX80 bentonite. The concluding remarks from this chapter are presented in section 5.6.

5.2 Stern theory for interacting clay platelet systems

Clay particles carry net negative charges on their surfaces due to isomorphous substitution in their crystal lattice (Mitchell, 1993). Exchangeable cations present in the clay media are attracted to these negative charges. The negatively charged surfaces of the clay platelets, the water, and the ions in the clay media, form an electrical double layer around the clay platelets. Stern (1924) proposed that the finite size of the ions (either hydrated or not), limits the closest approach of a counter-ion to the charged clay surfaces. Therefore, the concentration of ions near the clay surface is appreciably lesser as compared to that calculated by treating the ions as point charges.

The salient features of Stern and Gouy layer and charge distribution in clay-water electrolyte system are presented in Fig. 2.9. The application of the Stern theory in geotechnical engineering is presented in section 2.9. A review of literature suggested that there are two approaches of analysis using the Stern theory; (i) constant surface potential method and (ii) constant surface charge method. In the current investigation, the constant surface potential method was adopted.

5.2.1 Charge and potential distribution

The electrical charge and electrical potential distributions in a clay-water electrolyte system can be calculated from the Stern theory as applicable to interacting clay platelet systems. Verwey and Overbeek (1948) used the following equations (eqs. (5.1) to (5.6)) to establish the relationship between electrical charge, potential and the distance between clay platelets based on the constant surface potential.

$$\sigma = \frac{\varepsilon' \varepsilon_0}{\delta} (\psi_0 - \psi_\delta) \quad (5.1)$$

$$\sigma_1 = \frac{N_1 v e'}{1 + \frac{N_A \rho_w}{M n_0} e^{-\left(\frac{v e' \psi_\delta + \phi}{kT}\right)}} \quad (5.2)$$

$$\sigma = \sigma_1 + \sigma_2 \quad (5.3)$$

$$\sigma_2 = \sqrt{2 n_0 k T \varepsilon_0 D} \sqrt{2 \cosh z_\delta - 2 \cosh u_d} \quad (5.4)$$

$$z_\delta = \frac{v e' \psi_\delta}{kT} \quad (5.5)$$

$$u_d = \frac{v e' \psi_d}{kT} \quad (5.6)$$

where ε' is the dielectric constant of pore fluid in the Stern layer, ε_0 is the permittivity of a vacuum ($= 8.85 \times 10^{-12} \text{ C}^2 \text{J}^{-1} \text{m}^{-1}$), N_1 is the number of adsorption spots per m^2 area of surface (ions/ m^2), v is the valence of exchangeable cations, e' is the electrical charge ($= 1.6 \times 10^{-19} \text{ C}$), N_A is the Avogadro's number ($= 6.023 \times 10^{23}$ ions/mol), ρ_w is the density of solvent (Mg/m^3), ϕ is the specific adsorption potential (eV or Joules), k is the Boltzmann's constant ($= 1.38 \times 10^{-23}$ Joule/Kelvin), T is the absolute temperature in Kelvin, M is the molecular wt of solvent (Mg/mol), n_0 is the concentration of bulk fluid (ions/ m^3), D is the dielectric constant of bulk fluid ($= 80.4$ for water), z_δ is the

nondimensional potential function at the Stern plane, u_d is the nondimensional potential function in the Gouy-layer and ψ_d is the electrical potential in the Gouy-layer (V).

For a given value of ε' and a predetermined value of ψ_0 , σ is calculated from eq. (5.1) by varying the value of ψ_δ . For known bulk fluid properties and temperature, the chosen values of ψ_δ must be such that the calculated charge in the Stern-layer (σ_1) from eq. (5.2) will produce a positive charge in the Gouy-layer (σ_2) and also must satisfy the charge electroneutrality condition (i.e., eq. (5.3)). Knowing σ_2 from eq. (5.3) and for any suitable value of ψ_δ and z_δ from eq. (5.5), u_d can be calculated from eq. (5.4) and ψ_d from eq. (5.6).

5.2.2 Relationships of ψ_δ , ψ_d , σ , σ_1 and σ_2 with d

The diffuse double layer theory for interacting clay platelets is used to establish relationship between the midplane potential (u_d) and the distance function (Kd) (Verwey and Overbeek, 1948; van Olphen, 1977; Sridharan and Jayadeva, 1982; Tripathy and Schanz, 2007). The difference between the Gouy-Chapman diffuse double layer theory (without Stern-layer) and the Stern theory is on account of two important changes dealt with in the latter; (i) shifting of the start of the Gouy-layer by a thickness equal to the Stern-layer thickness (Fig. 2.6) and (ii) only a fraction of the total charge becomes available in the Gouy-layer (σ_2) that influences u_d . The resulting second integral of the Poisson-Boltzmann equation with interacting double layer boundary conditions (i.e., with integral limits $d - \delta$ and d) can be used to relate u_d (or ψ_d) and z_δ (or ψ_δ) to the distance function, Kd (Verwey and Overbeek 1948) (i.e., eq. (5.7)). Knowing K from eq. (5.8), d

can be determined. Therefore, the relationships of ψ_δ , ψ_d , σ , σ_1 and σ_2 with d can be established using eqs. (5.1) to (5.8).

$$\int_{z_\delta}^{u_d} \frac{1}{\sqrt{(2 \cosh y - 2 \cosh u_d)}} dy = - \int_{(d-\delta)}^d d\xi = -Kd \quad (5.7)$$

where K is the double layer parameter given as

$$K = \left(\frac{2n_0 e^2 v^2}{\epsilon_0 DkT} \right)^{1/2} \quad (5.8)$$

where y is the nondimensional potential at distance x from the Stern plane, d is the half the distance between parallel clay platelets (m) and ξ is the distance function equal to Kx .

5.2.3 Dry density-swelling pressure and vertical pressure-void ratio relationships

Bolt (1956) stated that the swelling pressure is the difference between the osmotic pressure in the central plane between two clay platelets and the osmotic pressure in the equilibrium solution. Equations (5.9) and (5.10) can be used to determine the pressure and the void ratio, respectively for interacting clay platelet systems (Verwey and Overbeek, 1948; Bolt, 1956; van Olphen, 1977). In eq. (5.9), p is the repulsive pressure (i.e., the osmotic pressure or the swelling pressure at the central plane of two parallel clay platelets) in (N/m²). The values of u_d calculated from eq. (5.4) can be used to determine the swelling pressures for known bulk fluid properties. Equation (5.10) proposed by Bolt (1956) is the interrelationship between the half-distance between parallel clay platelets

(d), the specific surface ($S \text{ m}^2/\text{g}$), the specific gravity of soil solids (G_s) and the void ratio (e) of the clay. For a known swelling pressure (p), the dry density (ρ_d) can be determined from eq. (5.11) where ρ_w is the density of water.

$$p = 2n_0kT(\cosh u_d - 1) \quad (5.9)$$

$$e = G_s \rho_w s d \times 10^6 \quad (5.10)$$

$$\rho_d = \frac{G_s}{1 + e} \rho_w \quad (5.11)$$

5.3 Gouy-Chapman diffuse double layer theory (constant surface potential case)

In case of the Gouy-Chapman diffuse double layer theory with constant electrical potential at the surfaces of the clay platelets (Verwey and Overbeek, 1948), the Stern layer is ignored and hence eqs. (5.1) - (5.3) are not required. The surface potential, ψ_0 , being a constant value, z (i.e., the nondimensional potential function at the surfaces of the clay platelets) can be calculated from eq. (5.12). This will be a unique value for given values of ψ_0 , v and T . For any assumed value of p , T and known bulk fluid properties, u_d can be calculated using eq. (5.9). Equation (5.7) can be used by replacing z_δ with z between limits of integration zero and d to determine Kd . In this case, the distance, d , becomes the clear distance from the surface of the clay platelets to the midplane between two parallel clay platelets. Once Kd is known and K from eq. (5.8), d can be calculated and e from eq. (5.10). Therefore, for any given vertical pressure, the void ratio of the clay can be determined. It is also possible to calculate the corresponding vertical pressures for

a set of assumed d values using the equations available. Note that the fabric effect is not considered in the diffuse double layer theory and the Stern theory. Therefore, swelling pressure in compacted systems and vertical pressure in consolidation tests are treated equally. Equation (5.13) is only used when determination of the total charge is of interest.

$$z_\delta = \frac{ve\psi_0}{kT} \quad (5.12)$$

$$\sigma = \sqrt{8nkT\epsilon D} \sqrt{2 \cosh z_\delta - 2 \cosh u_d} \quad (5.13)$$

Note that for the constant surface potential case, consideration of the specific surface area is only required while determining the void ratio using eq. (5.10) and is not at all used while establishing vertical pressure versus d relationship (i.e., eqs. (5.1) to (5.9)). Similarly, the total cation exchange capacity of the clay is not used in the Stern theory, whereas information on the valence of exchangeable cation is required at various stages of calculation.

5.4 Choice of parameters for theoretical calculations

5.4.1 Surface potential (ψ_0)

The electrical potential at the surfaces of clay particles can be determined by several currently available methods (van Olphen, 1954; Low, 1981; Miller and Low, 1990; Zhang et al., 1994; Sposito, 2008; Hou et al., 2009; Li et al., 2009), such as based on the surface charge, negative ionic adsorption measurements, zeta potential

measurements, ionic concentration equilibrium based on the diffuse double layer theory, and based on the chemical reactions at the surface and at various planes. Verwey and Overbeek (1948) and van Olphen (1954) stated that the calculated ψ_0 based on the specific surface and cation exchange capacity (i.e., based on the surface charge) is unusually a high value for hydrophobic colloids. Verwey and Overbeek (1948) considered a constant surface potential value of 200 mV. Li et al. (2009) shown that the surface potential of montmorillonites may vary between 257 mV and 297 mV. The above studies clearly indicated that the surface potential for montmorillonites may vary between 200 mV to about 300 mV, the latter being the upper limit.

5.4.2 Stern layer thickness (δ)

Verwey and Overbeek (1948) and van Olphen (1977) stated that σ_1 is concentrated at a distance of about 0.5 nm from the surface of the clay platelets. Shang et al. (1994) stated that δ may vary between 0.5 and 0.6 nm. Sridharan and Satyamurty (1996) considered δ equal to the hydrated ionic radii of exchangeable cations. Sposito (2008) stated that the type of exchangeable cations, the distribution of charge and the size and shape of the siloxane cavity formed on the surface of montmorillonite influence the cation adsorption. In general, the diameter of siloxane cavity is about 0.26 nm (Sposito, 2008). Note that the value of δ will influence the close approach of two interacting double layers and the minimum void ratio up to which the Stern theory can be applied. Partial hydration and unhydrated status of exchangeable cations in the Stern-layer have been discussed by van Olphen (1954) and Grim (1968). These considerations along with the consideration of the inner sphere complex (i.e., cations residing close to the surface and not separated by

water molecules or in the inner Helmholtz plane) (Sposito, 2008) support the choice of the thickness of the Stern-layer equal to about 0.5 nm.

5.4.3 Dielectric constant of fluid within Stern layer (ϵ')

The dielectric constant of the pore-fluid (ϵ') in the Stern-layer depends upon the water content of clays (Sridharan, 1968) and surface charge properties of clay particles (Shang et al. 1994). Sridharan (1968) stated that the ϵ' of the fluid next to the clay minerals is about 3. Based on an extensive literature review, Shang et al. (1994) stated that ϵ' may vary between 4 and 8, whereas Sridharan and Satyamurty (1996) stated that ϵ' may vary between 3 and 6. Verwey and Overbeek (1948) considered $\epsilon' = 6.5$, whereas van Olphen (1977) and Sridharan and Satyamurty (1996) considered $\epsilon' = 6$. Hunter (1981) stated that the limiting value of ϵ' is about 6. It appears from these studies that the lower and upper limits of ϵ' are 3 and 8, respectively. Since the total charge according to eq. (5.1) depends upon ϵ' and ψ_0 , the influence of these parameters on the pressure-void ratio relationship of bentonite needs further investigation.

5.4.4 Other parameters (ν , n_0 , and ϵ_0)

Extensive studies have been reported on the compressibility and swelling pressure of montmorillonites as affected by ν , n_0 , and ϵ_0 (Bolt, 1956; Mesri and Olson, 1971; Sridharan and Rao, 1973; Sridharan and Jayadeva, 1982; Bucher and Müller-Vonmoos, 1989). A decreasing order of the reported experimental compressibility curves with an increase in n_0 and ν has been noted to be concurrent with the predictions from the Gouy-Chapman diffuse double layer theory (without the Stern-layer and with constant charge at

the surfaces of the clay platelets). At low vertical pressures or high void ratios, it may be expected that the influence of these parameters on the results with an inclusion of the Stern-layer will be similar. On the other hand, Verwey and Overbeek (1948) and van Olphen (1954) showed that with a decrease in the platelet distance and for constant electrical potential at the surfaces of the clay platelets, the electrical potential increased with an increase in n_0 and v .

Experimental results showing crossing of the compressibility curves of bentonites with higher n_0 to that of bentonites with lower n_0 and crossing of the compressibility curves of higher valent bentonites to that of bentonites of lower valence have been reported by only a few researchers. Bucher and Müller-Vonmoos (1989) have shown that at very high compaction dry densities, Montigel bentonite (a divalent-rich German bentonite) exhibited greater swelling pressures than Na-rich MX80 bentonite. Laboratory compressibility tests results reported by Marcial et al. (2002) for various bentonites showed that with an increase in the applied vertical pressure, the void ratio of a divalent rich bentonite (Ca-Fourges) remained higher than that of Na-rich bentonites (Na-Ca MX80 and Na-Kunigel bentonites).

A number of examples have been discussed in the literature by considering $\phi = 0$ for calculating the electrical charge in the Stern-layer (Verwey and Overbeek, 1948; van Olphen, 1977; Shang et al., 1994; Sridharan and Satyamurty, 1996). Verwey and Overbeek (1948) stated that the properties of ions and the wall material are responsible for the Stern-layer thickness and the adsorption potential. van Olphen (1954) stated that the clay platelets do not spontaneously dissociate in solution despite the high charge density of the surfaces. Therefore, a considerable specific adsorption potential of the

exchangeable ions to surfaces of the clay platelets may be expected. Sposito (2008) stated that the inner-sphere surface complex mechanisms are likely to involve both ionic and covalent bonding. A review of literature on the microstructure of saturated bentonites reported by Marcial et al. (2002) indicated that the number of stacked clay platelets that are usually formed at very high water contents (suction = 3.2 kPa) depends upon the type of exchangeable cations present in the bentonite. Verwey and Overbeek (1948) and Sridharan and Satyamurty (1996) studied the influence ϕ on the electrical charge and Stern potential for single clay platelet systems. No studies available at this stage on the influence of ϕ on the swelling pressures for interacting clay platelet systems.

Based on the previous studies, the thickness of the Stern-layer (δ), the dielectric constant of pore fluid in the Stern-layer (ε'), the electrical potential at the surface of the clay (ψ_0) and the specific adsorption potential (ϕ) were considered for theoretical calculations. The thickness of the Stern layer considered for theoretical calculation was 0.5 nm. The effect of ε' on the pressure-void ratio (e -log p) and dry density-swelling pressure relationship were studied for $\varepsilon' = 3, 6.5$ and 8 . The specific adsorption potential (ϕ) was considered as $0, 0.05$ and 0.1 mV for parametric studies. The surface potential (ψ_0) was considered as 300 (0.3 V), 250 (0.25 V) and 200 mV (0.2 V).

5.5 Results and discussion

This section presents the parameters used to establish the dry density-swelling pressure relationships of bentonite from the diffuse double layer theory and the Stern theory. The itemised results from the diffuse double layer theory and the Stern theory are presented. An example calculation to establish the dry density-swelling pressure

relationship from the Stern theory is shown. The total surface charge (σ), the Stern-layer charge (σ_1), the Gouy-layer charge (σ_2), the swelling pressures (p), void ratio (e) for $2d$ varying from 1.0 to 10.0 nm were calculated from the Stern theory following eqs. (5.1) to (5.11). The parameters used for calculations are shown in Table 5.1. Note that for the case of constant potential at the surfaces of clay platelets, the specific surface is not required for determination of the charges and the potentials. Table 5.2 presents the itemised results from the Stern theory.

Table 5.1 Parameters used to establish relationships between electrical charge and electrical potential with $2d$

Parameters	Values
ε'	6.5
D	80.4
ψ_0	0.3 V or 300 mV
δ (nm)	0.5
N_1 (ions/m ²)	4.0×10^{17}
ν	1.0
ρ_w (Mg/m ³)	1.0
M (Mg/mol)	18.0
n_0 (moles/m ³)	0.1
φ (eV)	0
T (K)	298

The total surface charge, the Gouy-layer potential, the void ratio, and the dry density were calculated from the Gouy-Chapman diffuse double layer theory with constant surface potential. Table 5.3 show the itemised results from the diffuse double layer theory.

Table 5.2 Determination of charges, potentials, swelling pressures and void ratios from Stern theory for interacting clay platelets ($\psi_0 = 300$ mV)

$\psi_\delta/1000$ (V) (assumed)	σ (C/m ²) from eq. (5.1)	σ_1 (C/m ²) from eq. (5.2)	σ_2 (C/m ²) from eq. (5.3)	u_d from eq. (5.4)	z_δ from eq. (5.5)	$\Psi_d/1000$ (V) from eq. (5.6)	Kd from eq. (5.7)	K (1/m) from eq. (5.8)	$2d =$ ($2Kd/K$) (nm)	$p \times 10^6$ (Pa) from eq. (5.9)	e from eq. (5.10)
266.5	0.0039	0.00345	0.00046	10.38	10.38	266.5	0.0000	3.25×10^7	1.00	8.00	1.06
248.8	0.0059	0.00181	0.00408	9.69	9.69	248.73	0.0009		1.05	4.00	1.11
231.4	0.0079	0.00093	0.00696	9.00	9.01	230.97	0.0029		1.18	2.00	1.25
224.4	0.0087	0.00071	0.00799	8.71	8.74	223.65	0.0044		1.27	1.50	1.35
215.0	0.0098	0.00050	0.00930	8.32	8.38	213.51	0.0075		1.46	1.00	1.55
210.0	0.0104	0.00041	0.01000	8.10	8.18	207.90	0.0099		1.61	0.80	1.70
203.5	0.0111	0.00032	0.01080	7.80	7.93	200.24	0.0142		1.87	0.60	1.98
195.0	0.0121	0.00023	0.01190	7.37	7.60	189.26	0.0230		2.42	0.40	2.56
185.0	0.0132	0.00016	0.01310	6.76	7.21	173.54	0.0440		3.71	0.20	3.93
176.5	0.0142	0.00011	0.01410	6.00	6.88	154.06	0.0865		6.32	0.10	6.70
172.0	0.0147	0.00009	0.01464	5.32	6.70	136.60	0.1461		10.00	0.05	10.6

Table 5.3 Determination of charge, potential, swelling pressures and void ratios from Gouy-Chapman diffuse double layer theory ($\psi_0 = 300$ mV)

$p \times 10^6$ (Pa)	u_d	$\psi_d/1000$ (V)	z	Kd	K (1/m)	$2d = 2Kd/K$	e	σ (C/m ²)
(assumed)	from eq. (5.4)	from eq. (5.6)	from eq. (5.11)	from eq. (5.7)	from eq. (5.8)	(nm)	from eq. (5.10)	from eq. (5.12)
0.05	5.32	136.50	11.690	0.1580	32496275	13.71	13.90	0.2047
0.10	6.01	154.17		0.1500		9.23	9.80	0.2045
0.20	6.70	171.90		0.1040		6.40	6.80	0.2041
0.40	7.39	189.66		0.0720		4.43	4.70	0.2034
0.80	8.08	207.44		0.0490		3.02	3.20	0.2020
1.00	8.30	217.84		0.0440		2.40	2.87	0.2013
1.50	8.71	223.57		0.0350		2.15	2.28	0.1995
2.00	9.00	230.57		0.0290		1.78	1.89	0.1978
4.00	9.69	248.74		0.0190		1.17	1.24	0.1904
6.00	10.10	259.15		0.0143		0.88	0.93	0.1828
8.00	10.38	266.53		0.0142		0.87	0.93	0.1748
10.00	10.61	272.26		0.0094		0.58	0.61	0.1665
20.00	11.30	290.05		0.0042		0.26	0.25	0.1161

An example calculation to establish the dry density-swelling pressure relationship from the Stern theory is shown here. In Table 5.2 and row five from the top. For a surface potential, $\psi_0 = 0.3$ V, $n_0 = 10^{-4}$ mol/ltr = $10^{-4} \times 1000$ mol/m³ = $10^{-4} \times 1000 \times 6.02 \times 10^{23}$ ions/m³, for an assumed $\psi_\delta = 0.215$ V, $\varepsilon' = 6.5$ and $D = 8.85 \times 10^{-12}$ C²J⁻¹m⁻¹, the total surface charge σ (Eq. (5.1)) = 0.0098 C/m².

For $N_A = 6.023 \times 10^{23}$ ions/mol, $\nu = 1$, $e' = 1.6 \times 10^{-19}$ C, $\rho_w = 1$ Mg/m³, $M = (18/1000000)$ Mg/mol, $k = 1.38 \times 10^{-23}$ Joule/Kelvin, $T = 298$ K, $\phi = 0$, the number of adsorption spots per meter square area for hydrated ionic radii of Na⁺ (ionic radii = 0.79 nm), $N_1 = 1/(0.79 \times 10^{-9})^2 = 4 \times 10^{17}$ ions/m², using eq. (5.2), the Stern-layer charge, $\sigma_1 = 0.00050$ C/m².

Replacing σ and σ_1 values in eq. (5.3), the Gouy-layer charge (σ_2) = 0.0093 C/m². Substituting σ_2 in eq. (5.4), for known parameters and $\varepsilon = 80.4$, u_d can be found as 8.32. From eq. (5.5), $z_\delta = 8.375$. Substituting these values in eq. (5.7), $p = 1000,000$ Pa = 1.0 MPa. K from the eq. (5.8) = 32496275 (1/m). The distance between clay platelets ($2d = 2Kd/K$) = 1.46 nm. Substituting d in eq. (5.10) the void ratio, $e = 1.55$ for $G = 2.65$ and $S = 800$ m²/g.

The following section presents the distribution of electrical charge and potential with distance between clay platelets in clay-water system. The effects of the valence of exchangeable cations (ν), the concentration of bulk fluid (n_0), the dielectric constant of pore fluid in the Stern layer (ε'), the specific adsorption potential (ϕ) and the electrical potential at the surface of the clay (ψ_0) on the pressure-void ratio and the dry density-swelling pressure relationships established from the Stern theory are brought out. Comparisons

between the experimental and the theoretical dry density-swelling pressure relationships of compacted MX80 bentonite are presented.

5.5.1 Charge and potential distribution

Figure 5.1 shows the total surface charge (σ), the Stern-layer charge (σ_1) and the Gouy-layer charge (σ_2) for $2d$ varying from 1.0 to 10.0 nm. The electrical potentials at the Stern-plane (ψ_δ) and at the midplane of the Gouy-layer (ψ_d) for the same range of $2d$ are shown in Fig. 5.2. The total surface charge (σ) and the midplane electrical potential (ψ_d) calculated from the Gouy-Chapman diffuse double layer theory are shown in Figs. 5.1 and 5.2, respectively for comparison.

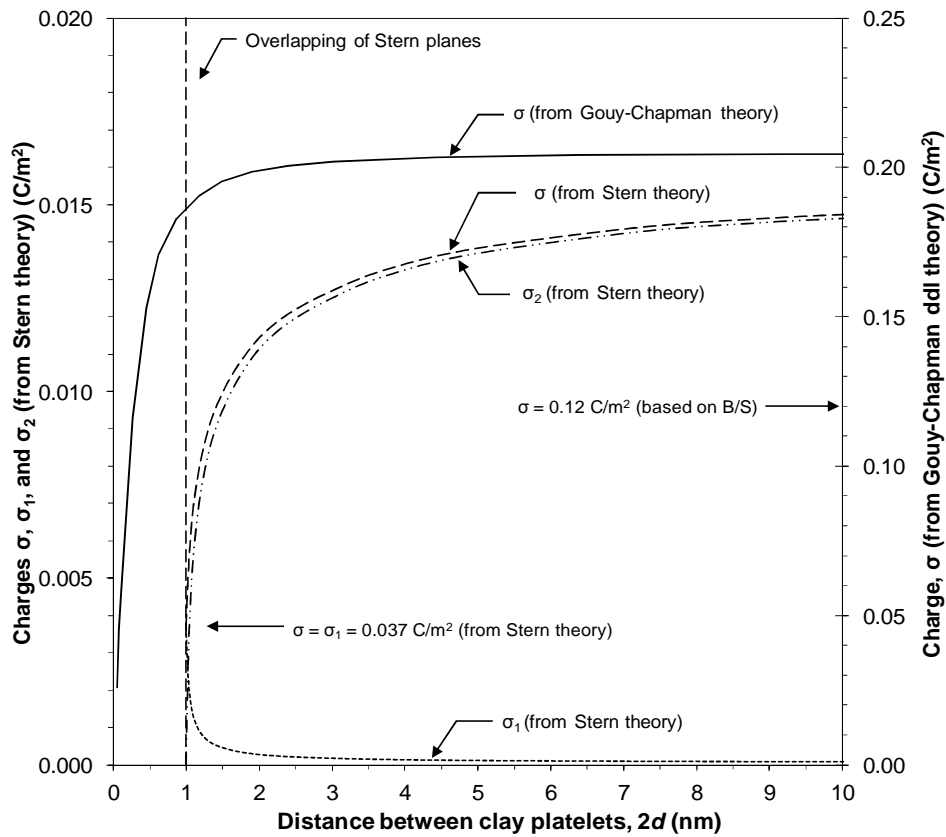


Figure 5.1. Change of charges with $2d$ from Stern theory and Gouy-Chapman diffuse double layer theory ($\psi_0 = 300$ mV).

Figure 5.1 and Table 5.2 show that both σ and σ_2 decreased, whereas σ_1 increased with a decrease of $2d$. The contribution of σ_1 to the total charge is very small as compared to that of σ_2 at large plate distances. At $2d = 1.0$ nm, where the Gouy-layers are completely pushed aside, σ_2 becomes zero and σ becomes equal to σ_1 ($= 0.0037$ C/m²) indicating the transition of the electrical charge from the Gouy-layer to the Stern-layer.

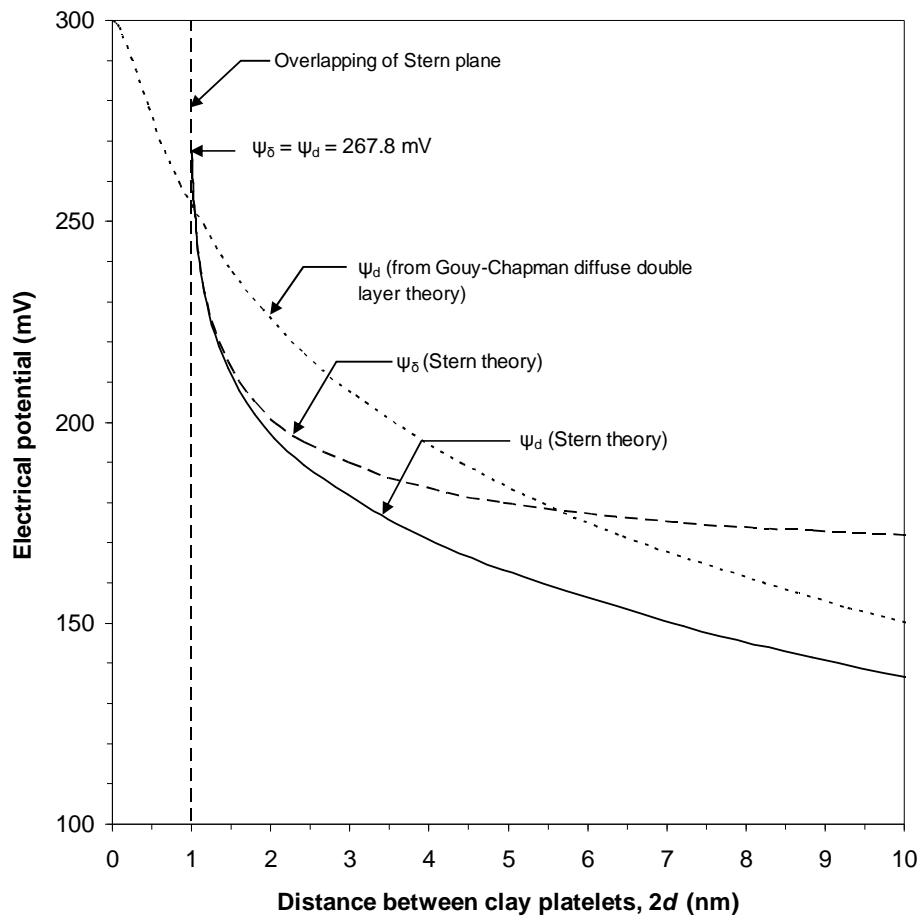


Figure 5.2. Change of electrical potentials with $2d$ from the Stern theory and the Gouy-Chapman diffuse double layer theory ($\psi_0 = 300$ mV).

A decrease of σ due to a decrease in $2d$ results in an increase in ψ_d and ψ_δ (Table 5.2 and Fig. 5.2). An increase in ψ_d and ψ_δ is more pronounced at about $2d = 2.0$ nm due to ψ_δ being a large fraction of ψ_0 for the case considered ($n_0 = 10^{-4}$ M). Verwey and Overbeek (1948) stated that the variation of the electrical potential is sensitive to the bulk fluid

concentration. At $2d = 1.0$ nm, the Gouy-layer is completely eliminated and thus ψ_δ and ψ_d becomes equal ($= 267.8$ mV) (Fig. 5.2). This is the limiting value of ψ_δ for $\psi_0 = 300$ mV that produced a positive σ_2 .

Figure 5.1 shows that the total charge (σ) calculated from the Gouy-Chapman diffuse double layer theory (eq. (5.13)) was far greater than that calculated from the Stern theory (refer right-hand side y-axis for the charge according to the Gouy-Chapman theory). At $2d = 10.0$ nm, σ is about 14.6 times larger, whereas at 1.0 nm, it is about 50 times larger than that of σ calculated from the Stern theory.

From the cation exchange capacity (B) and the specific surface (S) (say, 100 meq/100 g and 800 m²/g, respectively) consideration, the total charge (i.e., the ratio of B and S times the Faraday's constant) (van Olphen, 1977; Sridharan and Jayadeva, 1982) can be calculated as 0.12 C/m² (marked in Fig. 5.1). Although σ calculated from the Gouy-Chapman theory with $\psi_0 = 300$ mV (i.e., 0.205 C/m²) is far greater than 0.12 C/m²; however, due to a constant value of ψ_0 or z (eq. (5.12)), $2d$ versus ψ_d relationship from the Gouy-Chapman diffuse double layer theory is comparable to that of the calculated results from the Stern theory (Fig. 5.2). At $2d$ about 30 nm, the midplane potential from the Stern theory and the Gouy-Chapman theory were very nearly similar indicating that the Stern-layer has insignificant influence at very large platelet distances (not shown).

Mitchell (1993) and Sridharan and Satyamurty (1996) showed that for single clay platelet systems and at any distance away from the clay platelets, both the ion concentration and the electrical potential in the Gouy-layer based on the Stern theory was greater than that determined from the Gouy-Chapman theory. On the other hand, the results presented in

Fig. 5.2 clearly showed that the trend is reversed in the case of the interacting clay platelet systems. That is, the $2d-\psi_d$ relationship calculated from the Stern theory remained distinctly below that was established from the Gouy-Chapman theory. Some deviation was also noted at about $2d = 1.04$ nm or less in which case σ calculated from the Gouy-Chapman theory was found to be slightly greater than that calculated from the Stern theory. The distribution of ψ_d is expected to influence the dry density-swelling pressure and vertical pressure-void ratio relationship is discussed in the following section.

5.5.2 Parametric study

Using eqs. (5.1) to (5.10), calculations were made by varying one of the following parameters, v plus the corresponding hydrated ionic radii, n_0 , ε' , φ and ψ_0 while keeping all other parameters constant. The relevant parameters that were used for calculation are shown in Table 5.1. In all cases, the void ratio and corresponding dry densities were calculated based on the chosen specific surface area of $800 \text{ m}^2/\text{g}$. Using eq. (5.10), the void ratio corresponding to $2d = 1.0$ nm was found to be 1.06 for $G = 2.65$. The corresponding dry density was 1.29 Mg/m^3 . Therefore, the dry density-swelling pressure relationship of compacted bentonites can be established up to the maximum dry density of 1.29 Mg/m^3 using the Stern theory. Similarly, $e-\log p$ relationship of bentonite can be established up to a void ratio of 1.06.

5.5.2.1 Effect of valence

The influence of ν on the e -log p and dry density-swelling pressure relationship was studied, by varying the valence ν and the corresponding N_1 value, whereas all other parameters in Table 5.1 were used. The dry density-swelling pressure relationship was established for the valence ν of exchangeable cations as 1 and 2 using the Stern theory. Figure 5.3 presents the effect of valence of exchangeable cations on the pressure-void ratio (Fig. 5.3 (a)) and the dry density-swelling pressure (Fig. 5.3 (b)) relationships of bentonite.

It can be seen in Fig. 5.3 (a) that an increase in ν caused a decrease in the void ratio at smaller pressures. Additionally, when the Gouy-layer was completely pushed aside (i.e, at $2d = 1.0$ nm or at $e = 1.06$), the swelling pressure increased with an increase in ν . The over all effect was the crossing of the e -log p plots. For clarity, the effect of ν at large pressures are enlarged and shown in the inset of Fig. 5.3 (a).

The dry densities were calculated using eq. (5.11) for known void ratio and specific gravity of bentonites. The results showed that for the same dry density, the swelling pressures were calculated for $\nu = 2$ were greater than that calculated for $\nu = 1$ for the range of dry density between 1.0 and 1.29 Mg/m³ (Fig. 5.3 (b)).

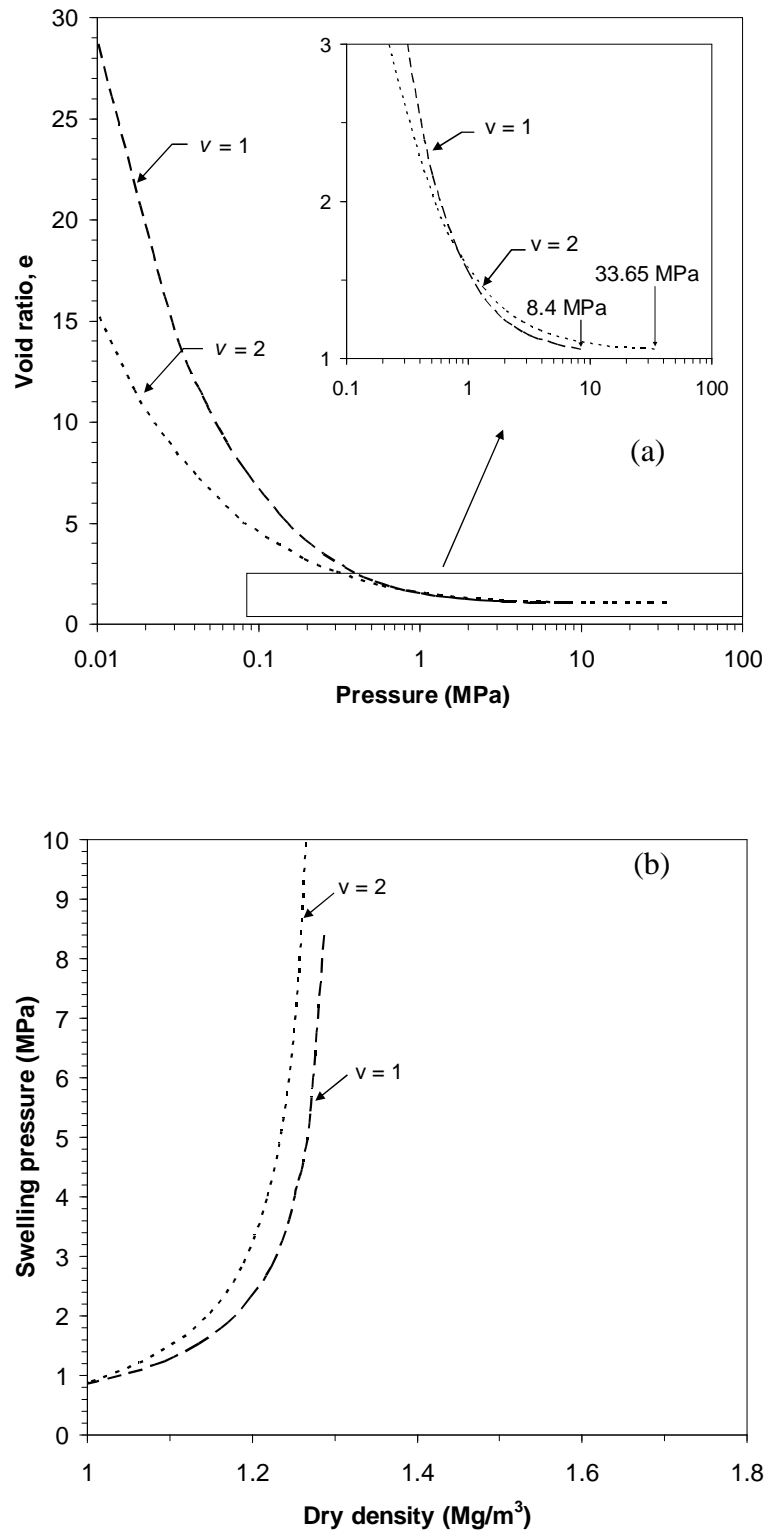


Figure 5.3. Influence of hydrated ionic radii and valence on (a) e -log p and (b) dry density-swelling pressure relationships.

5.5.2.2 Effect of electrolyte concentration

The effect of electrolyte concentration was studied for $n_0 = 10^{-4}$, 10^{-1} and 1.0 M using the Stern theory. The other parameters (v plus the corresponding hydrated ionic radii, ε' , ϕ and ψ_0) were considered to be constant.

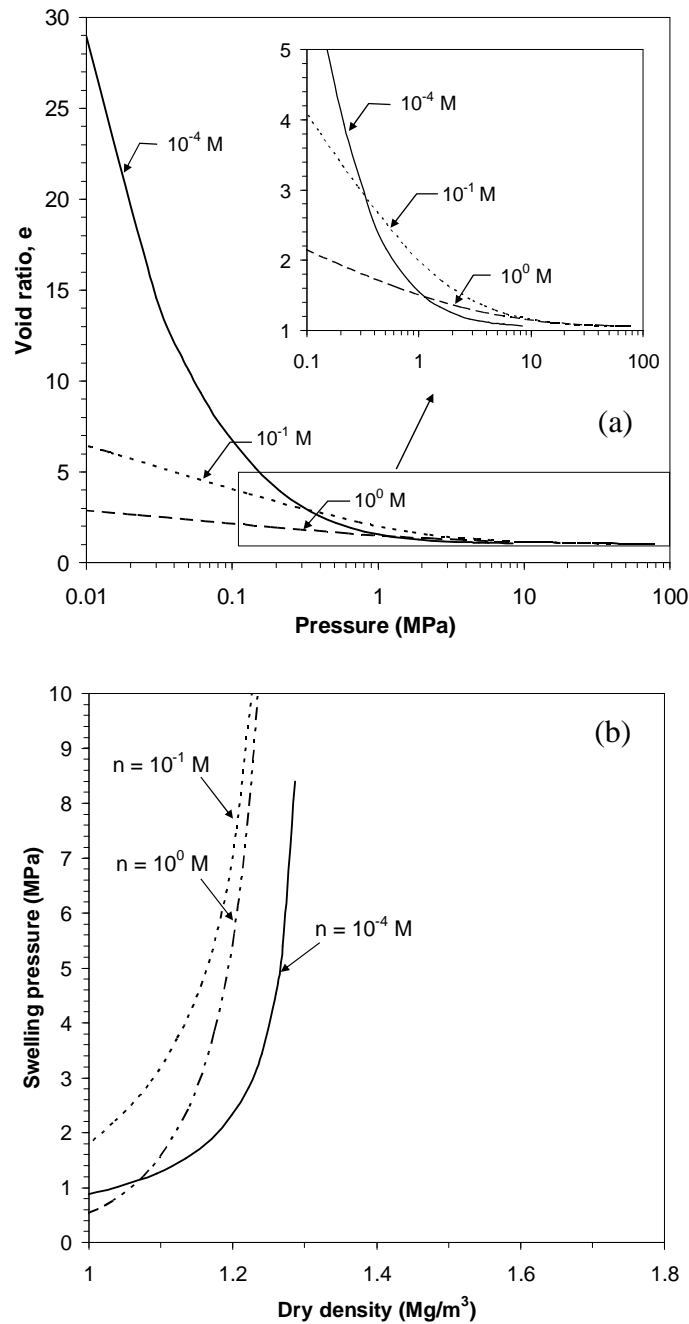


Figure 5.4. Influence of bulk fluid concentration on (a) e -log p and (b) dry density-swelling pressure relationships.

Figure 5.4 presents the effect of electrolyte concentrations on the pressure-void ratio (Fig. 5.4 (a)) and the dry density-swelling pressure (Fig. 5.4 (b)) relationships. Similar to the effect of v , an increase in n_0 resulted in decreasing of the void ratio at smaller pressures. At $2d = 1.0$ nm or at $e = 1.06$, the swelling pressure increased with an increase in n_0 . The effects of n_0 at large pressures are enlarged and shown in the inset of Figs. 5.4 (a).

Figure 5.4 (b) showed that with an increase in n_0 , the swelling pressure decreased. The decrease in swelling pressure is attributed to the suppression of diffuse double layer (Verwey and Overbreek, 1948).

5.5.2.3 Effect of dielectric constant of pore fluid in Stern layer

The effect of dielectric constant of pore fluid in the Stern layer was studied by varying ϵ' as 8.5, 6.5 and 3 while keeping other parameters (v plus the corresponding hydrated ionic radii, n_0 , ϕ and ψ_0) constant.

Figure 5.5 presents effect of dielectric constant on the pressure-void ratio (Fig. 5.5 (a)) and the dry density-swelling pressure (Figs. 5.5 (b)) relationships. Figure 5.5 showed that an increase in ϵ' increased the pressure at equal void ratio or dry density of the bentonite. The maximum swelling pressure that can be calculated using the Stern theory was found to increase with an increase in the ϵ' .

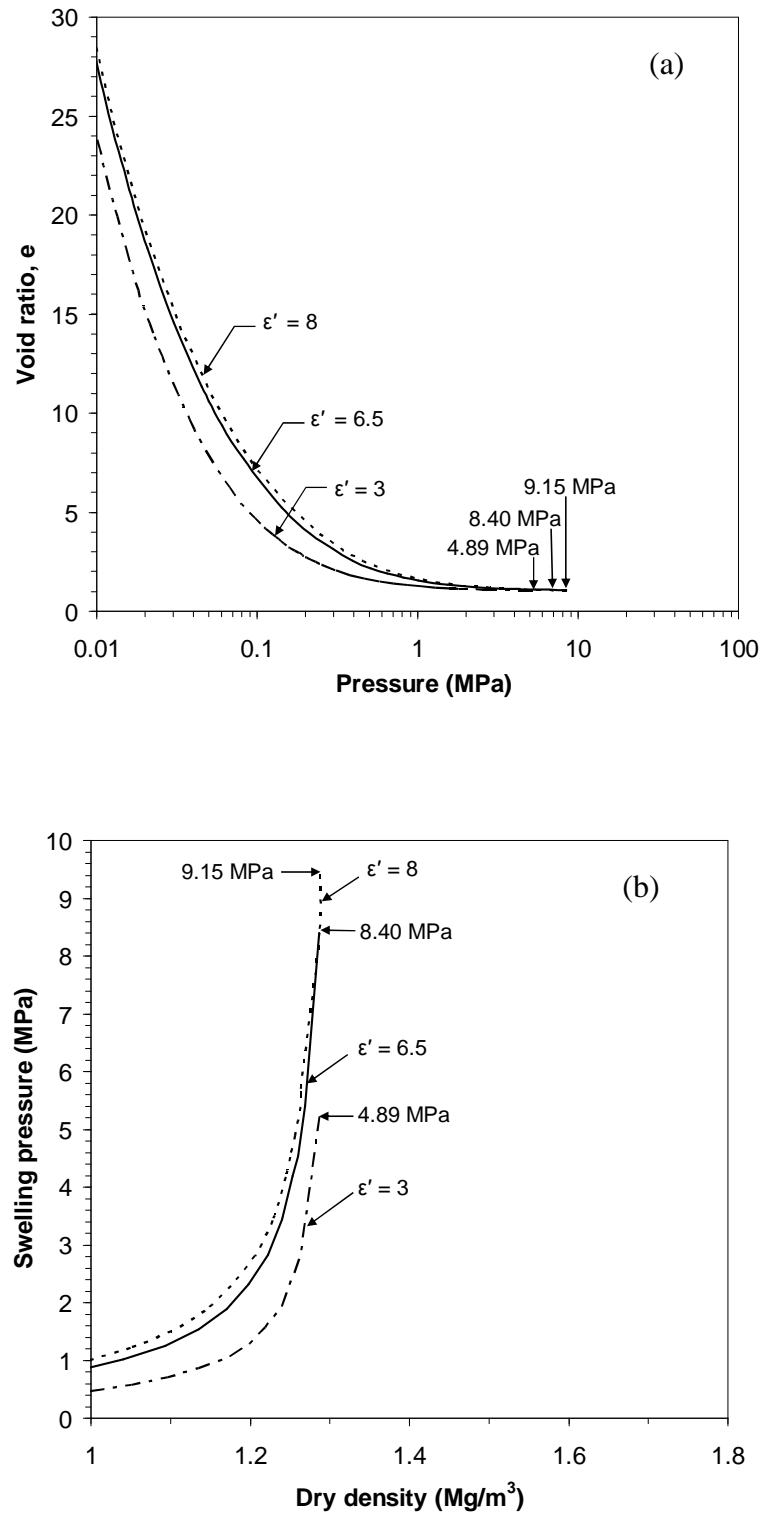


Figure 5.5. Influence of dielectric constant of pore fluid in Stern layer on (a) e - $\log p$ and (b) dry density-swelling pressure relationships.

5.5.2.4 Effect of specific adsorption potential

The effect of specific adsorption potential was studied by varying ϕ as 0.0, 0.05 and 0.1 eV. The pressure-void ratio and the dry density-swelling pressure relationships were established for the valence $\nu = 1$, the electrolyte concentration $n_0 = 10^{-4}$ M, dielectric constant of pore fluid in the Stern layer $\epsilon' = 6.5$ and the surface potential $\psi_0 = 300$ mV or 0.3 V (Table 4.1).

Figure 5.6 presents the effect of specific adsorption potential on the pressure-void ratio (Figs. 5.6 (a)) and the dry density-swelling pressure (Figs. 5.6 (b)) relationships of the bentonite. The effect of specific adsorption potential on the pressure-void ratio and the dry density-swelling pressure relationships was opposite to that was noted for variation of the dielectric constant of pore fluid in the Stern layer.

Figure 5.6 showed that an increase in the specific adsorption of potential reduces the pressure at equal void ratio or dry density of the bentonite. The pressure-void ratio relationship for $\phi = 0.0$ and 0.05 were very similar. However, significantly lesser pressures were calculated for $\phi = 0.1$ eV. The maximum swelling pressure that can be calculated using the Stern theory was found to decrease with an increase in the specific adsorption potential. For $\phi = 0.0, 0.05$ and 0.1 eV, the maximum calculated pressures were 8.40, 2.52 and 0.60 MPa, respectively.

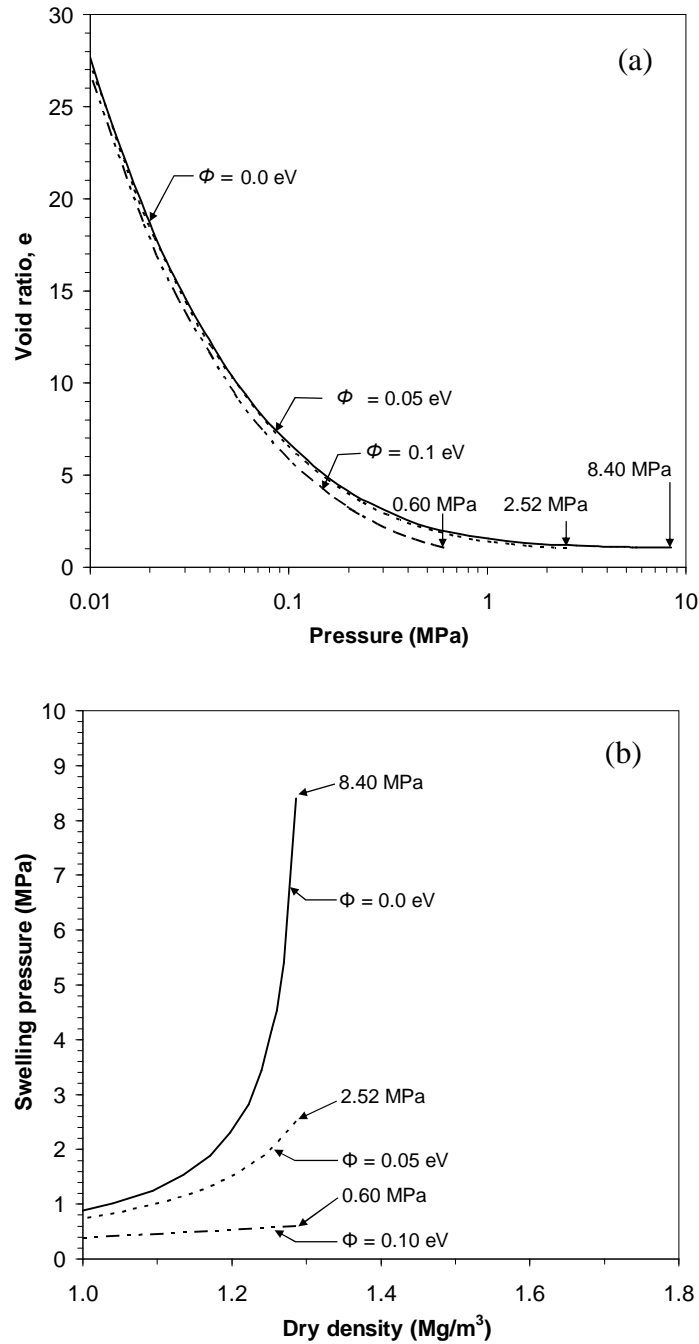


Figure 5.6. Influence of specific adsorption potential on (a) e -log p and (b) dry density-swelling pressure relationships.

5.5.2.5 Effect of surface potential

The effect of surface potential was studied by varying ψ_0 as 300, 250 and 200 mV and other parameters (v plus the corresponding hydrated ionic radii, n_0 , ϵ' and ϕ) shown in Table 4.1 were considered to be constant. Figure 5.7 presents the effect of surface potential

on the pressure-void ratio (Figs. 5.7 (a)) and the dry density-swelling pressure (Figs. 5.7 (b)) relationships of the bentonite.

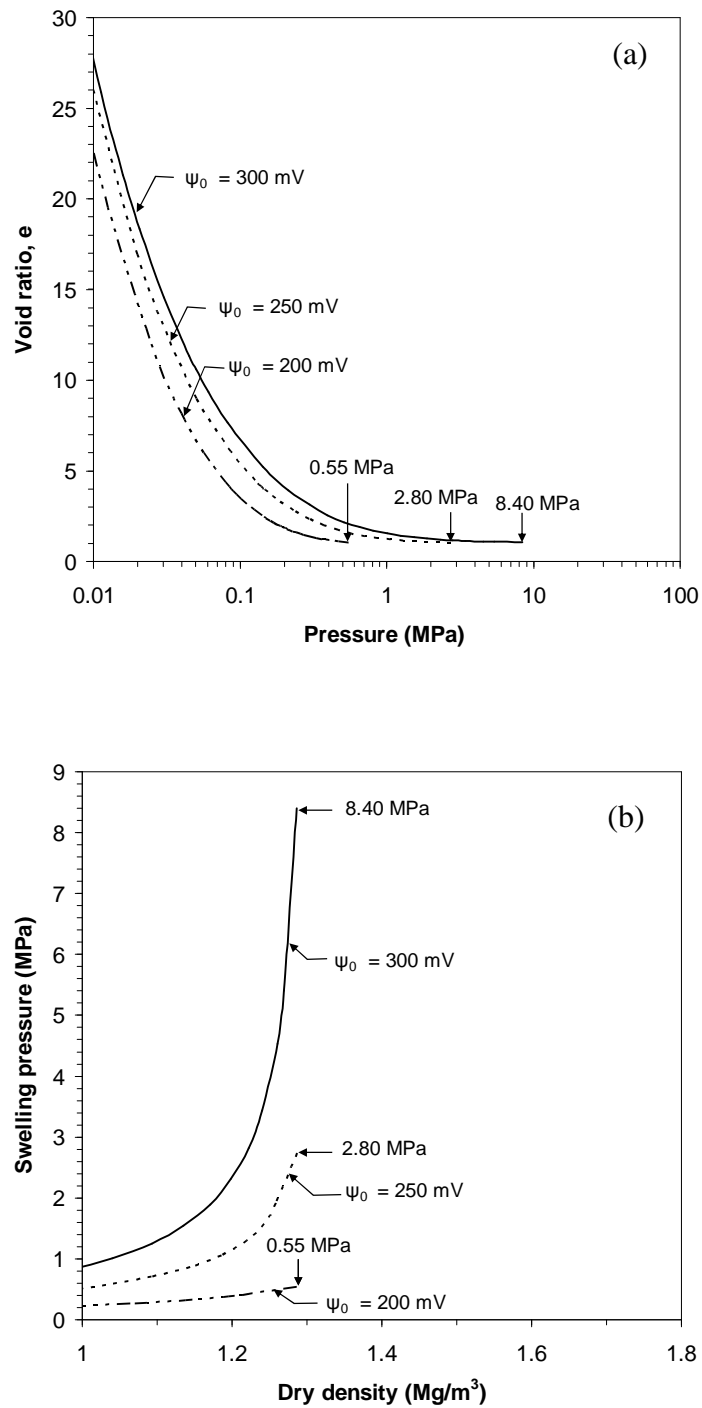


Figure 5.7. Influence of surface potential (ψ_0) on (a) e -log p and (b) dry density-swelling pressure relationship.

Figure 5.6 showed that an increase in the surface potential increases the swelling pressure at equal void ratio or dry density of the bentonite. The maximum swelling pressure that can be calculated using the Stern theory was found to increase with an increase in the specific adsorption potential. For $\psi_0 = 300, 250$ and 200 mV, the maximum calculated swelling pressures were 8.40, 2.8 and 0.55 MPa, respectively.

5.5.3 Comparison between experimental and theoretical swelling pressure results

The dry density-swelling pressure relationships established from the Stern theory and the diffuse double layer theory are compared with the experimental dry-density swelling pressure relationships in this section. The swelling pressure tests were conducted in seven series of tests at ambient (25°C) and elevated (70°C) temperatures. Series I, II, III and IV tests were conducted at ambient temperature (25°C), whereas series V, VI and VII tests were conducted at an elevated temperature of 70°C . In test Series I, compacted bentonite specimens were saturated using distilled water immediately after the compaction process was completed. Test series II, III, IV, V, VI and VII were conducted on the compacted bentonite specimens after extrusion and re-insertion processes prior to testing.

The theoretical dry density-swelling pressure relationships were established following the Stern theory (eqs. 5.1 to 5.11) and the Gouy-Chapman diffuse double layer theory (eqs. 5.6 to 5.12). The properties of the bentonite shown in Table 3.1 ($\nu = 1.47$, $S = 640\text{ m}^2/\text{g}$, $G = 2.76$) were used for the calculations. To establish the dry density-swelling pressure relationship of the bentonite from the Stern theory, the hydrated radii of exchangeable ions and the valence are important. MX80 bentonite constitutes 53% of exchangeable Na^+ and K^+ , whereas 47% are Ca^{2+} and Mg^{2+} . The ionic radii of Na^+ (0.79

nm) and valence $\nu = 1$ were used to establish the dry density-swelling pressure relationship from the Stern theory (eqs. 5.1 to 5.11) as the major exchangeable cations present in the bentonite was Na^+ . The actual valence of exchangeable ions ($\nu = 1.47$) was used for calculations using the diffuse double layer theory. Other parameters chosen in the case of the Stern theory calculations were: $\psi_0 = 300$ mV, $\delta = 0.5$ nm, $\epsilon' = 6.5$ and $\phi = 0$.

Test series I, II, III and IV were carried out at ambient temperature (25°C). Therefore, the dielectric constant of water at a temperature of 25°C was used for calculations. Test series V, VI and VII were conducted at an elevated temperature of 70°C . Therefore, $T = 70^\circ\text{C} = 243$ K and the dielectric constant of water at 70°C ($\epsilon_0 = 62.2$) (Mitchell, 1993) were used. The following sections present comparisons of the experimental and theoretical dry density-swelling pressure relationships.

5.5.3.1 Tests conducted at a temperature of 25°C using distilled water

Figure 5.8 shows the comparison between experimental and theoretical dry density-swelling pressure relationships for the specimens saturated using distilled water at ambient temperature of 25°C (Test series I and II; Test series I: bentonite specimens were tested immediately once the compaction process was completed; Test series II: compacted bentonite specimens were extruded and re-inserted back in the specimen rings before testing). The dry density-swelling pressure relationship established from the diffuse double layer theory and the Stern theory are shown in Fig. 5.8. The dry density-swelling pressure relationship established for valence $\nu = 1$ using the Stern theory and $\nu = 1.47$ ($\nu = 1$, 53%; $\nu = 2$, 47%) using the diffuse double layer theory.

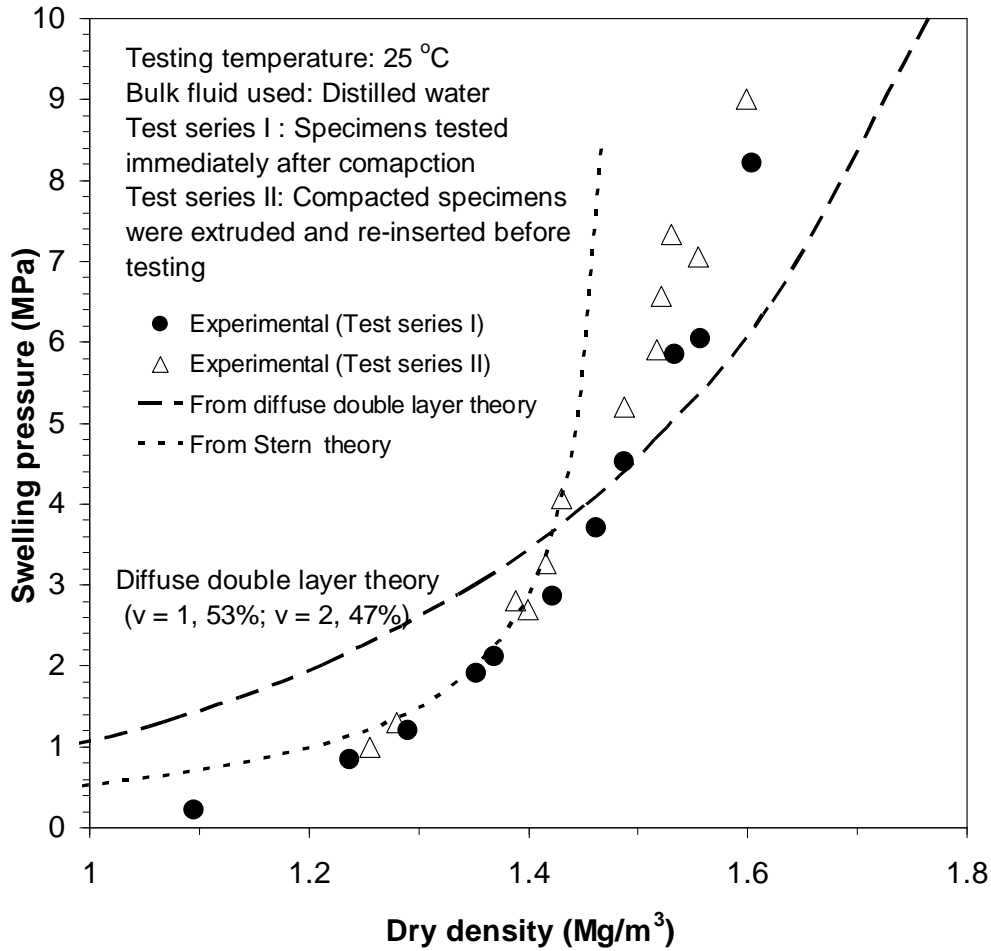


Figure 5.8. Experimental and theoretical dry density-swelling pressures for the specimens tested at 25 °C using distilled water as bulk fluid.

Reasonably good agreement was noted between the experimental and theoretically calculated dry density-swelling pressure relationship that were calculated using the Stern theory for a range of dry density between 1.0 and 1.45 Mg/m³. Swelling pressures calculated from the diffuse double layer theory for dry densities less than or equal to 1.45 Mg/m³ were found to be greater than that of the experimental swelling pressures. At dry densities greater than 1.45 Mg/m³, swelling pressures calculated from the diffuse double layer theory were found to be lesser than that of the experimental results, whereas greater swelling pressures were calculated from the Stern theory. At a dry density of 1.45 Mg/m³, the distance between two parallel clay platelets ($2d$) is equal to 1 nm, therefore, overlapping of Stern layers and Born repulsion takes place.

5.5.3.2 Tests conducted at a temperature of 70 °C using distilled water

Figure 5.9 shows a comparison between the experimental and the theoretical dry density-swelling pressure relationships for test series V (distilled water, 70 °C). In test series V, swelling pressure tests were conducted at an elevated temperature of 70 °C. Compacted bentonite specimens were hydrated using distilled water. The dry density-swelling pressure relationships established using the Stern theory and the diffuse double layer theory are shown in Fig. 5.9. For theoretical calculations morality of bulk fluid n_0 was considered as 0.0001 M. The temperature (T) was considered as 70 °C or 243 K. The dielectric constant of pore water (D) was considered as 62.2.

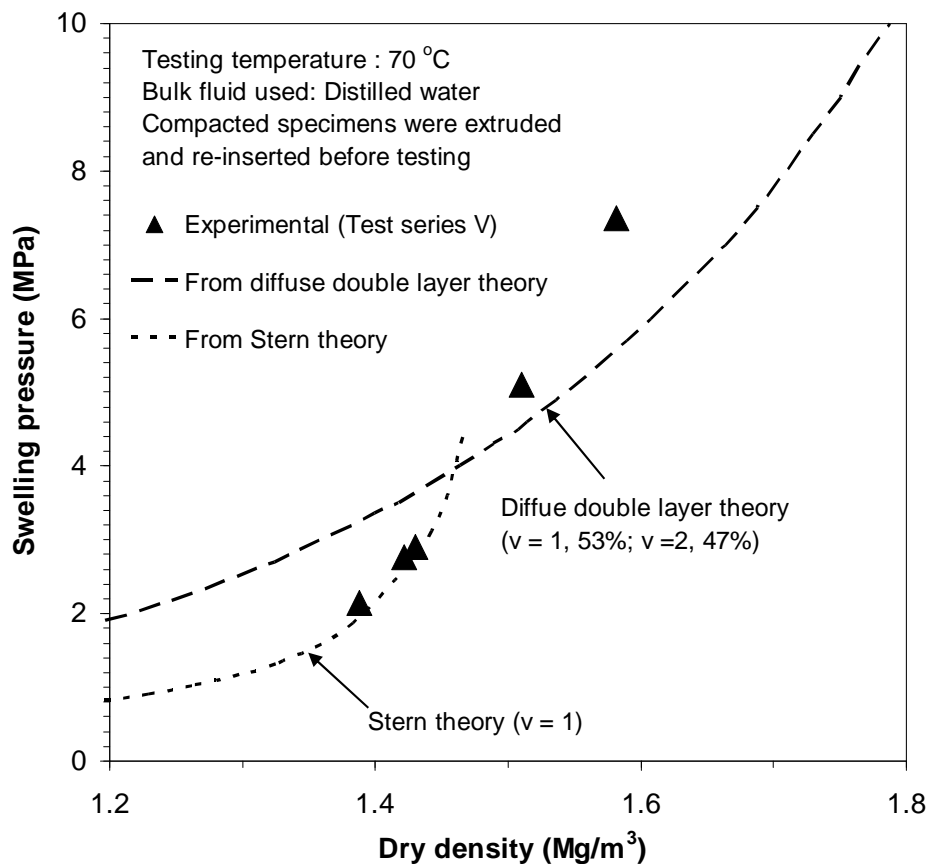


Figure 5.9. Experimental and theoretical dry density-swelling pressures for the specimens tested at a temperature of 70 °C using distilled water as bulk fluid.

Up to a dry density of 1.45 Mg/m^3 (3 experimental data points), a good agreement between the experimental and the theoretical dry density-swelling pressure relationships was noted. The swelling pressures calculated using the diffuse double layer theory were found to be greater than that of the experimental values at dry densities lower than 1.45 Mg/m^3 . At dry densities greater than 1.45 Mg/m^3 , the experimental swelling pressure values were found to be greater than that were calculated using the diffuse double layer theory.

Based on the results presented in Figs. 5.8 and 5.9, it was noted that the Stern theory improved the assessment of swelling pressure up to a maximum dry density of 1.45 Mg/m^3 , both for swelling pressures tests conducted at 25°C and 70°C and with bulk fluid as distilled water.

5.5.3.3 Tests conducted at temperatures of 25°C and 70°C using 0.1 M NaCl

Figure 5.10 compares the experimental and theoretical dry density-swelling pressure relationships for test series III (0.1 M NaCl , 25°C) and VI (0.1 M NaCl , 70°C). The swelling pressure tests were carried out by saturating the bentonite specimens with 0.1 M NaCl solution after extrusion and re-insertion processes. Series III tests were conducted at ambient temperature (25°C), whereas series VI tests were conducted at an elevated temperature of 70°C .

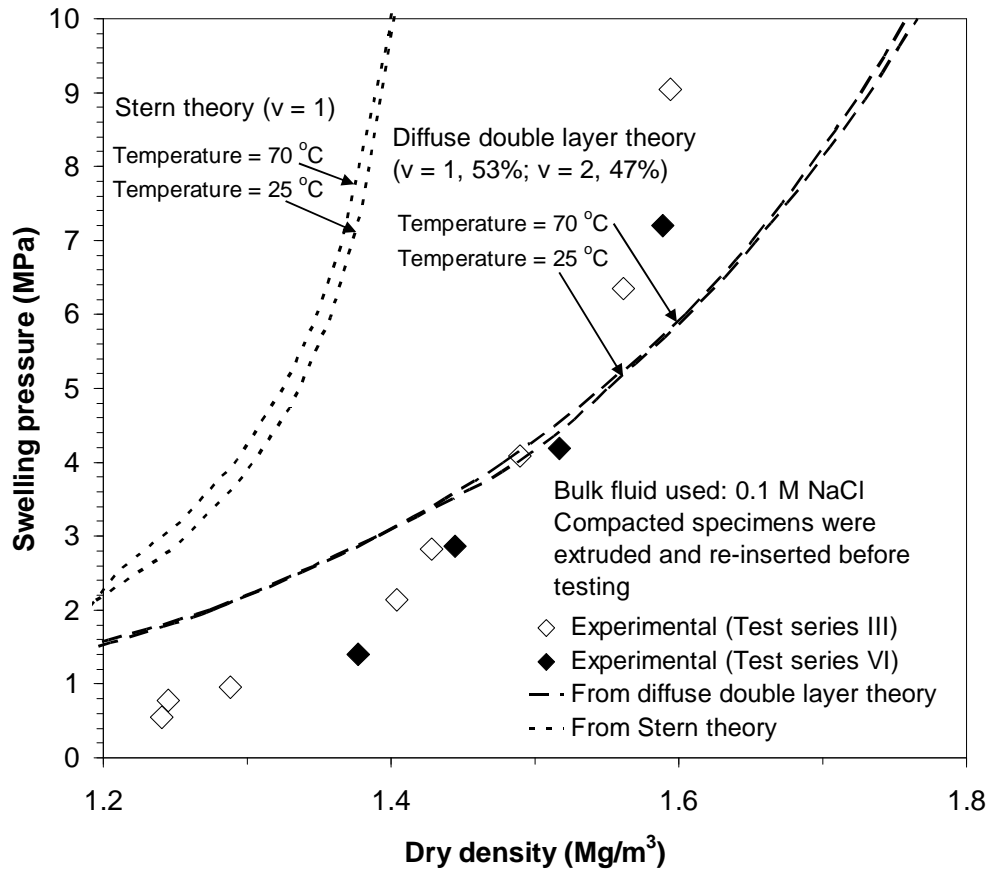


Figure 5.10. Experimental and theoretical dry density-swelling pressures the specimens tested at temperatures of 25 and 70 °C using 0.1 M NaCl as bulk fluid.

It was noted that following the Stern theory, the calculated swelling pressures were greater than that of the experimental swelling pressures at both 25 °C and 70 °C. On the other hand, the calculated swelling pressures from the diffuse double layer theory were greater at smaller dry densities and smaller at higher dry densities as compared to the experimental swelling pressure. The decrease in swelling pressure was due to decrease in dielectric constant of water at elevated temperature (Mitchell, 1993).

5.5.3.4 Tests conducted at temperatures of 25 °C and 70 °C using 1.0 M NaCl

Figure 5.11 compares the experimental and theoretical dry density-swelling pressure relationships for test series IV (1.0 M NaCl, 25 °C) and VII (1.0 M NaCl, 70 °C). The swelling pressure tests were conducted by saturating the bentonite specimens using 1.0 M NaCl solution after the extrusion and re-insertion processes. Series IV tests were conducted at ambient temperature (25 °C), whereas series VII tests were conducted at an elevated temperature of 70 °C. The theoretical dry density-swelling pressure relationships were established for $n_0 = 1.0$ M. The effect of elevated temperature (70 °C) was included to establish the dry density-swelling pressure relationship.

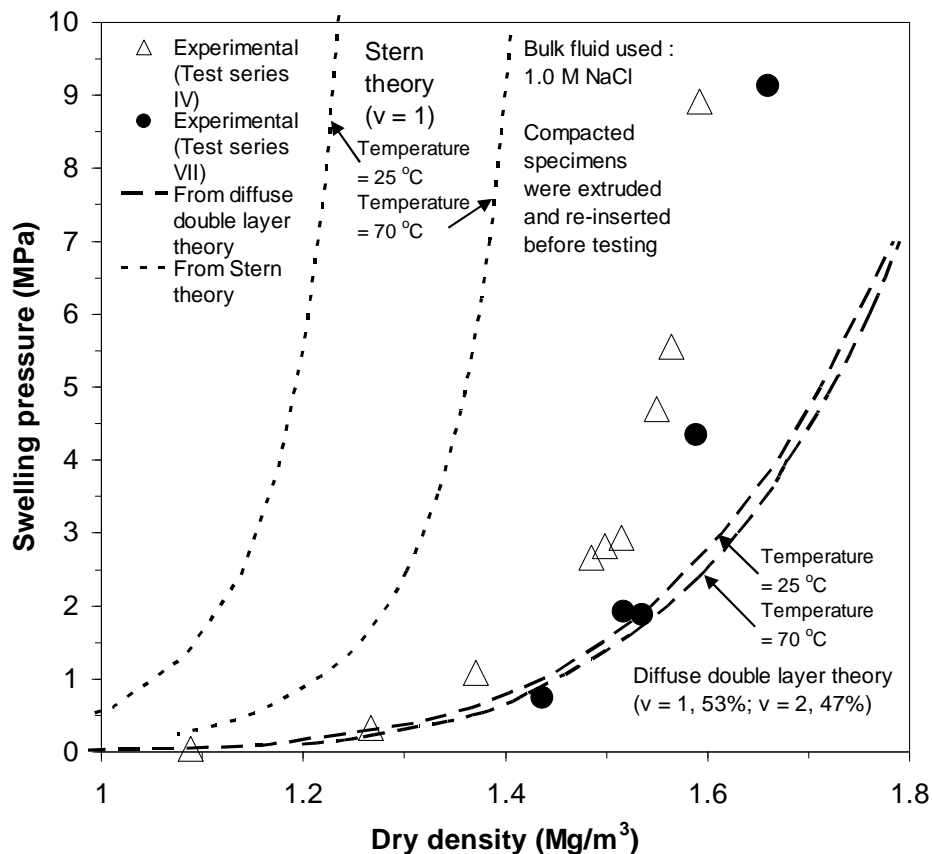


Figure 5.11. Experimental and theoretical dry density-swelling pressures the specimens tested at 25 °C and 70 °C using 1.0 M NaCl as bulk fluid.

Referring to Fig. 5.11, it was noted that the swelling pressures calculated from the Stern theory were found to reduce significantly with an increase in the temperature. Comparison between the experimental and the theoretical dry density relationships showed that the swelling pressures calculated from the Stern theory were found to be greater than that of the experimental results for the range of dry density considered in this study. However, a better agreement between the experimental and theoretical dry density-swelling pressure relationships that were calculated from the diffuse double layer theory was noted up to a dry density of 1.50 Mg/m^3 .

5.6 Concluding remarks

Comparisons of experimental swelling pressures and swelling pressures calculated from the diffuse double layer theory and the Stern theory are presented in this chapter. Assessments of swelling pressures of bentonites are commonly carried out using colloid theories. Using the theories, it is usual to determine a relationship between the distance between clay platelets (either d or $2d$) and the swelling pressure. From geotechnical and geoenvironmental engineering perspectives, the void ratio-vertical pressure and dry density-swelling pressure relationships are of interests. In this chapter, the e - $\log p$ and ρ_d - p relationships of bentonites are established from the Stern theory and the diffuse double layer theory, both applicable to interacting clay platelets systems. A constant electrical potential at the surfaces of the platelets is considered. Theoretical equations and a step-wise procedure are presented to establish e - $\log p$ and ρ_d - p relationship of bentonites.

The study showed that the electrical charge and the electrical potential in the Gouy-layer calculated from the Stern theory were distinctly smaller than that calculated from the

Gouy-Chapman diffuse double layer theory, in contrary to that was reported for single clay platelet system (Mitchell, 1993).

An increase in the valence and an increase in the bulk fluid concentration produced stronger interaction between the clay platelets that was manifested on both the maximum predicted swelling pressure and crossing followed by reordering of the e -log p plots. A decrease in the dielectric constant of the pore-fluid in the Stern-layer, an increase in the adsorptive potential and a decrease in the electrical potential at the surface of bentonite were found to reduce the void ratio at any given pressure.

The calculated swelling pressures of compacted MX80 bentonite from the Stern theory and the experimental swelling pressures agree well with in a range of dry density between 1.1 and 1.45 Mg/m³ for the case of specimens hydrated with distilled water. For the specimens tested using higher electrolyte concentrations and at higher temperature, the agreement between the experimental and the theoretical results were found to be poor.

At dry densities greater than 1.45 Mg/m³, agreements between the experimental and the theoretical results were poor. At a dry density of 1.45 Mg/m³, the distance between two parallel clay platelets ($2d$) is equal to 1 nm, therefore, overlapping of Stern layers and Born repulsion takes place. Therefore, the applicability of the Stern theory to assess the compressibility behaviour of initially saturated slurried bentonites was studied for a wide range of void ratios and is presented in chapter 6.

Chapter 6

Effect of Stern-layer on compressibility behaviour of bentonites

6.1 Introduction

In the previous chapter, the theoretical procedures required to establish the vertical pressure-void ratio and dry density-swelling pressure relationships for bentonites from the diffuse double layer theory and the Stern theory are presented. The dry density-swelling pressure relationships for various testing conditions obtained experimentally were compared with that of the theoretically established dry density-swelling pressure relationships. Good agreements were noted between theoretical and experimental dry density-swelling pressure relationships at low dry densities for compacted bentonite specimens saturated with distilled water (25 and 70 °C). However, the swelling pressures calculated from the Stern theory were found to be greater at higher dry densities.

Therefore, the study was extended to bring out the efficiency of the Stern theory for assessing the compressibility behaviour of saturated bentonites.

This chapter presents the comparison between the vertical pressure-void ratio relationships obtained from the consolidation tests with that of the pressure-void ratio relationships established from the Stern theory for MX80 bentonite, Na-Ca MX80 bentonite (Marcial et al., 2002) and Calcigel bentonite (Baille et al., 2010). Section 6.2 presents the properties of the MX80 bentonite and the consolidation test method. In section 6.3, comparisons between the experimental and the theoretical results are presented. The concluding remarks from this study are presented in section 6.4.

6.2 Consolidation test

6.2.1 Properties of the bentonites studied

Test methods of 3 bentonites were considered. One dimensional consolidation test was carried out on initially saturated slurried MX80 bentonite. Additionally, reported consolidation test results of two other bentonites, namely Na-Ca MX80 bentonite (Marcial et al., 2002) and Calcigel bentonite (Baille et al., 2010) were chosen for comparison with the calculated results from the Stern theory and the Gouy-Chapman diffuse double layer theory. The properties of the Na-ca MX80 bentonite and Calcigel bentonites are presented in Table 6.1. The properties of the MX80 bentonite used in this study presented in Table 3.1 are shown in Table 6.1 for the sake of comparison.

The exchangeable sodium percentage (ESP) shown in Table 6.1 was the basis for the selection of the bentonites in this study. Mitchell (1993) stated that for mixed cation

montmorillonites, the ESP which is defined as the ratio of sodium complex in the clay to the total exchange capacity of the clay influence the swelling behaviour of montmorillonites. The ESP is usually expressed as a percentage and is considered as an indicator for the distribution of cations within the clay system. For example, bentonites containing both Na^+ and Ca^{2+} and with an ESP of greater than 50% would indicate unlimited swelling between all plates on addition of water, whereas with an $\text{ESP} < 15\%$ would indicate that the interlayer exchange complex is predominantly Ca-saturated (Mitchell, 1993). The ESP of MX80 bentonite used in this study, Na-Ca MX80 and Calcigel bentonite was found to be about 52, 88 and less than 12%, respectively. The ESP of the bentonites clearly affected the Atterberg's limits (Table 6.1).

Table 6.1 Properties of the bentonites studied

Properties	MX80 bentonite*	Na-Ca MX80 bentonite from Marcial et al. (2002)	Calcigel bentonite from Baille et al. (2010)
Specific gravity	2.76	2.65	2.8
Liquid Limit (%)	385	520	178
Plastic Limit (%)	43	62	56
Specific surface area (m^2/g)	640	700	525
Total Cation exchange capacity (meq/100 g)	88.44	68	74
Ca^{2+}	31.9	5	65.12
Mg^{2+}	9.31	3	
Na^+	45.7	60	8.88
K^+	1.55	-	
ESP (%)	52	88.23	< 12
Weighted average valence of exchangeable cations	1.47	1.12	1.92

*Current study

6.2.2 Experimental Methods

For MX80 bentonite in this study, saturated specimens were prepared at an initial water content of 1.5 times the liquid limit by thoroughly mixing air-dry bentonite with deionised water. The bentonite-water mixture was stored in a closed-lid container and cured for 7 days for moisture equilibration prior to the specimen preparation. The height and diameter of the specimen was 10 and 38 mm, respectively. Saturated specimens were loaded from 6.25 kPa to 3200 kPa with a load increment ratio (LIR) of 1.0 using a conventional oedometer. The small diameter of the specimens allowed applying high pressure of 3200 kPa using the oedometer. Three identical specimens were tested. The test results were found to be very similar.

The test results of Na-Ca MX80 and Calcigel bentonite are available up to vertical pressure of 30.0 MPa and 21.0 MPa, respectively (Marcial et al., 2002; Baille et al., 2010). The LIR adopted for Na-Ca MX80 bentonite was 1.0, whereas that for Calcigel bentonite, the LIR adopted was 1.0 up to a vertical pressure of 800 kPa and further an LIR of 0.5 was adopted at higher pressures. The initial water content of the chosen bentonites from the literature was 1.1 times the corresponding liquid limit of the bentonites.

6.3 Comparison between experimental and theoretical results

The calculated pressure-void ratio (e - $\log p$) relationships and the experimental e - $\log p$ results of MX80 bentonite, Na-Ca MX80 bentonite, and Calcigel bentonite are shown in Figs. 6.1, 6.2 and 6.3, respectively. The weighted average valence of

exchangeable cations (Tripathy et al., 2004) were considered for establishing the theoretical e - $\log p$ relationships following the Gouy-Chapman diffuse double layer theory (eqs. (5.6) to (5.12)), whereas the Stern theory (i.e., eqs. (5.1) to (5.10)) results are for $\nu = 1$ for MX80 and Na-Ca MX80 and $\nu = 2$ for Calcigel bentonite with the corresponding hydrated ionic radii equal to that of Na^+ (0.79 nm) and Ca^{2+} (0.96 nm) ions were used. The void ratios were calculated based on the actual specific surfaces of the chosen bentonites (Table 6.1). Other parameters chosen in the case of Stern theory calculations were: $\psi_0 = 300$ mV, $\delta = 0.5$ nm, $\varepsilon' = 6.5$ and $\phi = 0$. Distilled water was used to prepare the clay-water mixture and flooding of the specimens. Therefore, ionic concentration of the bulk fluid was used as 10^{-4} M for the theoretical calculations.

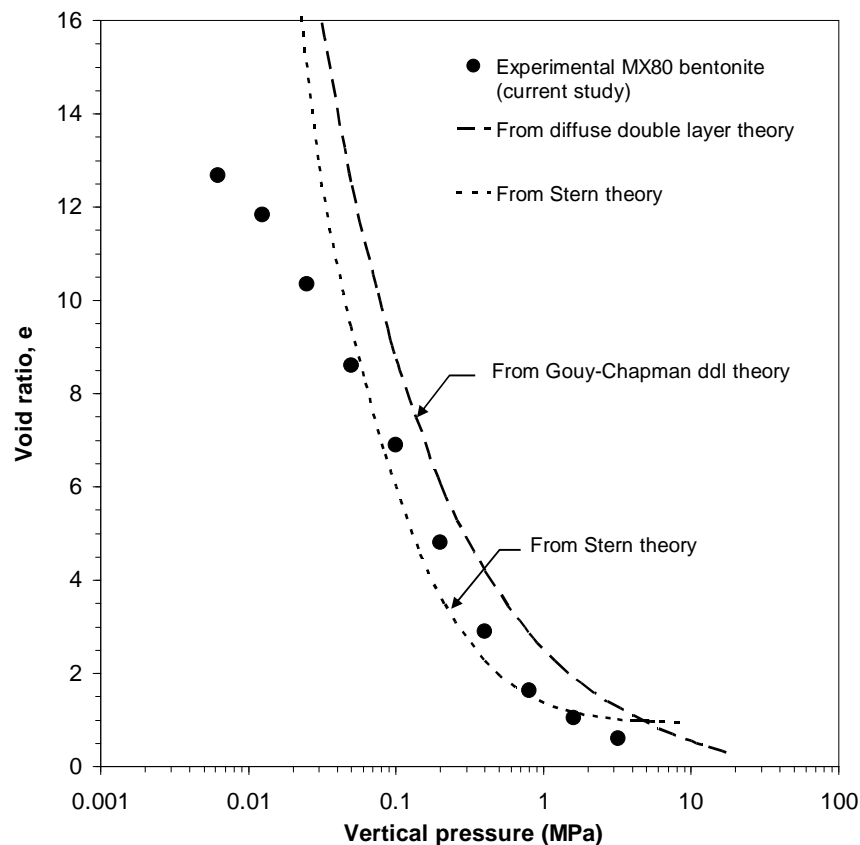


Figure 6.1. Theoretical and experimental e - $\log p$ relationships for MX80 bentonite (in this study).

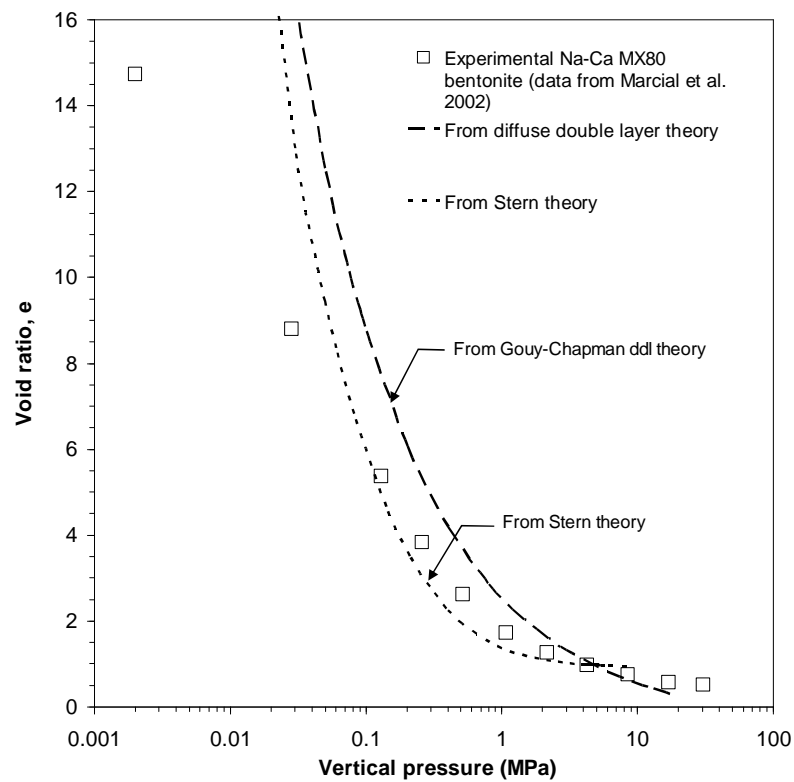


Figure 6.2. Theoretical and experimental e -log p relationships for Na-Ca MX80 bentonite.

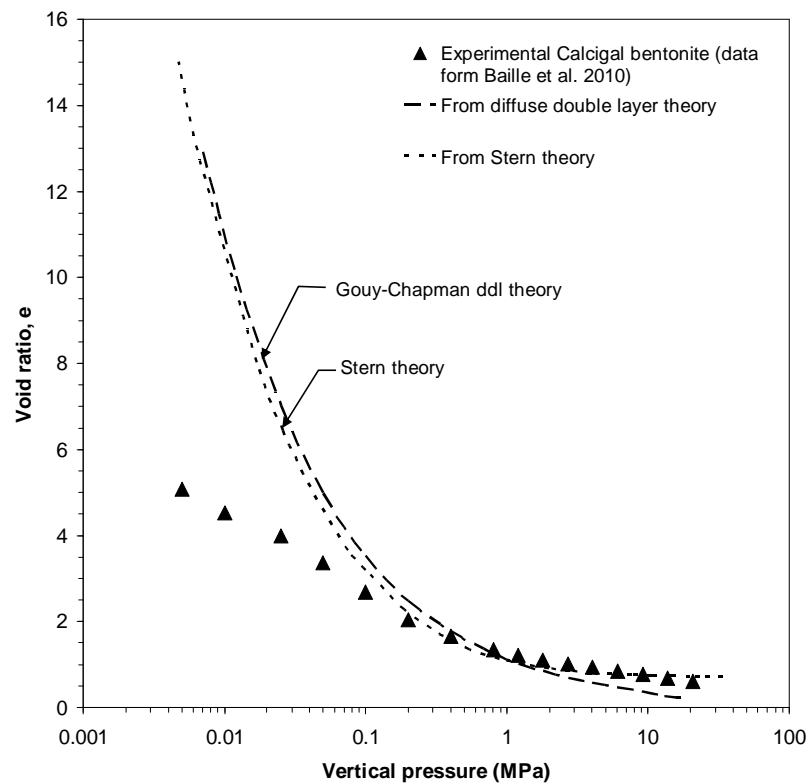


Figure 6.3. Theoretical and experimental e -log p relationships for Calcigel bentonite.

Figures 6.1, 6.2 and 6.3 showed that up to a vertical pressure of about 50 kPa for MX80 and Na-Ca MX80 bentonites and about 200 kPa for Calcigel bentonite, the calculated e -log p results from both the theories remained clearly above that of the experimental results indicating the influence of cation adsorption and less dispersive nature of the bentonites (Mitchell, 1993) even at the liquid limit water contents. The calculated e -log p relationships of the bentonites from the Gouy-Chapman diffuse double layer theory remained distinctly above that of the calculated e -log p relationships from the Stern theory at smaller pressures, whereas the reverse was true at higher pressures.

It was shown earlier that the specific adsorption potential (ϕ) (Fig. 5.6) had insignificant influence on the vertical pressure-void ratio relationship. Therefore, it appears that the specific surface of bentonites need some adjustments based on the number of clay platelets held together due to the specific adsorption effect. The calculated e -log p results from the Stern theory and the experimental results agreed reasonably well for pressures greater than 50 kPa for the MX80 and Na-Ca MX80 bentonites and greater than 200 kPa for Calcigel bentonite.

Beyond the limiting maximum pressures corresponding to $2d = 1.0$ nm ($e = 0.883$ for MX80 bentonite, $e = 0.928$ for Na-Ca MX80 bentonite and $e = 0.735$ for Calcigel bentonite), comparisons of the experimental results and the calculated results are not possible and this requires consideration of additional repulsive pressures (Verwey and Overbeek, 1948). In this context, studies carried out by Israelachvili and Wennerström (1996) and Marčelja (1997) have indicated that the hydration structure of ions and the osmotic effect of hydrated cations in the Stern-layer of two approaching clay platelets significantly influence the double layer repulsive pressure at close platelet spacing.

6.4 Concluding remarks

The applicability of the Stern theory on e - $\log p$ relationships of initially saturated bentonites (initial water content > liquid limit) is presented in this chapter. Comparisons of the calculated pressure-void ratio relationships from the Stern theory and the Gouy-Chapman diffuse double layer theory with the experimental consolidation test results for Na-rich bentonites (ESP > 50%) and a divalent-rich bentonite (ESP < 12%) showed that the Stern theory for interacting clay platelets improved the predictions, particularly within a vertical pressure range of 0.05 to 10.0 MPa for the Na-rich bentonites and between 0.2 and 10.0 MPa for the divalent-rich bentonite considered in this study.

Based on the results presented in chapter 5 and 6, it can be concluded that the Stern theory can be applied to establish the dry density-swelling pressure relationships of compacted MX80 bentonite up to a maximum dry density of 1.45 Mg/m³. However, the theory can be applied to determine the e - $\log p$ relationship of initially saturated bentonites for a wide range of void ratios.

Chapter 7

Effect of temperature and hydraulic gradients on thermo-hydro-mechanical behaviour of compacted bentonite

7.1 Introduction

In the past, several large scale laboratory and in-situ experimental investigations were carried out to study the behaviour of bentonites under various boundary conditions. Previous studies were conducted on compacted bentonites by simultaneous application of temperature and hydraulic loading (Yong and Mohammed, 1992; Villar et al., 1996; Yong et al., 1997; Selvadurai, 1996; Börgesson et al., 2001, Cuevas et al., 2002; Pintado et al., 2002; Fernández and Villar, 2010; Gómez-Espina and Villar, 2010). The temperature and the relative humidity variation with elapsed time were monitored during the tests along the depth of the bentonite specimens. Changes in the water content, the dry

density, the degree of saturation, the concentrations of cations and anions were measured after termination of the tests. However, the variation of swelling pressure during the thermal and the thermo-hydraulic tests were not monitored in the past. Therefore, the main objective of this chapter was to bring out the influence of thermal and thermal and hydraulic gradients on swelling pressure variation of the compacted bentonite specimens at the opposite end of heat source.

This chapter presents the influence of thermal and thermal and hydraulic gradients on the variation of temperature and relative humidity along the depth of bentonite specimens and development of swelling pressures at the opposite end of the heat source of bentonite specimens. Section 7.2 presents the detailed experimental program. Section 7.3 presents the temperature, relative humidity and suction variation with elapsed time at predetermined depths of the bentonite specimens tested, during the thermal and the thermo-hydraulic tests. The swelling pressure variation at the opposite end of the heat source of the bentonite specimens with elapsed time is presented. Changes in the water content, the dry density and the degree of saturation after termination of the thermal and the thermo-hydraulic tests are presented. The concluding remarks from this chapter are presented in section 7.4.

7.2 Experimental program

The device used to carry out the tests and the test set up are presented in chapter 3 (Figs. 3.21 and 3.23). The specimen compaction procedure and experimental methods are described in chapter 3 (section 3.4.3). The detailed experimental program is presented in Table 7.1.

In total three nos. of thermal tests and two thermo-hydraulic tests were carried out on compacted bentonite specimens with targeted dry density of 1.60 Mg/m^3 . After the compaction process was over, the actual height and mass of the compacted bentonite specimens were measured. The diameter of the specimens was equal to the inner diameter of the cell. Knowing the diameter and the height of the specimens volume of the specimens were calculated. For known mass, volume and water content, the dry density of the specimens were calculated. The actual compaction dry densities of the bentonite specimens were calculated from dimensions and mass measurements prior to testing.

Table 7.1 Experimental program for thermal and thermo-hydraulic tests

Test no.	Type of test	Initial conditions		Test duration (days)	Information gathered				
		w (%)	ρ_d (Mg/m ³)		During tests			After the tests	
					T (°C)	RH (%)	p (kPa)	w (%)	Concentrations of cations and anions
1.	Thermal	11	1.63	12	√	√	√	√	√
2.		11	1.61	65	√	√	√	√	√
3.		11	1.58	67	√	√	√	√	√
4.	Thermo-hydraulic	11	1.58	117	√	√	√	√	√
5.		11	1.60	182	√	√	√	√	√

ρ_d – Compacted dry density, T – Temperature, RH – Relative humidity, p – Swelling pressure, w – water content.

Figure 7.1 presents the test conditions applied and the information gathered during the thermal tests. Thermal tests (test nos. 1, 2 and 3) were carried out on compacted bentonite specimens by applying temperatures of 85°C and 25°C at the bottom end and at the top end of the cylindrical specimens (Fig. 7.1). The thermal tests were carried out for durations of 12, 65 and 67 days (Table 7.1). The temperature and the relative humidity of the bentonite specimens were monitored at distances of 20, 40 and 60 mm from the heater (Fig. 7.1). The relative humidity and the temperature along the height of the specimens were measured using the relative humidity and temperature measurement probes (section 3.4.3.2, chapter 3). The swelling pressure developed at the opposite end of the heat source of the bentonite specimens were monitored during the tests.

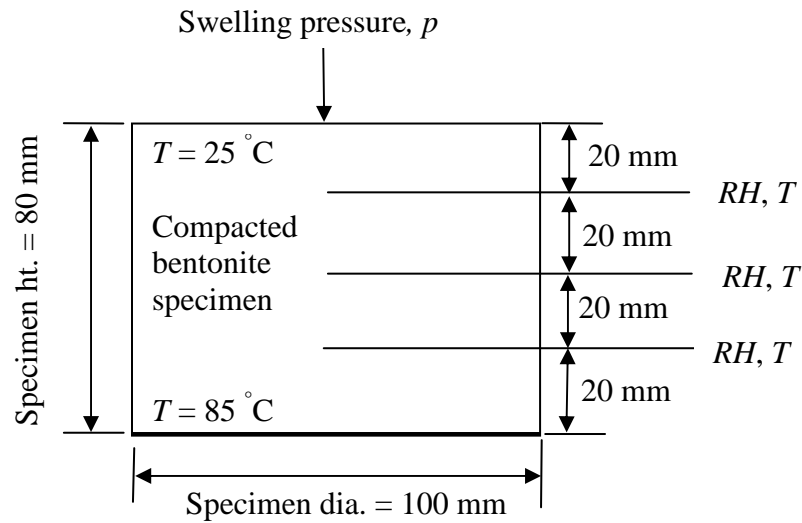


Figure 7.1. Schematic representation of temperature, relative humidity and swelling pressures measured in compacted bentonite specimens during thermal tests.

The experimental program adopted for the thermal tests was based on some trial tests carried out during the initial phase of the investigation. Trial tests indicated that swelling pressures developed at the opposite end of the heat source of the bentonite specimens due to any applied thermal gradients. In all cases, it was noted that the swelling

pressure increased and further decreased and equilibrated with an elapsed time. Therefore for the thermal tests, 3 specimens were tested. Test no. 1 was dismantled once the swelling pressure measured at the opposite end of the heat source of the specimen attained a maximum value. Test nos. 2 and 3 were terminated once the swelling pressures measured at the opposite end of the heat source of the compacted bentonite specimens were equilibrated.

Figure 7.2 presents the test conditions applied and the information gathered during the thermo-hydraulic tests. Two nos. of thermo-hydraulic tests (test nos. 4 and 5) were carried out for testing durations of 117 and 182 days (Table 7.1). The compacted bentonite specimens were initially subjected to temperatures of 85 and 25 °C at the bottom and at the top of the specimens (Fig. 7.1). Further, distilled water was supplied from the opposite end of the heat source of the specimens soon after the temperature and the relative humidity at specified heights along the depth of the bentonite specimens were equilibrated (Fig. 7.2). In test no. 4, the hydration of the bentonite specimens was started once the measured swelling pressure due to thermal loading attained the peak value (i.e. after 12 days of thermal loading). In test no. 5, distilled water was supplied after 72 days of thermal loading (i.e. once the measured swelling pressure due to thermal loading was equilibrated). Test nos. 4 and 5 were terminated once the temperature and the relative humidity along the depth of the specimens and the swelling pressure measured at the opposite end of the heat source were equilibrated.

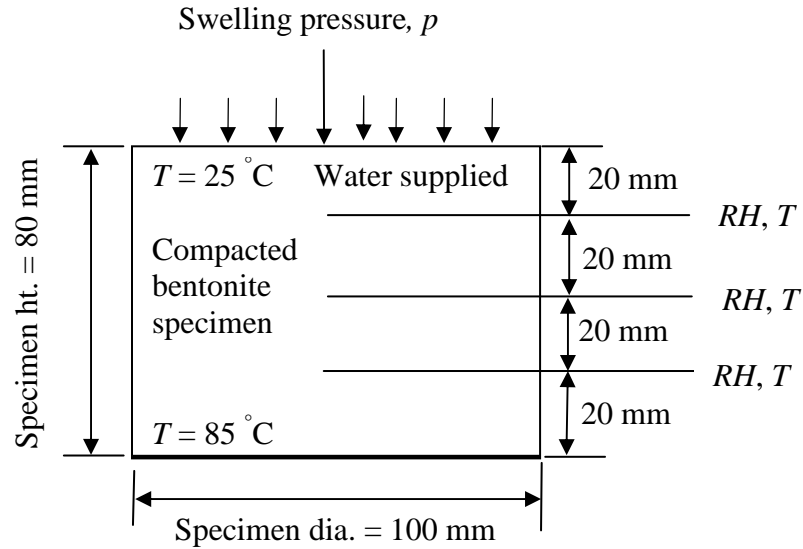


Figure 7.2. Schematic representation of temperature, relative humidity and swelling pressures measured in compacted bentonite specimens during thermo-hydraulic tests.

In order to study the thermal expansion of the PTFE liner of the device, two additional tests were carried out on a dummy PTFE specimen and a compacted Speswhite kaolin specimen. The details of these additional tests are presented in Table 7.2. A dummy PTFE specimen of diameter and height equal to the diameter and height of the compacted bentonite specimens was subjected to temperatures of $85\text{ }^{\circ}\text{C}$ and $25\text{ }^{\circ}\text{C}$ at the bottom and at the top end. The axial pressure measured at the opposite end of the heat source of the specimen was monitored during the test. A similar test was carried out using a compacted Speswhite kaolin specimen.

Table 7.2 Additional tests

Type of test	Material used	Information gathered
Thermal	Dummy PTFE specimen	Axial pressure measured
Thermal	Compacted Speswhite kaolin	

After termination of the thermal and the thermo-hydraulic tests, the bentonite specimens were sliced into 8 pieces of 10 mm thick using a hacksaw. The water content of each bentonite slice were determined. Additionally, a part of the specimen from each bentonite slice was used to measure the volume of tested bentonite slices using molten wax (ASTM D 4943-08-2008). The dry density and the degree of saturation of the bentonite specimens were calculated from the water content and the volume measurements.

The concentrations of cations and anions in each slice were measured by aqueous extraction technique using Ion Chromatography (IC) and Inductively Couple Plasma Optical Emission Spectroscopy (ICP-OES). The effects of thermal and thermo-hydraulic gradients on the distribution of cations and anions in the bentonite specimens are presented in chapter 8.

7.3 Results and discussion

The temperature and the relative humidity variation along the depth of the bentonite specimens during thermal loading was similar for all 5 tests. During the thermal

and hydraulic loadings, the variations of temperature and relative humidity along the depth of the bentonite specimens were similar for test nos. 4 and 5. Therefore, typical results of temperature and relative humidity/suction variation at distances of 20, 40 and 60 mm from the heater are presented for test no 5.

7.3.1 Transient temperature variation

Figure 7.3 presents the temperature variation with elapsed time at distances of 20, 40 and 60 mm from the heater for test no. 5. The inset of Fig. 7.3 shows that the temperatures at distances of 20, 40 and 60 mm from the heater were equilibrated within about 3 hours from the start of the thermal loading. The temperatures at distances of 20, 40 and 60 mm from the heater at equilibrium (about 180 minutes after the commencement of the tests) were 62, 54 and 41 °C, respectively.

Once the temperature and the relative humidity at distances of 20, 40 and 60 mm and the swelling pressure at the cold end of the specimen were equilibrated, distilled water was supplied. An immediate decrease in temperature was noted at the start of the hydraulic loading. At the start of the hydraulic loading, the temperatures at distances of 20, 40 and 60 mm from the heater were 57.5, 40 and 34.5 °C, respectively. A decrease in the temperature at the start of the hydraulic loading can be attributed to the differences between the temperature of hydrating water (25 °C) and the temperature of the bentonite specimen.

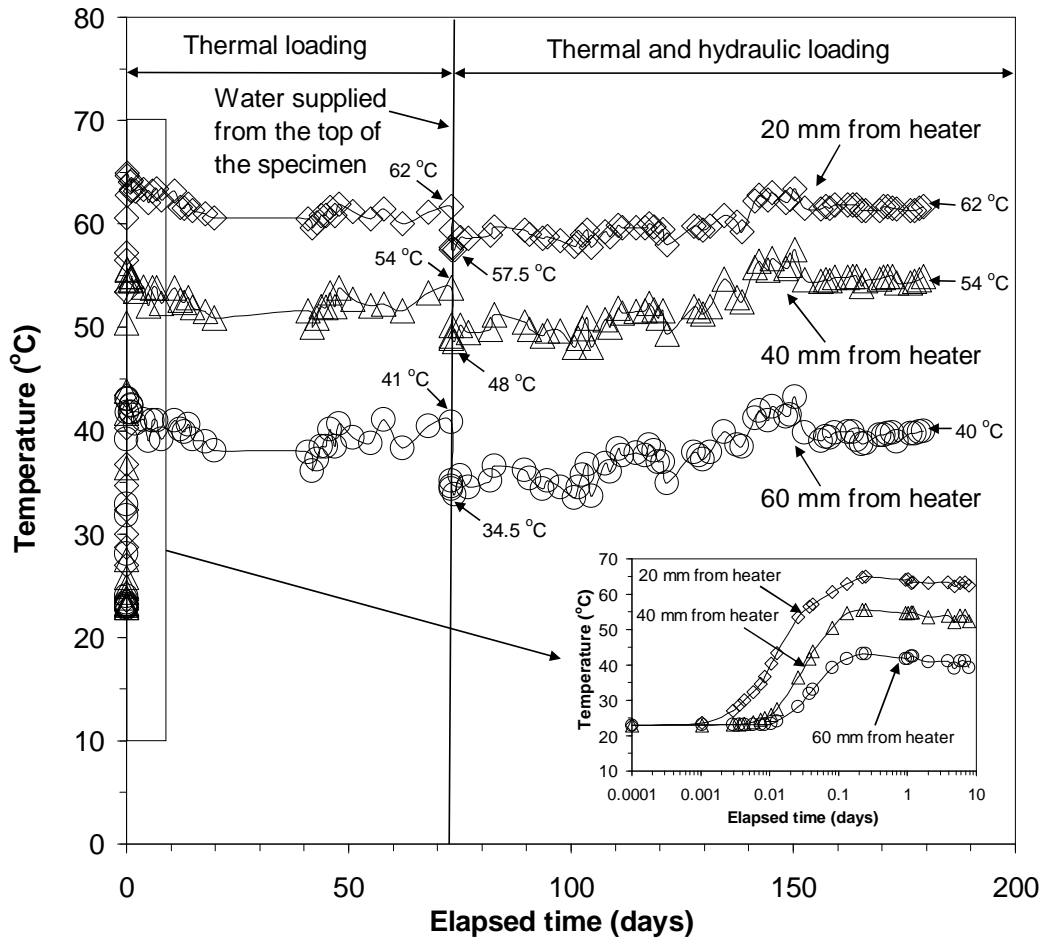


Figure 7.3. Transient temperature variations at specified depths of the specimens due to thermal, thermal and hydraulic loading (test no. 5).

The temperatures at distances of 20, 40 and 60 mm from the heater were found to increase during the hydraulic loading period. The equilibrium temperatures due to the thermal and hydraulic loading at salient levels of the bentonite specimen were equal to that of the equilibrium temperatures due to thermal loading. The thermal conductivity of bentonite increases with an increase in the water content (Tang et al., 2008). It was noted that during the thermal and hydraulic loadings, the temperatures at salient levels of the bentonite specimen were increased until the relative humidity at all levels were

equilibrated. Therefore, an increase in the temperature during the thermal and hydraulic loading was due to an increase in the thermal conductivity of the specimens.

7.3.2 Transient relative humidity variation

During the thermal and the thermo-hydraulic tests, the temperature and the relative humidity were measured at distances of 20, 40 and 60 mm from the heater. The measured relative humidity due to thermal loading was similar for all tests. The relative humidity variations with elapsed time due to the thermal and hydraulic loading for test nos. 4 and 5 were found to be similar. Therefore, typical result of the relative humidity variation along the depth of the bentonite specimen was considered.

Figure 7.4 presents the transient relative humidity variation at distances of 20, 40, and 60 mm from the heater for test no. 5 (thermal and thermo-hydraulic phases). The inset of Fig. 7.4 shows the variations of the relative humidity at predetermined heights of 20, 40 and 60 mm from the heater during the thermal loading period.

The relative humidity is the ratio of partial vapour pressure to the saturation vapour pressure at the same temperature. At the commencement of the thermal test, the temperature was found to increase at all predetermined heights of the specimen. An increase in the temperature caused an increase in the partial vapour pressure that was manifested on an increase in the relative humidity at all salient levels during the thermal equilibration period of about 2 hours. However, the relative humidities at all levels were found to decrease before an equilibration was attained. Similar relative humidity variation during Temperature Buffer Test (TBT) has been reported by Åkesson et al. (2009).

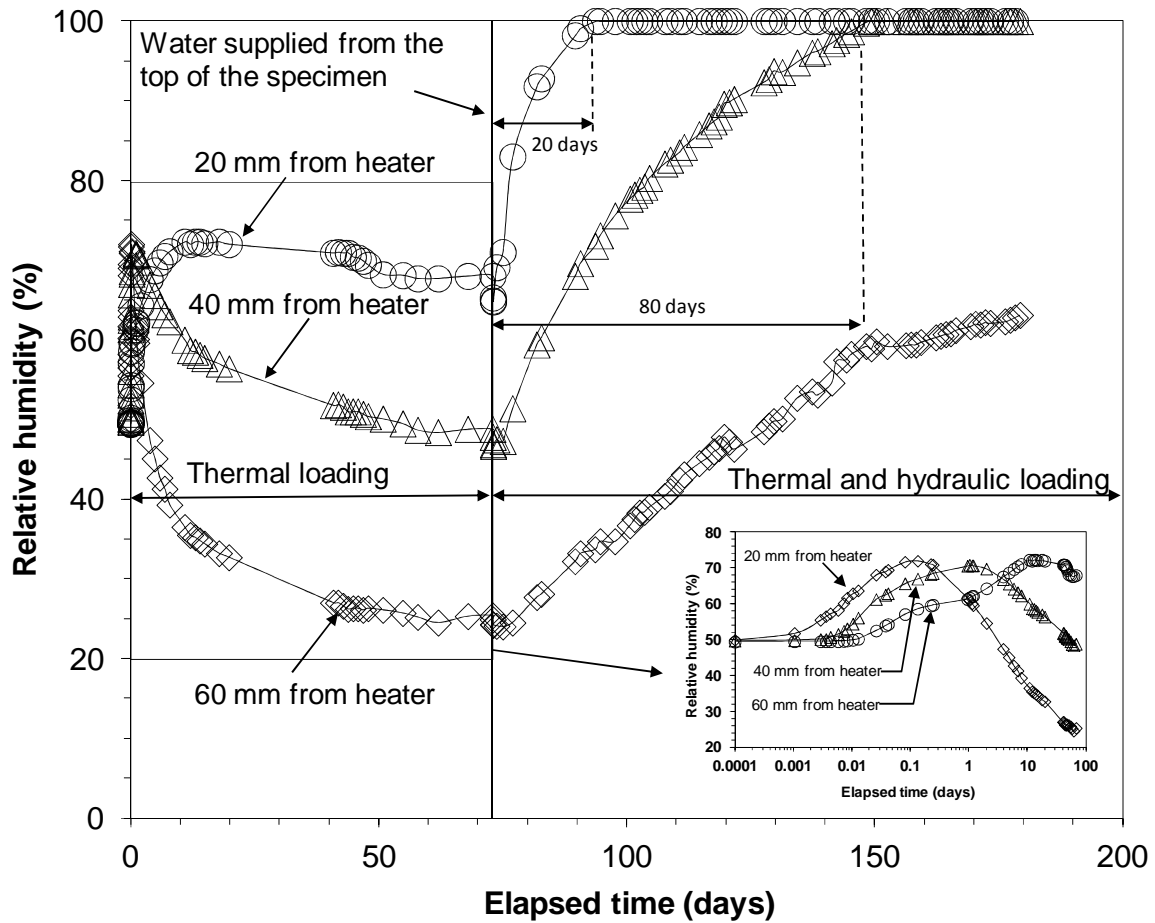


Figure 7.4. Transient relative humidity variations at specified depths of the specimens during thermal, and thermal and hydraulic loading (test no. 5).

The relative humidity at salient levels were equilibrated after about 50 days of thermal loading phase. At equilibrium, the relative humidities at distances of 20, 40 and 60 mm from the heater were 25%, 45% and 70%, respectively (Fig. 7.4). During the hydraulic loading, the relative humidities at all specified depths of the specimen were found to increase. At distances of 40 and 60 mm from the heater (closer to the hydration end), the relative humidity was found to be 100% after 20 and 80 days of hydraulic loading, respectively (Fig. 7.4). The relative humidity at a distance of 20 mm from the heater was about 60% at the time of terminating the test (Fig. 7.4).

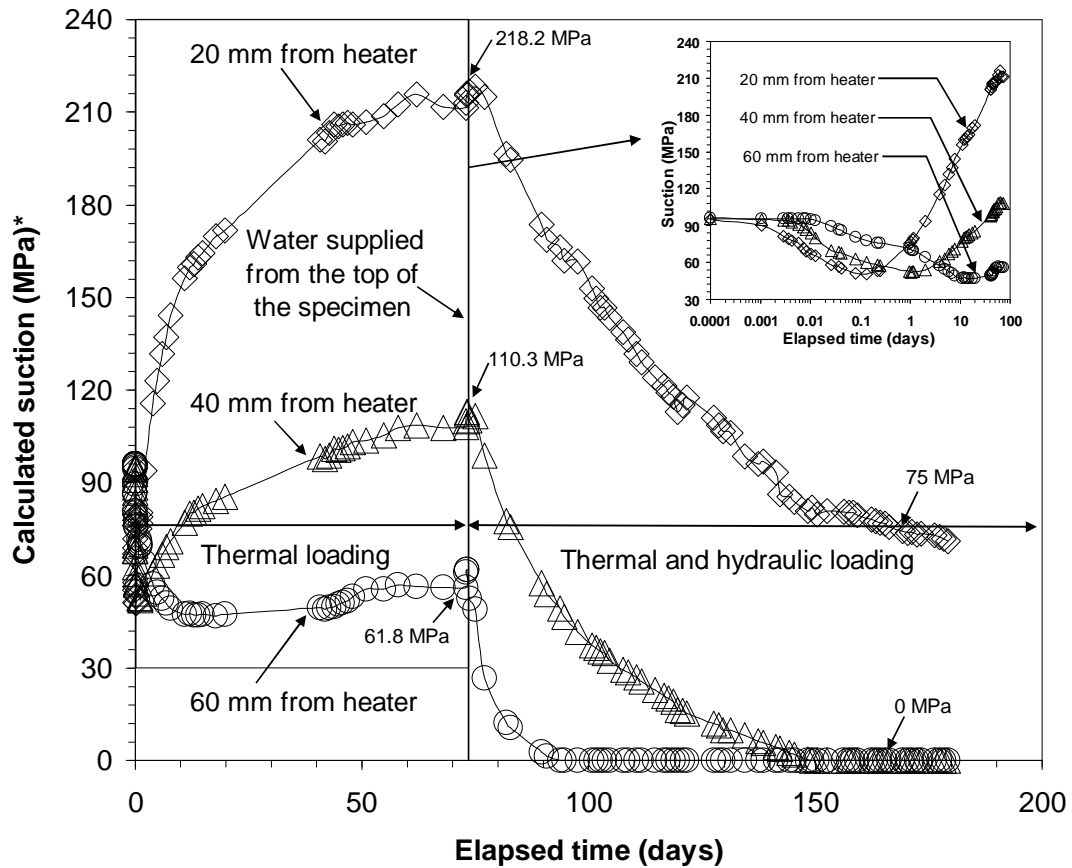
7.3.3 Transient suction variation

From the measured relative humidity and temperature data, the transient suction changes were calculated using the Kelvin's equation presented in chapter 3 (eq. 3.1). In eq. 3.1, a_w is the water activity. The relationship between the water activity (a_w) and the relative humidity (RH) is expressed as:

$$RH = 100 \times a_w \quad (7.1)$$

The relative and the temperature variation along the depth of the specimens were similar for all the tests during the thermal loading. Therefore, the calculated suction variation with elapsed time were similar for all the tests during the thermal loading. Similarly, the calculated suction variation during the thermal and hydraulic loading for test nos. 4 and 5 were similar. Therefore, typical results of suction variation with elapsed time along the depth of the specimen are presented.

Figure 7.5 presents the variation of suction at distances of 20, 40 and 60 mm from the heater for test no. 5 (thermal and thermo-hydraulic phases). The calculated initial suction at distances of 20, 40 and 60 mm from the heater was about 96 MPa. At the commencement of the test, the relative humidity was found to increase due to increase in partial vapour pressure at salient levels (distances of 20, 40 and 60 mm from the heater) (Fig. 7.4). Therefore, the suction at all predetermined heights were found to decrease (Fig. 7.5). At equilibrium, due to the thermal loading, the calculated suctions at distances of 20, 40 and 60 mm from the heater were 218.2, 110.3 and 61.8 MPa, respectively (Fig. 7.5).



*Calculated based on temperature and relative humidity measurements.

Figure 7.5. Transient suction variations at specified depths of the specimen (test no. 5).

During the hydraulic loading phase, the relative humidity at all salient levels were increased with an elapsed time (Fig. 7.4). Consequently, the calculated suctions at all salient levels were decreased. At a distance of 60 mm from the heater, the suction became zero after 20 days from the start of the hydraulic loading phase (Fig. 7.5). At distances of 40 and 60 mm from the heater, the calculated suctions were equilibrated after 75 days from the start of the hydraulic loading phase. The equilibrium suctions at distances of 40 and 60 mm from the heater were found to be zero and 75 MPa, respectively (Fig. 7.5).

The relative humidities were found to be 100% at distances of 40 and 60 mm from the heater at the time of terminating the test (Fig. 7.4). Therefore, the calculated suctions at

distances of 40 and 60 mm from the heater were zero (Fig. 7.5). At a distance of 20 mm from the heater, the calculated suction was equilibrated at 75 MPa, similar to the initial calculated suction of the specimen (Fig. 7.5). The rate of movement of water flow towards the heater was retarded due to constant heat source and hence the suction at a distance of 20 mm from the heater was equilibrated at 75 MPa.

7.3.4 Swelling pressure due to thermal loading

The time versus swelling pressure development at the opposite end of the heat source of the compacted bentonite specimens due to thermal loading (test nos. 1, 2 and 3) are shown in Figs. 7.6 (a) and 7.6 (b) in semi-logarithmic and arithmetic scale, respectively. The swelling pressures measured at at the opposite end of the heat source of the compacted bentonite specimens attained maximum swelling pressure after 7 to 10 days of thermal loading. The measured swelling pressures at at the opposite end of the heat source of the compacted bentonite specimens were found to be decreased for longer duration of thermal loading. Finally, the swelling pressures exerted by the compacted bentonite specimens at at the opposite end of the heat source were equilibrated after about 50 days of thermal loading. Water vapour was found to have been transferred from the hotter end of the compacted bentonite specimen to the cooler end, where it had subsequently condensed. This resulted in an increased water content that was observed at the cooler end. This increase in water content can cause expansion in the bentonite specimen, but under restrained conditions the bentonite specimens will respond to an increase in water content by demonstrating an increase in swelling pressure. Conversely, the hotter end may undergo shrinkage due to a desaturation effect; this was not found to be significant for the compacted bentonite system. Bentonite specimen from the middle layer

is subject to both wetting and drying. It should be noted that the swelling pressure measured at the opposite end of the heat source of the bentonite specimen was the overall swelling pressure that had been executed along the specimen depth.

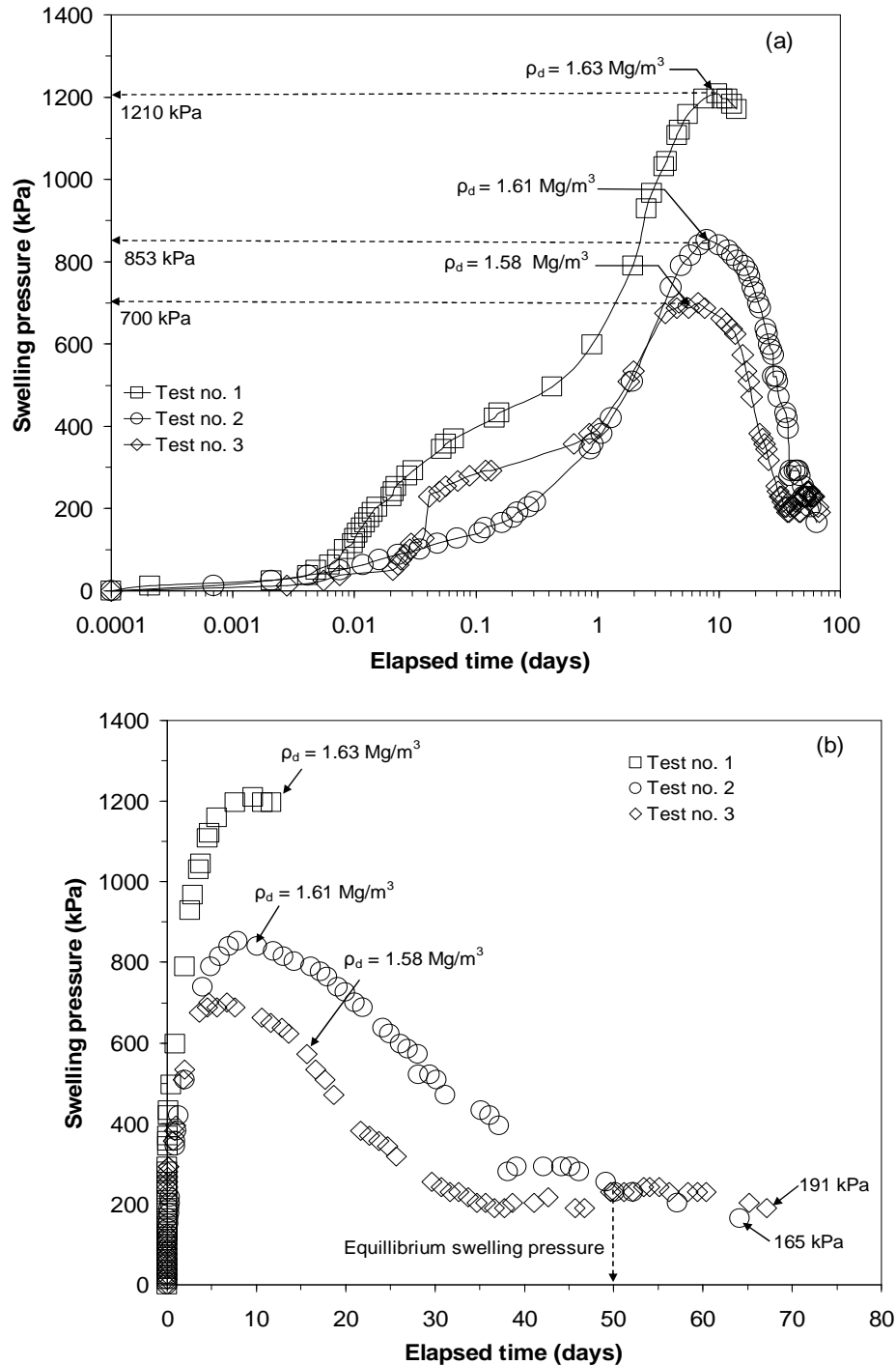


Figure 7.6. Time versus swelling pressure plots in (a) semi-logarithmic scale and (b) arithmetic scale during thermal tests on compacted bentonite specimens.

The maximum swelling pressures measured for test nos. 1, 2 and 3 were 1210, 853 and 700 kPa, respectively (Fig. 7.6 (a)). The swelling pressure was found to increase with an increase in the initial compaction dry density. The maximum swelling pressures were attained after 10, 8 and 7 days of the thermal loading phase for test nos. 1, 2 and 3, respectively. For test nos. 2 and 3, the swelling pressures were equilibrated after 50 days of thermal loading. The equilibrium swelling pressures were 165 and 191 kPa for the test nos. 2 and 3, respectively (Fig. 7.6 (b)). The axial pressure measured at the at the opposite end of the heat source of a dummy PTFE specimen and compacted Speswhite kaolin specimen are shown in Fig. 7.7 for comparison.

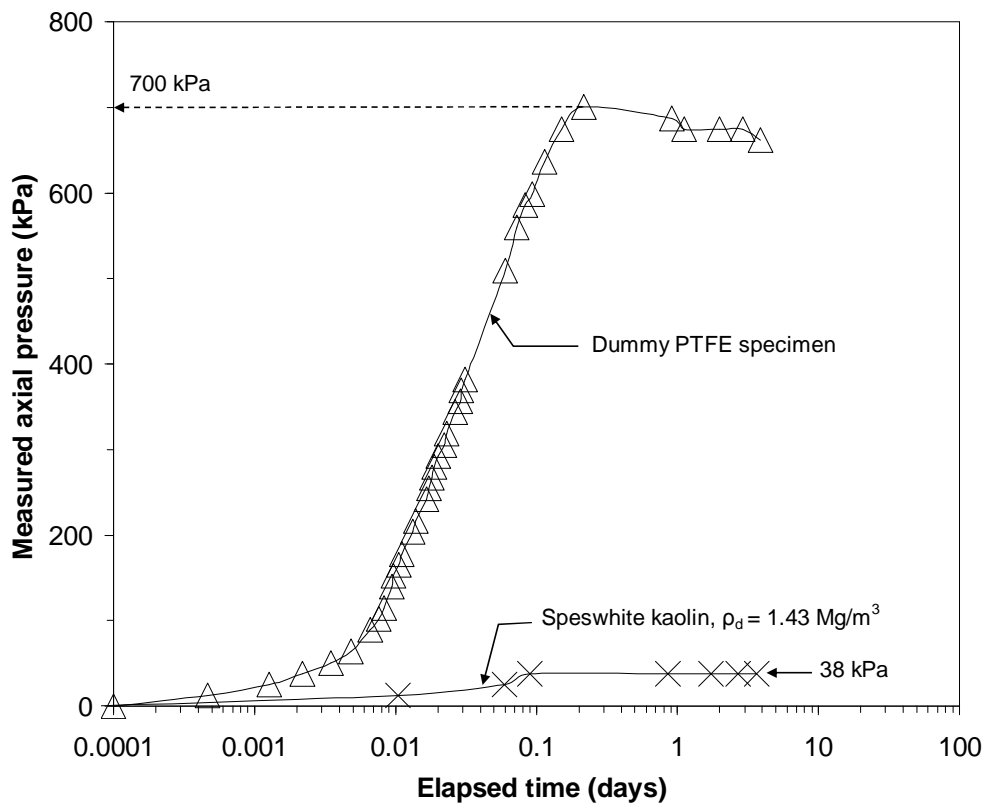


Figure 7.7. Time versus axial pressure plots during thermal tests on dummy PTFE specimen and compacted Speswhite kaolin.

The measured axial pressure at the opposite end of the heat source of the dummy PTFE specimen equilibrated within about 2 hours from the start of the test. The PTFE specimen exerted pressures of 700 kPa (Fig. 7.7). The axial pressure measured at the cold end of the dummy PTFE specimen can be attributed to the thermal expansion of the material. Compacted Speswhite kaolin specimen exerted an axial pressure of 38 kPa due to an applied thermal loading (Fig. 7.7).

The test results clearly indicated that due to the specific design of the testing device, the expansion of PTFE liner subjected to thermal loading was not reflected on the axial pressure exerted by Speswhite kaolin specimen. Therefore, it can be stated that the expansion of the PTFE liner did not influence the measured swelling pressures of the compacted bentonite specimens during the thermal tests.

If a certain volume of moist-soil is being heated at one side, the water in soil close to the heater will evaporate. The evaporated water vapour will be transported from the hotter area to the cooler region of the soil and will condense to form liquid water (Samper et al., 2001; Pusch and Yong, 2006). During the thermal tests on compacted bentonite specimens and subjected to elevated temperature at one end, the water vapour diffused away from the hotter area to the cooler area of the bentonite specimens and condensed (Samper et al., 2001). The condensation of the diffused water at the opposite end of the heat source of the bentonite specimen contributed to an increase in the water content as evident from the relative humidity results shown in Fig. 7.4. The restrained compacted bentonite specimens exhibited swelling pressure at the opposite end of the heat source due to an increase in the water content. Simultaneously, at the hot end, the bentonite specimen had undergone a shrinkage process. The overall effect of an increase in the swelling

pressures for the first 7 to 10 days of applied thermal loading is attributed to the higher rate of swelling at the cold end than the rate of shrinkage occurred at the hot end of the compacted bentonite specimens.

The reduction in swelling pressures can be explained from the relative humidity variations shown in Fig. 7.4. The relative humidity at the cold end of the bentonite specimens (at a distance of 60 mm from the heater) was equilibrated within 7-10 days of thermal loading. The relative humidity values at distances of 20 and 40 mm from the heater were found to decrease up to about 50 days of applied thermal loading. Therefore, a high suction gradient existed from the hot end to the cold end of the specimens. Due to a higher temperature at the bottom of the specimen, the water vapour transported from the hotter area to the cooler area of the specimens. However, a counter-opposing moisture flux occurred from the cold to the hot end of the specimens (Fig. 2.9). Therefore, water redistribution took place inside the compacted bentonite specimens (Åkesson et al., 2009).

Liquid water tends to move towards the hot end of the specimens due to a higher suction and water content gradient. On the other hand, the swelling of the restrained bentonite specimen at the cold end was due to a higher water content that resulted in the development of swelling pressure and local compression of the material (Pusch and Yong, 2006). The overall effect was manifested in a decrease in the swelling pressure at the cold end of the bentonite specimens for prolonged period of thermal loading. The water content of the bentonite specimens equilibrated after about 50 days of thermal loading that was manifested in the equilibrium swelling pressure results.

7.3.5 Swelling pressure due to thermal and hydraulic loadings

Figures 7.8 (a) and 7.8 (b) present the time versus swelling pressures measured at the cold end of the compacted bentonite specimens during the thermo-hydraulic tests (test nos. 4 and 5) in semi-logarithmic and arithmetic scale. Distilled de-aired water was supplied from the top end of the specimens after 12 days and 72 days of thermal loading phase for test nos. 4 and 5, respectively. Prior to supplying water, the swellings pressures of the specimens were 483 and 382 kPa for test nos. 4 and 5, respectively. The variation of swelling pressure during the thermal loading period was found to be similar to that was noted for test nos. 1, 2 and 3. Upon supplying water from the cold end of the bentonite specimens, the measured swelling pressure further increased. The maximum swelling pressure measured at equilibrium was about 2550 kPa for both tests (test nos. 4 and 5) after 105 and 110 days of hydration period (Fig. 7.8).

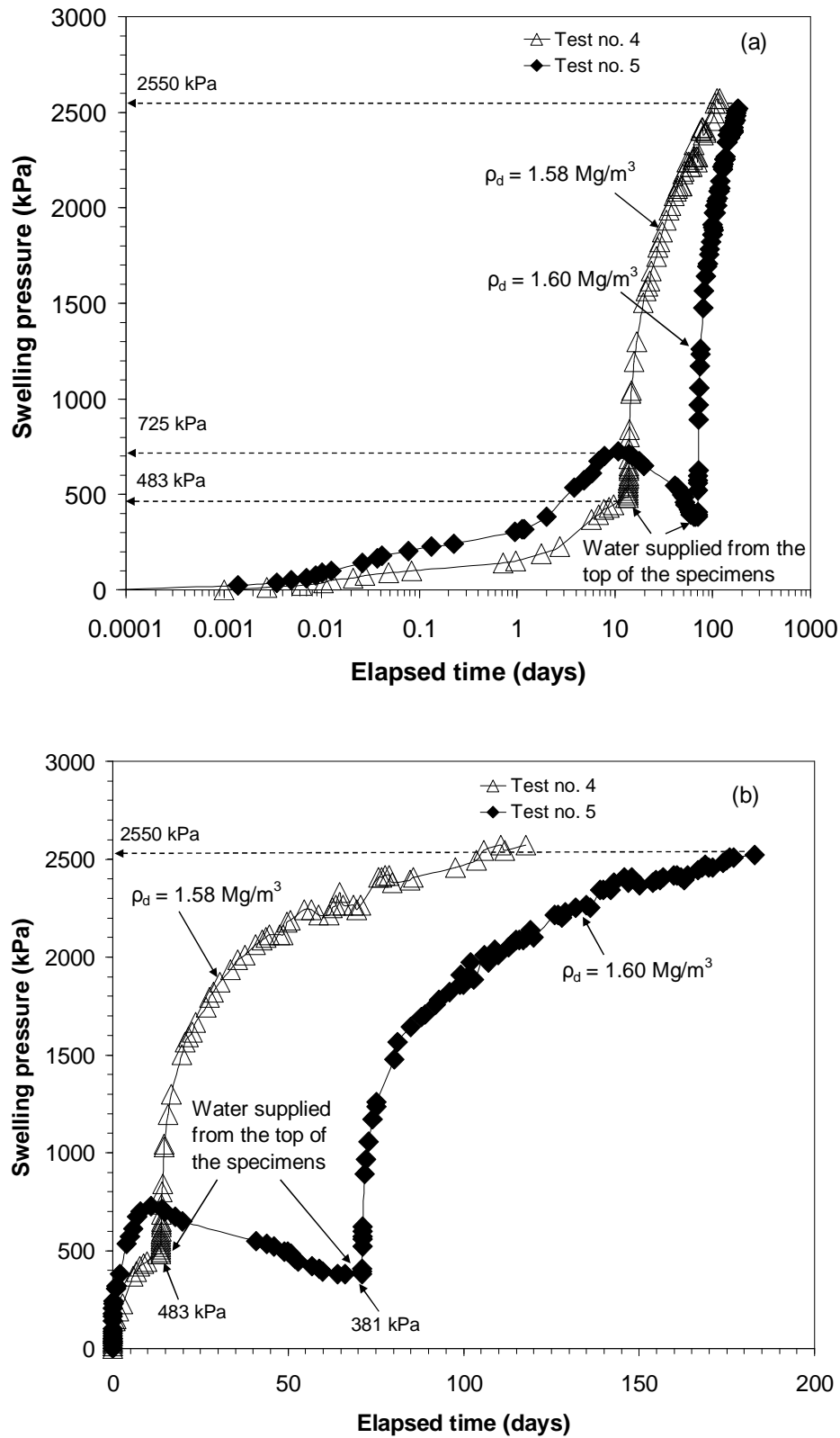


Figure 7.8. Time-swelling pressure plots in (a) semi-logarithmic scale and (b) arithmetic scale during thermo-hydraulic tests on compacted bentonite specimen.

7.3.6 Water content variation

7.3.6.1 Effect of thermal gradient

The measured water contents at various depths after termination of the thermal tests (test nos. 1, 2, 3) are shown in Fig. 7.9. The initial water content of the bentonite (11%) is shown for comparison. Due to the applied thermal gradient, the water contents at the heater end were lesser than the initial water content of the specimens as water vapour transferred from the hot end to the cold end.

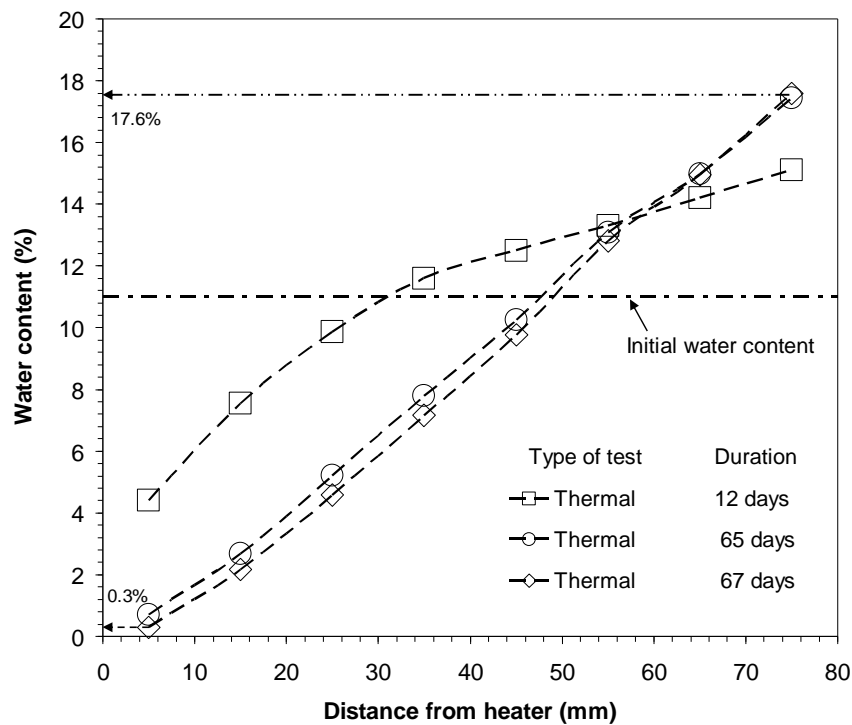


Figure 7.9. Distribution of water contents in bentonite specimens after thermal tests.

The measured water content along the depth the bentonite specimens was found to be similar after 65 and 67 days of thermal loading. The minimum and maximum water contents were found to be 0.3% and 17.6% after 65 and 67 days of thermal loadings, respectively (Fig. 7.9). The overall mass balance could not be obtained. An overall loss of

2% water content was noted after termination of the thermal test of 67 days. The results confirmed that water in the form vapour moved away from the heater and condensed at the cold end of the bentonite specimens.

7.3.6.2 Effect of thermal and hydraulic gradients

Figures 7.10 and 7.11 show the physical appearances of bentonite specimens after terminating the thermo-hydraulic tests (test nos. 4 and 5). The differences in darkness of the colour indicates the water content of the specimens were not uniform. The darker part of the specimen with higher water content was nearest to the hydration end, whereas the brightest part with lesser water content was close to the heater end.



At 20 mm distance
away from heater

At 40 mm distance
away from heater

At 60 mm distance
away from heater

Figure 7.10. Physical appearances of the bentonite specimen at three sensors level after thermo-hydraulic test no. 4 (Photographs were taken while dismantling).



Figure 7.11. Physical appearances of the bentonite specimen after dismantling thermo-hydraulic test no. 5.

Figure 7.12 presents the measured water contents along the depth of the bentonite specimens after dismantling the thermo-hydraulic tests (test nos. 4 and 5). At the cold end of the specimens, the measured water contents after 105 and 110 days of hydraulic loading were found to be similar (about 39.0%). At the heater end, the water contents were found to be 5.0% and 2.2% for test nos. 4 and 5, respectively (Fig.7.12).

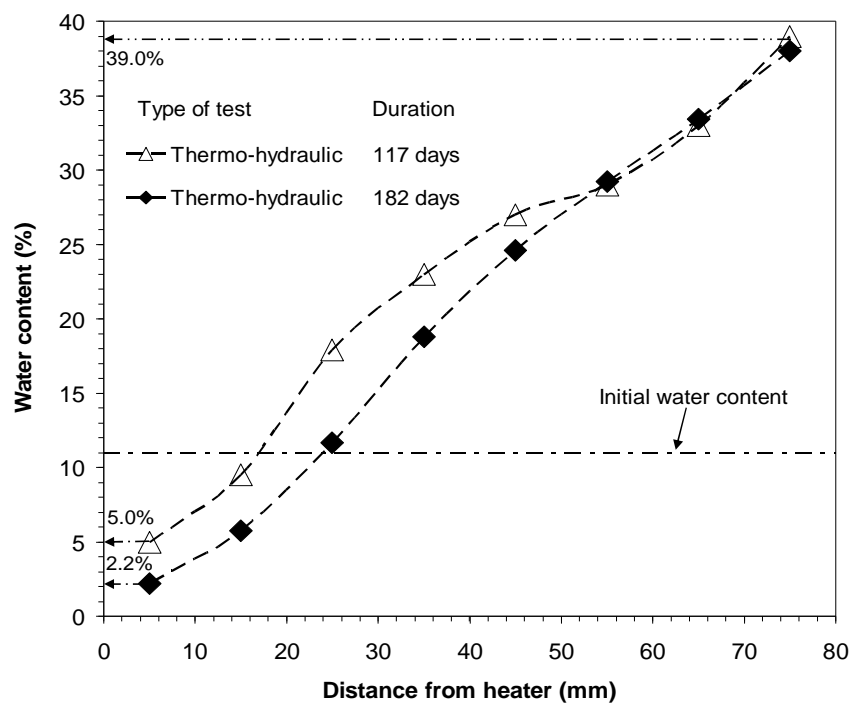


Figure 7.12. Distribution of water contents in bentonite specimens after thermo-hydraulic tests.

7.3.7 Comparison of swelling pressures with oedometer test results

The swelling pressure test results presented in chapter 4 were compared with the measured swelling pressures in the thermal and the thermo-hydraulic tests. The maximum water content at the cold end of the bentonite specimens after termination of thermal tests was found to be about 18%. The water contents along the depth of the bentonite specimens were varied between 0.3% and 18% (Fig. 7.9). The measured water content after termination of the thermal tests was lesser than the saturation water content (34-35%) for the specimens with similar compaction dry densities (Table 4.3). Therefore, the measured swelling pressures due to thermal loading (0.5 to 1.2 MPa) were far lesser than swelling pressures exerted by fully saturated specimen in series I tests (2500 kPa to 2800 kPa) (Table 4.3).

After termination of the thermo-hydraulic tests, the maximum water content at the cold end was found to be about 39%. The measured water content along the depth of the specimens were found to vary between 2.2% and 39% (Fig. 7.12). Therefore, the swelling pressure exhibited by the bentonite specimen is expected to be different along the depth of the bentonite specimen. The average water content of the bentonite specimen close to the hydration end (top 20 mm) was similar to the saturation water content of bentonite specimen at similar dry densities shown in chapter 4 (water content = 34.5%) (Table 4.3). The measured swelling pressures during the thermo-hydraulic tests were very similar to that was noted for constant volume swelling pressure tests at similar compaction dry densities (about 2.5 MPa). Therefore, the measured swelling pressure during thermo-hydraulic tests was due to the local swelling (top 20 mm) of the compacted bentonite specimens.

The actual dry density of the specimens was not measured during the development of swelling pressure. The dry densities of the specimens were determined after extruding the specimens from the cell. Therefore, the comparison is being made at similar compacted dry densities. On the other hand, due to the thermal and hydraulic gradients the chemical composition of the bentonite specimen may change. An overall increase of cations and anions population is expected close to the heater due to thermal and hydraulic gradients (see chapter 8) (Fernández et al., 2004; Cleall et al., 2007; Samper et al., 2008; Fernández and Villar, 2010). However, the measured swelling pressures after the thermo-hydraulic tests were found to be similar to that of the saturated bentonite specimens tested in oedometers. Therefore, it can be concluded that the swelling pressures exerted by the compacted bentonites due to the thermal and hydraulic loading primarily on account of dependent on the dry density and the water content of the specimens.

7.3.8 Dry density and degree of saturation variation

7.3.8.1 Effect of thermal gradient

The dry density and the degree of saturation of each bentonite slices were calculated from measured water content and measured volumes of the bentonite specimens after termination of the thermal and the thermo-hydraulic tests. The variation of the dry density and the degree of saturation for tests nos. 1, 2 and 3 were found to be similar. Therefore, typical results for test no. 3 are presented. Figure 7.13 presents the dry density and the degree of saturation along the depth of the bentonite specimen for test no. 3. The initial dry density and the degree of saturation of the specimen are also shown in Fig. 7.13 for comparison.

The dry density of the bentonite specimen at the cold end having higher water content was found to decrease after removal from the cell. The dry density of the specimen at the heater end was found to increase due to shrinkage. An overall decrease of dry density of the bentonite specimen was found to be 0.01 Mg/m^3 as against the initial dry density (1.58 Mg/m^3) of the compacted specimen prior to testing. The dry density of the specimen at the cold end was found to be 1.50 Mg/m^3 , whereas the dry density was found to be 1.61 Mg/m^3 at the hot end (Fig. 7.13).

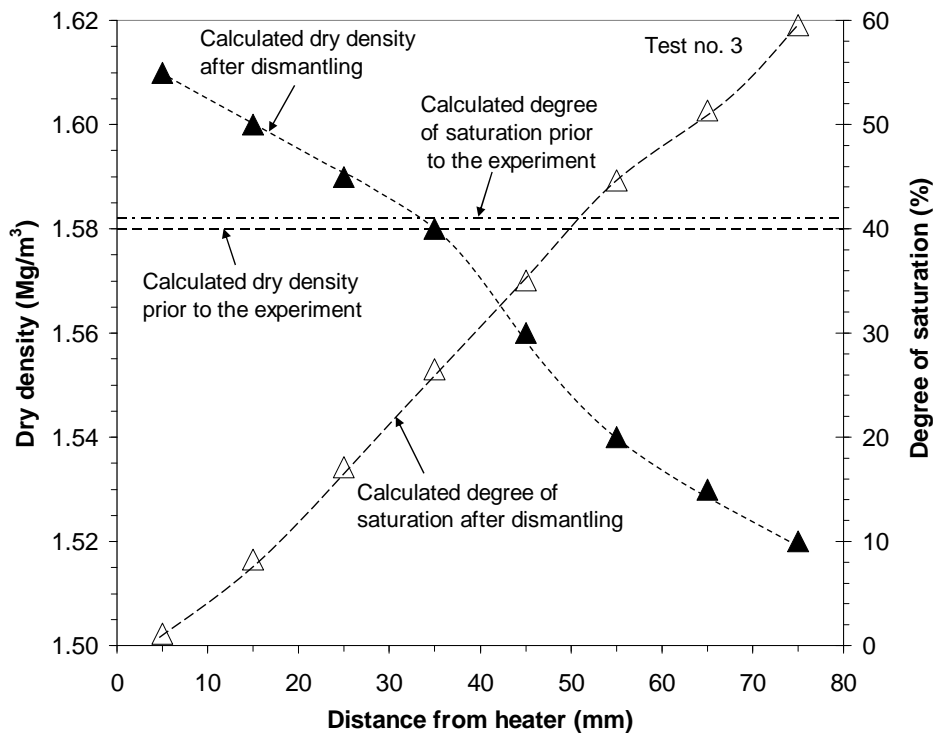


Figure 7.13. Dry density and degree of saturation variation along the depth of the specimen after thermal test of 67 days (test no. 3).

The degree of saturation was found to be increased due to an increase in the water content of the specimen away from the hot end. The degree of saturation of the specimen at the cold end was found to be 60%, whereas the specimen remained very dry at the hot end (degree of saturation $\approx 10\%$) (Fig. 7.13).

7.3.8.2 Effect of thermal and hydraulic gradients

The variation of dry density and the degree of saturation for tests nos. 4 and 5 were found to be similar. Therefore, typical results of test no. 5 are presented. Figure 7.14 shows the dry density and the degree of saturation at various depths for test no. 5. The initial dry density and the degree of saturation of the specimen are also shown in Fig. 7.14 for comparison. The partially saturated bentonite specimen expanded once the tested specimen was extruded from the device. Therefore, the dry density of the specimen at the cold end having higher water content was found to decrease. The dry density of the specimen at the heater end was found to increase due to shrinkage as noted during the thermal tests. An overall decrease of the dry density of the specimen was found to be 0.08 Mg/m^3 as against the initial dry density (1.60 Mg/m^3) of the compacted specimen prior to testing. Similar effect has been reported by several researchers (Villar et al., 1997; Villar et al., 2007; Åkesson et al., 2009; Espina-Gómez and Villar, 2010; Fernández and Villar, 2010). The dry density of the specimen at the cold end was found to be 1.35 Mg/m^3 , whereas the dry density was found to be 1.71 Mg/m^3 at the hot end.

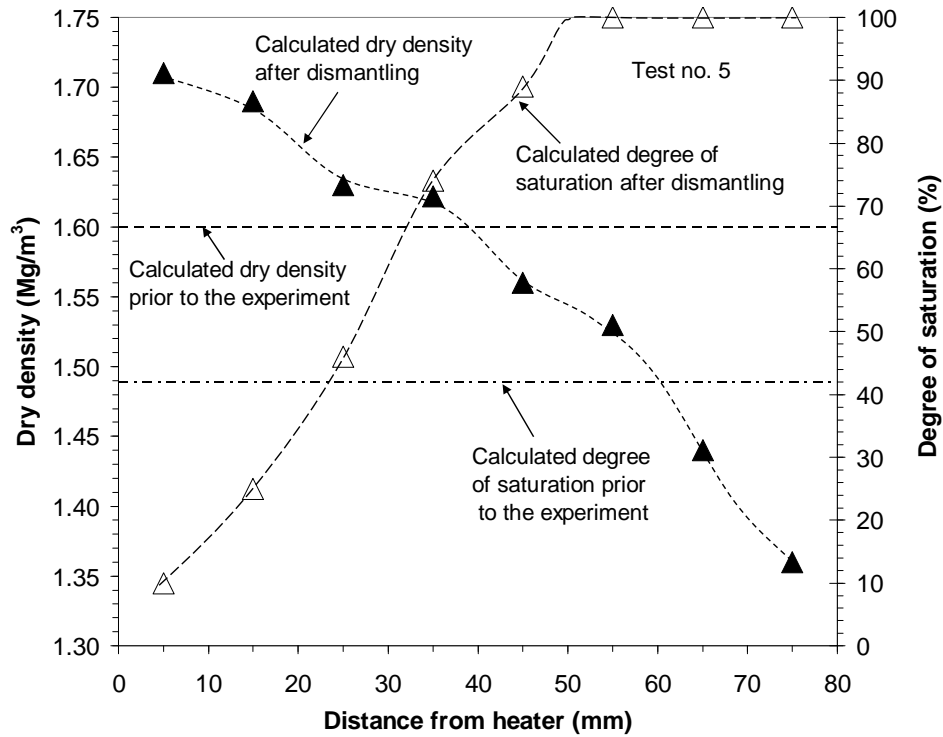


Figure 7.14. Dry density and degree of saturation variation along the depth of the specimen after thermo-hydraulic test of 182 days (test no. 5).

Similar to the effect of thermal loading, the degree of saturation was found to be increased due to an increase in the water content of the specimen away from the hot end. After termination of the thermo-hydraulic tests, the degree of saturation of the specimens close to the hydration end was found to be 100% (Fig. 7.14). However, the degree of saturation at the hot end was very similar to that was noted after termination of the thermal tests (degree of saturation $\approx 10\%$) (Fig. 7.14).

7.4 Concluding remarks

In this chapter, the influence of thermal and thermal and hydraulic gradients on thermo-hydro-mechanical behaviour of compacted bentonites is presented. A detailed

experimental program and the test methods adopted are described. The test results include: transient temperature, relative humidity and corresponding calculated suction profiles at specified depths of the compacted bentonite specimens, the time versus measured swelling pressure at the opposite end of the heat source of the compacted bentonite specimen due to the thermal and the thermo-hydraulic loading and change in the water content, the dry density and the degree of saturation along the depth of the compacted bentonite specimens after termination of the thermal and the thermo-hydraulic tests are presented. Based on the findings of this study, the following concluding remarks can be made.

The relative humidity, the water content and the degree of saturation were found to increase from the hot end to the cold end of the compacted bentonite specimens due to applied thermal and hydraulic gradients. However, the dry density was found to decrease from the hot end to the cold end of the bentonite specimens due to an increase in the water content. The above findings are in concurrent results reported in the literature.

Due to an applied thermal gradient, the bentonite specimens exerted swelling pressures of 0.5 to 1.2 MPa (initial compaction dry densities between 1.58 and 1.63 Mg/m³). The swelling pressures developed in compacted bentonite specimens at the opposite end of the heat source are primarily due to an increase in the water content. The difference in suction and water content gradients inside the bentonite specimens lead to redistribution of water and hence a decrease in the swelling pressures with an elapsed time.

Chapter 8

Effects of temperature and hydraulic gradients on solute transport in compacted bentonite

8.1 Introduction

Compacted bentonites are extensively used in several geotechnical engineering applications. One of the important applications of compacted bentonites is proposed to be used as barrier and backfilling materials in deep geological repositories. For the safety assessments of geological disposal of high-level radioactive waste, migration behaviour of radionuclide in compacted bentonite is of great interest. An understanding of the pore water composition of bentonite is essential, since the pore water composition influences the release and transport behaviour of radionuclide (Kozaki et al., 2001; Fernández et al., 2001, 2004).

The time required for the decay of radioactivity up to the threshold values of the natural radioactivity is several thousands of years. The chemical stability of bentonite during this period is crucial for satisfactory performance of engineered barrier systems. The clay barrier needs to be studied for some short-term processes to assure its long-term effectiveness (Martín et al., 2000). One of these processes is the accumulation of solutes transported through bentonites during the hydration period. This process can be influenced by the existence of a thermal gradient or even a thermo-hydraulic gradient. A thermal gradient can give rise to a concentration gradient. The higher concentration gradient due to chemical transport phenomenon may result in increasing hydraulic conductivity and decreasing osmotic swelling on compacted natural clays (Yong et al., 1992; Di Maio, 1996). The salinity of bentonite buffer accelerates the corrosion of the steel/copper canister containing spent fuel (Pusch and Yong, 2006).

This chapter presents the processes of salt migration in compacted bentonite and the possibility of accumulation of salts in specific regions due to thermal and hydraulic gradients across compacted cylindrical bentonite specimens. The compacted cylindrical bentonite specimens were subjected to heating followed by hydration at opposite ends of the specimens described in chapter 7. After termination of the tests, the specimens were sliced into several pieces and the variation of concentrations of anions and cations along the depth of the bentonite specimens were determined. Section 8.2 presents the experimental program for chemical analysis. Section 8.3 presents the test results and discussion. Concluding remarks from this chapter are presented in section 8.4.

8.2 Experimental program

A series of thermal and thermo-hydraulic tests were carried out on compacted bentonite specimens for different durations. The results concerning changes in the temperature, the relative humidity, the suction, the swelling pressure, the water content, the dry density and the degree of saturation are presented in chapter 7. Three nos. of thermal and two nos. of thermo-hydraulic tests were conducted (Table 7.1, chapter 7). After termination of the tests, the specimens were sliced into 8 pieces of 10 mm thick. The sliced specimens were stored in airtight containers and were oven dried. The oven dried specimens were grinded to powder. One gram of dry bentonite powder from each slices of the specimens were mixed thoroughly with 10 ml of distilled water. The solutions were then shaken horizontally for 24 hours using reciprocate shaker. Further, the solutions were centrifuged for 5 minutes and the supernatant solutions were collected. The supernatant solutions were filtered with Whatman 42 filter paper applying vacuum using a Buchner funnel.

The concentrations of commonest exchangeable ions present in clays are chloride, sulphate, nitrate, sodium, potassium, calcium and magnesium (Grim, 1968). The filtered solutions were tested using Anton Paar Ion Chromatography (IC) to determine the concentrations of Cl^- , SO_4^{2-} and NO_3^- ions. Inductively Coupled Plasma Optimal Emission Spectroscopy (ICP-OES) was used to determine the concentrations of Na^+ , K^+ , Ca^{2+} and Mg^{2+} ions. The measurements were repeated twice and the average of the measured values of each slices of the specimens were considered for analysis.

The concentrations of cations and anions were found out in mg/l of solution using Ion Chromatography (IC) and Inductively Couple Plasma Optimal Emission Spectroscopy (ICP-OES). The concentrations of cations and anions are also presented in meq/100 g. The concentration of soluble cations and anions in bentonite were measured from the aqueous extract of solutions prepared with dry bentonite: water ratio of 1:10. The measured concentrations were considered as reference values for analysis.

Table 8.1 presents the reference concentration values of cations and anions of MX80 bentonite in the study obtained from the aqueous extraction technique. The reference solubilised elements of MX80 bentonite reported by Gómez-Espina and Villar (2010) also presented in Table 8.1 for comparison. The discrepancies of the values obtained are attributed to the difference in solid: liquid ratio used during the aqueous extraction process.

In addition to dilution, several chemical processes take place during pore water extraction from clay samples, including dissolution of soluble minerals (halite, sulphates, and carbonates mostly), dissolution and ex-solution of gases and cation exchange (Samper et al., 2008). All these processes change the concentrations of dissolved species in a complex nonlinear manner which makes it difficult to derive the chemical composition of the clay pore water from aqueous extract data (Fernández et al., 2001; Samper et al., 2008). The cations and anions concentrations of two MX80 bentonites presented in Table 8.1 are comparable. However, slightly higher concentrations were observed in consequences of difference in chemical compositions of the two bentonites.

Table 8.1 Solubilised minerals of MX80 bentonite determined from aqueous extraction method

	Solubilised minerals (meq/100 g) (solid: liquid ratio of 1:10)	Solubilised minerals* (meq/100 g) (solid: liquid ratio of 1:8)
pH	9.85	9.20
Na ⁺	9.50	9.30
K ⁺	0.11	0.09
Ca ²⁺	0.63	0.50
Mg ²⁺	0.11	0.09
Cl ⁻	0.18	0.16
SO ₄ ²⁻	6.05	5.10
NO ₃ ⁻	0.14	--

* adopted from reported values by Gómez-Espina and Villar (2010).

Table 8.2 presents the experimental program and the list of anions and cations analysed after thermal and thermo-hydraulic tests. Three nos. of thermal test were conducted for the duration of 12, 65 and 67 days. Two nos. of thermo-hydraulic tests were conducted for the duration of 117 and 182 days (see also Table 7.1, chapter 7). The concentrations of Na⁺, K⁺, Ca²⁺, Mg²⁺, Cl⁻, SO₄²⁻ and NO₃⁻ ions were measured after termination of the thermal and the thermo-hydraulic tests along the depth of the bentonite specimens.

Table 8.2 Experimental program for chemical analysis

Test type	Duration of tests	List of cations and anions analysed
Thermal	12, 65, 67	Cl ⁻ , SO ₄ ²⁻ , NO ₃ ⁻ , Na ⁺ , K ⁺ , Ca ²⁺ , Mg ²⁺
Thermo-hydraulic	117, 182	Cl ⁻ , SO ₄ ²⁻ , NO ₃ ⁻ , Na ⁺ , K ⁺ , Ca ²⁺ , Mg ²⁺

8.3 Results and discussion

The chemicals are transported in compacted bentonite mainly by advection, molecular diffusion and mechanical dispersion (Samper et al., 2008). The measurement of chemical concentrations in bentonite is affected by aqueous complexation, acid-base, dissolution/precipitations and cation exchange (Murrinen and Lehtikoinen, 1998; Cleall et al., 2007; Samper et al., 2008; Fernández and Villar, 2010). The main mineral content in bentonite is montmorillonite that constitute about 80-85% of total minerals present. Several other accessory minerals such as gypsum, calcite, pyrite, quartz, mica, feldspar, siderite, albite, biotite (Bradbury and Baeyens, 2003; Montes-H et al., 2005) are present in bentonites. The accessory minerals participate in ion exchange reactions when dissolve in water.

The factors affecting the solute transport phenomenon due to applied thermal gradient across compacted bentonite specimens are increasing solute concentration resulted from evaporation at the hot end of the bentonite specimens and molecular diffusion. During a thermo-hydraulic loading phase, in addition to the concentration gradient and the diffusion processes, advection and dissolution/precipitation of solutes at the hydration end governs the solute transport phenomenon. The trend of concentration profiles of cations and anions along the depth of the bentonite specimen due to applied thermal gradient and thermal and hydraulic gradients are comparable. Therefore, the variation of cations and anions concentrations due to applied thermal gradient and thermal and hydraulic gradients are presented together in the following sections.

8.3.1 Chloride (Cl⁻) distribution

Figure 8.1 shows the profiles of chloride concentration along the depth of the specimens after termination of thermal and thermo-hydraulic tests. Chloride ion is the most mobile ion and remain inactive with other ions in clay water system (Fernández et al., 2001; Martín et al., 2000; Bradbury and Baeyens, 2003; Cleall et al., 2007; Fernández and Villar, 2010). The concentrations are shown in meq/100 g and mg/l with an increase in the distance from the heater. The initial chloride concentration (Table 8.1) is shown in Fig. 8.1 for comparison.

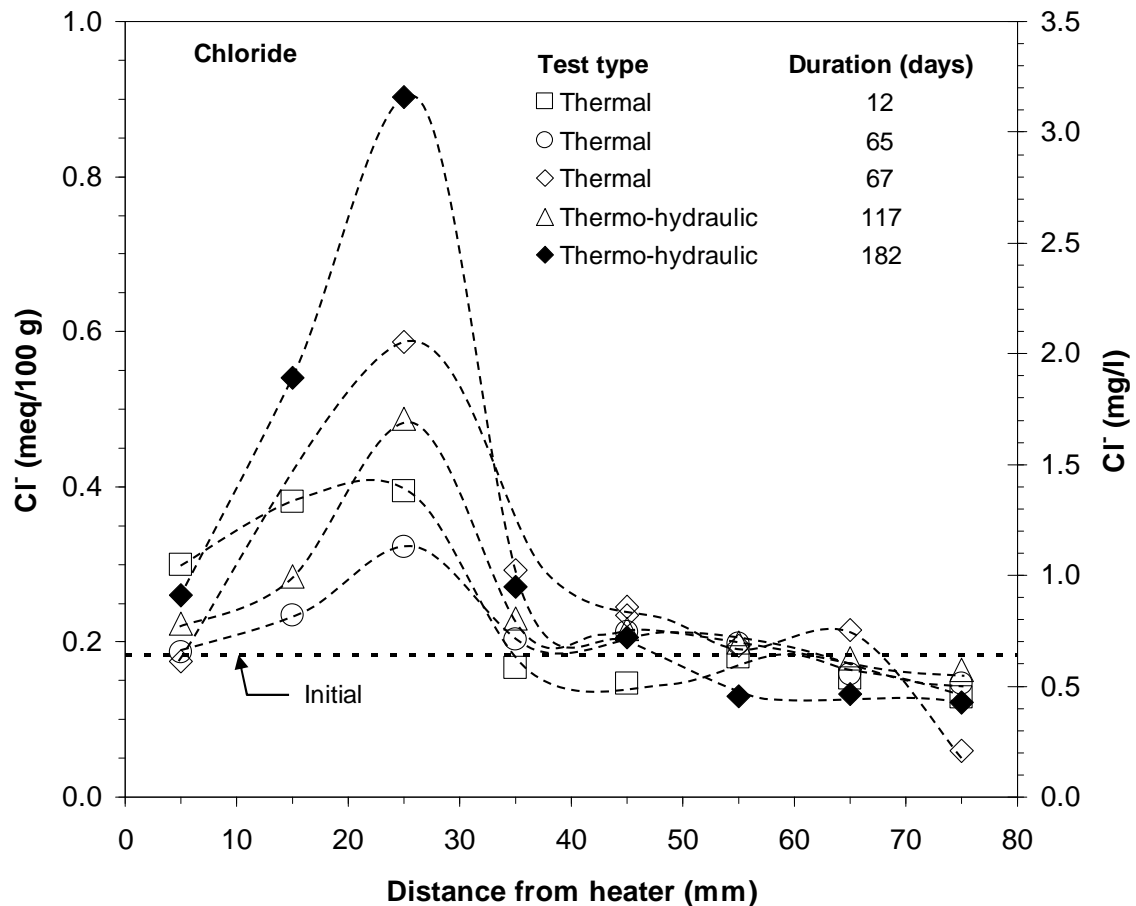


Figure 8.1. Influence of thermal and thermo-hydraulic gradients on chloride transport in compacted bentonite specimen.

Due to an applied thermal gradient, the chloride concentration builds up close to the heater due to evaporation and diffusion (Fernández and Villar, 2010). The maximum chloride concentration was observed between 25 to 30 mm away from the heater. The maximum chloride concentration after termination of the thermal test was found to be 0.6 meq/100 g.

Due to applied thermal and hydraulic gradients, the chloride ions were carried with liquid water towards the heater by advection. The chloride concentrations were not affected by ion exchange reactions. The maximum and minimum chloride concentrations were found to be 0.9 and 0.06 meq/100 g (Fig. 8.1). Gómez-Espina and Villar (2010) reported similar chloride concentration profiles measured after thermo-hydraulic test (0.89 and 0.066 meq/100 g).

8.3.2 Sulphate (SO_4^{2-}) distribution

The effect of temperature gradient and temperature and hydraulic gradients on sulphate concentration profiles after terminating thermal and thermo-hydraulic tests is presented in Fig. 8.2. The initial sulphate concentration is shown in Fig. 8.2 for comparison. During the thermal loading phase, a decrease in sulphate concentration at about 10 mm from the heater was noted. The decrease in sulphate concentration was due to precipitation of anhydrite (Fernández and Villar, 2010).

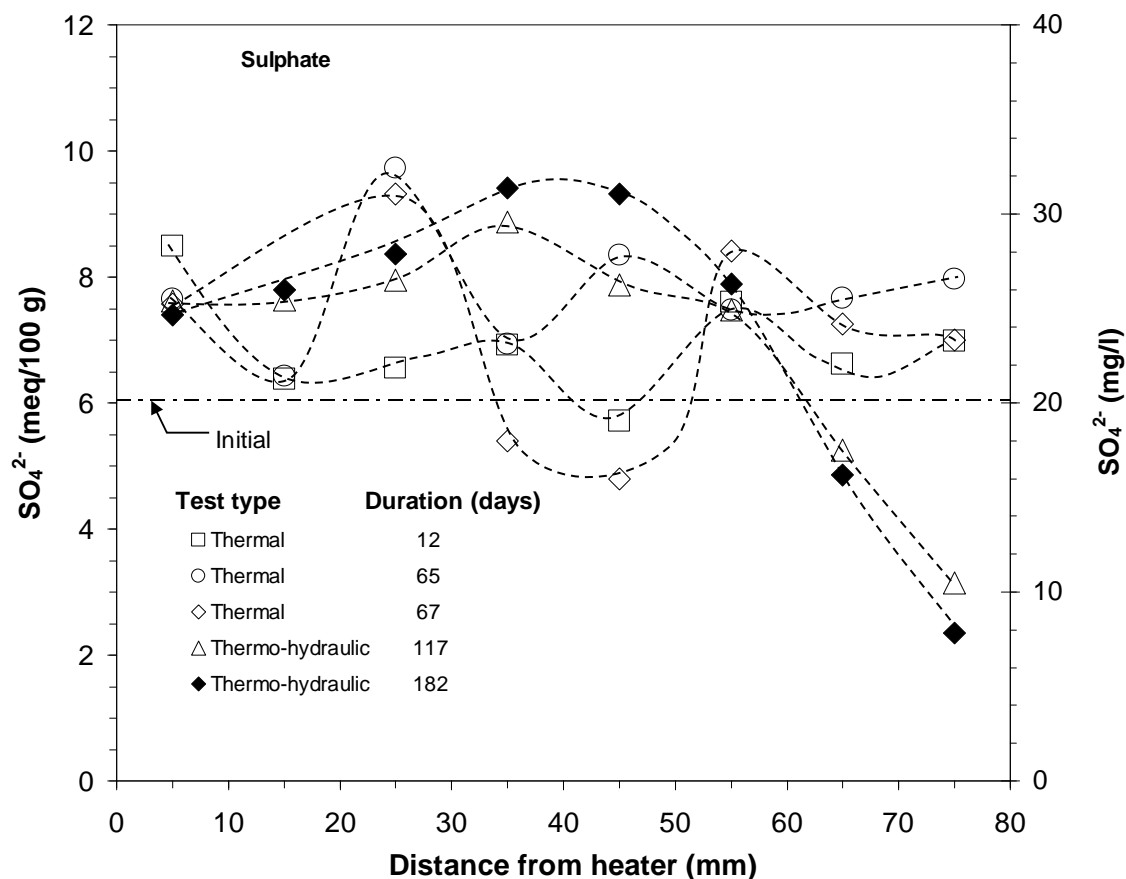


Figure 8.2. Influence of thermal and thermo-hydraulic gradients on sulphate transport in compacted bentonite specimen.

Due to an applied thermal gradient, the dissolution of sulphates at hydration end of the specimens resulted in decrease of sulphate concentrations (Fernández et al., 2001). The maximum concentration of sulphates was found at the mid height of the specimens measured after thermo-hydraulic tests (Fig. 8.2). The sulphate concentration measurements may be influenced by kinetic and solid to liquid ratio when calcite and dolomite both are present or by oxidation when pyrite is present (Fernández et al., 2004).

8.3.3 Nitrate (NO_3^-) distribution

Figure 8.3 presents the profiles of nitrate concentration along the depth of the bentonite specimens measured after termination of the thermal and the thermo-hydraulic tests. In Fig. 8.3 initial nitrate concentration is plotted for comparison. The concentration profiles show an uneven pattern without having any particular trend.

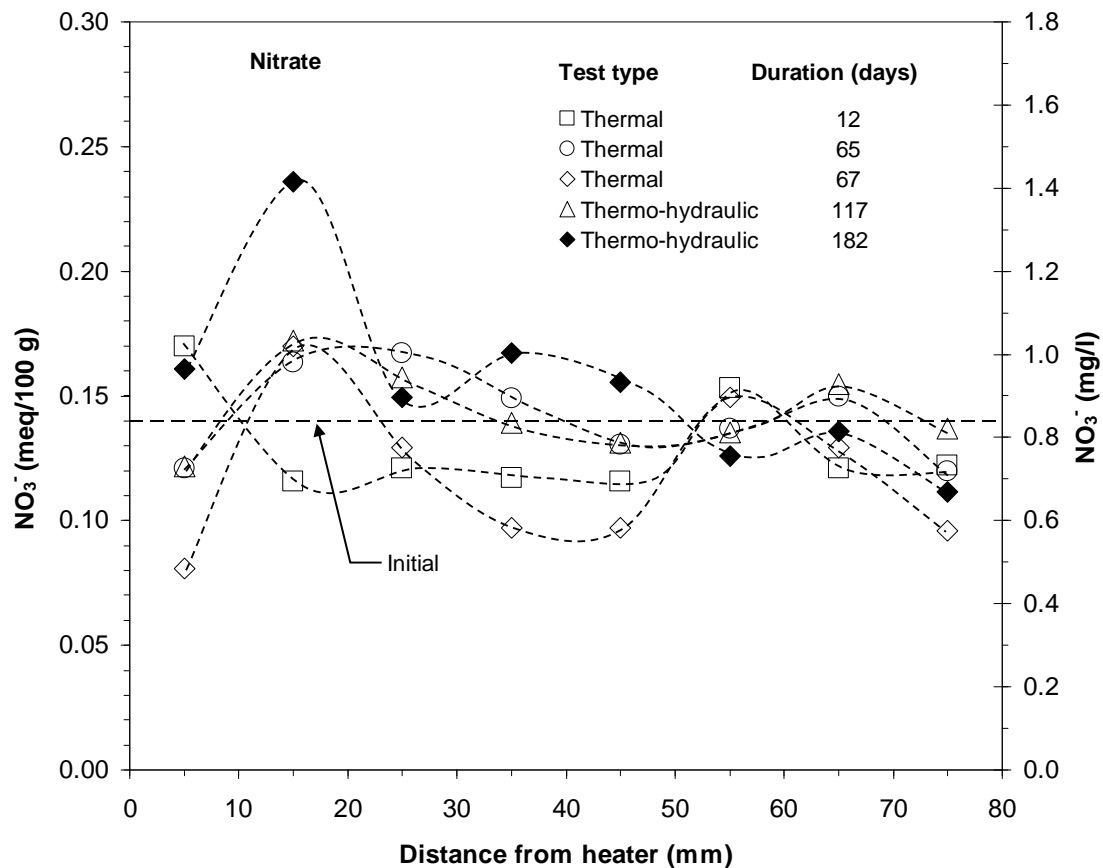


Figure 8.3. Influence of thermal and thermo-hydraulic gradients on nitrate transport in compacted bentonite specimen.

Due to an applied thermal gradient, the maximum nitrate concentration was observed at a distance of 15 mm from the heater due to evaporation and diffusion. The maximum nitrate concentration during thermal loading was found to be 0.17 meq/100 g (Fig. 8.3).

Due to applied thermal and hydraulic gradients, nitrate concentration profiles along the depth of the bentonite specimens were found to be similar to that was noted during thermal loading. The maximum nitration concentration after termination of thermo-hydraulic test was found to be 0.24 meq/100 g (Fig. 8.3). At the hydration end, the nitration concentration was found to lesser. Overall, a higher nitrate concentration towards the heater and a lesser concentration towards the hydration end were observed.

8.3.4 Sodium (Na^+) distribution

Figure 8.4 presents the concentration profiles of sodium ion measured after termination of the thermal and the thermo-hydraulic tests. The concentration profiles of sodium are nearly similar to that of chloride. The sodium concentration was not varied significantly along the depth of the specimen after thermal test of 12 days. The overall concentration of sodium ion was higher than that of initial concentration. The discrepancy is attributed to the dissolution/precipitation (Samper et al., 2008) processes during aqueous extraction technique. With longer duration of thermal tests, the concentration of sodium ion close to the heater increased due to evaporation of water and diffusion of salts driven by concentration gradient (Mitchell, 1993; Samper et al., 2008; Fernández and Villar, 2010). The peak concentration of sodium was observed at about 15 mm away from the heater after 65 and 67 days of thermal tests. Precipitation of salts close to the heater also increased the sodium ion concentration (Bear and Gilman, 1995).

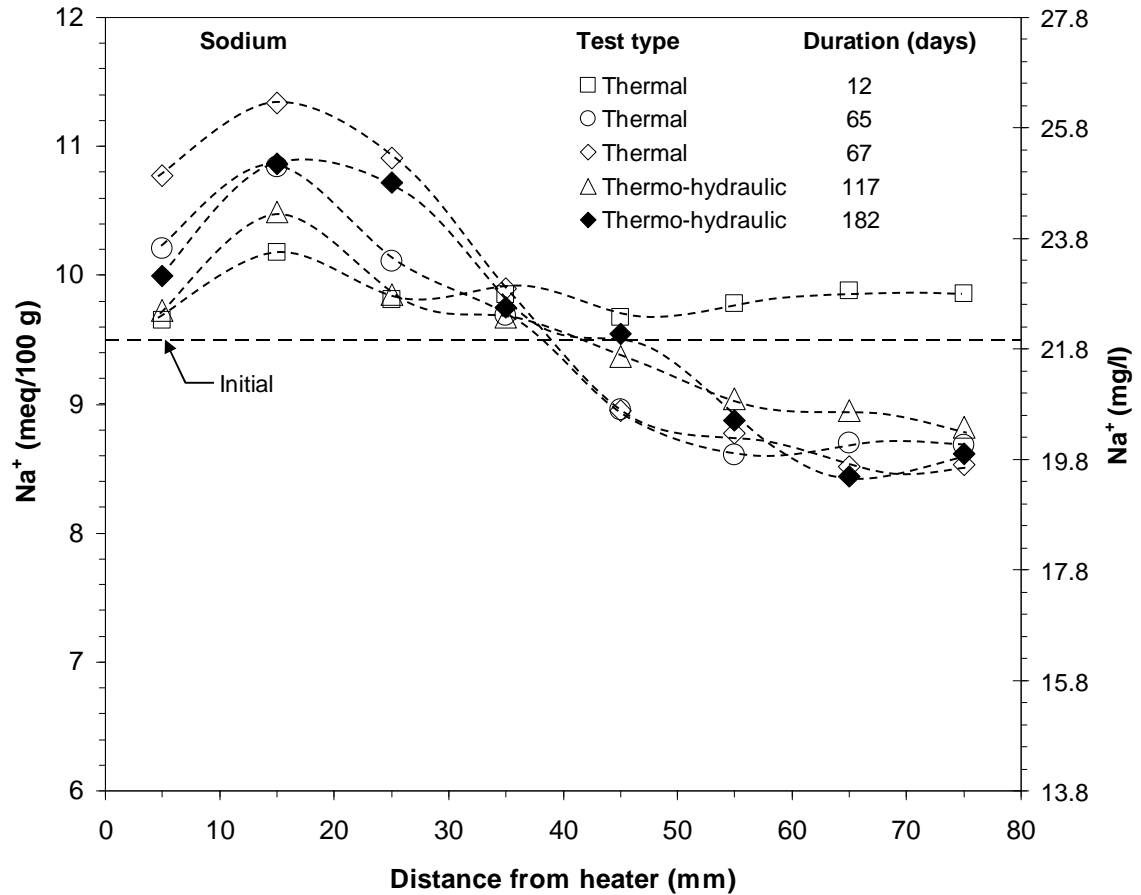


Figure 8.4. Influence of thermal and thermo-hydraulic gradients on sodium transport in compacted bentonite specimen.

Due to applied thermal and hydraulic gradients, the sodium ion was transported towards the heater by advection and a backward diffusion occurred towards the cold end (Cuevas et al., 2002; Cleall et al., 2007). The maximum sodium ion concentration measured after the thermo-hydraulic tests was found to be lower than the concentration measured after thermal tests (Fig. 8.4). The sodium concentration during thermo-hydraulic loading was affected by advection, backward diffusion and ion exchange reactions.

8.3.5 Calcium (Ca^{2+}) distribution

Figure 8.5 presents the concentration profiles of calcium ion measured after termination of the thermal and the thermo-hydraulic tests. During thermal loading, the concentration of calcium close to the heating source was found to decrease due to advection. The concentration of calcium was increased at a distance of 25 mm from the heater.

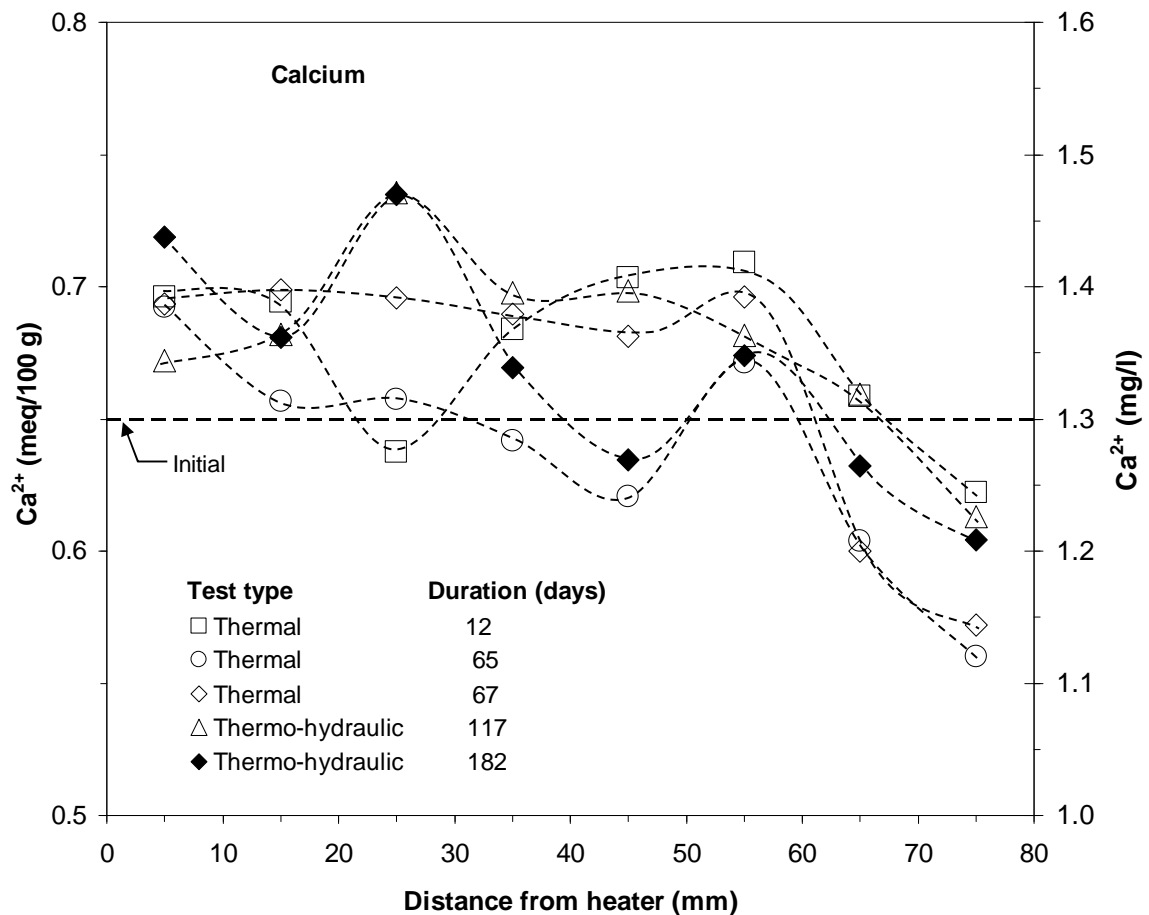


Figure 8.5. Influence of thermal and thermo-hydraulic gradients on calcium transport in compacted bentonite specimen.

Due to applied thermal and hydraulic gradients, the concentration of calcium was affected by dissolution precipitation and ion exchange reactions at the hydration end. The

advection and diffusion govern transport process and responsible for change in calcium concentration profiles due to the thermal and the thermo-hydraulic loading. Calcite dissolution occurred at hydration end resulted in a lower concentration profile (Fernández and Villar, 2010; Gómez-Espina and Villar, 2010).

8.3.6 Magnesium (Mg^{2+}) distribution

Figure 8.6 presents the concentration profiles of magnesium ion measured after termination of thermal and thermo-hydraulic tests. The magnesium concentration profile found to be similar with other cations. Due to an applied thermal gradient, the magnesium concentration was found to increase towards the heater.

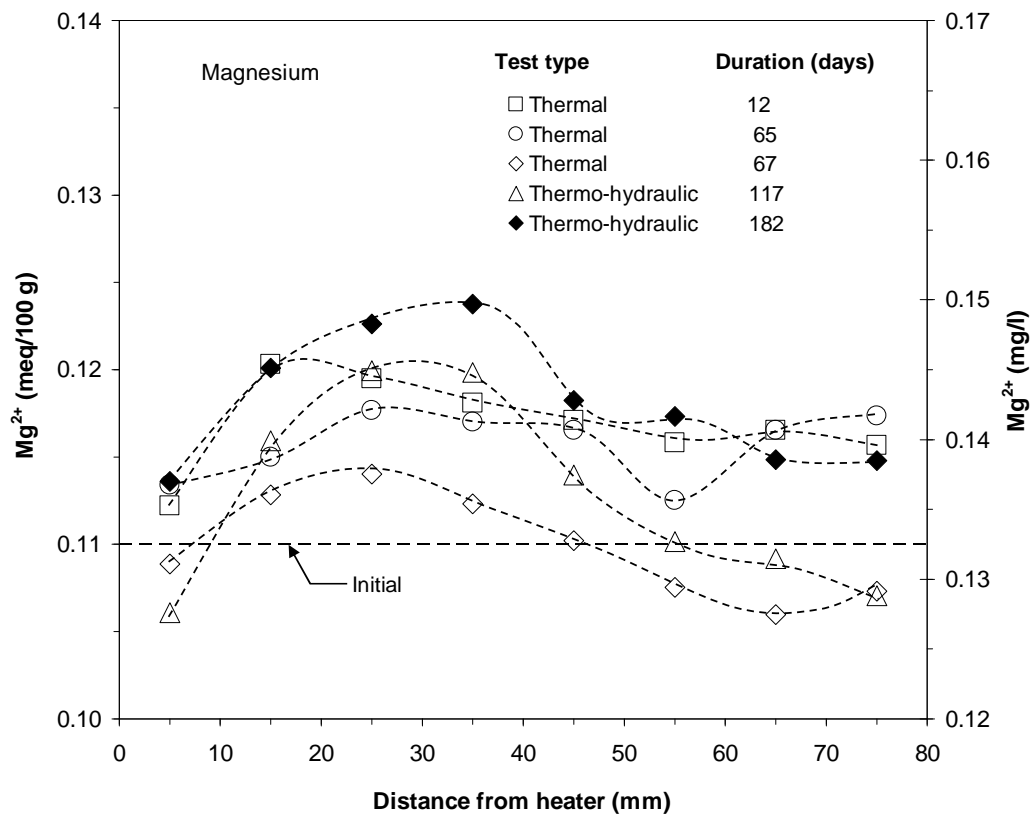


Figure 8.6. Influence of thermal and thermo-hydraulic gradients on magnesium transport in compacted bentonite specimen.

The peak concentration of magnesium during the thermal loading was found to be at a distance of 30 to 40 mm from the heater. The increase in magnesium concentration towards the hotter region of the specimens was controlled mainly by dissolution/precipitation process.

Due to applied thermal and hydraulic gradients, the calcite precipitate and dissolution of other accessory minerals such as dolomite and sulphate occurs (Fernández and Villar, 2010). The magnesium concentration also increased by ion exclusion in the cooler region of bentonite specimens in consequence of calcite/sulphate dissolution (Fig. 8.6).

8.3.7 Potassium (K^+) distribution

Figure 8.7 presents the concentration profiles of potassium ion measured after termination of the thermal and the thermo-hydraulic tests. The concentration profiles of magnesium are scattered in nature. Due to an applied thermal gradient, an increase in potassium concentration was noted towards the heater.

Due to applied thermal and hydraulic gradients, an increase in potassium concentration towards the heater was noted similar to that was noted for thermal loading. An increase in potassium concentration was observed at a distance of 15 mm from the heater (Fig. 8.7). The results show a lesser concentration at the hydration end due to advective transport. The general trend of the concentration profile of magnesium is nearly similar to the profiles of calcium and magnesium.

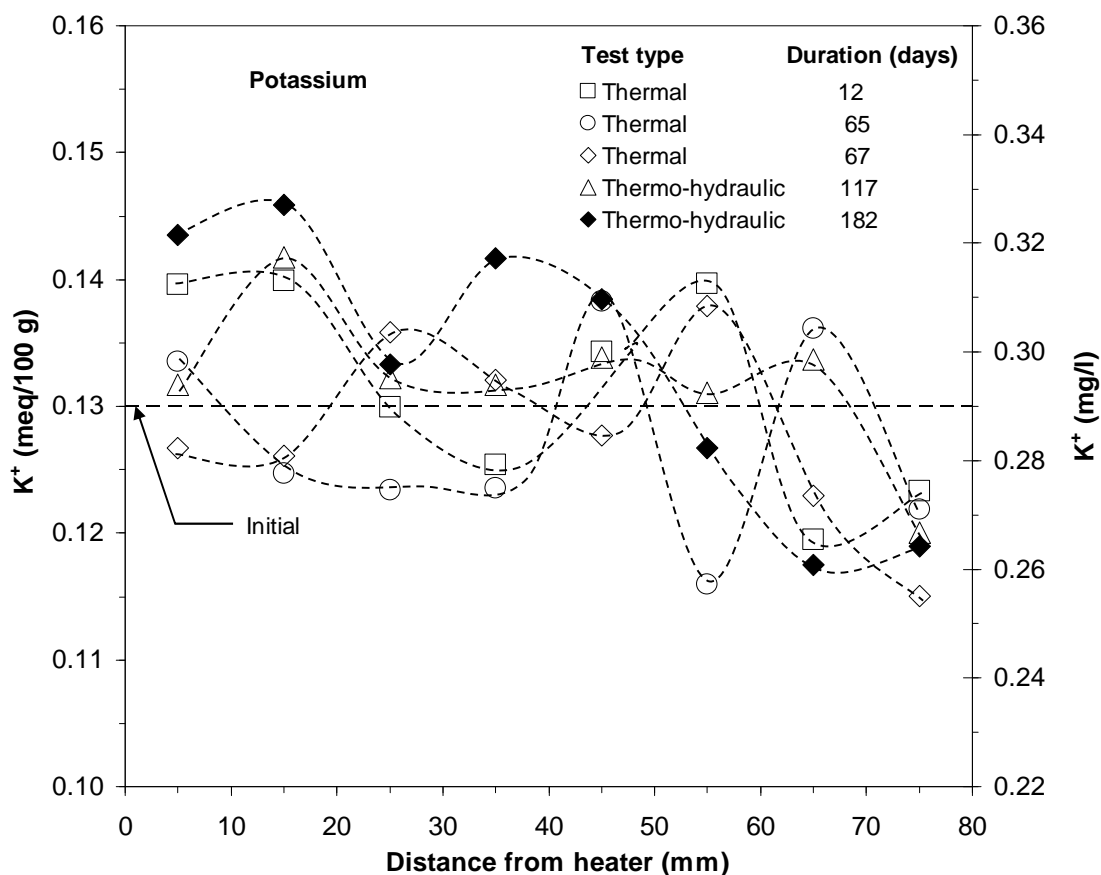


Figure 8.7. Influence of thermal and thermo-hydraulic gradients on potassium transport in compacted bentonite specimen.

8.4 Concluding remarks

The processes of salt migration in compacted bentonite due to thermal and hydraulic gradients are presented in this chapter. The possibility of accumulation of salts in specific regions due to thermal and hydraulic gradient across compacted cylindrical bentonite specimens are presented in this chapter. The concentration profiles of chloride, sulphate, nitrate, sodium, calcium, magnesium, and potassium ions in compacted bentonite specimens measured after termination of thermal and thermo-hydraulic tests are shown by aqueous extraction method using Inductively Couple Optical Emission Spectroscopy (ICP-OES) and Ion Chromatography (IC).

An overall increase of cations and anions close to the heater and a decrease at the cooler part of the specimens was observed. The chloride and sodium ion concentrations were found to be significantly higher at the hotter region of the specimens. Therefore, the salinity of the compacted bentonites is expected to be higher in vicinity to the heater. The solute transport processes were influenced by evaporation, condensation, molecular diffusion and advection. The determination of cations and anions concentrations was affected by ion exchange reaction and dissolution/precipitation.

Chapter 9

Numerical simulation of thermo-hydro-mechanical tests

9.1 Introduction

Several numerical investigations have been carried out in the past in order to study the behaviour of bentonite under thermal and hydraulic gradients. A brief review of the theoretical models used to study the coupled thermo-hydro-mechanical behaviour of unsaturated soil is presented in Chapter 2. In this investigation, a finite element based numerical modelling was undertaken in order to simulate the thermal and thermo-hydraulic test conditions and to compare the experimental temperature, suction and swelling pressure variation with that of the simulated results. The finite element based code COMPASS (COde for Modelling PARTially Saturated Soils) was developed at GRC, Cardiff University. The model was formulated to study coupled thermo/hydro/chemical/mechanical (THCM) behaviour of unsaturated soil (Thomas,

1985; Ewen and Thomas, 1987; Ewen and Thomas, 1989; Thomas and King, 1991; Thomas and He, 1994).

A theoretical model of coupled transient heat and moisture transfer in unsaturated soil was developed (Thomas, 1985; Ewen and Thomas, 1987, 1989). Philip and de Vries (1957) approach was adopted to model the vapour flow which considers liquid, vapour and heat flow independently and relate them to the gradients of temperature and moisture content using Fourier and Darcy's law. Ewen and Thomas (1987) carried out an experimental investigation on the behaviour of unsaturated sand surrounding a heating rod and modified the model to simulate coupled heat and moisture transfer processes in unsaturated soils (Ewen and Thomas, 1989). Thomas and King (1991) further developed the previous model by expressing the coupled heat and moisture transfer in unsaturated soils in terms of potentials for flow. The approach presented by Thomas and King (1991) was then extended to include the effect of elevated pore air pressure in unsaturated soil, deformation of the soil and transport of various chemical species by the various researchers (Thomas and Rees, 1990, 1993; Thomas and He, 1994, 1995; Thomas and Sansom, 1995; Thomas et al., 1996; Thomas and Li, 1997; Thomas and Cleall, 1997, 1999; Seetharam, 2003; Vardon, 2009).

This chapter presents the simulation of the thermal and thermo-hydro-mechanical test conditions and comparison between the experimental and the simulated results using COMPASS. Section 9.2 presents the theoretical formulations for the heat, liquid water and water vapour transfer and the deformation behaviour as applicable to unsaturated soil. Section 9.3 presents the details of numerical simulation and the material parameters used for the simulations. Section 9.4 presents the results and discussion. The concluding remarks from this study are presented in section 9.5.

9.2 Theoretical formulation

The detailed theoretical development of the coupled thermo-hydro-mechanical model called COMPASS can be found in Ewen and Thomas (1989), Thomas and King (1991), Thomas and He (1995, 1998), Thomas et al. (1996), Cleall (1998), Seetharam (2003) and Vardon (2009). Therefore, a brief description of the formulations for heat, liquid water and water vapour flow along with the deformation behaviour of unsaturated expansive soils are presented in the following sections. The governing equations are expressed in terms of four primary variables:

- (i) Pore water pressure (u_l),
- (ii) Pore air pressure (u_a),
- (iii) Temperature (T) and
- (iv) Displacement (\mathbf{u}).

The behaviour of all these variables are included within a coupled thermo-hydro-mechanical formulation (Seetharam, 2003; Vardon, 2009). Liquid and vapour water transfer are considered utilising the principle of conservation of mass as is the transfer of pore air. The pore air considered a binary mixture of dry air and water vapour. Heat transfer is governed by the conservation of energy taking into account of conduction and convection and the phase change via the latent heat of vapourisation. Radiation is assumed negligible (Seetharam, 2003). The mechanical behaviour is governed by a constitutive relationships developed using an elasto-plastic relationship for a swelling soil via consideration of stress equilibrium (Seetharam, 2003; Vardon, 2009).

9.2.1 Heat flow

The law of conservation of energy dictates that the temporal derivative of the heat content Ω , is equal to the spatial derivative of the heat flux, \mathbf{Q} . This may be expressed as (Seetharam, 2003):

$$\frac{\partial(\Omega \partial V)}{\partial t} = -\nabla \mathbf{Q}(\partial V) \quad (9.1)$$

where t is the time, ∇ is the gradient operator and ∂V is the incremental volume. The heat content of a partially saturated soil per unit volume, Ω , is assumed to be the sum of soil heat storage capacity and the contribution resulting from the latent heat of vapourisation and can be defined as (Seetharam, 2003):

$$\Omega = H_c (T - T_r) + L n S_a \rho_v \quad (9.2)$$

where H_c is the heat capacity of unsaturated soil, L is the latent heat of vapourisation, S_a is the degree of saturation of pore air, T is the absolute temperature and T_r is the reference temperature.

Thomas and He (1995) proposed the following equation for heat flow considering conduction, convection and latent heat of vapourisation:

$$\mathbf{Q} = -\lambda_T \nabla T + (\mathbf{v}_v \rho_v + \mathbf{v}_a \rho_a) L + (C_{pl} \mathbf{v}_l \rho_l + C_{pv} \mathbf{v}_v \rho_v + C_{pa} \mathbf{v}_a \rho_a + C_{pda} \mathbf{v}_a \rho_{da}) (T - T_r) \quad (9.3)$$

where \mathbf{Q} is the total heat flow, λ_T is the thermal conductivity, v_l , v_v , v_a are the velocity of liquid, vapour and air, respectively, C_{pl} , C_{pv} , C_{pda} are the specific heat capacities of liquid,

vapour and dry air, $\rho_l, \rho_v, \rho_{da}$ are the densities of liquid, vapour and dry air, respectively. The first term in equation (9.3) represents conductive flow, second term represents latent heat of vapourisation and the third term represents convective flow.

9.2.2 Water flow

Flow of water in unsaturated soil may be described as a two phase flow comprising, (i) the flow of liquid water and (ii) the flow of water vapour. The volumetric water content, θ , is defined as the sum of these two phases:

$$\theta = \theta_l + \theta_v \quad (9.4)$$

where θ_l is the volumetric liquid content and θ_v is the volumetric vapour content. Equation (9.4) can be used to split the flow into its liquid and vapour phases. The conservation of mass for each of the two phases may then be considered separately. The principle of thermodynamic equilibrium dictates that at any point, the volumetric liquid water and water vapour are in equilibrium (de Vries, 1958) giving:

$$\theta_v = \frac{(n - \theta_l) \rho_v}{\rho_l} \quad (9.5)$$

where n is the porosity, ρ_v is the density of water vapour and ρ_l is the density of liquid water. Firstly, the liquid water phase is dealt with. The law of conservation of mass dictates that the time derivative of the liquid content is equal to the gradient of the liquid flux \pm a sink/source. This can be expressed as:

$$\rho_l \frac{\partial \theta_l \partial V}{\partial t} = -\rho_l \partial V \nabla \cdot \mathbf{v}_l - \rho_l \partial V E_{ss} \quad (9.6)$$

where \mathbf{v}_l is the velocity of liquid, E_{ss} is a sink/source term representing vaporisation and condensation, the law of conservation of mass dictates that the time derivative of the vapour content is equal to the gradient of the vapour flux \pm a sink/source, can be expressed as:

$$\rho_l \frac{\partial \theta_v \partial V}{\partial t} = -\rho_l \partial V \nabla \cdot \mathbf{v}_v - \partial V \nabla \cdot (\rho_v \mathbf{v}_a) + \rho_l \partial V E_{ss} \quad (9.7)$$

where \mathbf{v}_v is the velocity of vapour and \mathbf{v}_a is the velocity of pore air. The volumetric air content, θ_a , can be expressed as:

$$\theta_a = (n - \theta_l) \quad (9.8)$$

Substituting eqs. (9.5) and (9.8) into eq. (9.7), the law of conservation of mass for liquid vapour flow may now be expressed in terms of porosity and volumetric air content:

$$\frac{\partial \rho_v \theta_a \partial V}{\partial t} = -\rho_l \partial V \nabla \cdot (\mathbf{v}_v) - \partial V \nabla \cdot (\rho_v \mathbf{v}_a) + \rho_l \partial V E_{ss} \quad (9.9)$$

Summing the eqs. (9.6) and (9.9), the conservation of mass for moisture can be expressed as:

$$\rho_l \frac{\partial \theta_l \partial V}{\partial t} + \frac{\partial \rho_v \theta_a \partial V}{\partial t} = -\rho_l \partial V \nabla \cdot \mathbf{v}_l - \partial V \nabla \cdot (\rho_l \mathbf{v}_v) - \partial V \nabla \cdot (\rho_v \mathbf{v}_a) \quad (9.10)$$

9.2.2.1 Mechanisms of liquid water flow

The mechanism of liquid water flow in unsaturated soil has been described by several researchers (Fredlund and Rahardjo, 1993; Mitchell, 1993). The formulations are based on the four mechanisms (Mitchell, 1993) causing the flow of water in an unsaturated soil:

- (i) Pressure head,
- (ii) Elevation head,
- (iii) Thermal gradients and
- (iv) Electrical gradients

The flow of liquid water due to electrical and chemical gradients was not considered (Seetharam, 2003; Vardon, 2009).

Fredlund and Rahardjo (1993) considered the hydraulic head gradient, that is, the sum of the pressure head, and elevation head as a driving potential for water flow. These mechanisms may be described by Darcy's law (1856), and this approach has been applied to unsaturated soil by Childs (1969) and Neilson et al. (1986). For multiphase flow in unsaturated soil, Darcy's law can be expressed as:

$$\mathbf{v}_l = -\frac{K_l}{\mu_l} \left[\nabla \left(\frac{u_l}{\gamma_l} \right) + \nabla z \right] = -k_l \left[\nabla \left(\frac{u_l}{\gamma_l} \right) + \nabla z \right] \quad (9.11)$$

where \mathbf{v}_l is the liquid velocity due to pressure and elevation heads, K_l is the effective permeability, μ_l is the absolute viscosity of pore liquid, k_l is the unsaturated hydraulic conductivity, γ_l is the unit weight of liquid and z is the elevation. The temperature strongly influences the absolute viscosity of water. Kaye and Laby (1973) showed the

relationship between the viscosity of liquid water and the temperature for a range of temperature between 0 and 100 °C.

$$\mu_l = 661.2(T - 229)^{-1.562} \times 10^{-3} \pm 0.5\% \quad (\text{Ns/m}^2) \quad (9.12)$$

In equation (9.12), the temperature T is in Kelvin.

9.2.2.2 Mechanisms of water vapour flow

Water vapour transfer occurs as a result of two main mechanisms (i) diffusive and (ii) pressure flow. The bulk air is considered to be a binary mixture of water vapour and dry air (Pollock, 1986) and is dealt with via a generalised Darcy's law. Philip and de Vries, 1957) proposed the following equation to measure the velocity of vapour, v_v , through an unsaturated soil:

$$\mathbf{v}_v = - \frac{D_{atms} v_v \tau_v \theta_a}{\rho_l} \nabla \rho_v \quad (9.13)$$

where D_{atms} is the molecular diffusivity of vapour through air, τ_v is the tortuosity factor. Considering the values of D_{atms} , v_v and ρ_v and rearranging the eq. (9.13) can be expressed as:

$$\begin{aligned} \mathbf{v}_v = & \frac{D_{atms} v_v \tau_v \theta_a}{\rho_l} \left(\rho_0 \frac{\partial RH}{\partial s} \right) \nabla u_l - \frac{D_{atms} v_v \tau_v \theta_a}{\rho_l} \left(RH \frac{\partial \rho_0}{\partial T} + \rho_0 \frac{\partial RH}{\partial T} \right) \nabla T \\ & - \frac{D_{atms} v_v \tau_v \theta_a}{\rho_l} \left(\rho_0 \frac{\partial RH}{\partial s} \right) \nabla u_a \end{aligned} \quad (9.14)$$

where ρ_0 is the density of saturated water vapour, RH is the relative humidity, s is the soil suction.

Philip and de Vries (1957) suggested that the simple theory defined in equation (9.14) was not fully valid at increased temperature gradients. They proposed two factors. A flow area factor (f), was included to achieve a reduction of the vapour flow as the available flow area decreased at higher moisture contents and a microscopic pore temperature gradient factor, $(\nabla T)_a/(\nabla T)$, was introduced, which is the ratio of the average temperature gradient in the air filled pores to the overall temperature gradient. This factor takes account of the microscopic effect of heat flow paths being shared between sections of solid and fluid paths, giving rise to microscopic temperature gradients in the fluid filled pores, which may be much higher than the macroscopic temperature gradients across the sample as a whole. Including these two amendments into equation (9.14) yields:

$$\mathbf{v}_v = \frac{D_{atms} v_v \tau_v \theta_a}{\rho_l} \left(\rho_0 \frac{\partial RH}{\partial s} \right) \nabla u_l - \frac{D_{atms} v_v \tau_v \theta_a}{\rho_l} f \frac{(\nabla T)_a}{(\nabla T)} \left(h \frac{\partial \rho_0}{\partial T} + \rho_0 \frac{\partial RH}{\partial T} \right) \nabla T - \frac{D_{atms} v_v \tau_v \theta_a}{\rho_l} \left(\rho_0 \frac{\partial RH}{\partial s} \right) \nabla u_a \quad (9.15)$$

Ewen and Thomas (1989) suggested two alterations to the extended vapour velocity equation proposed by Philip and de Vries (1957). These alterations affected the flow area factor (f). The extended vapour velocity equation proposed by Philip and de Vries (1957) did not account for the flow area factor in the moisture gradient terms and appear to show the choking of vapour flow at high moisture contents. Since it was assumed that the vapour velocity is proportional to the vapour density, Ewen and Thomas (1989) suggested that the vapour flow area factor should be present in both temperature

and moisture gradients terms. They also suggested that the form of flow area factor be modified to be equal to the porosity, and that no choking occurs. Adopting these suggestions the vapour velocity can be written as (Seetharam, 2003):

$$\mathbf{v}_v = \frac{D_{atms} v_v n}{\rho_l} \left(\rho_0 \frac{\partial RH}{\partial s} \right) \nabla u_l - \frac{D_{atms} v_v n}{\rho_l} \frac{(\nabla T)_a}{\nabla T} \left(RH \frac{\partial \rho_0}{\partial T} + \rho_0 \frac{\partial h}{\partial T} \right) \nabla T - \frac{D_{atms} v_v n}{\rho_l} \left(\rho_0 \frac{\partial RH}{\partial s} \right) \nabla u_a \quad (9.16)$$

It should be noted that the experimental work by Preerce (1975), de Vries (1966) and Ewen and Thomas (1989) was conducted on cohesionless soil (sand). The application of the approach in compacted bentonite specimens requires further investigation. Singh (2007) proposed two factors (η_1, η_2) in order to study the vapour flow in highly compacted bentonites based on experimental evidences. Considering the proposed material factors (Singh, 2007) the eq. (9.15) can be expressed as:

$$\begin{aligned} \mathbf{v}_v = & \eta_2 \frac{D_{atms} v_v \tau_v \theta_a}{\rho_l} \left(\rho_0 \frac{\partial h}{\partial s} \right) \nabla u_l - \eta_1 \frac{D_{atms} v_v \tau_v \theta_a}{\rho_l} f \frac{(\nabla T)_a}{\nabla T} \left(h \frac{\partial \rho_0}{\partial T} + \rho_0 \frac{\partial h}{\partial T} \right) \nabla T \\ & - \eta_2 \frac{D_{atms} v_v \tau_v \theta_a}{\rho_l} \left(\rho_0 \frac{\partial h}{\partial s} \right) \nabla u_a \end{aligned} \quad (9.17)$$

9.2.3 Governing equations for water flow

The previous sections defined the components of flow for the liquid and vapour phases. The components of liquid and vapour flow laws are now included in the equation of mass conservation for moisture flow, eq. (9.10). The eq. (9.10) may be rewritten in terms of its primary variables to yield the governing differential equation for moisture

flow. However, a number of terms must be expanded and developed as detailed in the following sections.

Expanding the first two terms of the equation (9.10) and noting that $S_a = 1 - S_l$, where S_l is degree of saturation of pore water and S_a is the degree of saturation of pore air, leads to the following expression:

$$e(\rho_l - \rho_v) \frac{\partial S_l}{\partial t} + e(1 - S_l) \frac{\partial \rho_v}{\partial t} + [\rho_l S_l + \rho_v (1 - S_l)] \frac{\partial e}{\partial t} + \rho_l (1 + e) \nabla \cdot \mathbf{v}_l + \rho_l (1 + e) \nabla \cdot \mathbf{v}_v + (1 + e) \nabla \cdot (\rho_v \mathbf{v}_a) = 0 \quad (9.18)$$

Dividing equation (9.18) by $(1 + e)$ and replacing $e/(1 + e)$ by n yields:

$$n(\rho_l - \rho_v) \frac{\partial S_l}{\partial t} + n(1 - S_l) \frac{\partial \rho_v}{\partial t} + [\rho_l S_l + \rho_v (1 - S_l)] \frac{\partial e}{(1 + e) \partial t} + \rho_l \nabla \cdot \mathbf{v}_l + \rho_l \nabla \cdot \mathbf{v}_v + \nabla \cdot (\rho_v \mathbf{v}_a) = 0 \quad (9.19)$$

Considering the third term, it can be shown that:

$$\frac{\partial e}{(1 + e) \partial t} = \frac{\partial \varepsilon_v}{\partial t} \quad (9.20)$$

where ε_v is the volumetric strain which by definition is the rate of change of void ratio with respect to initial volume. Substituting this term into equation (9.19) gives:

$$n(\rho_l - \rho_v) \frac{\partial S_l}{\partial t} + n(1 - S_l) \frac{\partial \rho_v}{\partial t} + [\rho_l S_l + \rho_v (1 - S_l)] \frac{\partial \varepsilon_v}{\partial t} + \rho_l \nabla \cdot \mathbf{v}_l + \rho_l \nabla \cdot \mathbf{v}_v + \nabla \cdot (\rho_v \mathbf{v}_a) = 0 \quad (9.21)$$

The first term of eq. (9.21) can be expressed as:

$$\begin{aligned} n(\rho_l - \rho_v) \frac{\partial \mathcal{S}_l}{\partial t} = & -n(\rho_l - \rho_v) \frac{\partial \mathcal{S}_l}{\partial s} \frac{\partial u_l}{\partial t} + n(\rho_l - \rho_v) \frac{\partial \mathcal{S}_l}{\partial T} \frac{\partial T}{\partial t} \\ & + n(\rho_l - \rho_v) \frac{\partial \mathcal{S}_l}{\partial s} \frac{\partial u_a}{\partial t} \end{aligned} \quad (9.22)$$

The second term of eq. (9.21) can be expressed as:

$$\begin{aligned} n(1 - S_l) \frac{\partial \rho_v}{\partial t} = \\ n(1 - S_l) \left[\left(h \frac{\partial \rho_0}{\partial T} + \rho_0 \frac{\partial h}{\partial T} \right) \frac{\partial T}{\partial t} + \left(\rho_0 \frac{\partial h}{\partial s} \right) \frac{\partial u_a}{\partial t} - \left(\rho_0 \frac{\partial h}{\partial s} \right) \frac{\partial u_l}{\partial t} \right] \end{aligned} \quad (9.23)$$

It can be shown that:

$$\frac{\partial \varepsilon_v}{\partial t} = (1 + e) \frac{\partial n}{\partial t} = \mathbf{m}^T \frac{\partial \varepsilon}{\partial t} = \mathbf{m}^T \mathbf{P} \frac{\partial \mathbf{u}}{\partial t} \quad (9.24)$$

where ε_v is the volumetric strain and ε is the strain vector. The strain matrix \mathbf{P} and the differential operator \mathbf{m} will be defined in section 9.2.4. The third term of equation (9.22) can therefore be expressed as:

$$(\rho_l S_l + \rho_v (1 - S_l)) \frac{\partial \varepsilon_v}{\partial t} = (\rho_l S_l + \rho_v (1 - S_l)) \mathbf{m}^T \mathbf{P} \frac{\partial \mathbf{u}}{\partial t} \quad (9.25)$$

Substituting equations (9.22), (9.23) and (9.24) for the first, second and third terms, respectively and equations (9.10), (9.13) and (9.15) for \mathbf{v}_l , \mathbf{v}_a and \mathbf{v}_v , respectively into equation (9.21) yields:

$$\begin{aligned}
C_{ll} \frac{\partial u_l}{\partial t} + C_{lT} \frac{\partial T}{\partial t} + C_{la} \frac{\partial u_a}{\partial t} + C_{lu} \frac{\partial \mathbf{u}}{\partial t} = \\
\nabla \cdot [K_{ll} \nabla u_l] + \nabla \cdot [K_{lT} \nabla T] + \nabla \cdot [K_{la} \nabla u_a] + \nabla \cdot \sum_{j=1}^n \rho_l K_{l_{cd}}^j \nabla c_d^j + J_l
\end{aligned} \tag{9.26}$$

where

$$C_{ll} = -n(\rho_l - \rho_v) \frac{\partial S_l}{\partial s} - n(1 - S_l) \rho_0 \frac{\partial h}{\partial s} \tag{9.27}$$

$$C_{lT} = n(\rho_l - \rho_v) \frac{\partial S_l}{\partial T} + n(1 - S_l) \left(h \frac{\partial \rho_0}{\partial T} + \rho_0 \frac{\partial h}{\partial T} \right) \tag{9.28}$$

$$C_{la} = n(\rho_l - \rho_v) \frac{\partial S_l}{\partial s} + n(1 - S_l) \rho_0 \frac{\partial h}{\partial s} \tag{9.29}$$

$$C_{lu} = (S_l \rho_l + (1 - S_l) \rho_v) \mathbf{m}^T \mathbf{P} \tag{9.30}$$

$$K_{ll} = \rho_l \left[\frac{k_l}{\gamma_l} - \frac{D_{atms} v_v n}{\rho_l} \left(\rho_0 \frac{\partial h}{\partial s} \right) \right] \tag{9.31}$$

$$K_{lT} = \rho_l \frac{D_{atms} v_v n (\nabla T)_a}{\rho_l \nabla T} \left(h \frac{\partial \rho_0}{\partial T} + \rho_0 \frac{\partial h}{\partial T} \right) \tag{9.32}$$

$$K_{la} = \rho_v k_a + \rho_l \left[\frac{D_{atms} v_v n}{\rho_l} \left(\rho_0 \frac{\partial h}{\partial s} \right) \right] \tag{9.33}$$

$$J_l = \rho_l \nabla \cdot (K_l \nabla z) \tag{9.34}$$

9.2.4 Deformation behaviour

The deformation behaviour of unsaturated soil has been formulated based on the elasto-plastic constitutive model developed by Alonso et al. (1990) known as Barcelona Basic model (BBM). Use of this model in coupled thermo/hydraulic/mechanical formulation has been presented previously by Thomas and He (1998), Cleall (1998), Mitchell (2002), Seetharam (2003) and Vardon (2009). It was assumed that the change in stress, suction and temperature causes the deformation of soil.

Alonso et al. (1990) proposed an elasto-plastic work hardening constitutive model using net mean stress and suction as the relevant stress variables. BBM model was based on Cam-clay model (Roscoe and Schofield, 1963). Cam-clay model was developed to study the behaviour of normally consolidated soil which distinguishes between the yield surface and the surface properties of the material. BBM was modified to study the behaviour of overconsolidated or compacted soils. The net mean stress was defined as:

$$\sigma'' = \sigma - u_a \quad (9.35)$$

where σ'' and σ represent the net mean stress and the total stress, respectively. In the formulation a tension positive sign convention was adopted for stress, but the pore pressures, u_l and u_a were defined as positive in compression.

For an element of soil with unit length and a cross sectional area of $dx dy$ under a system of two-dimensional stresses and body forces (Fig. 9.1), the stress equilibrium equation in an incremental form can be represented as:

$$\mathbf{P}d\boldsymbol{\sigma} + \mathbf{P}\mathbf{m}du_a + d\mathbf{b} = 0 \quad (9.36)$$

where \mathbf{b} is the vector of body forces and \mathbf{P} is the strain matrix given as:

$$\mathbf{P} = \begin{bmatrix} \frac{\partial}{\partial x} & 0 & \frac{\partial}{\partial y} & 0 \\ 0 & \frac{\partial}{\partial y} & 0 & \frac{\partial}{\partial x} \end{bmatrix} \quad (9.37)$$

For a two dimensional plane stress or plane strain analysis, the vector \mathbf{m} is defined as:

$$\mathbf{m}^T = (1, 1, 0, 0) \quad (9.38)$$

For axisymmetric analysis analysis:

$$\mathbf{m}^T = (1, 1, 0, 0) \quad (9.39)$$

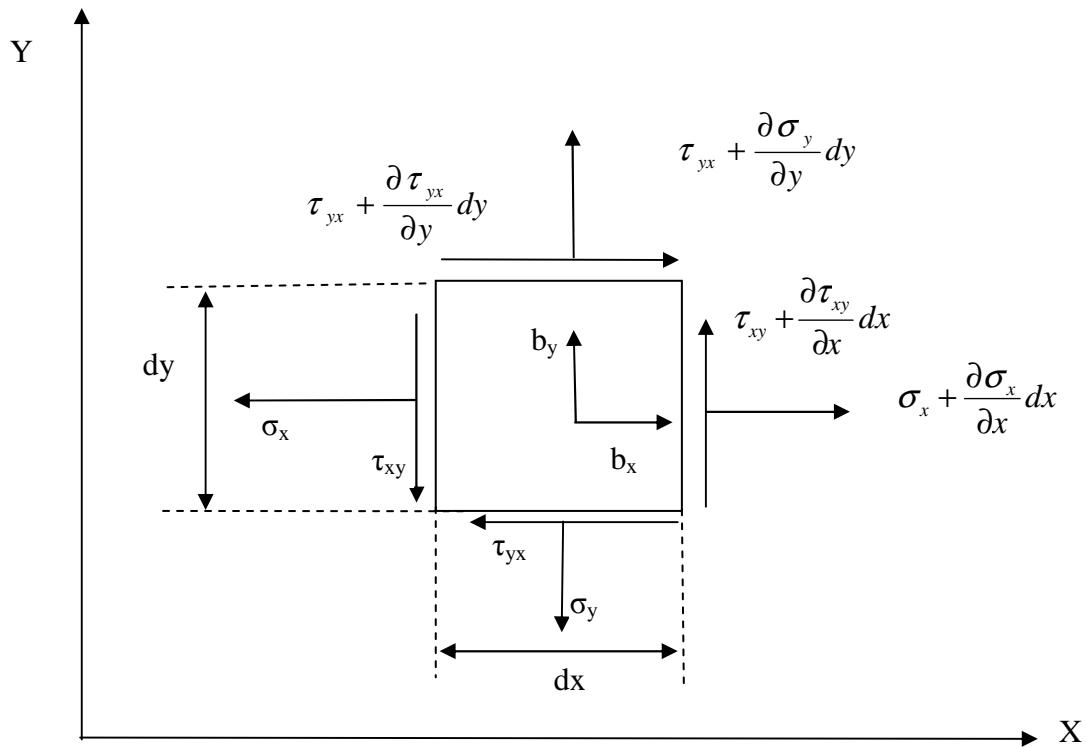


Figure 9.1. A general two dimensional stress system.

9.2.4.1 Elasto-plastic constitutive relationships

The deformation behaviour of soil has been studied considering an elasto-plastic model (Alonso et al., 1990). In order to determine the elastic and plastic strain components four relationships have to be defined (Britto and Gunn, 1987; Owen and Hinton, 1980), such as (i) a stress/elastic strain relationship, (ii) a yield criterion, defining a yield surface in stress space, (iii) a flow rule, defining the magnitude of plastic strains produced when the material is yielding and (iv) a hardening law, defining the relationship between the amount a material hardens and the plastic strain experienced.

9.2.4.2 Material behaviour under elastic condition

The change in specific volume with loading and unloading follow elastic behaviour for constant suction values (Schofield and Worth, 1968):

$$dv = -\kappa \frac{dp}{p} \quad (9.40)$$

where dv is the change in specific volume, dp is the change in mean stress, κ is the elastic stiffness parameter for change in net mean stress. Alonso et al. (1990) proposed the following relationship to determine the specific volume change due to suction changes:

$$dv_s = -\kappa_s \frac{ds}{(s + p_{atms})} \quad (9.41)$$

where dv_s is the change in specific volume due to swelling (wetting path), κ_s is the elastic stiffness parameters for changes in suction.

9.2.4.3 Yield function

Alonso et al. (1990) proposed the following equation to define a set of yield values for each associated suctions and expressed as:

$$\left(\frac{p_0}{p^c}\right) = \left(\frac{p_0^*}{p^c}\right)^{[\lambda(0)-\kappa]/[\lambda(s)-\kappa]} \quad (9.42)$$

where p_0 is the preconsolidation stress, p_0^* is the preconsolidation stress for saturated conditions, p^c is the reference stress.

9.2.4.4 Flow rule

In order to derive the relationship between the plastic strain component and the stress increment, it is assumed that the plastic strain increment is proportional to the stress gradient of the plastic potential. This theoretical assumption is termed as the flow rule as it governs the plastic flow after yielding. Therefore, flow rules are required to define the magnitude of plastic strains produced when the material is yielding. Alonso et al. (1990) proposed two types of flow rules. An associated plastic flow rule for the SI (Suction-Increase) surfaces and a non-associated flow rule for the LC (loading-collapse) yield surface. The plastic potential for LC yield surface, Q_1 as defined by non-associated flow rule as:

$$Q_1 = \alpha_q q^2 - M^2 (p + p_s)(p_0 - p) \quad (9.43)$$

The plastic potential for SI yield surface Q_2 , as defined by associated flow rule is:

$$Q_2 = s - s_0 \quad (9.44)$$

9.2.4.5 Hardening Laws

Strain hardening occurs during plastic deformation. Following yielding the stresses level at which further deformation occurs depends on the amount of plastic strain. The yield curves demonstrate that the soils exhibit strain hardening. After yielding, the stress level at which further plastic deformation occurs is dependent on the current degree of plastic straining. Josa et al. (1987) found that there was a coupling between the hardening of the two yield surfaces. The yield surfaces are controlled by the hardening parameters p_0^* and s_0 , and they depend on the plastic volumetric strain increment $d\epsilon_v^p$.

$$d\epsilon_v^p = d\epsilon_{vp}^p + d\epsilon_{vs}^p \quad (9.45)$$

The two hardening laws for the yield surfaces due to change in pressure and change in suction are shown in the following eqs. (Alonso et al., 1990)

$$\frac{dp_0^*}{p_0^*} = \frac{v}{\lambda(0) - \kappa} d\epsilon_v^p \quad (9.46)$$

$$\frac{ds_0}{s_0} = \frac{v}{\lambda_s - \kappa_s} d\epsilon_v^p \quad Q_2 = s - s_0 \quad (9.47)$$

The governing differential equation of deformation can then be written as:

$$C_{ul} du_l + C_{uT} dT + C_{ua} du_a + C_{uu} d\mathbf{u} - \mathbf{PDep} d\epsilon_s^p + d\mathbf{b} = 0 \quad (9.48)$$

where **Dep** is the elasto-plastic stress-strain matrix.

$$C_{ul} = \mathbf{PDep}A_s \quad (9.49)$$

$$C_{uT} = \mathbf{PDep} \left(-A_T - A_s \frac{dS_r}{dT} \right) \quad (9.50)$$

$$C_{ua} = -\mathbf{PDep}A_s + \mathbf{mP} \quad (9.51)$$

$$C_{uu} = \mathbf{PDepP}^T \quad (9.52)$$

9.3 Numerical simulation

Numerical simulation was performed using the theoretical formulations presented in section 9.2. The simulation was carried out in two stages. In the first phase (phase I), only thermal gradient was applied at opposite ends of the model. In the second phase (phase II), higher temperature was applied at the bottom end of the model and hydraulic pressure was applied at the top end of the model. The experimental results of thermo-hydraulic test (test no. 5) presented in chapter 7 were compared with the simulation results. The test (test no. 5) was conducted considering both thermal and thermo-hydraulic phases (Table 7.1 and Fig. 7.2). The transient temperature profile, the variation in suction and the swelling pressure measured at the cold end of the specimen were compared with the simulated results. The model geometry, the initial and boundary conditions and the material parameters used for the simulations are presented in the following sections.

9.3.1 Geometry and discretisation

The soil specimen used for the investigation had diameter of 100 mm and height of 80 mm. A two dimensional, axi-symmetric mesh was generated for the simulations. The mesh consisted of 40 nos. of 4 noded, quadrilateral elements with a total of 82 nodes. The geometry of the model used for the simulations is shown in Figs. 9.2 and 9.3.

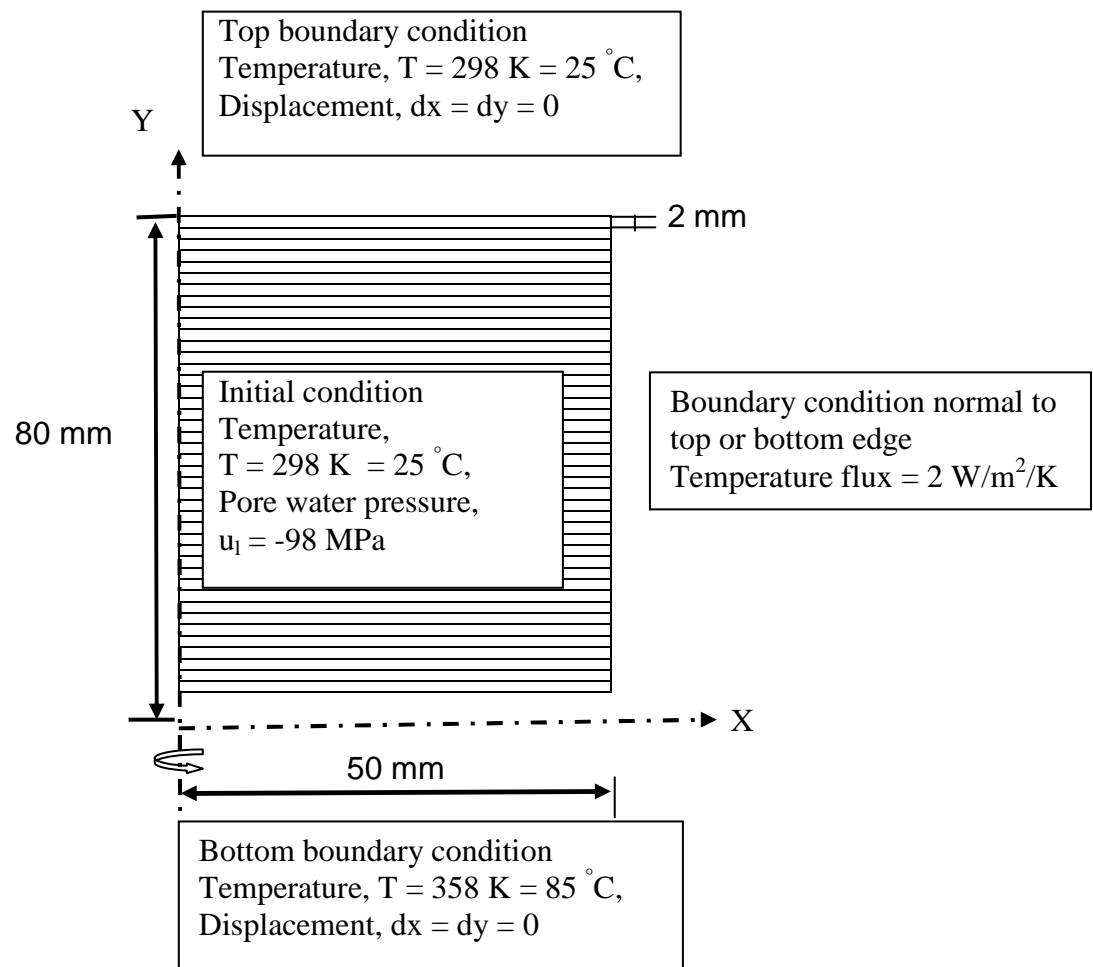


Figure 9.2. Geometry of the model and initial and boundary conditions for first phase (phase I) of simulation.

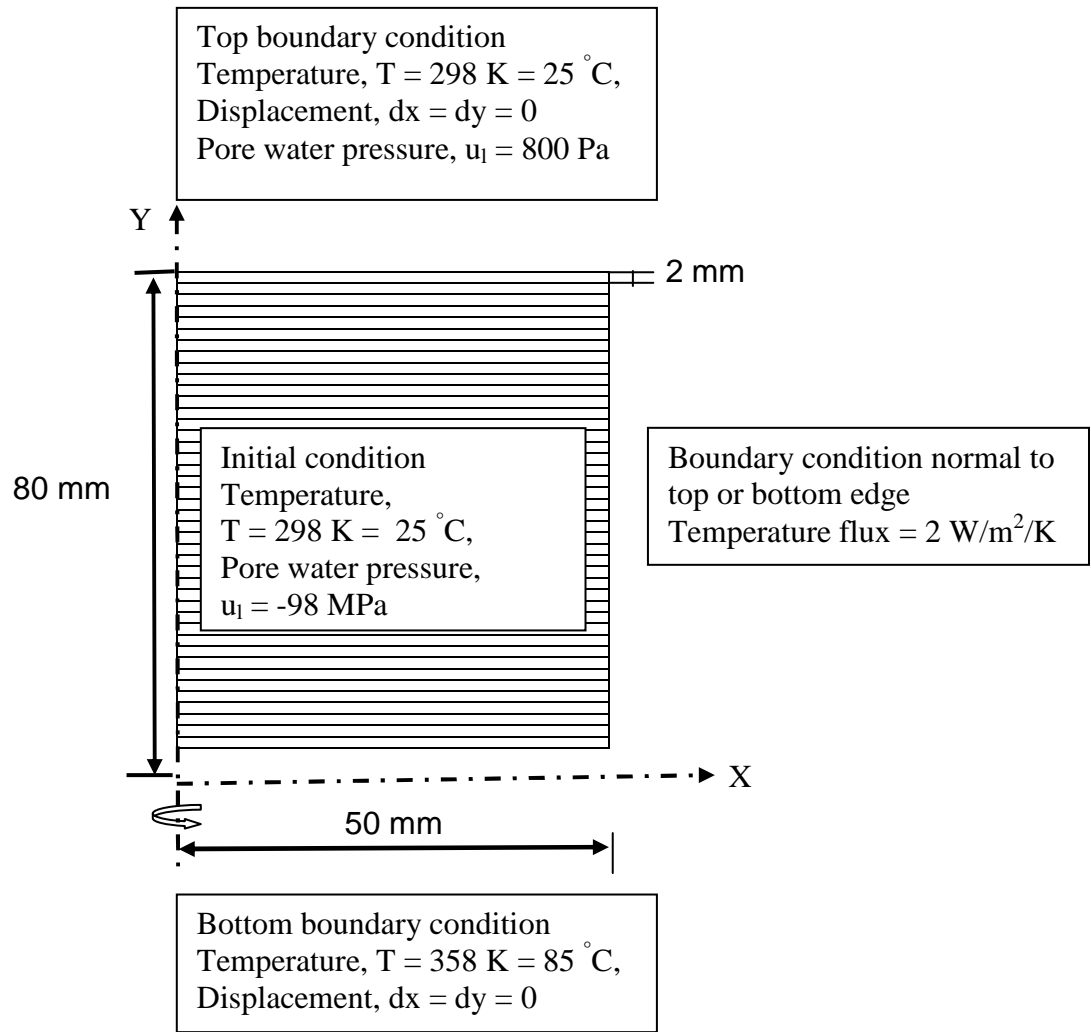


Figure 9.3. Geometry of the model and initial and boundary conditions for second phase (phase II) simulation.

9.3.2 Initial conditions

The thermo-hydro-mechanical simulations were carried out with initial temperature of 298 K ($25 \text{ }^{\circ}\text{C}$) based on the temperature of the laboratory. The initial suction of 96 MPa was applied to the model for simulation. The initial suction was calculated based on the measure temperature and relative humidity of the specimen. The simulated equilibrium temperature and suction values of the thermal phase (phase I) noted. The equilibrium temperature and suction values of first phase (phase I) of

simulation were considered as initial conditions for the second phase (phase II - thermal and hydraulic loading) of the simulation. The initial conditions of first phase (phase I) and second phase (phase II) of simulations are presented in Figs. 9.2 and 9.3, respectively.

9.3.3 Boundary conditions

A constant temperature of 358 K (85 °C) and 298 K (25 °C) were applied at the bottom and top end of the model during of the simulations representing the testing conditions. A fixed temperature flux of 2 W/m²/k was applied at the vertical boundary of the specimen.

During hydraulic loading of the experiment (phase II), distilled water was supplied from the top of the specimens without any fluid injection pressure. Therefore, the applied hydraulic pressure was equivalent to the pressure of a water column equal to the height of the specimen. The calculated hydraulic pressure of 800 Pascal was applied as initial pressure for the simulation. The model was restrained against displacements normal to the boundaries. The boundary conditions applied of phase I (temperature gradient only) and phase II (temperature and hydraulic gradients at bottom and top end of the model) simulations are shown in Figs. 9.2 and 9.3.

9.3.4 Material parameters

The material parameters used for simulations are presented in Table 9.1. The density of soil solids and density of water was considered as 2.76 Mg/m³ and 1.0 Mg/m³, respectively. The dry density of the specimen was 1.6 Mg/m³. The porosity of the specimens were calculated from the dry density using volume-mass relationships as 0.42.

Table 9.1 Material parameters used for simulations

Material Parameters	Value
Density of solid (ρ_s)	2.76 Mg/m ³
Density of water (ρ_l)	1.0 Mg/m ³
Dry density (ρ_d)	1.6 Mg/m ³
Porosity (n)	0.42

9.3.4.1 Thermal parameters

Kaye and Laby (1973) have presented the specific heat capacities of solid, liquid, vapour and air, the latent heat of vapourisation and specific gas constant. The latent heat of vapourisation and specific heat capacities of solid, liquid water, water vapour, dry air were adopted from Kaye and Laby (1973). Table 9.2 presents the thermal parameters used for the simulations. The thermal conductivity of MX80 bentonite was considered from the results reported by Tang et al. (2008).

Tang et al. (2008) shown that the thermal conductivity of compacted MX80 bentonite is lowest (constant) for the degree of saturation below 20% and highest (constant) for the degree of saturation above 80%. However, the thermal conductivity of MX80 bentonite varied with degree of saturation of the material for the range degree of saturation between 20 and 80%. The maximum and minimum thermal conductivity of bentonite used for the simulations were 1.2 and 0.3 W/mK. A thermal conductivity value of 0.3 W/mK was used for the degree of saturation between 0 and 20%. For the degree of saturation between 20% and 80%, the thermal conductivity was considered as a function of the degree of saturation from the experimental data reported by Tang et al. (2008). A

thermal conductivity value of 1.2 W/mK was used for degree of saturations greater than 80%.

Table 9.2 Thermal parameters used for the numerical simulations

Thermal Parameters	Value/ Expression
Latent heat of vapourization, L (Kaye and Laby, 1973)	2.4×10^6 (J/kg)
Specific heat capacity of solid, C_{ps} (Kaye and Laby, 1973)	800×10^6 (J/kgK)
Specific heat capacity of liquid, C_{pl} (Kaye and Laby, 1973)	4180 (J/kgK)
Specific heat capacity of vapour C_{pv} (Kaye and Laby, 1973)	1870 (J/kgK)
Specific heat capacity of dry air C_{pda} (Kaye and Laby, 1973)	1000 (J/kgK)
Thermal conductivity relationship (Tang et al., 2008)	$\lambda_T = 0.3$ W/mK (for $S_r = 0$ to 20%) $= 1.5351 \times S_r - 0.0385$ (for $S_r = 20$ to 80%) where S_r is the degree of saturation $= 1.2$ (for $S_r > 80\%$)

9.3.4.2 Hydraulic parameters

The saturated hydraulic conductivity of MX80 bentonite was considered from the experimental results reported by Börgesson et al. (1996). At a dry density of 1.6 Mg/m^3 the hydraulic conductivity of MX80 bentonite reported as $6.5 \times 10^{-14} \text{ m/s}$. A change in the hydraulic conductivity with degree of saturation was included by using the following

relationship, $K_{unsat} = k \times S_r^{0.3}$ (Huertas et al., 2000, Cleall et al., 2007). The hydraulic conductivity relationships used in model simulations are presented in Table 9.3.

Table 9.3 Hydraulic conductivity relationships used for the numerical simulations

Hydraulic parameters	Value/ Expressions
Saturated hydraulic conductivity (Börgesson et al., 1996)	$k_{sat} = 6.5 \times 10^{-14}$ m/s
Unsaturated hydraulic conductivity (Huertas et al., 2000; Cleall et al., 2007)	$k_l = k_{sat} \times S_r^n$, where S_r is the degree of saturation and $n = 3$

9.3.4.2.1 Suction versus degree of saturation relationship

The suction versus degree of saturation relationship of MX80 bentonite used in this investigation was established by desiccators test (section 3.3.1). The water content, mass and the volumes of the bentonite specimens were measured after the tests. Based on the water content, mass and volume measurement, corresponding dry density and degree of saturation of the specimens were calculated. In the current study hysteresis effect was not considered. The experimentally established suction versus degree of saturation relationship was best fitted using van Genuchten (1980) and Fredlund and Xing (1994) model for determining the degree of saturation for the range of suction between 0 to 1000 MPa. van Genuchten (1980) proposed the following relationship (eq. 9.53) between suction and volumetric water content of an unsaturated soil considering two non-dimensional parameters:

$$\Theta = \frac{\theta - \theta_r}{\theta_s - \theta_r} \quad (9.53)$$

and

$$\Theta = \left[\frac{1}{1 + (\alpha h)^n} \right]^m \quad (9.54)$$

where Θ is the normalized water content; θ is the volumetric water content; s and r represent saturated and residual conditions, h is the suction head; α , n , m are non-dimensional parameters, and:

$$m = 1 - \frac{1}{n} \quad (9.55)$$

Fredlund and Xing (1994) proposed the following relationship (eq. 9.56) to determine the suction versus degree of saturation relationship. The residual suction considered to be 1000 MPa.

$$\theta(\psi, a, n, m) = C(\psi) \frac{\theta_s}{\left\{ \ln \left[e + \left(\frac{\psi}{a} \right)^n \right] \right\}^m} \quad (9.56)$$

where $C(\psi)$ is the correction factor and defined as:

$$C(\psi) = 1 - \frac{\ln(1 + \psi / \psi_r)}{\ln[1 + (1000000 / \psi_r)]} \quad (9.57)$$

and ψ_r is the residual suction corresponding to the volumetric water content θ_r ; a , n , m are material parameters.

Table 9.4 presents the hydraulic parameters used for the simulations. Figure 9.4 presents the suction versus degree of saturation relationships established using van Genuchten model (1980) and Fredlund and Xing (1994) model along with the experimental results.

It was noted that Fredlund and Xing (1994) model showed a better agreement with experimental suction versus degree of saturation relationship. Fredlund and Xing (1994) model considered 1000 MPa (Croney and Coleman, 1961) as the residual suction in very dry condition. The van Guenutchen (1990) model yield very high suction values at lower water contents compared to the experimental values. Considering the limitation of van Genuchten model (1980) at very dry conditions the Fredlund and Xing's (1994) approach was adopted for the simulations.

Table 9.4 Hydraulic parameters used for the numerical simulations

Hydraulic parameters	Value/ Expressions
Soil-water retention relationship (Fredlund and Xing, 1994)	$\theta(\psi, a, n, m) = C(\psi) \frac{\theta_s}{\left\{ \ln \left[e + \left(\frac{\psi}{a} \right)^n \right] \right\}^m}$ <p>where $C(\psi) = 1 - \frac{\ln(1 + \psi / \psi_r)}{\ln[1 + (1000000 / \psi_r)]}$,</p> <p>$\theta$ is the volumetric water content, ψ is the corresponding suction, $\theta = s \times n$, $a = 60000$, $n = 1.35$, $m = 1.8$, $\psi_r = 10^6$ KPa, θ_s = porosity = 0.42</p>

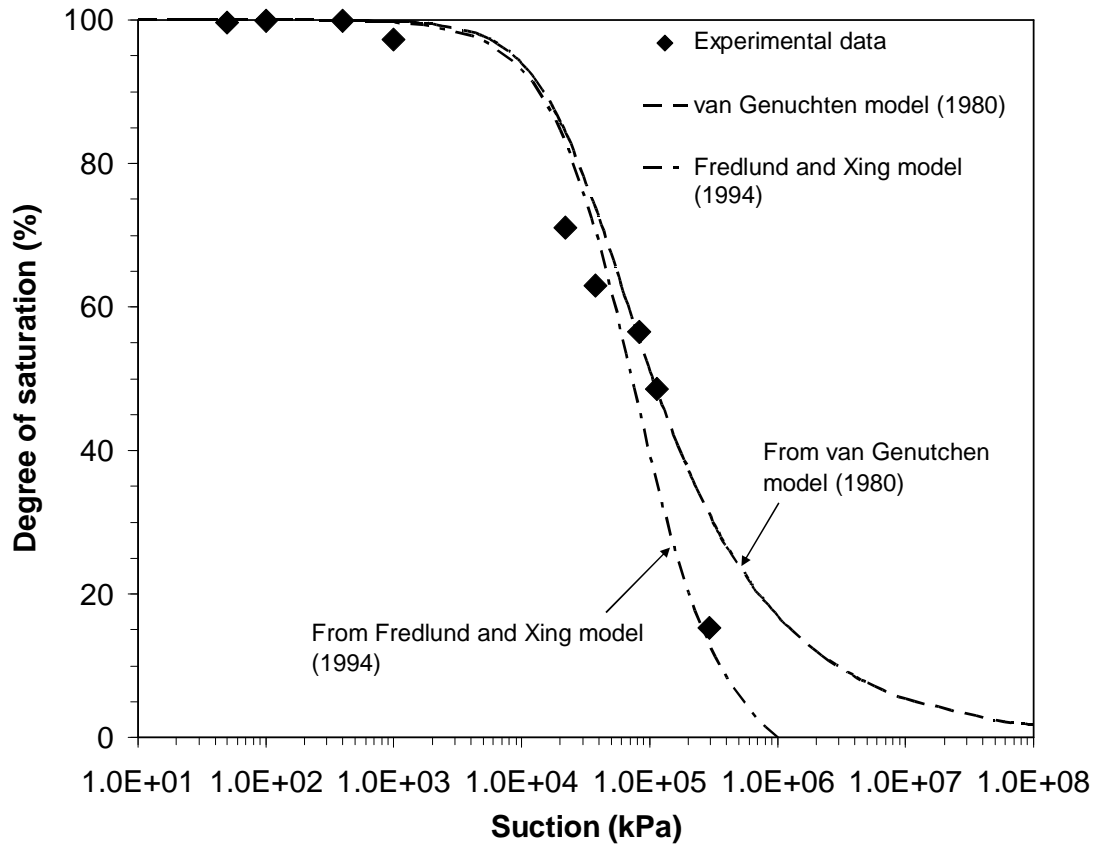


Figure 9.4. Suction versus degree of saturation relationships.

9.3.4.3 Mechanical parameters

The deformation behaviour of model simulation was carried out using Barcelona Basic Model (Alonso et al., 1990) presented in section 9.2. In eq. 9.40, κ is the stiffness parameter in the virgin state of the soil due to change in net mean stress stress. A one dimensional consolidation test was carried out with saturated bentonite specimen. Figure 9.5 presents the suction and vertical pressure versus void ratio relationship of MX80 bentonite. From the experimental results the slope of the virgin compression curve ($\lambda(0)$) was found to be 0.74. The slope of the unloading curve κ was found to be 0.23. The results are consistent with reported results by Baille et al. (2010).

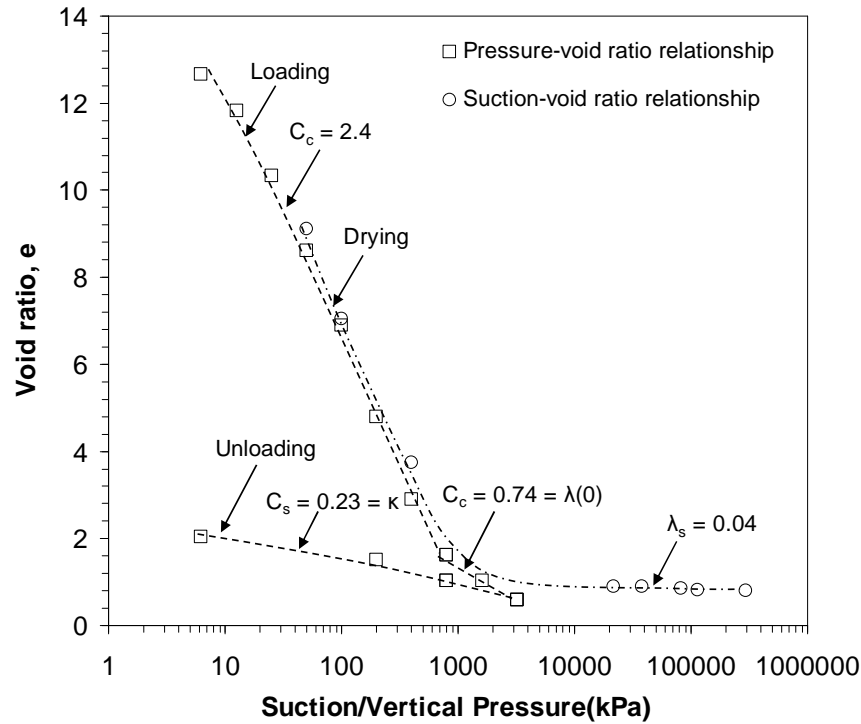


Figure 9.5. Suction and vertical pressure versus void ratio of MX80 bentonite.

A change in the void ratio due to a change in suction is known to be very small beyond the air-entry value (Fleureau et al., 1993; Fredlund and Rahardjo, 1993; Tripathy et al., 2010). The slope of the suction-void ratio curve (λ_s) from the drying path was found to be 0.04 (Fig 9.5). Fleureau et al. (1993) showed that at higher suctions, the slope of the drying-wetting paths were similar. Therefore, κ_s was considered to be equal to λ_s for the simulation. Table 9.5 presents the parameters used for the simulations to study the deformation behaviour of the specimen. The shear modulus and Poisson's ratio values used in this study are considerably higher.

Table 9.5 Mechanical parameters used for the numerical simulations

Mechanical parameters	Value/Expression
Shear modulus, G (Man and Martino, 2009)	1.0 MPa
Poisson's ratio, ν (Börjesson et al., 1996)	0.5
Compressibility coefficient for the saturated state along virgin loading, $\lambda(0)$	0.74 (1/kPa)
Compressibility coefficient for the saturated state along elastic stress path, κ	0.23 (1/kPa)
Compressibility coefficient for increments of suction along virgin states, λ_s	0.04 (1/kPa)
Compressibility coefficient for changes in suction within the elastic region, κ_s	0.04 (1/kPa)

9.4 Results and discussion

9.4.1 Influence of thermal and hydraulic gradients on temperature profile

Figure 9.6 compares the experimental and simulated temperature profiles at predetermined heights of the specimen during the thermal loading of test no. 5. A good agreement between experimental and numerical simulation results was found. The simulated temperature at distances of 20, 40 and 60 mm from the heater was found to equilibrated at about 300 minutes from the commencement of the thermal phase of the simulation (Fig. 9.6). The results showed that the simulated temperature at distances of 20, 40 and 60 mm from the heater tend to decrease with elapsed time. The thermal conductivity of soil is known to change with a change in the water content. Tang et al. (2008) reported that the thermal conductivity of compacted MX80 bentonite decreased with a decrease in the degree of saturation. Due to an applied temperature, the evaporated

water transported away from the heater end. Therefore, the thermal conductivity decreased with longer duration of thermal loading as evident from the Fig. 9.6.

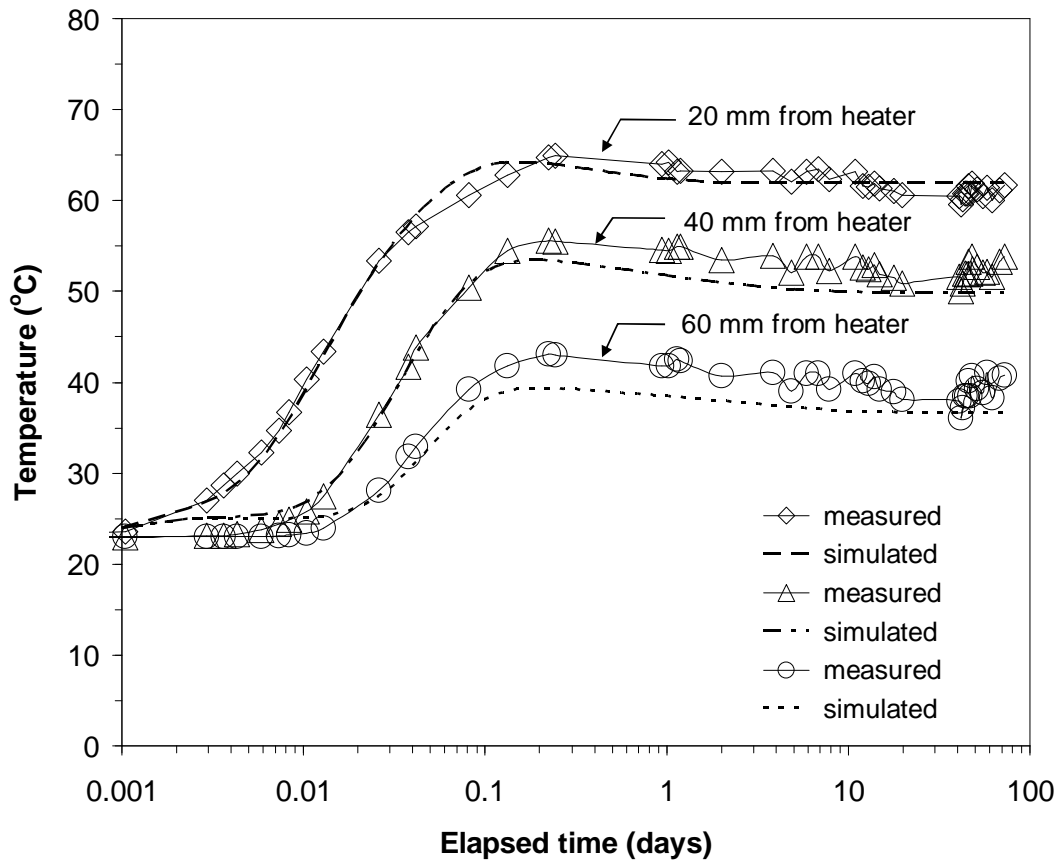


Figure 9.6. Transient temperature changes along the depth of the specimen during thermal loading.

The increment of temperature at distances of 20, 40 and 60 mm from the heater was found to be agreed very well with that of the experimental results (Fig. 9.6). The results also indicated that the temperature flux at the vertical boundary of the specimen was responsible for the non-linearity of temperature profile along the depth of the specimen.

A comparison between the measured and the simulated temperature profiles at 20, 40, and, 60 mm distance away from the heater for both thermal and thermo-hydraulic loading phase of the test are shown in Fig. 9.7. It was noted that the numerical simulation predicted very well the temperature profiles along the depth of the specimens with and without hydraulic loading conditions (Fig. 9.7).

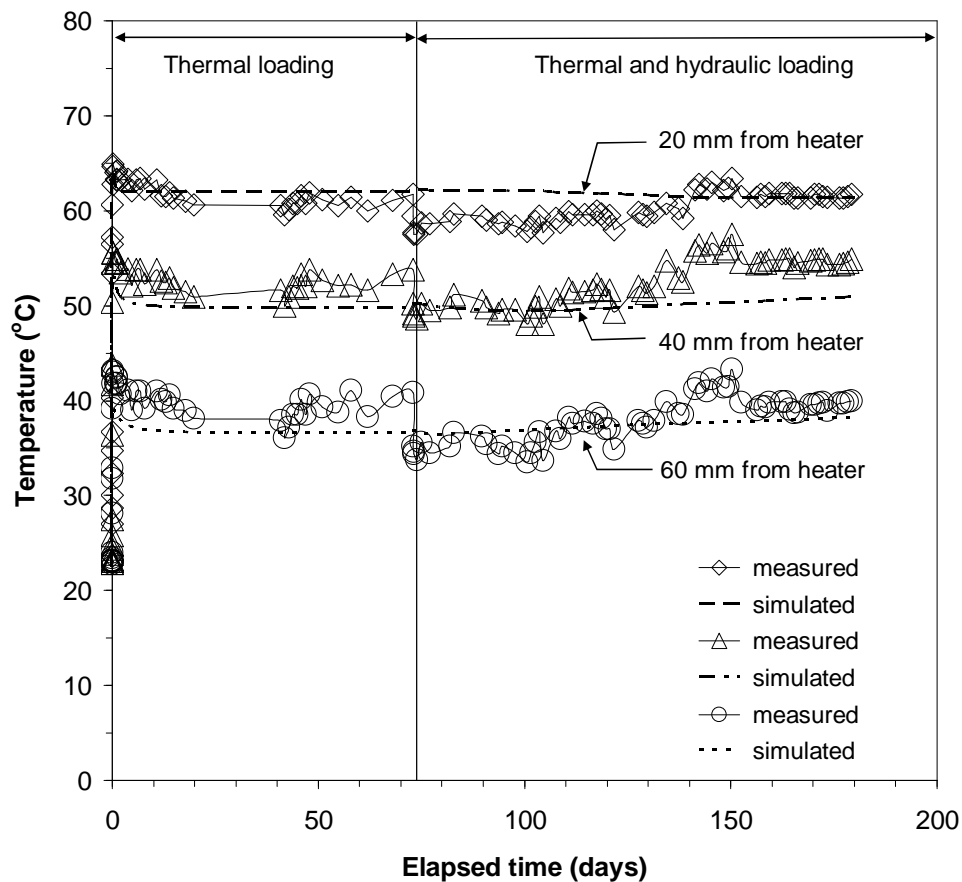
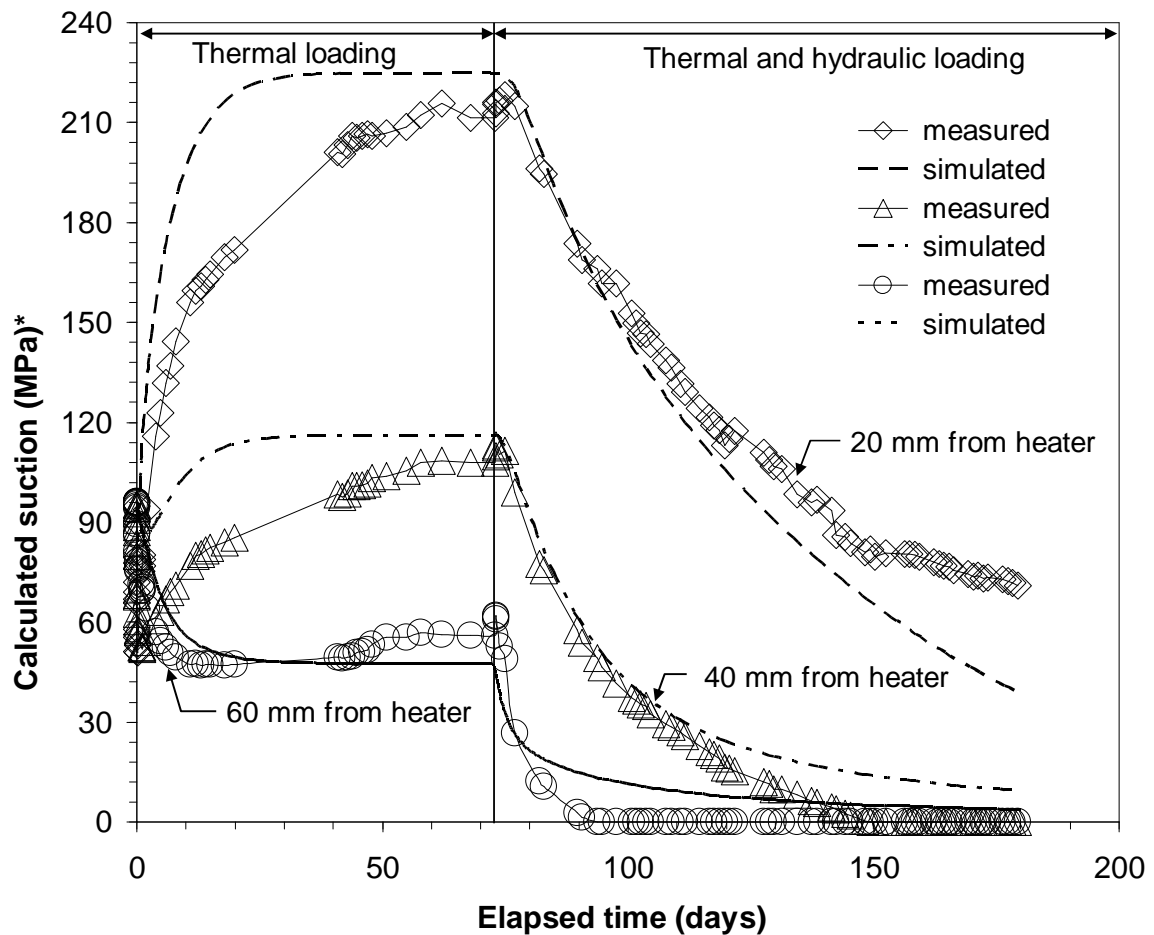


Figure 9.7. Transient temperature changes along the depth of the specimen during thermal and thermo-hydraulic loading.

9.4.2 Effects thermal and hydraulic gradients on suction profile

During the thermal and thermo-hydraulic loading of the experiment the temperature and the relative humidity at distances of 20, 40 and 60 mm from the heater were measured using the temperature and relative humidity measurement probes (chapter

3). The corresponding suction values were calculated using Kelvin's equation. Figure 9.8 compares the experimental and simulated suction variations with time at distances of 20, 40 and 60 mm from the heater.



*Calculated based on relative humidity and temperature measurements at different heights of the specimen.

Figure 9.8. Transient suction changes along the depth of the specimens during thermal and thermo-hydraulic tests.

The calculated suctions from experimental results at distances of 20 and 40 mm from the heater increased continuously up to about 50 days of applied thermal loading period. However, the simulation suction values at distances of 20 and 40 mm from the heater were equilibrated faster than the experimental suction values. The simulated

suctions at predetermined heights (distances of 20, 40 and 60 mm from the heater) were equilibrated within 20 days from the start of the applied thermal loading. The calculated suctions at distances of 20 and 40 mm from the heater increased gradually due to water vapour transported from the hotter area to the cooler area of the specimen. At a distance of 60 mm from the heater, the water content increased due to condensation of water vapour transferred from the hotter region of the specimen. Therefore, the suction at a distance of 60 mm from the heater was found to decrease from the commencement of the thermal loading. The equilibrium suctions at predetermined heights of the specimens were very similar to that of the experimental results.

At the commencement of the hydraulic loading for test no. 5, at distances of 20, 40 and 60 mm from the heater, the calculated suctions decreased as a result of an increase in the water content. At a distance of 20 mm from the heater, the rate of decrease in suction during the thermal and hydraulic of test no. 5, was found to be lesser after about 80 days applied hydraulic loading. However, the simulation results showed a continuous suction decrease with elapsed time (Fig. 9.8). The change in hydraulic conductivity of the bentonite with the degree of saturation was not considered in the simulations. At the heater end, due to constant heat source, the movement of hydrating water was retarded towards the heater. Due to these two effects, the rate of decrease in suction was found to be lesser after 80 days of applied hydraulic loading (Fig. 9.8). However, the model predicted a constant rate of change of suction with time.

After about 80 days of applied hydraulic loading, the simulated results (Fig. 9.8) show slightly higher suctions than the experimental results at distance of 40 and 60 mm from the heater. The experimental suction values calculated at a distance of 60 mm from the heater was zero after about 80 days of hydration, whereas simulated suction values

were equilibrated with some residual suction (Fig. 9.8). Although some quantitative differences were noted between the experimental and the simulated suction values at distances of 20, 40 and 60 mm from the heater, the model simulations predicted the experimental results reasonably well.

9.4.3 Development of swelling pressure due to thermal and hydraulic gradients

The variation of swelling pressure at the opposite end of the heat source of the compacted bentonite specimens were monitored due to the application of the thermal and the thermal and hydraulic loading conditions (chapter 7, section 7.3.4). In the model simulation, the stresses in y-direction were considered as the axial swelling pressure (Figs. 9.1, 9.2 and 9.3).

Figure 9.9 presents the comparison between the experimental and the simulated swelling pressures measured at the opposite end of the heat source of the compacted bentonite specimens due to the application of the thermal and the thermal and hydraulic loading conditions. During the thermal loading, the measured swelling pressure was found to attain the peak value at about 10 days from the commencement of the thermal loading. For longer duration of thermal loading, the measured swelling pressure was found to reduce. The simulation results showed a faster equilibration of swelling pressure during the thermal loading period. The variation of swelling pressure at the opposite end of the heat source of the compacted bentonite specimens during the thermal loading was not able to assess from the simulation. During the development of the code, the stress redistribution due to redistribution of moisture has not been considered.

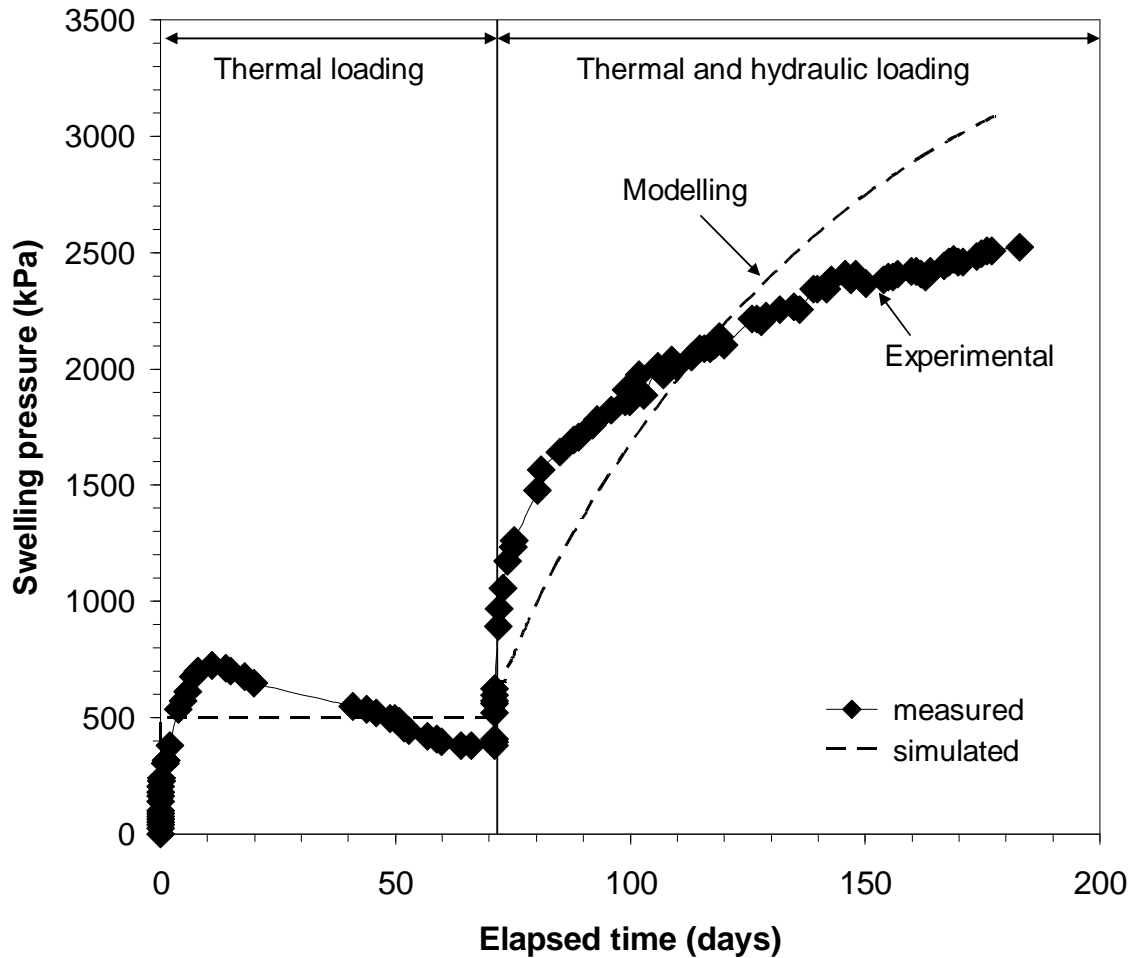


Figure 9.9. Swelling pressure development at the cold end of the specimen due to thermal and thermo-hydraulic loading.

During the thermal and hydraulic loading stage, the experimental and simulated results showed continual increase of the swelling pressure. The experimental swelling pressures were equilibrated after about 80 days of application of hydraulic loading. However, the simulated swelling pressure was found to be increased gradually (Fig. 9.9). Although, the agreement between the experimental and simulated equilibrium swelling pressure results were not good, the trend of swelling pressure developed at the opposite end of the heat source of the specimen was obtained.

9.5 Concluding remarks

In this chapter, the development of finite element based model COMPASS is briefly discussed. The salient equations of the model formulation are presented. The experimental thermal and thermo-hydraulic test conditions were simulated using COMPASS to compliment the experimental thermal and thermo-hydraulic test results. The mesh geometry, initial and boundary conditions of the simulations are presented. The material parameters used for the simulations are presented. The material parameters required for the simulations were calculated from experimental results as well as chosen from the parameters reported in the literature. The transient temperature and suction variation along the depth of the bentonite specimens due to thermal and thermo-hydraulic loading are presented. The swelling pressure developed due to thermal and thermo-hydraulic loading at the opposite end of the heat source of cylindrical specimen are presented.

Comparisons between the experimental and the simulated results showed that the finite element based code COMPASS enabled assessing the transient temperature and suction profiles during the thermal and the thermo-hydraulic tests reasonably well. Although there were some quantitative differences between the experimental and simulated swelling pressure values, the model was able to predict the swelling pressure development with elapsed time in compacted unsaturated bentonite due to the thermal and hydraulic loading conditions.

Chapter 10

Conclusions

The objective of this thesis was to study the coupled thermo-hydro-mechanical-chemical behaviour of MX80 bentonite in geotechnical applications by experimental, theoretical and numerical investigation.

Commercially available MX80 bentonite was used for the investigation. The properties of the bentonite were determined by standard laboratory tests prior to the testing programme. Constant volume swelling pressure tests were carried out on compacted bentonite specimens to study the swelling pressure at ambient and elevated temperatures. The effects of dry density, post compaction residual stress, electrolyte

concentration and temperature on the swelling pressure of compacted bentonite were investigated. The experimental swelling pressures obtained were compared with swelling pressures calculated using the Gouy-Chapman diffuse double layer theory and the Stern theory as applicable to interacting clay platelet systems. Constant surface potential was considered for calculating the swelling pressures using the diffuse double layer theory and the Stern theory. Compressibility tests were carried out using a conventional oedometer with initially saturated bentonite specimen. The compressibility behaviour was studied using the Stern theory and the diffuse double layer theory.

Thermal and thermo-hydraulic tests were carried out using a custom made thermo-hydraulic device. The thermal and thermo-hydraulic tests were carried out on compacted bentonite specimens for durations between 12 and 182 days. At the bottom end of the bentonite specimens the temperature was maintained at 85 °C, whereas the temperature at the top end of bentonites specimens was 25 °C. Distilled water was supplied from the top of the specimens during the thermo-hydraulic tests. The temperature and the relative humidity were monitored along the depth of the bentonite specimens during the thermal and thermo-hydraulic tests, and the swelling pressures of the bentonite specimens were monitored at the opposite end of the heat source. After termination of the thermal and thermo-hydraulic test, water content, dry density, degree of saturation and change in soluble cations and anions concentration along the depth of the bentonite specimens were measured. Cations and anions concentrations were measured using Ion Chromatography (IC) and Inductively Coupled Plasma Optical Emission Spectroscopy (ICP-OES). An elasto-plastic two dimensional finite element thermo-hydro-mechanical model was generated, which simulated the thermal and the thermo-hydraulic test conditions in COMPASS. Comparisons between the experimental

and the simulated temperature, suction and swelling pressure variation with elapsed time were studied in detail.

Based on the findings reported in this thesis, the following conclusions are drawn.

1. The swelling pressure of compacted bentonite increased with an increase in the compaction dry density. Higher electrolyte concentration of the bulk fluid reduced the swelling pressure up to a swollen dry density of 1.6 Mg/m^3 . At an elevated temperature of 70°C , the swelling pressure decreased by about 30 to 40% for a range of compaction dry density of 1.10 to 1.55 Mg/m^3 as compared to the specimens tested at 25°C . The saturated water content of compacted bentonite specimens reduced with an increase in the dry density. These findings are concurrent with the experimental results reported in literature.
2. Release of post compaction residual stresses increased the swelling pressures of compacted bentonite specimens. The difference in the swelling pressures of compacted specimens with and without post compaction residual stresses are attributed to differences in structure and fabric owing to applied compaction loads during preparation of the specimens.
3. The Gouy-Chapman diffuse double layer theory and the Stern theory enabled assessment of swelling pressures of compacted bentonite. The Stern theory improved the assessment of the swelling pressure up to a dry density of 1.45 Mg/m^3 when the specimens were hydrated using distilled water. However, agreements between the experimental and theoretical dry density-swelling

pressure relationships for the tests conducted at elevated temperature and using higher electrolyte concentrations were found to be poor. The swelling pressures calculated using the diffuse double layer theory was found to be less than that of the experimental results at lower dry densities and greater at higher dry densities.

4. The Stern theory was found to be more appropriate to be used for initially saturated slurried bentonites. Good agreements were noted between the experimental and the theoretical vertical pressure-void ratio relationships.
5. Due to applied thermal and thermo-hydraulic gradients, the relative humidity, the water content and the degree of saturation were found to increase from the hot end to the cold end of the compacted bentonite specimens tested. In the past, studies on the thermo-hydro-mechanical-chemical behaviour of compacted bentonites by other researchers have also noted similar trends.
6. Compacted bentonite specimens exhibited swelling pressures at the opposite end of the heat source due to an applied thermal gradient. The measured swelling pressures of the specimens at the opposite end of the heat source remained between 0.5 to 1.2 MPa. Development of swelling pressures at the opposite end of the heat source is attributed to an increase in the water content on account of vapour flow from hotter region towards the cooler region of the specimens and further condensation of water molecules at the cooler region.
7. The measured swelling pressures of the bentonite specimens at the opposite end of the heat source due to an applied thermal gradient were found to decrease after 7

to 10 days from commencement of the tests. A decrease in the swelling pressure during longer period of thermal loading is attributed to the combined influence of a higher suction gradient towards the hot end, shrinkage of the specimens at the hot end and redistribution of water content within the specimens to attain a new equilibrium state.

8. Due to applied thermal and thermo-hydraulic gradients, the concentrations of cations and anions were found to increase towards the hot end of the specimens. The increase in concentrations of cations and anions were initiated by diffusion and advection processes.
9. Finite element code COMPASS enabled assessment of the changes in suction with elapsed time along the depth of the bentonite specimens and swelling pressure variation at the cold end of the specimens for both applied thermal and thermo-hydraulic gradients. The agreement between experimental and simulated swelling pressure results was found to be poor. However, the trend of swelling pressure development with time at the cold end of the specimen for the specific geometry of cell was obtained.

References

- Agus, S.S. (2005). An experimental study on compacted bentonite-sand mixtures. PhD thesis, Bauhaus-University, Weimar, Germany.
- Agus, S.S. and Schanz, T. (2005). Comparison of four methods for measuring total suction. *Vadose Zone Journal-Soil Science Society of America*, 4(4), 1087-1095.
- Åkesson, M., Jacinto, A.C., Gatabin, C., Sanchez, M. and Ledesma, A. (2009). Benonite THM behaviour at high temperatures: experimental and numerical analysis. *Géotechnique*, 59(4), 307-318.
- Alonso, E.E., Gens, A. and Josa, A. (1990). A constitutive model for partially saturated soils. *Géotechnique*, 40(3), 405-430.
- Alonso, E.E., Vaunat, J. and Gens, A. (1999). Modelling the mechanical behaviour of expansive clays. *Engineering Geology*, 54, 173-183.
- Alonso, E.E., Pereira, J.M., Vaunat, J and Olivella, S. (2010). A microstructurally based effective stress for unsaturated soils. *Géotechnique*, 40(12), 913-925.
- Alonso, A.E., Springman, S.M. and Ng, C.W.W. (2008). Monitoring large-scale tests for nuclear waste disposal. *Geotechnical and Geological Engineering*, 26, 817-826.
- Anderson, D.W. and Low, P.F. (1957). Density of water adsorbed on wyoming bentonite. *Nature*, 180, 1194
- Arifin, Y.E. (2007). Thermo-hydro-mechanical behaviour of compacted bentonite-sand mixtures: an experimental study, PhD thesis, Bauhaus-University, Weimar, Germany.
- ASTM. (1997). Annual Book of Standards. Volumes 04.08 and 04.09, Soil and rock, ASTM International. West Conshohocken. PA.
- ASTM D 4943-08 (2008). Standard test methods for shrinkage factors of soils by the wax method.

- ASTM D 6836-02 (2003). Standard test methods for determination of the soil water characteristic curve for desorption using a Hanging Column, Pressure Extractor, Chilled Mirror Hygrometer, and/or Centrifuge.
- ASTM E 104-85 (1998). Standard Practice for Maintaining Constant Relative Humidity by Means of Aqueous Solutions.
- Baille, W., Tripathy, S. and Schanz, T. (2010). Swelling pressures and one-dimensional compressibility behaviour of bentonite at large pressures. *Applied Clay Science*, 48, 324-333.
- Baver, L.D. and Winterkorn, H.W. (1936). Sorption of Liquids by Soil Colloids: II. Surface Behaviour in the Hydration of Clays. *Soil Science*, 40, 403-418.
- Bear, J. and Gilman, A. (1995). Migration of salts in the unsaturated zone caused by heating, *Transport in porous media*, 19(2), 139-156.
- Benson, C. (2005). Materials stability and applications, in barrier systems for environmental contaminant containment and treatment, C. Chen, H. Inyang, and L. Everett, eds., CRC Press, Boca Raton, FL, 143-208.
- Blatz, J.A., Cui, Y.J. and Oldecop, L. (2008). Vapour equilibrium and osmotic technique for suction control. *Geotechnical and Geological Engineering*, 26, 661-673.
- Bolt, G. H. (1956). Physico-chemical analysis of the compressibility of pure clays. *Géotechnique*, 6(2), 86-93.
- Börgesson, L., Karnland, O. and Johanneson, E.K. (1996). Modelling of the physical behaviour of clay barriers close to water saturation. *Engineering Geology*, 41, 127-144.
- Börgesson, L., Chijimatsub, M., Fujitab, T., Nguyenc, T.S., Rutqvistd, J. and Jinge, L. (2001). Thermo-hydro-mechanical characterisation of a bentonite-based buffer material by laboratory tests and numerical back analyses. *International Journal of Rock Mechanics and Mining Sciences*, 38, 95-104.

- Bourg, I.C., Bourg, A.C.M. and Sposito, G. (2003). Modeling diffusion and adsorption in compacted bentonite: a critical review. *Journal of Contaminant Hydrology*, 61(1-4), 293-302.
- Bourg, I.C., Sposito, G. and Bourg, A.C.M. (2006). Tracer Diffusion in Compacted, Water-saturated Bentonite. *Clays and Clay Minerals*, 54(3), 363-374.
- Bradbury, M.H. and Baeyens, B. (2002). Pore water chemistry in compacted re-saturated MX 80 bentonite: Physico-chemical characterisation and geochemical modelling. PSI Bericht Nr Switzerland.
- Bradbury M.H. and Baeyens B. (2003). Porewater chemistry in compacted re-saturated MX 80 bentonite. *Journal of Contaminant Hydrology*, 61, 329-338.
- Britto, A.M. and Gunn, M.G. (1987). *Critical state soil mechanics via finite element*, Ellis Horwood Ltd.
- BS 1377-2 (1990). *Soils for civil engineering purposes. Part 2: Classification tests*. British Standards Institution.
- BS 1377-3 (1990). *Soils for civil engineering purposes. Part 3: Chemical and electrochemical tests*. British Standards Institution.
- Bucher, F., and Müller-Vonmoos, M. (1989). Bentonite as a containment barrier for the disposal of highly radioactive waste. *Applied Clay Science*, 4(2), 157–177.
- Buil, B., Gómez, J., Peña, A., Garralón, A., Turrero, M.J., Escribano, A., Sánchez, L. and Durán, J.M. (2010). Modelling of bentonite-granite solutes transfer from an in situ full-scale experiment to simulate a deep geological repository (Grimsel Test Site, Switzerland). *Applied Geochemistry*, 25(12), 1797-1804.
- Bulut, R., Par, S.W. and Lytton, R.L. (2000). Comparison of total suction values from psychrometer and filter paper methods. *Proceedings of the Asian conference on unsaturated soils, UNSAT-ASIA 2000, Singapore*, 269–273.
- Bulut, R. Lytton, R.L. and Wray, W.K. (2001). Soil suction measurements by filter paper. In: Vipulanandan, C., Addison, M.B., Hasen, M. (eds) *Expansive clay soils and*

- vegetative influence on shallow foundations, ASCE geotechnical special publication no. 115. Houston, Texas, 243–261.
- Bulut, R. and Leong, E. C. (2008). Indirect measurement of suction. *Geotechnical and Geological Engineering Journal*, 26(6), 633-644.
- Castellanos, E., Villar, M.V., Romero, E., Lloret, A. and Gens, A. (2008). Chemical impact on the hydro-mechanical behaviour of high-density FEBEX bentonite. *Physics and Chemistry of the Earth*, 33, S516-S526.
- Chijimatsu, M. and Sugita, Y. (2001). Aspo Hard Rock Laboratory: Selection of THMCB Models. SKB International Progress Report IPR-01-66. Swedish Nuclear Fuel and Waste Management Co (SKB). SKB, Stockholm, 37–46.
- Chan, D.Y.C., Pashley, R.M. and Quirk, J.P. (1984). Surface potentials derived from co-ion exclusion measurements on homoionic montmorillonite and illite. *Clays and Clay Minerals*, 32, 131-138.
- Chapman, D.L. (1913). A Contribution to the theory of electrocapillarity. *Philosophical Magazine*, 25(148), 475-481.
- Childs, E.C. (1969). An introduction to the physical basis of the soil water phenomena. John Wiley, London.
- Cho, W.J., Lee, J-O. and Kang, C-H. (2002). Influence of salinity on the hydraulic conductivity of compacted bentonite. *Materials Research Society, Symp. Proc*, Vol.713, JJ1150, 1-7.
- Cleall, P.J. (1998). An investigation of the thermo/hydraulic/mechanical behaviour of unsaturated soils, including expansive clays. PhD Thesis, Cardiff University.
- Cleall, P.J., Seetharam, S.C. and Thomas, H.R. (2007). Inclusion of some aspects of chemical behaviour of unsaturated soil in Thermo/Hydro/Mechanical models. II: Application and Transport of soluble salts in Compacted Bentonite. *Journal of Engineering Mechanics ASCE*, 133(3), 348-356.

- Cleall, P.J., Singh, R.M. and Thomas, H.R. (2011). Non-isothermal moisture movement in unsaturated kaolin-an experimental and theoretical investigation. *ASTM Geotechnical Testing Journal*, 34(5), 1-11.
- Collin, F., Li, X.L., Radu, J.P. and Charlier, R. (2002). Thermo-hydro-mechanical coupling in clay barriers. *Engineering Geology*, 64, 179-193.
- Cresswell, H.P., Green, T.W. and McKenzie, N.J (2008). The adequacy of pressure plate apparatus for determining soil water retention. *Soil Science Society of American Journal*, 72(1), 41-49.
- Croney, D., Coleman, J.D. and Curren, E.W.H. (1952). The suction of moisture held in soil and other porous materials. *Road Research Technical Paper*, No. 24, London..
- Croney, D. and Coleman, J.D. (1961). Pore pressure and suction in soils. *Conference on Pore Pressure and Suction in Soils*, London, 31-37.
- Cruz-Guzmán, M., Celis, R., Hermosín, M.C., Koskinen, W.C., Nacer, E.A. and Cornejo, J. (2006). Heavy metal adsorption by montmorillonites modified with natural organic cations. *Soil Science Society American Journal*, 70, 215–221.
- Cuevas, J., Villar, M., Martyn, M., Cobena, J.C. and Leguey, S. (2002). Thermohydraulic gradients on bentonite: distribution of soluble salts, microstructure and modification of the hydraulic and mechanical behaviour. *Applied Clay Science*, 22, 25-38.
- Cui, Y.J. and Delage, P. (1996). Yielding and plastic behaviour of an unsaturated compacted silt. *Géotechnique*, 46, 291–311.
- Darcy, H. (1856). *Les fontaines publiques de la ville de Dijon*. V. Dalmont, Paris, 590-594.
- de Vries, D.A. (1958). Simultaneous transfer of heat and moisture in porous media. *Transactions American Geophysical Union*, 39(5), 909-916.
- Deeg, E. and Huber, O. (1955). Dielectric constant of clays in decimetre wavelength as a function of water content. *Berichte der Deutschen Keramischen Gesellschaft*, 32, 261-272.

- Delage, P., Suraj de Silva, G.P.R. and De Laure, E. (1987). Un nouvel appareil triaxial pour les sols non saturés. Proceedings of 9th European Conference on Soil Mechanics and Foundation Engineering, Dublin, 1, 26–28.
- Delage, P., Howat, M. and Cui, Y.J. (1998). The relationship between suction and swelling properties in a heavily compacted unsaturated clay. *Engineering Geology*, 50(1-2), 31-48.
- Delage P., Marcial D., Cui Y.J. and Ruiz, X. (2006). Ageing effects in the compacted bentonite: a microstructure approach. *Géotechnique*, 56(4), 291-304.
- Delage, P., Romero, E.E. and Tarantino, A. (2008). Recent developments in the techniques of controlling and measuring suction in unsaturated soils. Proceeding of 1st European conference on Unsaturated soil, Eds. Toll, D., Gallipoli, D., Wheeler, S., 33-52.
- Dixon, D.A. and Gray, M.N. (1985). The engineering properties of buffer material. Technical report TR-350, Underground Research Laboratory, Atomic Energy of Canada Limited, Pinawa MB, Canada.
- Dixon, D.A., Graham, J. and Gray, M.N. (1999). Hydraulic conductivity of clays in confined tests under low hydraulic gradients. *Canadian Geotechnical Journal*, 36, 815-825.
- Edlefsen, N.E. and Anderson, A.B.C. (1943). Thermodynamics of Soil Moisture, Hilgardia, 15, 31-298.
- Empresa Nacional de Residuos Radiactivos SA, (2000). FEBEX project— Full scale engineered barriers experiments for a deep geological repository for high level radioactive waste in crystalline host rock, Publ. Tech. 1/2000, Madrid.
- ENRESA, (2004). FEBEX II Project Final report on thermo-hydro-mechanical laboratory tests. Final report, Publicación técnica 10/2004, Empresa Nacional de Residuos Radiactivos SA (ENRESA), Madrid, Spain.
- Ewen, J. and Thomas, H.R. (1987). The thermal probe – a new method and its use on an unsaturated sand. *Géotechnique*, 37(1), 91-105.

- Ewen, J. and Thomas, H.R. (1989). Heating unsaturated medium sand. *Géotechnique*, 39, 455-470.
- Fernández, A.M., Cuevas, J. and Rivas, P. (2001). Pore Water Chemistry of the FEBEX Bentonite. Material research society, symposium Proceedings, 663, 573-588.
- Fernández, A.M., Baeyen, B., Bradbury, M. and Rivas, P. (2001). Analysis of the porewater composition of a Spanish compacted bentonite used in an engineered barrier. *Physics and Chemistry of Earth*, 29, 105-118.
- Fernández, A.M., Cuevas, J. and Rivas, P. (2008). Pore Water Chemistry of the FEBEX Bentonite. Material research society, symposium Proceedings, vol. 902.
- Fernández, A.M. and Villar, M.V. (2010). Geochemical behaviour of a bentonite barrier in the laboratory after up to 8 years of heating and hydration. *Applied Geochemistry*, 25, 809-824.
- Fleureau, J.M., Kheirbek-Saoud, S., Soemitro, R. and Taibi, S. (1993). Behaviour of clayey soils on drying-wetting paths. *Canadian Geotechnical Journal*, 30, 287-296.
- Fleureau, J.M., Verbrugge, J.C., Huergo, P.J., Correia, A.G. and Kheirbek-Saoud, S. (2002). Aspects of the behaviour of compacted clayey soils on drying and wetting paths. *Canadian Geotechnical Journal*, 39, 1341-1357.
- Fredlund, D.G., Shuai, F., and Feng, M. (2000). Increased accuracy in suction measurements using an improved thermal conductivity sensor. *Proceedings of the Seventh International Conference on Tailing and Mine Waste*, Fort Collins, Colorado, USA. 443-450.
- Feng, M., and Fredlund, D.G., (2003). Calibration of thermal conductivity sensors with consideration of hysteresis. Technical Note, *Canadian Geotechnical Journal*, 40(5), 1048-1055.
- Feng, M., Fredlund, D.G., & Shuai, F. (2002). A laboratory study of the hysteresis of a thermal conductivity soil suction sensor. *Geotechnical Testing Journal*, 25(3), 303-314.

- Fredlund, D.G. (2006). Unsaturated Soil Mechanics in Engineering Practice. *Journal of Geotechnical and Geoenvironmental Engineering*, 132(3), 286-321.
- Fredlund, D.G. and Xing, A. (1994). Equations for the soil-water characteristic curve. *Canadian Geotechnical Journal*, 31, 521-532.
- Fredlund D.G. and Rahardjo, H. (1993). *Soil mechanics for unsaturated soils*, John Willey and Sons, Canada.
- Fredlund, D.G. and Wong, D.K.H. (1989). Calibration of thermal conductivity sensors for measuring soil suction. *ASTM Geotechnical Testing Journal*, 12(3), 188-194.
- Fredlund, D.G., Shuai, F. and Feng, M. (2000). Increased accuracy in suction measurements using an improved thermal conductivity sensor. *Proceedings of the Seventh International Conference on Tailing and Mine Waste*, Fort Collins, Colorado, 443-450.
- Folly, J.P.W. (2001). Thermo-hydro-mechanical behaviour of unsaturated soil: An experimental study. PhD thesis, School of Engineering, Cardiff University.
- Gardner, R. (1937). A method of measuring the capillary tension of soil moisture over a wide moisture range. *Soil Science*, 43, 227-283.
- Gatabin, C. and Billaud, P. (2005). Bentonite THM mock up experiments. Sensors data report. CEA, Report NT-DPC/SCCME 05-300-A, Cedex.
- Gens, A. and Alonso, E.E. (1992). A framework for the behaviour of unsaturated expansive clays. *Canadian Geotechnical Journal*, 29, 1013-1032
- Gens, A. and Olivella, S. (2000). Non isothermal multiphase flow in deformable porous media: Coupled formulation and application to nuclear waste disposal. In *Developments in theoretical geomechanics: The John Booker Memorial Symposium* (eds D. W. Smith and J. P. Carter), Rotterdam, 619–640.
- Gens, A., Vaunat, J., Garitte, B. and Wileveau, Y. (2006). Response of a saturated mudstone under excavation and thermal loading. In *EUROCK 2006: Multiphysics coupling and*

- long-term behaviour in rock mechanics, eds. Van Cotthem, A., Charlier, R., Thimus, J. F. and Tshibangu, J. P. Taylor & Francis, London, 35–44
- Gens, A., Vaunt, J., Garite, B. and Wileveau, Y. (2007). In situ behaviour of a stiff layered clay subject to thermal loading: observations and interpretation. *Géotechnique*, 57(2), 207–228.
- Gens, A., Sanchez, M., Guimaraes, L. Do, N., Alonso, E.E., Lloret, A., Olievella, S, Villar, M.V. and Huertas, F. (2009). A full-scale in situ heating test for high-level nuclear waste disposal: observations, analysis and interpretation. *Géotechnique*, 59(4), 377–399.
- Gomez-Espina, R. and Villar, M.V. (2010). Geochemical and mineralogical changes in compacted MX-80 bentonite submitted to heat and water gradients. *Applied Clay Science*, 47, 400-408.
- Gonçalvès, J., Rousseau-Gueutin, P. and Revil, A. (2007). Introducing interacting diffuse layers in TLM calculations: A reappraisal of the influence of the pore size on the swelling pressure and the osmotic efficiency of compacted bentonites. *Journal of Colloid and Interface Science*, 316, 92–99.
- Gouy, G. (1910). Electrical charge on the surface of an electrolyte. *Journal of Physics*, 4(9), 457-468.
- Grim, R.E. (1968). *Clay mineralogy*. 2nd ed. McGraw-Hill, New York.
- Gurr, C.G., Marshall, T.J. and Hutton, J.T. (1952). Movement of water in soil due to a temperature gradient. *Soil Science*, 74(5), 335-345.
- Harrison, B.A. and Blight, G.E. (2000) A comparison of in-situ soil suction measurements. In *Proceedings of the 1st Asian Conference on Unsaturated Soils (UNSAT-ASIA 2000)*, Singapore, 2000 (Eds. H. Rahardjo, D.G. Toll, and E.C. Leong), Balkema, Rotterdam: 281-286.
- Heilman, M.D., Carter, D.L. and Gonzalez, C.L. (1965). The ethylene glycol monoethyl ether (EGME) technique for determining soil-surface. *Soil Science*, 100(6), 409-413.

- Herbert, H.J. and Moog, H.C. (1999). Cation exchange, interlayer spacing and water content of MX 80 bentonite in high molar saline solutions. *Engineering Geology*, 54, 55-65.
- Horikawa, Y, Murray, R.S. and Quirk, J.P. (1988). The effect of electrolyte concentration on the zeta potentials of homoionic montmorillonite and illite. *Colloids and Surfaces*, 32, 181-195.
- Hou, J., Li, H. and Zhu, H. (2009). Determination of clay surface potential: a more reliable approach. *Soil Science Society of American Journal*, 73, 1658-1663.
- Houston, S.L., Houston, W.N. and Wagner, A.-M. (1994). Laboratory filter paper suction measurements. *ASTM Geotechnical Testing Journal*, 17(2), 185-194.
- Huertas, F., Fuentes-Cantillana, J.L., Jullien, F., Linares, J., Fariña, P., Ghoreychi, M., Jockwer, N., Kickmaier, W., Martínez, M.A., Samper, J., Alonso, E. and Elorza, F.J. (2000). Full-scale engineered barriers experiment for a deep geological repository for high-level radioactive waste in crystalline host rock (FEBEX project). European Union.
- Hunter, R.J. (1981). *Zeta potential in colloid science*. Academic press Inc., London.
- Imbert, C. and Villar, M.V. (2006). Hydro-mechanical response of a bentonite pellets/powder mixture upon infiltration, *Applied Clay Science*, 32, 197– 209.
- International Atomic Energy Association, (2009). Geological disposal of radioactive waste: technical implications for retrievability. IAEA Nuclear Energy Series. NW-T-1.19.
- Israelachvili, J. and Wennerström, H. (1996). Role of hydration and water structure in biological and colloidal interactions. *Nature*, 379, 219–225.
- Jacinto, A.C., Villar, M.V., Gomez-Espina, R. and Ledesma, A. (2009). Adaptation of the van Genuchten expression to the effects of temperature and density for compacted bentonites. *Applied Clay Science*, (42), 575–582.
- Josa, A., Alonso, E.E., Lloret, A. and Gens, A. (1987). Stress-strain behaviour of partially saturated soils. *Proceedings of the 9th European Conference on Soil Mechanics and Foundation Engineering*, Dublin, 2, 561-564.

- Jullien, M., Raynal, J., Kohler, E. and Bildstein, O. (2005). Physicochemical reactivity in clay rich materials: tools for safety assessment. *Oil and Gas Science Technology*, 60(1), 107–120.
- Kanno, T., Kato, K. and Yamagata, J. (1996). Moisture movement under a temperature gradient in highly compacted bentonite. *Engineering Geology*, 41, 287-300.
- Karnland, O., Olsson, S. and Nilsson, U. (2006). Mineralogy and sealing properties of various bentonites and smectite-rich clay materials. SKB Technical Report TR-06-30.
- Karnland, O., Olsson, S., Nilsson, U. and Sellin, P. (2007). Experimentally determined swelling pressures and geochemical interactions of compacted Wyoming bentonite with highly alkaline solutions. *Physics and Chemistry of the Earth*, 32, 275-286.
- Kassif, G. and Ben Shalom, A. (1971). Experimental relationship between swell pressure and suction. *Géotechnique*, 21 (3), 245–255.
- Kaye, G.W.C. and Laby, T.M. (1973). Tables of physical and chemical constant, 14th Edition, Harlow, Longman.
- Kjellander, R. and Marčelja, S. (1985). Inhomogeneous Coulomb fluids with image interactions between planar surfaces. *Journal of Chemical Physics*, 82(4), 2122-2135.
- Klute, A. (1986). Water retention: Laboratory Methods. *Methods of Soil Analysis Part 1 Physical and Mineralogical Methods*, ed. Klute A. Madison, WI: American Society of Agronomy and Soil Science Society of America, 635-662.
- Komine, H. and Ogata, N. (1994). Experimental study on swelling characteristics of compacted bentonite. *Canadian Geotechnical Journal*, 31(4), 478–490.
- Komine, H. and Ogata, N. (1996). Prediction for swelling characteristics of compacted bentonite. *Canadian Geotechnical Journal*, 33(1), 11–22
- Komine, H. and Ogata, N. (2003). New equations for swelling characteristics of bentonite based buffer materials. *Canadian Geotechnical Journal*, 40(2), 460–475.

- Komine, H. (2004). Simplified evaluation on hydraulic conductivities of sand-bentonite mixture backfill. *Applied Clay Science*, 26, 13-19.
- Komine, H., Yasuhara, K. and Murakami, S. (2009). Swelling characteristics of bentonites in artificial seawater. *Canadian Geotechnical Journal*, 46(2), 177-189.
- Komine, H., Yasuhara, K. and Murakami, S. (2009). Swelling characteristics of bentonites in artificial seawater. *Canadian Geotechnical Journal*, 46(2), 177-189.
- Koniger, F., Emmerich, K., Kemper, G., Gurner, M., Garner, W., Nuesch, R. and Schuhmann, R. (2008). Moisture spreading in a multi-layer hydraulic sealing (HTV-1). *Engineering Geology*, 98, 41-49.
- Kozaki, T., Inada, K., Sato, S. and Ohashi, H. (2001). Diffusion mechanism of chloride ions in sodium montmorillonite. *Journal of Contaminant Hydrology*, 47(2-4), 159-170.
- Krahn, J. and Fredlund, D.G. (1972). On total, matric and osmotic suction. *Soil Science*, 115(5), 339-348.
- Lagaly, G. and Ziesmer, S. (2003). Colloid chemistry of clay minerals: the coagulation of montmorillonite dispersions. *Advances in Colloid and Interface Science*, 100–102, 105–128.
- Laird, D.A. (2006). Influence of layer charge on swelling of smectites. *Applied Clay Science*, 34, 74-87.
- Langmuir, I. (1917). The constitution and Fundamental Properties of Solids and Liquids. *Journal of American Chemical Society*, 39, 1848-1906.
- Lee, J.O., Park, J.H., and Cho, W.J. (2008). Engineering-scale test on the thermal-hydro-mechanical behaviors in the clay barrier of a HLW repository. *Annals of Nuclear Energy*, 35, 1386-1396.
- Ledsema, A. and Chen, G. (2003). T-H-M modeling of the Prototype Repository Experiment at Äspö, Hard Rock Laboratory, Sweden, *Proc. Of Geoproc Conference*, KTH, Stockholm, 37-46.

- Leong, E.C., Tripathy, S. and Rahardjo, H. (2003). Total suction measurement of unsaturated soils with a device using chilled mirror dew-point technique. *Géotechnique*, 53(2), 173-182.
- Leong, E.C., Tripathy, S. and Rahardjo, H. (2004). Modified pressure plate apparatus. *ASTM Geotechnical Testing Journal*, 27(3), 322-331.
- Leong, E.C., Zhang, X-H. and Rahardjo, H. (2011). Calibration of a thermal conductivity sensor for field measurement of matric suction. *Géotechnique*, DOI:10.1680/geot.9.P.008.
- Leory, P. and Revil, A. (2004). A triple-layer model of the surface electrochemical properties of clay minerals. *Journal of Colloid and Interface Science*, 270, 371–380.
- Likos, W. J. and Lu, N. 2002. Filter paper technique for measuring total soil suction. *Transportation Research Record*, 1786, 120–128
- Linderson, F.T. and Piver, W.T. (1986). Vertical-horizontal transport and fate of low-solubility chemicals in unsaturated soils. *Journal of Hydrology*, 86, 93-131.
- Li, H., Peng, X., Wu, L., Jia, M. and Zhu, H. (2009). Surface potential dependence of the Hamaker Constant. *Journal of Physical Chemistry C*, 113, 4419–4425.
- Lloret, A., Villar, M.V., Sanchez, M., Gens, A., Pintado, X. and Alonso, E.E. (2003). Mechanical behaviour of heavily compacted bentonite under high suction changes. *Géotechnique*, 53(1), 27-40.
- Low, P.F. (1979). Nature and properties of water in montmorillonite-water systems. *Soil Science Society of American Journal*, 45, 651.
- Low, P.F. and Margheim, J.F. (1979). The swelling of clay. I. Basic concepts and empirical equations. *Soil Science Society of America Journal*, 43, 473-481.
- Low P.F. (1980). The swelling of clay: II montmorillonites. *Soil Science Society of America Journal*, 44(4), 667-676.

- Low, P.F. (1981). The swelling of clay: III. Dissociation of exchangeable cations. *Journal of the Soil Science Society America*, 45, 1074–1078.
- Lu, N. and Likos, W.J. (2004). *Unsaturated Soil Mechanics*. John Wiley and Sons, New Jersey,
- Man, A. and Martino, J.B. (2009). Thermal, hydraulic and mechanical properties of sealing materials. Atomic Energy of Canada Limited. Technical Report, TR-2009-20.
- Marcial, D., Delage, P. and Cui, Y.J. (2002). On the high stress compression of bentonites. *Canadian Geotechnical Journal*, 39, 812–820.
- Marcial, D. (2010). A simple method to consider water density changes in the calculation of the degree of saturation of swelling clays. *Unsaturated Soils - Alonso, E., Gens, A., (eds.), CRC press-Taylor and Francis Group, London*, 473-478.
- Madsen, F.T. and Müller-Vonmoos, M. (1985). Swelling pressure calculated from mineralogical of a Jurassic Opalium Shale, Switzerland. *Clay and Clay Minerals*, 33(6), 501-509.
- Madsen, F.T. (1989). Clay mineralogical investigation related to nuclear waste disposal. *Clay Mineral*, 33, 109-129.
- Madsen, F.T. and Müller-Vonmoos, M. (1989). The swelling behaviour of clays. *Applied Clay Science*, 4, 143-156.
- Marinho F.A.M. and Oliviera, O.M. (2006). The filter paper method revised. *ASTM Geotechnical Testing Journal*, 29(3), 250–258.
- Marshall, W.L. (2008). Dielectric constant of water discovered to be simple function of density over extreme ranges from – 35 to + 600oC and to 1200 MPa (12000 Atm.), Believed Universal. *Nature Proceedings*, doi:10.1038/npre.2008.2472.1.
- Martín, M., Cuevas, J. and Leguey, S. (2000). Diffusion of soluble salts under a temperature gradient after the hydration of compacted bentonite. 17, 55-70.
- Martin, R.T. (1960). Adsorbed water on clay: A review. *Clays and Clay Minerals*, 9, 28–70.

- McKeen, R.G. (1992). A model for predicting expansive soil behaviour. Proceedings of 7th International Conference on Expansive soils. Dallas, 1-6.
- Mesri, G. and Olsen, R.E. (1971). Consolidation characteristics of montmorillonite. *Géotechnique*, 21(4), 341–352.
- Marčelja, S. (1997). Hydration in electrical double layers. *Nature*, 385, 689-690.
- McCormack, D., Carnie, S. L., and Chan, D.Y.C. (1995). Calculations of electric double-layer force and interaction free energy between dissimilar surfaces. *Journal of Colloid and Interface Science*, 169, 177-196.
- Miller, S.E. and Low, P.F. (1990). Characterization of the electrical double layer of montmorillonite. *Langmuir*, 6(3), 572-578.
- Mishra, M., Schanz, T. and Tripathy, S. (2008). A column device to study THM behaviour of expansive soils. Proceedings of 12th International conference of International Association for Computer Methods in Advances in Geomechanics, 1149-1156.
- Mitchell, J.K. (1993). *Fundamentals of Soil Behaviour*, 2nd ed., John Wiley, New York.
- Mitchell, H.P. (2002). An investigation into the thermo/hydro/mechanical interactions involved in high level nuclear waste disposal, Ph.D thesis. University of Wales, Cardiff, U.K.
- Mitchell, J.K. and Soga, K (2005). *Fundamentals of Soil Behaviour*, 3rd ed., John Wiley, New York.
- Mooney, R.W., Keenan, A.G. and Wood, L.A. (1952). Adsorption of water in montmorillonite, II. *Journal of American Chemical society*, 74, 1371-1374.
- Müller-Vonmoos, M. and Kahr, G. (1982). *Bereitstellung von Bentonit für Laboruntersuchungen*, NTB 82-04, NAGRA, Wettingen, Switzerland.
- Müller-Vonmoos, K. and Kahr, G. (1983). *Mineralogische Untersuchungen von Wyoming Bentonit MX80 und Montigel*. NTB 83-12, NAGRA, Wettingen, Switzerland.

- Muurinen, A. (2009). Studies on the chemical conditions and microstructure in the reference bentonites of alternative buffer materials project (ABM) in Äspö. Posiva Oy.
- Muurinen, A., Karnland, O. and Lehtikainen, J. (2004). Ion concentration caused by an external solution into the porewater of compacted bentonite. *Physics and Chemistry of the Earth, Parts A/B/C*, 29(1), 119-127.
- Nagaraj, T.S. and Murthy, B.R.S. (1985). Prediction of preconsolidation pressure and compression index of soils. *Geotechnical Testing Journal*, 8(4), 199-203.
- Nassar, I.N and Horton, R. (1989). Water transport in unsaturated nonisothermal salty soils. I. Experimental results. *Soil Science Society of American Journal*, 53, 1323-1329.
- Nekrasova, É.G., Zhilenkov, I.V. and Fedorov, V.M. (1968). On the dielectric constant of sorption-structured water. *Journal of Structural Chemistry*, 9(3), 340-343.
- Nielson, D.R., Van Genuchten, M. and Biggar, J.W. (1986). Water flow and transport processes in the unsaturated zone. *Water Resources Research*, 22(9), 89s-108s.
- Nichol, C., Leslie, S. and Beckie, R. (2003). Long-term measurement of matric suction using thermal conductivity sensors. *Canadian Geotechnical Journal*, 40, 587-597.
- Norrish, K. and Quirk, J.P. (1954). Crystalline swelling of montmorillonite. *Nature*, 173, 255-256.
- Nuclear Decommissioning Authority (NDA), (2009). Geological Disposal; Generic Design Assessment: Summary of disposability assessment for wastes and spent fuel arising from operation of the UK EPR. NDA Technical note no. 11261814.
- Olivella, S., Carrera, J., Gens, A. and Alonso, E. E. (1994). Nonisothermal multiphase flow of brine and gas through saline media. *Transport in Porous Media* 15(3), 271–293.
- Oliverira, O.M. and Fernando, F.A.M (2006). Study of equilibrium time in pressure plate. *Proceedings of 4th International Conference on Unsaturated soil*, Eds. Miller, A.G., Zapata, C.E., Houston, S.L. Fredlund, D.G., 1864-1874.

- Owen, D.R.J. and Hinton, E. (1980). Finite elements in plasticity: Theory and practice, Pineridge Press Ltd., Swansea.
- Pan, H., Qing, Y. and Yong, L.P. (2010). Direct and Indirect measurement of suction in the laboratory. *Electronic Journal of Geotechnical Engineering*, 15, 1-14.
- Pashley, R.M. (1981). DLVO and hydration forces between mica surfaces in Li⁺, Na⁺, K⁺, and Cs⁺ electrolyte solutions: A correlation of double-layer and hydration forces with surface cation exchange properties. *Journal of Colloid and Interface Science*, 83(2), 531-546.
- Péron, H., Hueckel, T. and Laloui, L. (2007). An improved volume measurement for determining soil water retention curves. *ASTM Geotechnical Testing Journal*, 30(1), 1-8.
- Preece, R.J. (1975). The measurement and calculation of physical properties of cable bedding sands. Part 2; specific thermal capacity, thermal conductivity and temperature ratio across 'air' filled pores, C.E.G.B. Laboratory Note No., RD/L/N 231/74.
- Philip, J.R. and de Vries, D.A. (1957). Moisture movement in porous materials under temperature gradients. *Transactions American Geophysical Union*, 38, 222-232.
- Pintado, X., Ledesma, A. and Lloret, A. (2000). Backanalysis of thermohydraulic bentonite properties from laboratory tests. *Engineering Geology*, 64, 91-115.
- Pollock, D.W. (1986). Simulation of fluid flow and energy transport processes associated with high-level radioactive waste disposal in unsaturated alluvium, *Water Resources Research*, 22(5), 765-775.
- Pusch, R. (1980). Swelling pressure of highly compacted bentonite. SKB Technical report, TR-80-13.
- Pusch, R. (1982). Mineral-water interactions and their influence on the physical behaviour of highly compacted Na bentonite. *Canadian Geotechnical Journal*, 19, 381-387.

- Pusch, R. (2001). The microstructure of MX-80 clay with respect to its bulk physical properties under different environmental conditions. SKB Technical report , TR-01-08.
- Pusch, R. and Carlsson, T. (1985). The physical state of pore water of Na smectite used as barrier component. *Engineering Geology*, 21, 257-265.
- Pusch, R., Karliland, O. and Hokmark, H. (1990). GMM-a general microstructural model for qualitative and quantitative studies of smectite clays. SKB Technical Report 90-43, Stockholm, Sweden.
- Pusch, R. and Moreno, L. (2001). Saturation and permeation of buffer clay. *Proceedings of 6th international workshop on Key Issues in Waste Isolation Research*, Paris, 71–81.
- Pusch, R. and Yong, R.N. (2006). *Microstructural behaviour of smectite clay*, Taylor and Fransis, London.
- Pusch, R., Kasbohm, J. and Thao, H.T.M. (2010). Chemical stability of montmorillonite buffer clay under repository-like conditions-A synthesis of relevant experimental data. *Applied clay science*, 47, 113-119.
- Rahardjo, H. and Leong, E.C. (2006). Suction measurement. Keynote, *Unsat 2006*, ASCE Geotechnical Special Publication, 147(1), 81-104.
- Richards, L.A. (1941). A pressure membrane extraction apparatus for soil suction. *Soil Science*, 51, 377–386.
- Richards, B.G. (1965). Measurement of the free energy of soil moisture by the psychrometric technique using thermistors. In *Moisture Equilibria and Moisture Changes in Soils Beneath Covered Areas*, A Symposium in Print, Butterworths, Australia, 39-46.
- Ridley, A.M. and Wray, W.K. (1996). Suction measurement: a review of current theory and practices. In *Proceedings of the 1st International Conference on Unsaturated Soils (UNSAT 95)*, Paris, 1995 (Eds. E.E. Alonso and P. Delage), Balkema, Rotterdam: 1293-1322.

- Ridley, A.M., Dineen, K., Burland, J.B. and Vaughan, P.R. (2003). Soil matrix suction: some examples of its measurement and application in geotechnical engineering. *Géotechnique*, 53(2), 241–253.
- Roffey, R. (1990). The Swedish final repository and the possible risk of interactions by microbial activities. *Experientia*, Birkhäuser Verlag, CH-4010 Basel/ Switezerland, 46, 792-794.
- Romero, E. (1999). Characterisation and Thermo-hydro-mechanical behaviour of unsaturated Boom clay: An experimental study, PhD Thesis, Universitat Polytechnica de Catalunya, Barcelona.
- Romero, E. Gens, A. and Lloret, A. (2000). Temperature effects on water retention and water permeability of an unsaturated clay. *Proceeding of Unsaturated Soils for Asia* (Eds.Rahardjo, Toll and Leong), Balkema, Rotterdam, 433-438.
- Romero E., Gens A. and Lloret A. (2003). Suction effects on a compacted clay under nonisothermal conditions. *Géotechnique*, 53(1), 65-81.
- Romero, E., Villar, M.V. and Lloret, A. (2005). Thermo-hydro-mechanical behaviour of two heavily overconsolidated clays. *Engineering Geology*, 81, 255-268.
- Roscoe, K.H. and Scholfield, A.N. (1963). Mechanical behaviour of an idealized wet clay. *Proceedings of 2nd European Conference on Soil Mechanics and Foundation Engineering*. Wiesbaden, 1, 47-53.
- Rowe, R.K., Quigley, R.M. and Booker, J.R. (1995). *Clayey Barrier Systems for Waste Disposal Facilities*. E and FN Spon, London.
- Millard, A., Rejeb, A., Chijimatsu, M., Jing, L., De Jonge, J., Kohlmeier, M., Nguyen, T.S., Rutqvist, J., Souley, M. and Sugita, Y. (2004). Evaluation of THM Coupling on the Safety Assessment of a Nuclear Fuel Waste Repository in a Homogeneous Hard Rock. *Coupled Thermo-Hydro-Mechanical-Chemical Processes in Geo-Systems*, 2, 211-216.

- Saiyouri, N., Hicher, P. Y. and Tessier, D. (1998). Microstructural analysis of highly compacted clay swelling. Proceedings of 2nd international conference on Unsaturated Soils, Beijing, 1, 119–124.
- Saiyouri, N., Hicher, P. Y. and Tessier, D. (2000). Microstructural approach and transfer water modelling in highly compacted unsaturated swelling clays. *Mechanics of Cohesive Frictional Material*, 5, 41–60.
- Saiyouri N, Tessier, D. and Hicher P.Y. (2004). Experimental study of swelling in unsaturated compacted clays. *Clay Minerals*, 39, 469-479.
- Samper, J., Juncosa, R., Navarro, V., Delgado, J., Montenegro, L. and Vázquez, A. (2001). Coupled thermo-hydro-geochemical models of engineered barrier systems: The Febex Project. Material Research Society, Sydney, 1-13.
- Samper, J., Zheng, L., Montenegro, L., Fernandez, A.M. and Rivas, P. (2008). Coupled thermo-hydro-chemical models of compacted bentonite after FEBEX in situ test. *Applied Geochemistry*, 23, 1186-1201.
- Schanz, T. and Tripathy, S. (2009). Swelling pressure of a divalent-rich bentonite: Diffuse double-layer theory revisited. *Water Resources Research*, 45, W00C12, doi:10.1029/2007WR006495.
- Schofield, A. and Wroth, P. (1968). *Critical state soil mechanics*, McGraw-Hill, London.
- Seetharam, S.C. (2003). An investigation of the thermo/hydro/chemical/mechanical behaviour of unsaturated soils. PhD thesis, Cardiff School of Engineering, UK.
- Selvadurai, A.P.S. (1996). Heat-induced moisture movement in a clay barrier I. Experimental modeling of borehole emplacement. *Engineering Geology*, 41, 239-256.
- Shang, J.Q., Lo, K.Y. and Quigley, R.M. (1994). Quantitative determination of potential distribution in Stern-Gouy double-layer model. *Canadian Geotechnical Journal*, 31, 624-636.
- Sharma, H. and Reddy, K. (2004). *Geo-Environmental Engineering, Site Remediation, Waste Containment, and Emerging Waste Management Technologies*. Wiley.

- Shaw, B. and Baver, L.D. (1939). An electro-thermal method for following moisture changes of the soil in situ. In *Proceedings of Soil Science Society of America*, 4, 78-83.
- Singh, R.M. (2007). An experimental and numerical investigation of heat and mass movement in unsaturated clays, Ph.D Thesis, School of Engineering, Cardiff University.
- Skipper, N.T., Refson, K. and McConnell, J.D.C. (1991). Computer simulation of interlayer water in 2:1 clays. *Journal of chemical physics*, 94(11), 7434-7445.
- Sposito, G. (2008). *The chemistry of soils*. 2nd ed. Oxford University press, New York.
- Sridharan, A., Altschaeffl, A.G. and Diamond, S. (1971). Pore size distribution studies. *Journal of Soil Mechanics and Foundation Division, Proc. ASCE*, 97, 771-787.
- Sridharan, A. (1968). Some studies on the strength of partly saturated clays. Ph.D. thesis, West Lafayette: Purdue University.
- Sridharan, A. and Jayadeva, M.S. (1982). Double layer theory and compressibility of clays. *Géotechnique*, 32 (2), 133– 144.
- Sridharan A., Rao, A.S. and Sivapullaiah P.V. (1986). Swelling pressure of clays. *ASTM Geotechnical Testing Journal*, 9(1), 24-33.
- Sridharan, A. and Choudhury, D. (2002). Swelling pressure of sodium montmorillonites. *Géotechnique*, 53(4), 449.
- Sridharan, A. and Satyamurty, P.V. (1996). Potential-distance relationship of clay-water systems considering the Stern theory. *Clays and Clay Minerals*, 44(4), 479-484.
- Sridharan, A. and Rao, G.V. (1973). Mechanisms controlling volume change of saturated clays and the role of effective stress concept. *Géotechnique*, 23, 359–382.
- Steefel, C., Rutqvist, J., Tsang, C.H., Liu, H.H., Sonnenthal, E., Houseworth, J. and Birkholzer, J. (2010). Reactive transport and coupled THM processes in Engineering Barrier System (EBS). Lawrence Berkeley National Laboratory. Technical report, LBNL-3901E.

- Stern, O. (1924). Zur theorie der elektolytischen doppelschicht. Zeitschrift Electrochem, 30, 508-516.
- Shuai, F., Fredlund, D.G. and Samarasekera L. (2003). Numerical simulation of water movement in the suction equalization of a thermal conductivity sensor. ASTM Geotechnical Testing Journal, 26(2), 142-151.
- Suzuki, S., Sato, H., Ishidera, T. and Fujii, N. (2004). Study on anisotropy of effective diffusion coefficient and activation energy for deuterated water in compacted sodium bentonite. Journal of Contaminant Hydrology, 68(1-2), 23-37.
- Swedish Nuclear Fuel and Waste Management Company, (1983). Final storage of spent nuclear fuel-KBS-3, III barriers, KBS Technical report 9:1– 16:12, Stockholm.
- Tang, A.M. and Cui, .J. (2005). Controlling suction by the vapour equilibrium technique at different temperature and its application in determining the water retention properties of MX 80 clay. Canadian Geotechnical Journal, 42, 287-296.
- Tang, A.M., Cui, Y.J. and Le, T.T. (2008). A study on the thermal conductivity of compacted bentonites. Applied Clay Science, 41, 181-189.
- Tang, A.M. and Cui, Y.J. (2010). Effects of mineralogy on thermo-hydro-mechanical parameters of MX80 bentonite. Journal of Rock Mechanics and Geotechnical Engineering, 2(1), 91 – 96.
- Tang, G.X., Graham, J., Blatz, J., Gray, M., and Rajapakse, R.K.N.D. (2002). Suctions, stresses and strengths in unsaturated sand-bentonite. EngineeringGeology, 64,147-156.
- Tarantino, A., Gallipoli, D., Augarde, C.E., De Gennaro, V., Gomez, R., Laloui, I., Mancuso, C., El Mountassir, G. Munoz, J.J., Pereira, J.M., Peron, H., Pisoni, G., Romero, E., Raveendraraj, A., Rojas, J.C., Toll, D.G., Tombolato, S. and Wheeler, S. (2011). Benchmark of experimental techniques for measuring and controlling suction. Géotechnique, 61(4), 303-312.

- Thomas, G.W. (1982). Exchangeable cations. Methods of soil analysis, Part 2, 2nd ed Agronomy Monograph 9, American Society of Agronomy, Madison, WI.
- Thomas, H.R. (1985). Modelling two-dimensional heat and moisture transfer in unsaturated soils, including gravity effects. *International Journal of Analytical Methods in Geomechanics*, 9, 573-588.
- Thomas, H.R. and Cleall, P.J. (1997). Chemico-osmotic effects on the behaviour of unsaturated expansive clays. *Geoenvironmental engineering, Contaminated ground; fate of pollutants and remediation*. Yong, R.N. and Thomas, H.R., eds., Thomas Telford, London, 272-277.
- Thomas, H.R. and Cleall, P.J. (1999). Inclusion of expansive clay behaviour in coupled thermo hydraulic mechanical models. *Engineering Geology*, 54, 93-108.
- Thomas, H.R. and King, S.D. (1991). Coupled temperature/capillary potential variations in unsaturated soil. *Journal of Engineering Mechanics, American Society of Civil Engineers*, 117(11), 2475-2491.
- Thomas, H.R. and He, Y. (1994). An elasto-plastic analysis of the thermo/hydraulic/mechanical behaviour of unsaturated soil. *Proceedings of the 8th International Conference on Computer Methods and Advances in Geomechanics, Morgantown*. Siriwardane, H.J. and Zaman, M.M. eds., Balkema, Rotterdam, 1171-1176.
- Thomas, H.R. and He, Y. (1995). Analysis of coupled heat, moisture and air transfer in a deformable unsaturated soil. *Géotechnique*, 45(4), 677-689.
- Thomas, H.R. and Li, C.L.W. (1997). An assessment of a model of heat and moisture transfer in unsaturated soil. *Géotechnique*, 47(1), 113-131.
- Thomas, H.R. and Rees, S.W. (1990). An examination of the performance of a 3-level time stepping algorithm – Coupled heat and mass transfer computing. *Proceedings of the 1st International Conference, Advances in Computer Methods in Heat Transfer, Southampton, U.K.*

- Thomas, H.R., Rees, S.W. and Sloper, N.J. (1998). Three-dimensional heat, moisture and air transfer in unsaturated soils. *International Journal of Numerical and Analytical Methods in Geomechanics*, 22(2), 75-95.
- Thomas, H.R. and Rees, S.W. (1993). The numerical simulation of seasonal soil drying in an unsaturated clay soil. *International Journal of Numerical and Analytical Methods in Geomechanics*, 17(1), 119-132.
- Thomas, H.R. and Sansom, M.R. (1995). Fully coupled analysis of heat, moisture and air transfer in unsaturated soil. *Journal of Engineering Mechanics, ASCE*, 121(3), 392-405.
- Thomas, H.R., Cleall, P.J., Chandler, N., Dixon, D. and Mitchell, H.P. (2003). Water infiltration into a large-scale in-situ experiment in an underground research laboratory. *Géotechnique*, 53 (2), 207–224.
- Tripathy, S., Sridharan, A. and Schanz, T. (2004). Swelling pressures of compacted bentonites from diffuse double layer theory. *Canadian Geotechnical Journal*, 41, 437-450.
- Tripathy, S. and Schanz, T. (2007). Compressibility behaviour of clays at large pressures. *Canadian Geotechnical Journal*, 44, 355-362.
- Tripathy, S., Bag, R. and Thomas, H.R. (2010). Desorption and Consolidation Behaviour of Initially Saturated Clays. In *proceedings of Fifth International Conference on Unsaturated Soils, Barcelona*, Eds. Alonoso, E., Gens, A., 381-386.
- van Genuchten, M.Th. (1980). A closed-form equation for predicting the hydraulic conductivity of unsaturated soils. *Soil Science Society of America*, 44(5), 892-898.
- Vanapalli, S.K., Fredlund, D.G. and Pufahl, D.E. (1999). The influence of soil structure and stress history on the Soil-Water characteristics of a compacted Till. *Géotechnique*, 49(2), 143-159.
- van Olphen, H. (1977). *An Introduction to Clay Colloid Chemistry: For Clay Technologists, Geologists and Soil Scientists*, 2nd ed., Wiley-Interscience, New York.

- Vardon, P.J. (2009). A three-dimensional numerical investigation of the thermo-hydro-mechanical behaviour of a large-scale prototype repository. PhD Thesis, Cardiff University.
- Vašíček, R. (2010). The thermal conductivity of highly compacted bentonite in the fully saturated state. *Clays in Natural & Engineered barriers for radioactive waste confinement- 4th International meeting*, Nantes, France, 709-710.
- Vaunat, J. and Gens, A. (2007). Analysis of the hydration of a bentonite seal in a deep radioactive waste repository. *Engineering Geology*, 81, 317-328.
- Verwey, E.J.W. and Overbeek, J.Th.G. (1948). *Theory of the stability of lyophobic colloids*. Elsevier, Amsterdam.
- Villar, M.V. (2000). *Caracterización termo-hidro-mecánica de una bentonita de cabo de gata*. Tesis de doctorado, Universidad complutense de Madrid, España.
- Villar, M.V., Cuevas, J. and Martin, P.L. (1996). Effects of heat/water flow interaction on compacted bentonite: Preliminary results. *Engineering Geology*, 41, 257-267.
- Villar, M.V. and Lloret, A. (2004). Influence of temperature on the hydro-mechanical behaviour of a compacted bentonite. *Applied Clay Science*, 26, 337-350.
- Villar, M.V., Fernández, A.M., Gómez, R., Barrenechea, J.F., Luque, J.F., Martín, P.L. and Barcala, J.M. (2007). State of bentonite barrier after 8 years of heating and hydration in the laboratory. *Materials Research Society, Symposium Proceedings*. Vol. 985.
- Villar, M.V., Sánchez, M. and Gens, A. (2008). Behaviour of a bentonite barrier in the laboratory: experimental results up to 8 years and numerical simulation. *Physics and Chemistry of Earth* 33, S 476–S 485.
- Villar, M.V. and Lloret, A. (2008). Influence of dry density and water content on the swelling of a compacted bentonite. *Applied Clay Science*, 39, 38–49.
- Wang, P. and Anderko, A. (2001). Computation of dielectric constants of solvent mixtures and electrolyte solutions. *Fluid Phase Equilibria*, 186, 103-122.

- Winterkorn, H.F. and Reno, W.H. (1967). The thermal conductivity of kaolinite clay as a function of type of exchange ion, density and moisture content. Soil Science, Highway Research Board, Washington, USA, 79-85.
- Yang, N. and Barbour, S.L. (1992). The impact of soil structure and confining stress on the hydraulic conductivity of clays in brine environments. Canadian Geotechnical Journal, 29, 730-739.
- Yong, R.N. (1999). Soil suction and soil-water potentials in swelling clays in engineered clay barriers. Engineering Geology, 54, 3-13.
- Yong, R.N. and Mohammed, A.M.O. (1992). A study of particle interaction energies in wetting of unsaturated expansive clays. Canadian Geotechnical Journal, 29, 1060-1070.
- Yong, R.N., Mohammed, A.M.O., Shooshapasha, I. and Onofrei, C. (1997). Hydrothermal performance of unsaturated bentonite-sand buffer material. Engineering Geology, 47, 351-365.
- Yong, R.N., Mulligan, C.N. and Fukue, M. (2006). Geoenvironmental Sustainability. CRC Press, Taylor and Francis.
- Zhang, Z.Z., Sparks, D.L. and Scrivner, N.C. (1994). Characterization and modeling of Aioxide/ aqueous solution interface: 1. Measurement of electrostatic potential at the original of diffuse layer using negative adsorption on Na⁺ ions. Journal of Colloid Interface Science, 162, 244–251.
- Zur, B. (1966). Osmotic control of soil water matric potential. I. Soil-water system. Soil Science 102, 394–398.